Atomic Sensors for Plasma Field Diagnostics and for Inertial Measurement

by

Bineet Kumar Dash

A dissertation submitted in partial fulfillment
of the requirements for the degree of
Doctor of Philosophy
(Physics)
in The University of Michigan
2026

Doctoral Committee:

Professor Georg Raithel, Chair
Professor Scott Baalrud
Assistant Professor Alex Burgers
Professor Tim Chupp
Assistant Professor Shankari Rajagopal

Bineet Kumar Dash
bkdash@umich.edu
ORCID iD: 0000-0001-8184-8414

© Bineet Kumar Dash 2026

To my loving family and to the cherished memory of my mother.

ACKNOWLEDGEMENTS

My graduate school years held many ups and downs, including a global pandemic, and I have been carried through them by many wonderful people who made this work possible.

First and foremost, I am profoundly grateful to my advisor, Prof. Georg Raithel, an extraordinary physicist and mentor. With his mastery over every aspect of modern physics, from theories and nimble Fermi estimates to keen engineering and experimental insights, Georg brought textbook principles to life during every meeting. I have benefited immeasurably from the countless hours he spent helping me at each stage of this work; from building vacuum chambers and fixing lasers to wrestling with simulations. He always had an explanation for the next bump along the way, the odd feature in a spectrum, the small quirks that AMO experiments delight in throwing at us. I am truly grateful for his patience through the initial months as I transitioned to AMO experiments, when rubidium stubbornly refused to survive in the plasma experiment, and through every long stretch in between. As we embarked on the first plasma experiment in our group, Georg generously shared his boundless expertise, from Smith charts to plumbing, compressing into weeks what would have taken me months. He supported my journey into plasma physics, and cultivated a warm, collaborative group in which I learned a great deal of AMO physics from the people around me. He has set an enduring example that I will try to emulate for years to come.

My PhD trajectory and my time in the Raithel Lab were remarkably enriched by the senior graduate students I had the fortune of working with. In the early years, Ryan Cardman and Alisher Duspayev set superlative models of researchers with their work ethic, curiosity, and generosity. Thank you, Ryan, for sharing your encyclopedic knowledge of AMO physics and every experiment in the lab. You once told me that every AMO experiment should feel doable by the end of a PhD, and you embodied that standard so completely that I have spent years trying to live up to it. Alisher was instrumental in helping me join the Raithel Lab during the difficult pandemic years, offered sage advice at every turn (including the early conviction that the plasma project was worth pursuing, long before I could see where it would lead), and gave generously of his time on each aspect of research: from instrumentation to project management to writing. My career trajectory would have been entirely different but for Alisher. Thank you for believing in me and showing me the ropes, for the many ideas we have discussed about our experiments and careers, for the lunches and coffees, and for

always being a text away, even after you graduated. It was one of the great gifts of graduate school to find in you a colleague, a mentor, and a dear friend.

My later years in the Raithel Lab brought many new faces: Lefeng Zhou, Carlos Owens, Xinyan Xiang, Shuaijie Li, Anne Graf, and Xinyu Feng. Xinyan joined me in the SB-283 experiments for my last couple of years and, within a few months, had taken full ownership of the cold-atom-based 3D ion microscope project. Xinyan, I have been thoroughly impressed by your sincerity, work ethic, and diligence. I benefited enormously from bouncing ideas off you, from your careful work on so many electronics and optics projects, and from the long hours we spent taking data together. I take real comfort in your stewardship of the ion imaging experiment, which goes unmentioned in this thesis and still has many challenges ahead of it. I am truly grateful for your warmth and friendship as I look forward to the years ahead, both to our collaborations and to watching you grow as a scientist. I have learned a great deal from Lefeng's engineering and experimental instincts. Thank you, Lefeng, for sharing your expertise in CAD, finite element simulations, RF, and BEC physics. Although we worked on different projects, I have enjoyed many warm conversations with Carlos, Shuaijie, and Anne: the troubleshooting sessions, the feedback on writing and presentations, chats at DAMOP and many coffee hours. And I spent many evenings with Xinyu in stimulating discussions of AMO concepts and the design of his upcoming tweezer experiment. Xinyu, I am inspired by your work ethic and your desire to understand things from first principles. I spent more than a year working with Dingkun, who diligently learned every aspect of the EIT experiment and ran many underlying FEM simulations. I also thank Ian Hoffman, Bingkun Yu and Ansh Shah, who contributed to projects in our group during their undergraduate years.

Beyond the lab, I am grateful to several collaborators for invaluable contributions to papers and projects. Eric Paradis and Nithiwadee Thaichaoren gave the plasma project early momentum with vapor cell experiments and many discussions. I sincerely thank Michael Goerz, Sebastian Carrasco, and Vladimir Malinovsky for their collaboration on the TAI project. I would also like to thank my committee members Alex Burgers, Tim Chupp, Scott Baalrud and Shankari Rajagopalan for serving on my committee and suggesting improvements to my dissertation. I am grateful for the various sources of my funding over the past six years: DOE, NASA, NSF, the Rackham International Fellowship and the Norman E and Mary E Barnett Fellowship. I owe special thanks to Dave Anderson, Jim Carey and Luís Gonçalves for their mentorship during my internship at Rydberg Technologies. This experience proved invaluable in shaping my aspirations and future career trajectory. My cohort members made the department a vibrant and welcoming place. I am grateful for the time I shared with Gabriela Martin, Nicholas Kyriacou, Avik Mondal, Blake Hipsley, Xiaoyu Guo, Taigao Ma, Sergio Garcia, Joseph Hollowed, and Jem Guhit. And I owe thanks to Cory Steiner, Paul

Thurmond and Heather Wolfe who kept the department running smoothly.

I have been equally fortunate to have an incredible support system outside the lab. Janak, Arpit, Sindhu, Bibhu, Rishav, Vikramjit, Pappus, Diptanil, Abhishek, and Subhobrata, thank you all for carrying me through these years. Janak, no words I write here will quite portray what your friendship has meant to me, through years of being flatmates, gym partners, and travel buddies in our adventures from the Upper Peninsula to the Rockies to the High Sierra, as we navigated PhD together. So many times my loose-footed worries have melted away in our radiantly optimistic conversations over lunches and trips. Looking back, it is a quiet wonder that I stumbled into a brother in the trench of graduate school. And thank you, Sindhu, for your warmth and for the quiet way you and Janak have shown me how to take on life and its curve-balls with cheerful aplomb. Arpit, your incessant creativity, your deep feel for academia and methods of research, and your exuberant willingness to help have been a real inspiration. Your delicious biryanis fueled many of my writing sessions. Rishav set an early example of a passionate scholar - thank you for the long evenings of conversation across every subject under the sun, and for the wisdom you shared about science and life as a researcher that has only grown truer with time. To Pappus, Diptanil, Abhishek, and Subho — thank you for staying with me through more than a decade of this journey, even as life scattered us across the world. I am painfully aware that I am leaving many others out in this non-exhaustive list.

My journey from rural India to this point would not have been possible without the steady support of my family, and most of all my father, Asita Dash. He sparked my love for science and carefully tended to it, as we built kaleidoscopes, took apart and fixed motors, and charted the night sky together when I was small. His thoughtful attention and steady encouragement have lifted me through all these years. Even today he tries to learn about modern academia, my research, and the questions that keep me up at night, with the same patience and delight that he once brought to my earliest curiosities. Whatever I have built in this life rests on a foundation he laid.

Finally, to my partner Sania : words will fall short to express my gratitude for the life you chose to share with me, bridging continents and cultures with an open heart, and fighting through endless bureaucratic nightmares. Your steadfast support and tender warmth carried me through many trying times; your tenacity and courage made the future look larger than any problems; your far-reaching curiosity nourished my own sense of wonder through dreary years. And you did all this while pursuing your own PhD. I am grateful for the awe we have shared at many a sunset, at the rich tapestry of landscapes we explored, at the wonders we chased in our labs, and at the beauty of life. I look forward to the chapters ahead with sheer excitement and the deepest gratitude for the serendipity of having met you.

TABLE OF CONTENTS

DEDICATION ii

ACKNOWLEDGEMENTS iii

LIST OF FIGURES ix

LIST OF TABLES xi

LIST OF ACRONYMS xii

ABSTRACT xiv

CHAPTER

1 Introduction 1

1.1 Rydberg atoms for plasma diagnostics 3
1.2 Thesis Outline 5

2 Atomic Physics Background 6

2.1 Hydrogen-like Atom 6
2.1.1 Alkali atoms 9
2.1.2 Metastable Argon atoms 11
2.2 Interaction with electromagnetic field 15
2.2.1 Magnetic fields 15
2.2.2 Stark Effect 15
2.3 Interaction with radiation 16
2.3.1 Atom ensembles as a dispersive medium 17
2.3.2 Two-level atom 18
2.3.3 Three-level atoms 22
2.4 Spectroscopy with room temperature atoms 26
2.4.1 Rydberg-EIT in thermal vapor 27

3 Physics of Rydberg Atoms and Plasma 29

3.1 Rydberg atoms 29
3.1.1 Quantum Defects 29
3.1.2 Scaling Laws 30
3.2 Collision theory of Rydberg atoms 33

3.2.1 Origin of line shapes . . . 34
3.2.2 Collisional Broadening in the Impact Approximation . . . 34
3.2.3 Elastic Collisions: Phase-Shift Representation . . . 35
3.2.4 Inelastic Collisions . . . 36
3.3 Plasma Physics . . . 38
3.3.1 Collective electrostatics . . . 38
3.3.2 Electron and Ion Energy Distributions . . . 40
3.3.3 The Plasma Sheath . . . 40
3.3.4 Collisional Processes . . . 41
3.3.5 Global Balance . . . 42
3.3.6 Radio-Frequency Driven Plasmas . . . 44

4 Rydberg-EIT in Inert Gas Background . . . 47

4.1 Introduction and Motivation . . . 47
4.2 Methods . . . 48
4.3 Results . . . 50
4.4 Semiclassical Model . . . 53
4.4.1 Inelastic cross-sections with Fermi Pseudopotential . . . 58
4.4.2 Validity of semiclassical model . . . 60
4.5 Effects beyond the Fermi pseudopotential treatment . . . 61
4.5.1 Relaxation effects at high pressures . . . 61
4.5.2 Shielding of photoinduced electric field . . . 62
4.6 Conclusion . . . 65

5 Plasma Field Measurement Using Rydberg Atoms . . . 67

5.1 Motivation . . . 67
5.2 Experimental Methods . . . 70
5.2.1 The Inductively Coupled Plasma Source . . . 70
5.2.2 UHV Plasma Chamber . . . 72
5.2.3 EIT spectroscopy . . . 75
5.3 Rydberg atom in ICP antenna without plasma . . . 76
5.3.1 Analysis . . . 78
5.3.2 Simulation . . . 80
5.4 Rydberg atoms in plasma . . . 82
5.4.1 Rydberg-plasma interaction . . . 83
5.5 Conclusion . . . 93

6 Tractor Atom Interferometry . . . 95

6.1 Introduction and Motivation . . . 96
6.2 Pinwheel optical lattice design . . . 97
6.3 Operation . . . 101
6.4 Numerical Simulation . . . 105
6.4.1 Quantum methods . . . 105
6.4.2 Path integral method . . . 106
6.4.3 Rotation sensitivity . . . 108

6.5 Nonadiabatic effects in lattice spin-up and -down 109
6.5.1 Optimal Control 114
6.6 Conclusion 115
7 Conclusion and Outlook 116
7.1 Tractor Atom Interferometry 117
7.2 Rydberg atoms for plasma physics 117
Appendix A Generalized Crout Reduction 120
BIBLIOGRAPHY 122

LIST OF FIGURES

FIGURE

2.1 Energy level structure of rubidium 12
2.2 Energy level structure of argon 14
2.3 Atom-light interaction in a three-level cascade configuration 22

3.1 Stark map of ^{85}Rb (a) in the range between 26H and 27H manifolds, (b) for the $28D$ state 32

4.1 (a) Energy levels of ^{85}Rb used in our experiment. The probe laser (λ_p =780 nm) is locked to the $5S_{1/2}, F = 3 \leftrightarrow 5P_{3/2}, F' = 4$ resonance, and the coupling laser is scanned across the $5P_{3/2} \leftrightarrow 36D_{5/2}$ transition. (b) Experimental setup. Some elements are omitted for simplicity. 48
4.2 Rydberg-EIT spectra for selected Argon pressures 51
4.3 Rydberg-EIT spectra for selected Neon pressures. 52
4.4 Rydberg-EIT spectra for selected Nitrogen pressures 53
4.5 Absolute values of EIT line shift in the inert-gas-filled cells versus pressure . . . 54
4.6 Full widths at half maxima (FWHM) of the EIT line in the inert-gas-filled cells versus pressure 55
4.7 EIT spectra in 5 Torr Neon (a) direct vs lock-in measurement, (b) temperature dependence. 62
4.8 Relaxation effects in 5 Torr Neon. Dependence on (a) coupler scan rate and (b) coupler scan direction 63
4.9 Transient response of EIT at high inert gas pressure, measured as time-resolved transmission of the frequency-locked probe laser with a pulsed coupler laser. . . 63
4.10 (a) Experimental setup and (b) energy level diagram for three-color Rydberg-EIT in inert gas cells 65
4.11 Rydberg-EIT with the rf-coupled triplet $25F_{5/2} \leftrightarrow 25H_{9/2} \leftrightarrow 25I_{11/2}$ (left column) and with the $50F_{5/2}$ state (right column), without and with the 453-nm light shone onto the cell walls 66

5.1 (a) Schematic of the experimental setup for plasma discharge and EIT spectroscopy. (b) The plasma chamber, as viewed into the glass dome. 69
5.2 Transient effects in Rb vapor density upon plasma ignition at moderate rf power. 74
5.3 (a) Illustration of the discharge volume and EIT interrogation region, (b) Rb energy levels used in this work. 75
5.4 Fields arising inside the ICP chamber from applied rf power. 77
5.5 Measured Rydberg-EIT spectra (solid lines) of Rb $27S_{1/2}$ without plasma. . . . 78

5.6 Within Ar plasma, the rf fields are shielded due to the skin effect, leaving the stochastic microfield as the dominant field. The microfield distribution is given by the Holtsmark distribution (inset). 83
5.7 Rydberg-EIT spectra of Rb $27S_{1/2}$ in plasma generated from 12 mTorr of argon 84
5.8 Rydberg-EIT spectra of Rb $30S_{1/2}$ (a) without plasma and (b) in plasma generated from 12 mTorr of argon. 84
5.9 Incorporating radial plasma density variation into line shape analysis. (a) A representative, background-subtracted plasma emission profile, (b) Averaged intensity profile in region of interest, (c) Refraction effects from ray tracing, (d) the recovered radial emissivity $\varepsilon(r) \propto n_e(r)$ following Abel inversion. 89
5.10 Plasma parameters extracted from Rydberg-EIT spectra for $25S_{1/2}$. (a) Central plasma density n_e extracted from the Holtsmark part of the fits, (b) Collisional broadening rate is estimated from $2\pi\gamma/n_e$. 90
5.11 Electron density from Fig. 5.10, plotted vs Ar pressure, reflecting the increase in power absorption for $p \gtrsim 25$ mTorr. 91
5.12 Optical emission spectrum of the Ar discharge with and without Rb present. . . 93

6.1 Concept of TAI as a Sagnac rotation sensor. 97
6.2 An 8-site pinwheel ^{87}Rb optical lattice is created from LG_{20} and LG_{28} laser modes: (a) Optical potential in the $r - z$ plane. (b) Optical potential in the transverse plane at the focus $z = 0$. (c) Potential along the radial direction for $z = 0$ and $\theta = 0$ and $\pi/8$. (d) Potential along the azimuthal direction 100
6.3 Adiabatic wave-function evolution in a rotating pinwheel optical lattice (a) Expectation value of the azimuthal displacement of the wave packets relative to the initial position, (b) Momentum expectation value in the lab frame, (c) Azimuthal-angle expectation value of the wave packet components in the lattices' moving frames, (d) Angular-momentum expectation value in the moving frame, *i.e.*, average angular momentum relative to $\pm I\omega(t)$. 104
6.4 Interferometric response of TAI in a pinwheel optical lattice to a constant background rotation Ω for $V_0 = h\times 2.2\,\mathrm{MHz}$, $t_r = 100\,\mathrm{ms}$, and $T = 300\,\mathrm{ms}$. Population in $|-\rangle$ for a recombination after (a) $n = 2$ cycles, (b) $n = 10$ cycles 107
6.5 Fidelity of the initial splitting operation for varying separation time t_r and V_0 of the trapping potential. The separation fidelity is the overlap of the state $|\Psi(t_r)\rangle$ resulting from the evolution under Eq. (6.10a) with the ground state of the moving potential at t_r. 110
6.6 Dynamics of the TAI interferometer for a nonadiabatic separation time $t_r = 150\,\mu\mathrm{s}$ and a shallow potential with $V_0 = 0.2\,\mathrm{MHz}$, as marked by the red diamond in Fig. 6.5. All other parameters are as in Fig. 6.3. Panels (b–e) show the results under the analytic drive function $\omega(t)$ given by Eq. (6.10) 111
6.7 Dynamics of the TAI interferometer for a nonadiabatic separation time $t_r = 150\,\mu\mathrm{s}$ and a shallow potential with $V_0 = 0.2\,\mathrm{MHz}$, as marked by the red diamond in Fig. 6.5. Panels (g–k) shows the results for an optimized field $\omega_{\mathrm{opt}}(t)$ (see text for details). Panel (f) shows the interferometric response of the un-optimized and the optimized drive functions to a constant background rotation Ω. 112

LIST OF TABLES

TABLE

2.1 Ritz expansion coefficients for rubidium [1, 2] 10
2.2 Frequency scaling factors in a wavelength-mismatched ladder-EIT 28

3.1 Scaling laws of Rydberg atoms 30

4.1 Survey of s-wave scattering length (a_s) of Ar reported from past experiments. . 57
4.2 Reported values of s-wave scattering length (a_s) and dipole polarizability (α) for gases used in this experiment. For a_s we show the upper and lower bounds of the results from the references cited. a_s is estimated by using MERT to extend scattering results from crossed-beam or swarm experiments to $k \to 0$. The values shown for α are consistent with the references cited, at the level of precision given in our table. 57
4.3 Line shifts and broadenings rate (in MHz/Torr), based on pseudo-potential model calculated using Eq. 4.7. In our calculation of Δ_* and γ_*, with $* = sc$, p or r, we use the most commonly accepted values of a_s *i.e.*, $-1.49\ a_0$, $0.214\ a_0$ and $0.404\ a_0$ for Ar, Ne and N_2, respectively, as well as the α-values shown. 58

5.1 Operating regime of the ICP source 71

LIST OF ACRONYMS

AI Atom Interferometry

AMO Atomic, Molecular, and Optical physics

CCP Capacitively Coupled Plasma

CN Crank-Nicolson

CPT Coherent Population Trapping

CW Continuous Wave

E-CARS Electric field-induced Coherent Anti-Stokes Raman Scattering

EDM Electric Dipole Moment

EEDF Electron Energy Distribution Function

E-FISH Electric field-induced Second-Harmonic Generation

EIT Electromagnetically Induced Transparency

FOGs Fiber-Optic Gyroscopes

FWHM Full Width at Half Maximum

HFS Hyperfine Splitting

ICP Inductively Coupled Plasma

LG Laguerre-Gaussian

LIF Laser-Induced Fluorescence

LIF-dip Laser-Induced Fluorescence-dip

LRL Laplace-Runge-Lenz

MOT Magneto Optical Trap

OBEs Optical Bloch Equations

PBC Periodic Boundary Conditions

RF Radio Frequency

RWA Rotating-Wave Approximation

SAE Single-Active-Electron

SP Split-Propagator

TAI Tractor Atom Interferometry

UHV Ultra-High Vacuum

MRI Magnetic Resonance Imaging

ABSTRACT

Quantum sensing exploits the sensitivity of quantum systems to their environment, translating external fields and forces into measurable shifts in quantum-mechanical observables. Neutral atoms constitute a highly effective and scalable sensing platform owing to their identical nature and extended coherence times. This dissertation investigates two implementations of atom-based quantum sensing: electric field diagnostics in low-pressure plasma discharges using Rydberg electromagnetically induced transparency (EIT), and inertial sensing via tractor atom interferometry (TAI).

Non-invasive electric field measurement is crucial for understanding plasma dynamics without disturbing the local environment, for which high-resolution, coherent spectroscopy of Rydberg states via EIT is a promising candidate. Deploying EIT in plasma environments requires a systematic characterization of collisional effects. To this end, Rydberg-EIT is analyzed in rubidium vapor interacting with plasma precursor gases such as argon, neon, and nitrogen at pressures up to 5 Torr. The observed frequency shifts and collisional broadening are consistent with semiclassical predictions from the Fermi pseudopotential model. Crucially, collisional broadening remains narrower than typical EIT linewidths below 100 mTorr, identifying this pressure range as an operational window for EIT-based plasma field diagnostics.

Rydberg-EIT is subsequently applied to a low-pressure, inductively coupled plasma (ICP). In a custom ultra-high-vacuum plasma chamber, Rydberg Stark shifts of rubidium tracers seeded into a continuous argon discharge are mapped via EIT. Prior to plasma ignition, Rydberg spectra exhibit modulation sidebands driven by both electric and magnetic near-fields of the ICP coil. Upon ignition, the bulk plasma screens the rf drive field, suppressing the sidebands. The resulting in-plasma lineshapes are instead governed by V/cm-scale plasma microfields and collisional broadening. Modeling the microfield with a Holtsmark distribution enables the extraction of plasma electron densities as a function of pressure and rf power. By resolving a Rydberg resonance whose lineshape is governed by the plasma environment rather than by spectroscopic limits, these measurements establish a framework for sensitive and non-invasive plasma field diagnostics.

The second part of the dissertation investigates inertial sensing via a tractor atom interferometer (TAI). Unlike free-space propagation, TAI utilizes continuous three-dimensional

confinement and coherent atomic transport. This mitigates wave packet dispersion, guarantees path closure, permits variable holding times, and enables complex spatial trajectories. The proposed experimental framework employs a Laguerre-Gaussian "pinwheel" optical lattice to drive multi-loop interferometric sequences. Numerical simulations confirm that TAI implementations may achieve rotation sensitivities comparable to those of established free-space interferometers. In the fast-transport regime required for large enclosed areas, where nonadiabatic excitations would otherwise degrade contrast, quantum optimal control is used to design acceleration sequences that remain fast while preserving coherence.

These results illustrate the versatility of neutral atoms as a sensing platform, probing electromagnetic fields through their internal structure and inertial forces through their center-of-mass motion.

CHAPTER 1

Introduction

Most of the innovations that defined the late twentieth century, ranging from semiconductor electronics and lasers to MRI, emerged from the success of quantum mechanics in explaining and predicting the behavior of materials and radiation in bulk. In recent decades, the focus has shifted to coherent control of individual quantum systems [3], such as atoms, photons and solid-state spins. Advances in laser technology, material science and control electronics have made it possible to prepare and probe well-defined internal quantum states with coherence maintained over experimentally useful timescales [4–6]. The applications enabled by this level of control translate the principles of quantum mechanics for a host of emerging technologies, such as quantum sensors [7–12] and transducers [13–15], processors [16] and communication networks for quantum information [17–19], and quantum simulation [20–22]. Among these, quantum sensing has matured most rapidly into deployable technology [23], and it is the focus of this dissertation.

As a general principle, quantum sensing relies on the response of quantized energy levels of systems like atoms, ions or solid state spins to external fields or forces [24]. When prepared in states appropriate for the sensing objectives, such systems encode the external field as shifts in energy levels or accumulated phase that is read out through spectroscopy or interferometry. Atoms are a particularly attractive sensing platform because every atom of a given isotope is exactly identical, with the same level structure and transition strengths [25]. This eliminates the overhead from fabrication defects and allows for massive statistical advantage in signal-to-noise ratio. Moreover, interaction of atoms with electromagnetic fields is described by one of the most precisely tested theoretical frameworks, complemented by a wealth of spectroscopic data on atomic levels and transitions [26], in particular for alkali and alkaline-earth atoms.

The toolkit for manipulating atoms, built up over decades of atomic physics, is now extensive enough that the same atomic species can serve in widely different sensing modalities by utilizing internal states or the center-of-mass wavefunction. Atomic clocks provide a canonical example [27], where the frequency of atomic transitions provides frequency references

with relative stability pushing to 10^{-19} [28–30]. To present a sense of scale, gravitational redshift due to the Earth can now be measured over a millimeter [31]. Atomic clocks aid in tests of general relativity and Lorentz invariance [32], and monitor variations in fundamental constants in searches for beyond the Standard Model physics [33, 34]. Beyond the curiosities of fundamental physics, the time standard powered by atomic clocks defines the SI unit of time [35], enables global navigation systems [36] and synchronizes distributed telecommunications and financial infrastructure [37]. Atomic magnetometers are another example that use the Zeeman effect and the dispersive nature of atomic vapor for magnetic field sensing [38]. With a long history dating back to the discovery of optical pumping, current state-of-the-art atomic magnetometers have reached sensitivity of sub-fT/$\sqrt{\text{Hz}}$ [39]. The applications stretch from searches for physics beyond the Standard Model, including EDM measurements [40], muon $g-2$ [41] and axion-like dark matter [42] to biomedical imaging via wearable MEG [43] and ultra-low-field NMR/MRI [44].

The atomic toolkit, however, is not symmetric between electric and magnetic fields. While magnetic fields couple directly to the magnetic moment of the electron spin, parity symmetry forbids a permanent electric dipole moment in the low-lying states, which are non-degenerate in ℓ. Therefore, unless near an atomic transition, electric fields elicit a substantially weaker response in the low-lying state through an induced dipole. For instance, in cesium, which has the largest ground-state polarizability of any stable atom, the Stark shift from a 1 kV/cm dc field is smaller than the splitting produced by the Earth's magnetic field. The picture changes dramatically for atomic states excited close to the ionization threshold. As the principal quantum number n increases, level spacings decrease as $1/n^3$ while dipole matrix elements grow as n^2 between adjacent Rydberg levels, thus the resulting electric-field response increases by many orders of magnitude [45]. These highly-excited states, known as Rydberg states, are extraordinarily large. Their valence electron orbits the ionic core at separations of hundreds of nanometers; a length scale comparable to a *Mycoplasma* bacterium. The weakly bound, large electron cloud leads to pronounced scaling behaviors with n and exaggerated atomic properties, such as large electric dipole polarizabilities, strong long-range interactions and long lifetimes. These features underpin a range of technologies [46] from quantum information processing based on Rydberg blockade [47, 48] to quantum simulation of strongly correlated many-body systems [49].

Additionally, the large dipole polarizability of Rydberg atoms makes them excellent electric field sensors [50, 51]. Combining optical and microwave excitation of Rydberg states with electromagnetically induced transparency (EIT) [52], a quantum interference effect, allows non-destructive spectroscopic measurement of Stark shifts of Rydberg states in response to local electric fields. Rydberg-EIT is well suited for SI-traceable electrode-free microwave

electrometry [53, 54], radio frequency (rf) reception [55, 56] and spectrum analysis [57], dc electric field [58] and magnetic field sensing [59]. The enhanced field sensitivity of high-angular-momentum Rydberg states ($\ell \sim 4 - 6$) has been leveraged to measure weak electric fields in room-temperature vapor cells [60] and laser-cooled ion clouds [61]. This thesis extends Rydberg-EIT beyond vapor cells to enable *in situ* electric field sensing in delicate environments such as plasmas. Relevant concepts of coherent spectroscopy and EIT as well as Rydberg physics are presented in Chapters 2 and 3.

Apart from the internal state of atoms, the center-of-mass wave function of atoms offers another sensing resource. Matter-wave interferometry encodes inertial forces as phase shifts accumulated along the atomic trajectory [62]. The de Broglie wavelengths associated with atoms are several orders of magnitude smaller than optical waves, raising the potential of quantum inertial sensors that surpass the sensitivity of current MEMS or laser-based gyroscopes and accelerometers. Recent progress in atom interferometry (AI) has raised promising prospects in fundamental physics [63–67], precision measurements [68–71] and practical applications [72] including geodesy, seismology and inertial sensing with atomic acceleration and rotation sensors. Free-space atom interferometers, which form the majority of the current implementations, face sensitivity floors arising from limited interrogation time, wavefunction dispersion and inefficient path closure, along with large space and power requirements. The last chapter of this thesis presents our efforts towards rotation sensing in a compact atom interferometer, where the atoms are trapped continuously in three dimensions in counter-rotating lattices.

1.1 Rydberg atoms for plasma diagnostics

Plasma, often described as the fourth state of matter, is a partially or fully ionized gas in which free electrons and ions coexist. Plasma is distinguished from a mere cloud of charged particles by collective behaviors arising from long-range electromagnetic interactions. The character of a plasma varies enormously depending on its operating conditions. At low pressures (below ∼100 mTorr), the mean free path of electrons and ions becomes comparable to the physical dimensions of the system, fundamentally altering the transport, energy distribution, and loss mechanisms that govern the discharge. Electrons are lost to surfaces at plasma boundaries faster than ions due to their higher thermal velocities, creating the plasma sheath, a positively charged boundary layer that mediates plasma-surface interactions. This regime of non-equilibrium, weakly ionized plasma underpins critical technologies including semiconductor manufacturing and electric propulsion [73], yet open questions remain regarding electron heating, sheath dynamics, and power coupling [74–77]. Resolving the spatial and temporal structure of electric fields, particularly near sheaths and boundaries, is essential

for understanding transport, energy deposition, and plasma-surface interactions.

There is growing interest [78, 79] in replacing traditional electrostatic probe-based measurements with laser-based, non-invasive plasma field diagnostics. Current state-of-the-art methods rely on electric field-induced non-linear effects, *e.g.*, four-wave mixing (E-CARS) [80, 81] and second-harmonic generation (E-FISH) [82, 83]. While recent efforts have improved the sensitivity limits by two to three orders of magnitude [84], these methods are typically intended for atmospheric-pressure discharges featuring electric fields larger than 100 V/cm. For over a century, optical emission spectroscopy of Stark broadening and Stark-mixed forbidden lines has served as a workhorse diagnostic of electron density and electric field strength in dense plasmas featuring fields in excess of kV/cm [85–87]. With the advent of lasers, early attempts used laser-induced fluorescence (LIF) with light sheets for electric field measurement [88, 89]. Using two-photon excitation to Rydberg states in laser-induced fluorescence-dip (LIF-dip) spectroscopy, spectral resolution of the order of several GHz was achieved, allowing electric field measurements on the order of 10 V/cm [90–93]. The sensitivity of LIF-dip is fundamentally limited by the spectral resolution of the detection scheme, which relies on a semiclassical population transfer to the Rydberg state to obtain the dip. By taking advantage of quantum interference in EIT, Rydberg states can be resolved with ∼MHz linewidth, potentially enabling *in situ*, spatially resolved electric field measurements at sub-V/cm level.

However, the coherent effect that enables narrow linewidth spectroscopy also renders Rydberg-EIT vulnerable to collisional dephasing in a hostile environment like plasma as well as the precursor gas. Collisional effects on atomic spectra have a remarkably long experimental history over more than a century, beginning with Plucker and Hittorf's finding of line broadening [94] in vacuum tubes in the 1860s. The first quantitative results came from Humphrey and Mohler's electric arc experiments in 1895 and subsequent derivation of the collisionally broadened line shape by Lorentz in 1906, which predates quantum mechanics. The discovery of density-dependent shifts of Rydberg series in alkali vapors motivated Fermi's 1934 introduction of the pseudopotential [95] in one of the earliest applications of quantum scattering theory. Seminal theoretical work by Foley, Baranger, Omont and others extended the theory to inelastic collisions and state-mixing processes [96–99]. Astrophysical applications drove a parallel line of work, using Stark-broadened atomic lines in stellar atmospheres and radio recombination lines from interstellar plasmas to diagnose the density and temperature of remote plasmas [85]. The advent of tunable lasers in the 1970s opened up high-resolution measurements of Rydberg line shifts and broadening in buffer gases [100–103]. However, these experiments typically used two-photon excitation in the absence of any resonant intermediate states, with the goal of transferring population to Rydberg states which

were detected directly and destructively with field ionization. In contrast, Rydberg-EIT uses a resonant intermediate state and relies on the atomic coherence to monitor the Rydberg resonance. This thesis investigates the effect of commonly used inert gases on Rydberg-EIT of rubidium, revisiting the physics of collisions in Rydberg spectroscopy. The low-pressure regime below 100 mTorr, where many optical plasma field diagnostics techniques meet their sensitivity limits, is found to have minimal deleterious effect on Rydberg-EIT, raising the prospect of Rydberg-EIT as a complementary field measurement technique to the suite of non-invasive plasma diagnostics.

1.2 Thesis Outline

The thesis is structured as follows. Chapter 2 presents the basic concepts of low-lying atomic states and the principles of atomic spectroscopy. Chapter 3 discusses the physics of highly excited Rydberg states, collisional effect on Rydberg transitions and basics of plasma physics with an emphasis on low-temperature rf plasma. Chapter 4 describes the experimental investigation into the effect of inert gases on Rydberg-EIT. Chapter 5 presents the first demonstration of Rydberg-EIT in a continuous rf plasma. A UHV plasma chamber featuring continuous flow of argon with rubidium vapor, high-resolution spectroscopy of Rydberg spectra inside a plasma, and all-optical measurement of the plasma microfield are discussed. Chapter 6 transitions to an inertial sensor design for rotation sensing using matter-wave interferometry. The thesis is concluded with future outlooks in Chapter 7.

CHAPTER 2

Atomic Physics Background

Atomic physics owes much of its precision to a fortunate phenomenon of scale separation. In alkali atoms, the dynamics that bind quarks into nucleons, nucleons into nuclei, and electrons into closed shells unfold at energies well above an optical photon, leaving a lone valence electron above a closed core as the only relevant degree of freedom. The dynamics of this electron across several orders of magnitude in energy, ranging from precision measurements at sub-Hz levels to ionization effects at the electron-volt scale, is described in a unified quantum mechanical framework with a few empirical parameters capturing the entire effect of the closed core. This chapter presents the physics of such deeply bound electronic states and their interaction with radiation. A symmetry-motivated description of a single electron atom is provided in Sec. 2.1. Interaction with static electromagnetic fields is covered in Sec. 2.2. The semiclassical formulation of atom-light interaction and its extension to thermal ensembles are presented in Sec. 2.3 and Sec. 2.4.

2.1 Hydrogen-like Atom

The theoretical foundation of atomic physics is rooted in the description of the hydrogen atom. Treating the nucleus as infinitely massive relative to the electron, the dynamics of this two-body system are governed by the Coulomb Hamiltonian, given by

$$\hat{H} = \frac{\hat{\mathbf{p}}^2}{2m_e} - \frac{e^2}{4\pi\epsilon_0 \hat{r}}$$

where m_e is the electron mass, $\hat{\mathbf{p}}$ is the momentum operator, and $r = |\hat{\mathbf{r}}|$ is the radial distance from the nucleus.

While the eigen energies of this Hamiltonian can be obtained from the Schrödinger equation via separation of variables in spherical coordinates, a more illuminating approach proceeds algebraically by identifying the conserved quantities underlying the symmetry of the $1/r$ potential. In addition to the standard orbital angular momentum operator $\hat{\mathbf{L}} = \hat{\mathbf{r}} \times \hat{\mathbf{p}}$,

the Coulomb problem possesses an additional constant of motion: the quantum mechanical Laplace-Runge-Lenz (LRL) vector. To ensure Hermiticity, the LRL operator is symmetrically ordered as

$$\hat{\mathbf{A}} = \frac{1}{2m_e}\left(\hat{\mathbf{p}} \times \hat{\mathbf{L}} - \hat{\mathbf{L}} \times \hat{\mathbf{p}}\right) - \frac{e^2}{4\pi\epsilon_0}\frac{\hat{\mathbf{r}}}{r}$$

Both vectors commute with the Hamiltonian, such that $[\hat{H}, \hat{A}_i] = [\hat{H}, \hat{L}_i] = 0$. By restricting our focus to the subspace of bound states where the energy eigenvalue is strictly negative ($E < 0$), we can introduce a scaled, dimensionless LRL vector defined by $\hat{\mathbf{K}} = \sqrt{\frac{-m_e}{2E}}\hat{\mathbf{A}}$. Evaluating the commutation relations among the components of $\hat{\mathbf{L}}$ and $\hat{\mathbf{K}}$ reveals the closed algebra:

$$\begin{aligned} [\hat{L}_i, \hat{L}_j] &= i\hbar\epsilon_{ijk}\hat{L}_k \\ [\hat{L}_i, \hat{K}_j] &= i\hbar\epsilon_{ijk}\hat{K}_k \\ [\hat{K}_i, \hat{K}_j] &= i\hbar\epsilon_{ijk}\hat{L}_k \end{aligned} \tag{2.1}$$

This set of commutators is isomorphic to the Lie algebra of $SO(4)$, demonstrating that the bound states of the Coulomb Hamiltonian possess a hidden rotational symmetry in four-dimensional space. To extract the energy spectrum, this $SO(4)$ algebra can be decoupled into two independent $SU(2)$ algebras. We define the generators $\hat{\mathbf{J}}_\pm = \frac{1}{2}\left(\hat{\mathbf{L}} \pm \hat{\mathbf{K}}\right)$, which satisfy

$$\begin{aligned} [\hat{J}^i_\pm, \hat{J}^j_\pm] &= i\hbar\epsilon_{ijk}\hat{J}^k_\pm \\ [\hat{J}^i_+, \hat{J}^j_-] &= 0 \end{aligned} \tag{2.2}$$

By noting that $\hat{\mathbf{L}}.\hat{\mathbf{K}} = 0$, we find $\hat{\mathbf{J}}^2_+ = \hat{\mathbf{J}}^2_-$, so that these operators can be parameterized by a single half-integer quantum number j for degenerate bound states with energy $E < 0$, yielding eigenvalues $\hbar^2 j(j+1)$. We can relate this algebraic structure back to the Hamiltonian by summing the Casimir operators: $\hat{\mathbf{J}}^2_+ + \hat{\mathbf{J}}^2_- = \frac{1}{2}\left(\hat{\mathbf{L}}^2 + \hat{\mathbf{K}}^2\right)$. By substituting the definition of $\hat{\mathbf{K}}$ and utilizing the identity for the square of the LRL vector, $\hat{\mathbf{A}}^2 = \frac{2\hat{H}}{m_e}(\hat{\mathbf{L}}^2 + \hbar^2) + \left(\frac{e^2}{4\pi\epsilon_0}\right)^2$, the sum evaluates to

$$2j(j+1)\hbar^2 = -\frac{1}{2}\left(\hbar^2 + \frac{m_e e^4}{2E(4\pi\epsilon_0)^2}\right)$$

Solving this relation for the energy E directly yields the Bohr spectrum:

$$E = -\frac{m_e e^4}{2\hbar^2(4\pi\epsilon_0)^2(2j+1)^2} \equiv -\frac{E_H}{2n^2} \tag{2.3}$$

By identifying the principal quantum number as $n = 2j+1$ (where $n = 1, 2, 3, \dots$), we recover

the familiar $1/n^2$ energy dependence with $E_H = m_e(e^2/4\hbar\pi\epsilon_0)^2 = \alpha^2 m_e c^2 \approx 27.21$ eV. Furthermore, because the state space is formed by the tensor product of two identical spin-j representations, the total number of states for a given n is $(2j+1) \times (2j+1) = n^2$, which elegantly captures the accidental degeneracy of the non-relativistic hydrogen atom.

Although the $SO(4)$ treatment yields the energies and degeneracies, computing matrix elements for interactions with external fields requires the position-space wavefunctions obtained from the time-independent Schrödinger equation:

$$\left(-\frac{\hbar^2\nabla^2}{2m_e} - \frac{e^2}{4\pi\epsilon_0 r}\right)\psi(\mathbf{r}) = E\psi(\mathbf{r}) \tag{2.4}$$

Exploiting the spherical symmetry of the central potential, the wavefunctions are separable into radial and angular components, denoted by the quantum numbers n, ℓ, and m. The normalized spatial wavefunctions take the exact form:

$$\psi_{n,\ell,m}(r,\theta,\phi) = \sqrt{\left(\frac{2}{na_0}\right)^3 \frac{(n-\ell-1)!}{2n[(n+\ell)!]^3}} e^{-\frac{r}{na_0}} \left(\frac{2r}{na_0}\right)^\ell \left[L_{n-\ell-1}^{2\ell+1}\left(\frac{2r}{na_0}\right)\right] Y_\ell^m(\theta,\phi) \tag{2.5}$$

where $a_0 = \frac{4\pi\epsilon_0\hbar^2}{m_e e^2}$ is the Bohr radius, and $L_{n-\ell-1}^{2\ell+1}$ are the generalized Laguerre polynomials. The angular distribution is entirely governed by the spherical harmonics:

$$Y_\ell^m(\theta,\phi) = \xi_m \sqrt{\frac{2\ell+1}{4\pi}\frac{(\ell-|m|)!}{(\ell+|m|)!}} e^{im\phi} P_\ell^{|m|}(\cos\theta) \tag{2.6}$$

where $P_\ell^{|m|}(\cos\theta)$ are the associated Legendre polynomials. The Condon-Shortley phase factor is defined as $\xi_m = (-1)^m$ for $m > 0$ and $\xi_m = 1$ for $m \leq 0$. Here, the orbital angular momentum quantum number ℓ is bounded by $0 \leq \ell \leq n-1$, and the magnetic quantum number m spans $-\ell \leq m \leq \ell$, completely characterizing the unperturbed orbital structure.

A nonrelativistic Hamiltonian omits electron spin, and with it the fine structure observed in atomic spectra. In a semiclassical picture, the electron spin ($\hat{\mathbf{S}}$) couples to the orbital angular momentum ($\hat{\mathbf{L}}$) via the magnetic interaction of their respective moments, with a relativistic correction from Thomas precession. With spin-orbit coupling, the total electronic angular momentum $\hat{\mathbf{J}} = \hat{\mathbf{L}} + \hat{\mathbf{S}}$ emerges as the conserved quantum number. The Dirac equation for a hydrogenic system with core charge Z incorporates spin from the outset and yields a spectrum characterized by the quantum number for $\hat{\mathbf{J}}$

$$E_{nj} = m_e c^2 \left[\left(1 + \frac{(Z\alpha)^2}{\left(n - (j+1/2) + \sqrt{(j+1/2)^2 - (Z\alpha)^2}\right)^2}\right)^{-1/2} - 1\right] \tag{2.7}$$

where $c = 2.998 \times 10^8$ m/s and $\alpha = e^2/4\pi\epsilon_0\hbar c \approx 1/137$ are the speed of light and fine structure constant, respectively. Expanding in order of $(Z\alpha)^2$, Eq. 2.7 provides the fine-structure correction

$$E_{nj} \approx -\frac{Z^2 E_H}{2n^2}\left[1 + \frac{(Z\alpha)^2}{n^2}\left(\frac{n}{j+1/2} - \frac{3}{4}\right)\right] \tag{2.8}$$

The first term reproduces the energy spectrum given in Eq. 2.3. For atoms with a single valence electron, the fine structure splitting between the $j = \ell \pm 1/2$ states is given by the second term as

$$\Delta E_{FS} = \frac{E_H}{2n^3\ell(\ell+1)} \tag{2.9}$$

There is no spin-orbit splitting for S states ($\ell = 0$), so the largest fine structure splitting arises in the lowest P states.

2.1.1 Alkali atoms

Alkali atoms have a single valence electron outside a closed-shell core, resulting in a theoretically tractable and experimentally accessible spectrum. Spectroscopy of alkali atoms has been central to the development of AMO physics for decades, from foundational tests of quantum mechanics and precision spectroscopy to laser cooling, quantum information processing [4, 48, 49] and quantum sensing [104, 105]. Rubidium in particular has become a workhorse of the field owing to its convenient transition wavelengths, well-characterized atomic structure and favorable vapor pressure. It serves as the sensing medium throughout this thesis, both as a Rydberg-EIT probe in Chapters 3–5 and as the matter-wave interferometry platform in Chapter 6. This section presents a brief discussion of the structure of alkali atoms with particular emphasis on rubidium.

Because the core of an alkali atom is tightly bound and the valence electron spends most of its time outside it, we can treat the atom as an effective one-electron system, known as the single-active-electron (SAE) approximation. The radial Schrödinger equation then reads

$$\left[-\frac{\hbar^2}{2m_e}\frac{d^2}{dr^2} + \frac{\hbar^2\ell(\ell+1)}{2m_e r^2} + V_{\text{model}}(r)\right] u_{n\ell}(r) = E_{n\ell} u_{n\ell}(r) \tag{2.10}$$

where $u_{n\ell}(r) = rR_{n\ell}(r)$ is the reduced radial wavefunction and $V_{\text{model}}(r)$ is a phenomenological central potential describing the valence electron's interaction with the core. To account for the non-Coulombic physics at short range, Marinescu et al. [106] parameterize this potential as

$$V_{\text{model}}(r) = -\frac{Z_\ell(r)}{r} - \frac{\alpha_c}{2r^4}\left(1 - e^{-(r/r_c)^6}\right) \tag{2.11}$$

ℓ	j	δ_0	δ_2
0	1/2	3.1311804(10)	0.1784(6)
1	1/2	2.6548849(10)	0.2900(6)
1	3/2	2.6416737(10)	0.2950(7)
2	3/2	1.34809171(40)	−0.60286(26)
2	5/2	1.34646572(30)	−0.59600(18)
3	5/2	0.0165192(9)	−0.085(9)
3	7/2	0.0165437(7)	−0.086(7)

Table 2.1: Ritz expansion coefficients for rubidium [1, 2]

The first term describes the screened Coulomb attraction: $Z_\ell(r) = 1+(Z-1)e^{-a_1 r}-r(a_3+a_4 r)e^{-a_2 r}$ is an ℓ-dependent effective charge, equal to Z at $r = 0$ and tending to 1 as $r \to \infty$. The ℓ-dependence reflects the fact that low-ℓ orbits penetrate the core more deeply than high-ℓ orbits and therefore sample a different effective charge distribution. The second term accounts for core polarization: α_c is the static dipole polarizability of the core, and r_c cuts off the unphysical r^{-4} divergence at short range. Assuming spherical symmetry of $V_{\rm model}(r)$ implicitly treats the core as rigid and isotropic, neglecting deformation and non-scalar polarizabilities induced by the valence electron. Although this is a reasonable approximation in the first order, accurate calculation of dipole matrix elements and polarizabilities require sophisticated numerical methods [107].

A phenomenological description encompassing the non-Coulombic physics of the core is afforded by correcting the energy levels to

$$E_{n\ell j} = -\frac{E_H}{2(n-\delta_{n\ell j})^2} \equiv -\frac{E_H}{2n^{*2}}. \tag{2.12}$$

where $n^* = n - \delta_{n\ell j}$ is the effective principal quantum number, and quantum defects $\delta_{\ell j}$ are parameterized by Ritz expansion as

$$\delta_{n\ell j} = \delta_0 + \frac{\delta_2}{(n-\delta_0)^2} + \frac{\delta_4}{(n-\delta_0)^4}\ldots \tag{2.13}$$

The empirical parameters δ_i are determined from fit to spectroscopic data, and the values for rubidium listed in Table 2.1. Quantum defects are large for penetrating low-ℓ orbits and fall off rapidly with ℓ, since the centrifugal barrier keeps high-ℓ electrons outside the core where they see a nearly pure Coulomb potential.

Relativistic corrections responsible for fine-structure splitting are added semiclassically

through the spin-orbit term as

$$V_{\text{total}}(r) = V_{\text{model}}(r) + \frac{1}{2m_e^2c^2}\frac{1}{r}\frac{dV_{\text{model}}(r)}{dr}\,\hat{\mathbf{L}}\cdot\hat{\mathbf{S}}, \tag{2.14}$$

where α is the fine-structure constant. In the $|n,\ell,s,j,m_j\rangle$ basis, $\langle\hat{\mathbf{L}}\cdot\hat{\mathbf{S}}\rangle = \frac{1}{2}[j(j+1)-\ell(\ell+1)-s(s+1)]$. Solving the radial equation with V_{total} lifts the j-degeneracy, giving distinct wavefunctions and energies for the $nP_{1/2}$ and $nP_{3/2}$ manifolds with splitting

$$\Delta E_{FS} = \frac{\alpha^2\, Z_i^2 Z_o^2}{2\, n^{*3}\, \ell(\ell+1)}\, E_H, \tag{2.15}$$

where Z_i is the effective charge seen by the electron inside the core and $Z_o = 1$ is the asymptotic charge. The Z-scaling makes this splitting dramatically larger in heavy alkalis than in hydrogen: while the $2P_{1/2}$–$2P_{3/2}$ separation in hydrogen is 10.9 GHz, the analogous Rb $5P_{1/2}$–$5P_{3/2}$ splitting is 7.1 THz, which separates the D1 (795 nm) and D2 (780 nm) lines used throughout this work.

The nuclear spin $\hat{\mathbf{I}}$ produces a further splitting through its magnetic and electric-multipole couplings to the electronic system. This so-called hyperfine structure (HFS) is the terminal energy splitting for alkali atoms. The leading magnetic-dipole and electric-quadrupole terms give the HFS Hamiltonian

$$\hat{H}_{HFS} = A\,\hat{\mathbf{I}}\cdot\hat{\mathbf{J}} + B\,\frac{3(\hat{\mathbf{I}}\cdot\hat{\mathbf{J}})^2 + \frac{3}{2}\hat{\mathbf{I}}\cdot\hat{\mathbf{J}} - I(I+1)J(J+1)}{2IJ(2I-1)(2J-1)}, \tag{2.16}$$

where A and B are the (experimentally measured) magnetic-dipole and electric-quadrupole hyperfine constants. In the coupled basis, the total angular momentum $\hat{\mathbf{F}} = \hat{\mathbf{J}}+\hat{\mathbf{I}}$ is conserved in zero external field and labels the hyperfine eigenstates. These splittings are well-resolved in the spectroscopy described later, making F the relevant quantum number for our experiments. The level structure for rubidium, including the hyperfine structure utilized in the later experiments is presented in Fig. 2.1.

2.1.2 Metastable Argon atoms

Quantum sensing enabled field diagnostics in low-temperature plasmas forms a primary thrust of this dissertation. Such discharges are essentially a weakly ionized gas created by applying power to a precursor gas, often an inert gas such as argon or neon. Argon serves as the precursor gas in this dissertation, and interpreting the emission spectrum of this discharge requires familiarity with its atomic structure.

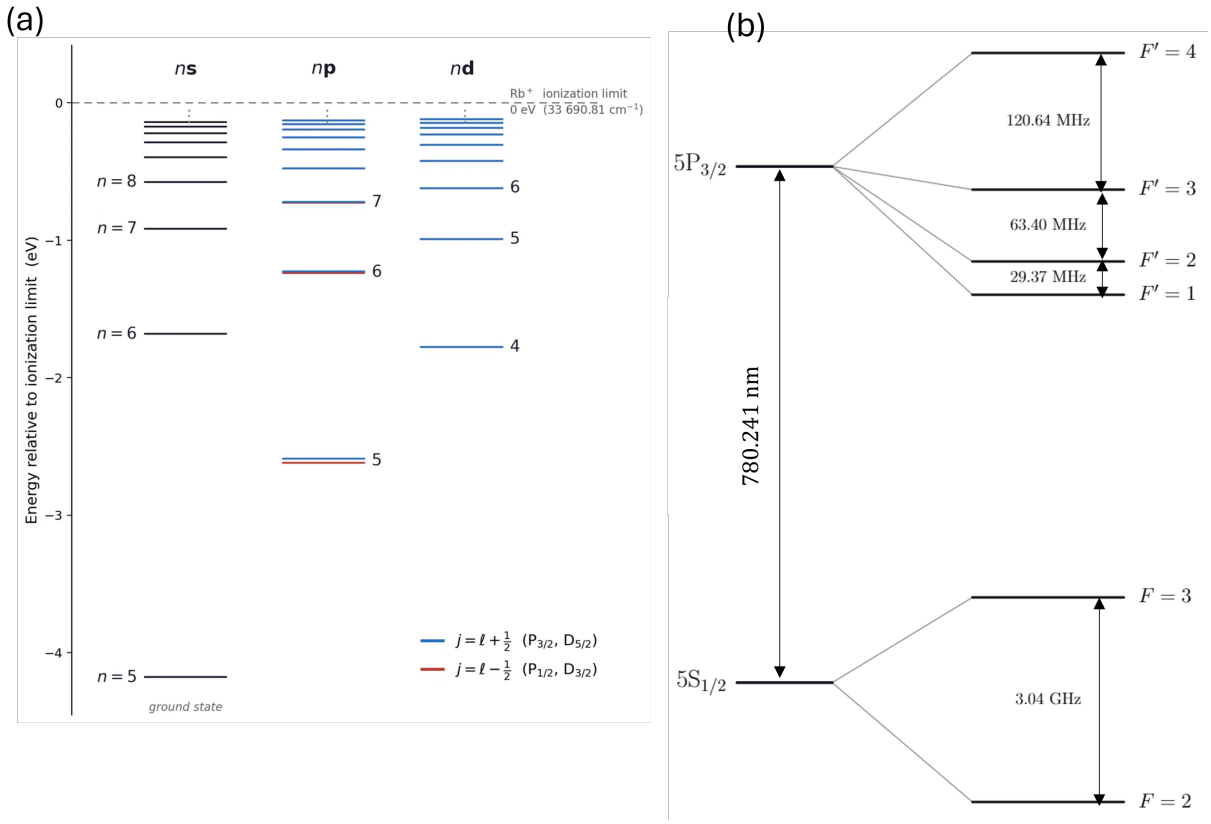


Figure 2.1: (a) Energy level structure of rubidium. Due to the single valence electron, the fine structure splittings result in doublets for $\ell > 0$. (b) Hyperfine structure of D_2 line in ^{85}Rb utilized in this work (adapted from [108])

The ordering of perturbative corrections developed for hydrogenic and alkali atoms does not carry over to every atomic system. The first excited state of argon has an electron promoted to higher orbital leaving two open shells, which superficially resembles alkaline earth atoms. However, alkaline earth atoms have a dominant electrostatic exchange interaction due to the strong overlap of the valence electrons, justifying the $L-S$ coupling. In argon $3p^5n\ell$, the core experiences a larger spin-orbit interaction as it is tightly bound to the nucleus where the potential gradient is steep. The weaker core-hole overlap results in a smaller exchange interaction. The angular momentum ordering in this regime is given by $j\ell$-coupling (Racah coupling) as

1. Spin-orbit coupling of the core: $\hat{\mathbf{j}}_c = \hat{\mathbf{L}}_c + \hat{\mathbf{S}}_c$. The orbital angular momentum of the core hole ($L_c = 1$) couples with its spin ($S_c = 1/2$) to form the total core angular momentum j_c. For Argon $3p^5$ core, $j_c = 1/2$ or $3/2$.

2. Exchange interaction: $\hat{\mathbf{K}} = \hat{\mathbf{j}}_c + \hat{\boldsymbol{\ell}}$. j_c couples with the orbital angular momentum of the excited electron (ℓ) to form an intermediate angular momentum K.

3. Spin-orbit coupling of the electron: $\hat{\mathbf{J}} = \hat{\mathbf{K}} + \hat{\mathbf{s}}$. K couples with the spin of the excited electron ($s = 1/2$) to define the total atomic angular momentum J.

4. The dominant naturally occurring isotope of argon (^{40}Ar) possesses a nuclear spin of $I = 0$, therefore the fine-structure manifold constitutes the terminal energy splitting for the Ar* states relevant to the spectroscopic measurements in this work.

Excited fine-structure levels of Argon are denoted in the standard Racah notation $n\ell[K]_J$ or $n\ell'[K]_J$, where the prime indicates the higher-energy $j_c = 1/2$ core. Electric dipole transitions from these odd-parity states to the even-parity $3p^6\ {}^1S_0$ ground state are governed by the selection rules $\Delta J = 0, \pm 1$ and exclusion of $J = 0 \leftrightarrow J = 0$ transitions. Consequently, the $J = 2$ and $J = 0$ states are prohibited from electric dipole decay to the ground state, rendering them metastable. Within the noble gas discharge literature, these four levels are more commonly identified by their empirical Paschen labels: $1s_5$ ($J = 2$, $\tau \approx 38$ s), $1s_4$ ($J = 1$, $\tau \approx 8.5$ ns), $1s_3$ ($J = 0$, $\tau \approx 45$ s), and $1s_2$ ($J = 1$, $\tau \approx 2$ ns) [109, 110], ordered from lowest to highest energy with respect to the ground state. The energy levels of Argon atoms are shown in Fig. 2.2, and further discussed in Chapter 5.

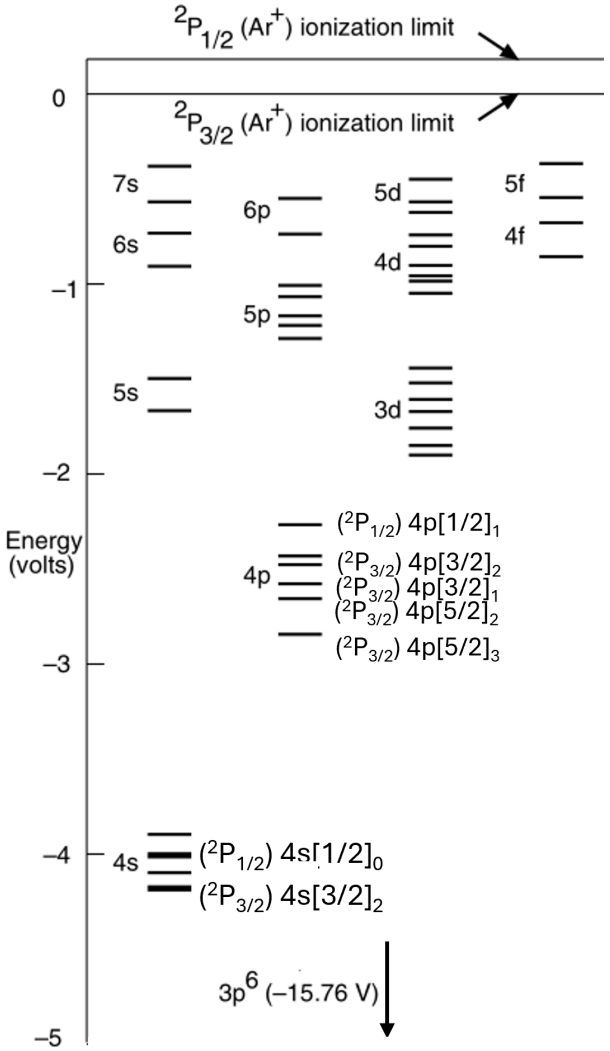


Figure 2.2: Energy level structure of argon, loosely adapted from Ref. [111]. The metastable $4s$ states are highlighted in bold. The Rydberg series of $^2P_{1/2}4s[1/2]_0$ is prone to autoionization. Among the $4p$ states, only those with a significant transition probability to $^2P_{3/2}4s[3/2]_2$ are shown.

2.2 Interaction with electromagnetic field

2.2.1 Magnetic fields

The interaction of an atom with a static magnetic field $\mathbf{B}$ is

$$H_B = -\boldsymbol{\mu} \cdot \mathbf{B} = \frac{\mu_B}{\hbar}(g_L \hat{\mathbf{L}} + g_S \hat{\mathbf{S}} - g_I \frac{m_e}{m_p} \hat{\mathbf{I}}) \cdot \mathbf{B}, \tag{2.17}$$

where μ_B is the Bohr magneton and the nuclear term is negligible. The structure of the Zeeman spectrum depends on how H_B compares to the internal couplings.

When the Zeeman energy is small compared to the hyperfine splitting, $\mathbf{F} = \mathbf{J} + \mathbf{I}$ remains a good quantum number and the field shifts m_F sublevels linearly:

$$\Delta W = g_F \mu_B m_F B, \qquad g_F = g_J \frac{F(F+1) + J(J+1) - I(I+1)}{2F(F+1)} \tag{2.18}$$

F ceases to be a good quantum number at larger fields. Provided H_B remains small compared to the fine-structure splitting, which for alkalis is in the THz range, J remains a good quantum number. The Zeeman and hyperfine Hamiltonians must be diagonalized together in the $|J, m_J; I, m_I\rangle$ basis. Alkali atoms with $J = 1/2$ are a special case featuring a closed-form solution, known as the Breit-Rabi formula:

$$W_{F=I\pm1/2,m_F} = -\frac{\Delta E_{hfs}}{2(2I+1)} + g_I \mu_B m_F B \pm \frac{\Delta E_{hfs}}{2}\sqrt{1 + \frac{4m_F x}{2I+1} + x^2}, \tag{2.19}$$

where $x = (g_J - g_I)\mu_B B / \Delta E_{hfs}$ and $\Delta E_{hfs} = A(I + 1/2)$.

2.2.2 Stark Effect

The Stark shift arises from an odd parity electric-dipole operator $H_E = e\mathbf{E} \cdot \mathbf{r}$. Quantum defects lift the ℓ-degeneracy of the Coulomb spectrum in alkalis, so low-lying states $|n, \ell, j, m_j\rangle$ have definite parity $(-1)^\ell$ and the first-order Stark shift vanishes

$$\langle n, \ell, j, m_j | H_E | n, \ell, j, m_j \rangle = 0.$$

The leading shift is therefore second order:

$$\Delta W_k^{(2)} = \sum_{j \neq k} \frac{|\langle j | H_E | k \rangle|^2}{E_k^{(0)} - E_j^{(0)}}. \tag{2.20}$$

Physically, the field mixes $|k\rangle$ with opposite-parity states, producing an induced dipole moment proportional to E and an energy shift quadratic in E. Conventionally,

$$\Delta W_k = -\tfrac{1}{2}\alpha_k E^2,$$

where α_k is the static dipole polarizability of the state. For the ground state, $\alpha > 0$, thus electric field always lowers the ground-state energy. For states with $J \geq 1$, the polarizability has both scalar and tensor components, and the shift depends on m_J:

$$\Delta W = -\tfrac{1}{2}\alpha_0 E^2 - \tfrac{1}{2}\alpha_2 \frac{3m_j^2 - j(j+1)}{j(2j-1)} E^2, \tag{2.21}$$

where α_0 and α_2 are the scalar and tensor polarizabilities. The scalar term shifts all $|m_j|$ levels equally; the tensor term lifts the m_J-degeneracy without breaking the $m_j \to -m_j$ symmetry. The polarizability is evaluated by summing over opposite-parity dipole-allowed intermediate states, including the continuum.

It should be noted that the assumption of definite parity and hence the quadratic Stark shift breaks down in near-degenerate ℓ manifolds with vanishing quantum defects. Prominent examples include the Hydrogen atom and high angular momentum Rydberg states [112]. However, linear Stark shifts arising in such states are beyond the scope of this dissertation.

2.3 Interaction with radiation

For the experiments presented in this dissertation, a semiclassical model of atom-light interaction suffices, wherein the atomic states are quantized but the electromagnetic field of the radiation are given by Maxwell Equations. Since optical wavelengths are much larger than atomic dimensions, the field phase is essentially uniform across the atom in what is known as electric-dipole approximation. The interaction Hamiltonian in this limit is given by

$$\hat{H}_I(t) = -\hat{\mathbf{d}} \cdot \hat{\epsilon} E_0 \cos(\omega t), \qquad \hat{\mathbf{d}} = -e\hat{\mathbf{r}}.$$

The Schrödinger equation given by this Hamiltonian can handle only unitary evolution of pure states. Technically, all atom-environment interaction is electromagnetic in nature and hence unitary at our energy scale of interest. For example, an excited atom decays spontaneously by coupling to the infinite continuum of vacuum electromagnetic modes, or collisional effects are mediated by various interaction potentials. However, when restricted to the atomic degrees of freedom, such coupling to environmental modes constitute decoherence mechanisms, beyond the scope of the Schrödinger equation. A more tractable formulation,

known as the master equation approach, generalizes the atom dynamics to an open quantum system by tracing out the environmental modes under the Born–Markov approximations of weak coupling and no memory. The time evolution in master equation approach is given in terms of density matrix $\hat{\rho}$

$$\dot{\hat{\rho}} = -\frac{i}{\hbar}[\hat{H}, \hat{\rho}] + \mathcal{L}(\hat{\rho}). \tag{2.22}$$

For a pure state, density matrix is given by $\hat{\rho} = |\psi\rangle \langle\psi|$. The first term in Eq. 2.22 is an alternative formulation of Schrödinger equation. The dissipative part of this evolution is the Lindblad dissipator

$$\mathcal{L}(\hat{\rho}) = \sum_k \gamma_k \left(\hat{C}_k \hat{\rho} \hat{C}_k^\dagger - \tfrac{1}{2}\{\hat{C}_k^\dagger \hat{C}_k, \hat{\rho}\} \right), \tag{2.23}$$

the most general form for a Markovian, trace-preserving, completely-positive evolution of the density matrix. The jump operators $\hat{C}_k$ describe each decay channel at rate γ_k. The first term in the dissipator repopulates the destination states through quantum jumps, and the anticommutator provides the balancing continuous decay of the source states.

2.3.1 Atom ensembles as a dispersive medium

The deliverable from the master equation, density matrix, needs to be related to experimentally measured quantities. The key observable in atomic spectroscopy is the transmission of a laser through an atomic media. Their connection is made clear through Maxwell-Bloch equations that describe the propagation of light through a dielectric medium.

For a laser near resonant with an atomic transition and propagating along z, the key observable is change in intensity $I = \frac{1}{2}\epsilon_0 c|E|^2$, i.e.

$$\frac{\partial I}{\partial z} = \epsilon_0 c \mathrm{Re}\left(E^* \frac{\partial E}{\partial z} \right) \tag{2.24}$$

The electric field propagating in the z-direction is given by

$$\frac{\partial^2 E}{\partial z^2} - \frac{1}{c^2}\frac{\partial^2 E}{\partial t^2} = \mu_0 \frac{\partial^2 P}{\partial t^2}$$

where P = polarization density of the atomic medium. Separating the amplitudes into a slowly varying spatial envelope and a rapidly oscillating carrier wave *i.e.*, $E(z,t) = \mathrm{Re}\left(\mathcal{E}(z)e^{i(kz-\omega t)}\right)$ and $P(z,t) = \mathrm{Re}\left(\mathcal{P}(z)e^{i(kz-\omega t)}\right)$ yields

$$\frac{\partial^2 E}{\partial z^2} \approx \frac{1}{2}\left(2ik\frac{\partial \mathcal{E}}{\partial z} - k^2 \mathcal{E} \right) e^{i(kz-\omega t)} + c.c.$$

with $k = \omega/c$ and slowly varying envelope approximation *i.e.*, $|\partial^2 \mathcal{E}/\partial z^2| \ll |k \partial \mathcal{E}/\partial z|$ since

the field envelope changes negligibly over the span of a single optical wavelength. Moreover, in the steady state of a continuous wave (CW) experiment, $\partial_t \mathcal{E} = \partial_t \mathcal{P} = 0$, yielding

$$\frac{\partial \mathcal{E}}{\partial z} = i\frac{\omega}{2\epsilon_0 c}\mathcal{P} \tag{2.25}$$

The bridge between microscopic quantum dynamics and macroscopic observables lies in the fact that the polarization is the ensemble average of atomic dipole moments. For an atomic density N and a real dipole moment μ:

$$P(z,t) = N\mathrm{Tr}(\rho\hat{d}) = Nd_{12}\left(\tilde{\rho}_{12}e^{-i(kz-\omega t)} + c.c.\right)$$

Here $d_{12} = \langle 2|\,\hat{d}\,|1\rangle$ is the transition dipole moment and $\tilde{\rho}_{12}$ is the slowly varying coherence obtained by solving the master equation. Thus $\mathrm{Re}\,(\partial E/\partial z) = -Nd_{12}\omega\mathrm{Im}(\tilde{\rho}_{21})/\epsilon_0 c$ which reduces Eq. 2.24 to

$$\frac{\partial I}{\partial z} = -\alpha I, \quad \alpha = -\frac{2Nd_{12}\omega}{\epsilon_0 c\mathcal{E}}\mathrm{Im}(\tilde{\rho}_{21}) \tag{2.26}$$

The absorptivity α governs the exponential decay of the intensity of a near-resonant laser beam as $I(z) = I_0 e^{-\alpha z}$, known as the Beer-Lambert law. The real part of the coherence determines the refractive index. Eq. 2.26 is a linear, low-density, steady-state approximation of light-matter interaction, and thus appropriate for weak probe beams in dilute atomic vapors.

2.3.2 Two-level atom

When the field is tuned near a single atomic transition $|g\rangle \to |e\rangle$, its coupling to all other transitions is far off-resonant and produces only small perturbative corrections. Truncating the atomic Hilbert space to these two levels reduces the Hamiltonian to

$$\hat{H}(t) = \begin{pmatrix} \hbar\omega_e & -\mathbf{d}_{eg}\cdot\boldsymbol{\epsilon}\,E_0\cos(\omega t) \\ -\mathbf{d}_{eg}^*\cdot\boldsymbol{\epsilon}^*\,E_0\cos(\omega t) & \hbar\omega_g \end{pmatrix},$$

where $\mathbf{d}_{eg} = \langle e|\hat{\mathbf{d}}|g\rangle$ is the transition dipole moment and the coupling strength is set by the resonant Rabi frequency $\Omega_0 = -\mathbf{d}_{eg}\cdot\boldsymbol{\epsilon}\,E_0/\hbar$.

Transforming to a frame rotating at the optical field frequency ω yields terms rotating at the detuning $\Delta = \omega - (\omega_e - \omega_g)$ and at the sum frequency $\sim 2\omega$. The latter is much faster than any atomic dynamical timescale, and dropped in the so-called rotating-wave approximation

(RWA). With the zero of energy at the midpoint of the levels, the RWA Hamiltonian is

$$\hat{H}_{2\mathrm{L}} = \frac{\hbar}{2}\begin{pmatrix} -\Delta & \Omega_0 \\ \Omega_0 & \Delta \end{pmatrix}. \tag{2.27}$$

The eigenstates of $\hat{H}_{2\mathrm{L}}$ (dressed states) are stationary in the rotating frame. Diagonalization gives the generalized Rabi frequency $\Omega = \sqrt{\Omega_0^2 + \Delta^2}$ and eigenvalues $E_\pm = \pm\hbar\Omega/2$. The dressed states are superpositions of the bare states set by a mixing angle $\theta \in [0, \pi/2)$ as:

$$|+\rangle = \cos\theta\,|e\rangle + \sin\theta\,|g\rangle, \qquad |-\rangle = -\sin\theta\,|e\rangle + \cos\theta\,|g\rangle, \qquad \tan(2\theta) = -\Omega_0/\Delta \tag{2.28}$$

On resonance ($\Delta = 0$, $\theta = \pi/4$), the field mixes the bare states equally into symmetric and antisymmetric combinations separated by $\hbar\Omega_0$, known as the Autler-Townes splitting.

Far off-resonance $|\Delta| \gg \Omega_0$, the dressed states approach the bare states but pick up energy shifts from the off-resonant coupling. Expanding to leading order in Ω_0/Δ, the bare ground and excited states shift by

$$\delta E_g \approx +\frac{\hbar\Omega_0^2}{4\Delta}, \qquad \delta E_e \approx -\frac{\hbar\Omega_0^2}{4\Delta}. \tag{2.29}$$

This is the AC Stark effect (or light shift). Since $\Omega_0^2 \propto I$, the off-resonant field produces a conservative potential $U(\mathbf{r}) \propto I(\mathbf{r})/\Delta$. This is utilized in optical dipole traps, which attract atoms to intensity maxima for red detuning ($\Delta < 0$) and to intensity minima for blue detuning ($\Delta > 0$).

2.3.2.1 Optical Bloch Equations

For a two-level atom with spontaneous emission from $|e\rangle$ to $|g\rangle$ at rate Γ, the jump operator is $\hat{\sigma}^- = |g\rangle\langle e|$ and the dissipator is

$$\mathcal{L}(\hat{\rho}) = \begin{pmatrix} -\Gamma\rho_{ee} & -\frac{\Gamma}{2}\rho_{eg} \\ -\frac{\Gamma}{2}\rho_{ge} & \Gamma\rho_{ee} \end{pmatrix}.$$

Population flows incoherently from $|e\rangle$ to $|g\rangle$ at rate Γ, preserving $\mathrm{Tr}(\hat{\rho}) = 1$, and coherences decay at $\Gamma/2$. In practice, additional dephasing from collisions, laser linewidth, and stray fields contributes a pure dephasing rate γ_d; while non-zero atom velocity adds a correction to the detuning. These effects are considered in later sections.

Restricting ourselves to a stationary atom in the purely radiative limit, Eq. 2.22 in the

rotating frame gives the optical Bloch equations (OBEs):

$$\begin{aligned}\dot{\rho}_{ee} &= -\Gamma\rho_{ee} - \tfrac{i\Omega_0}{2}(\tilde{\rho}_{ge} - \tilde{\rho}_{eg}) \\ \dot{\tilde{\rho}}_{ge} &= -\left(\Gamma/2 + i\Delta\right)\tilde{\rho}_{ge} - \tfrac{i\Omega_0}{2}(\rho_{ee} - \rho_{gg}),\end{aligned} \tag{2.30}$$

with $\tilde{\rho}_{ge} = \rho_{ge}\exp(-i\Delta t)$, $\tilde{\rho}_{eg} = \tilde{\rho}^*_{ge}$ and $\rho_{ee} + \rho_{gg} = 1$. Since this dynamics plays out over a fast timescale of several microseconds, the steady state solution is of particular interest. Setting $\dot{\rho} = 0$ gives

$$\rho^{\text{ss}}_{ee} = \frac{\Omega_0^2/4}{\Delta^2 + \Gamma^2/4 + \Omega_0^2/2},$$

a Lorentzian in Δ. On resonance, $\rho^{\text{ss}}_{ee} \to 1/2$ as $\Omega_0 \gg \Gamma$ *i.e.*, the transition saturates. The FWHM defines the power-broadened linewidth

$$\Gamma' = \Gamma\sqrt{1+s},$$

with the on-resonance saturation parameter $s = 2\Omega_0^2/\Gamma^2$. At $s = 1$ the intensity equals the saturation intensity I_{sat}. The photon scattering rate is given by

$$R_{\text{sc}} = \rho_{ee}\Gamma = \frac{\Gamma}{2}\frac{s}{1 + s + (2\Delta/\Gamma)^2} \tag{2.31}$$

By noting that $\text{Im}(\tilde{\rho}_{ge}) = \Gamma\rho_{ee}/\Omega_0$ in steady state, the absorptivity from Eq. 2.26 reduces to

$$\frac{\partial I}{\partial z} = -N\hbar\omega R_{sc} \tag{2.32}$$

denoting loss of intensity through resonant fluorescence.

2.3.2.2 Principles of laser cooling

With the steady state solution for density matrix, the force on an atom in an optical field follows from Ehrenfest's theorem:

$$\mathbf{F} = -\langle\nabla\hat{H}_I\rangle = \text{Tr}[\hat{\rho}\,\nabla(\hat{\mathbf{d}}\cdot\mathbf{E}(\mathbf{r},t))].$$

For a field $\mathbf{E}(\mathbf{r},t) = E_0(\mathbf{r})\hat{\boldsymbol{\epsilon}}\cos(\omega t - \phi(\mathbf{r}))$, the gradient splits into an amplitude-gradient part (∇E_0) and a phase-gradient part ($\nabla\phi$).

$$\mathbf{F} = -\hbar\,\nabla\Omega_0\,\text{Re}[\tilde{\rho}^{\text{ss}}_{ge}] - \hbar\,\Omega_0\,\nabla\phi\,\text{Im}[\tilde{\rho}^{\text{ss}}_{ge}].$$

The first term, driven by the dispersive (in-phase) part of the coherence, is conservative.

Using the steady state solution for $\tilde{\rho}_{ge}^{\text{ss}}$ from Eq. 2.30 gives the conservative dipole force

$$\mathbf{F}_{\text{dip}} = -\frac{\hbar\Delta}{4}\frac{\nabla\Omega_0^2}{\Delta^2 + \Gamma^2/4 + \Omega_0^2/2}. \tag{2.33}$$

Notably, this force reduces to the gradient of the AC Stark shift found in Eq. 2.29 for far off-resonant light *i.e.,* $\Delta \gg \Gamma, \Omega_0$. Red-detuned light ($\Delta < 0$) pulls atoms toward high intensity, while blue-detuned light ($\Delta > 0$) pushes them toward low intensity. This forms the basis of optical dipole traps and optical lattices, which underpin the trapping mechanism in Chapter 6.

The second term, driven by the out of phase component, provides a dissipative force. It evaluates to the product of photon momentum and scattering rate:

$$\mathbf{F}_{\text{diss}} = \hbar\mathbf{k}\,\Gamma\,\rho_{ee}^{\text{ss}} = \hbar\mathbf{k}\,\Gamma\,\frac{\Omega_0^2/4}{\Delta^2 + \Gamma^2/4 + \Omega_0^2/2}. \tag{2.34}$$

Each absorbed photon imparts momentum $\hbar\mathbf{k}$; spontaneous emission is isotropic on average, so its recoils cancel and only the directed absorption contributes.

Eq. 2.34 is the foundational principle of laser cooling [113]. A velocity-dependent damping force can be generated by two counter-propagating red-detuned beams ($\Delta < 0$). An atom moving with velocity $\mathbf{v}$ sees the two beams Doppler-shifted to $\Delta \mp \mathbf{k}\cdot\mathbf{v}$, so it scatters preferentially from the beam it's moving into. Below saturation intensities, expanding the net force to first order in $\mathbf{v}$ gives

$$\mathbf{F}_{\text{molasses}} = -\alpha\mathbf{v}, \qquad \alpha = -\hbar k^2 \frac{16\Delta\Omega_0^2\Gamma}{(\Gamma^2 + 4\Delta^2 + 2\Omega_0^2)^2}. \tag{2.35}$$

Red detuning ensures viscous damping i.e. $\alpha > 0$. With counter-propagating beams in all three dimensions, atoms can be cooled in a so-called optical molasses. The finite linewidth limits the cooling to the Doppler limit $k_B T_D = \hbar\Gamma/2$. For the Rb D2 line, it is $T_D \approx 146\,\mu\text{K}$.

Although molasses damps velocity, atoms diffuse out of the cooling region due to the lack of a restoring force. Spatial confinement is afforded by superimposing a quadrupole magnetic field $\mathbf{B}(\mathbf{r}) = B'(x\hat{\mathbf{x}} + y\hat{\mathbf{y}} - 2z\hat{\mathbf{z}})$ at the intersection of the molasses beams, with opposite circular polarizations on each pair (σ^+ and σ^-). The Zeeman shift of the excited sublevels, combined with the selection rules for $\sigma^\pm$, ensures that atoms displaced from the trap center scatter preferentially from the beam that pushes them back. For low velocities and small displacements, the net force along each axis is

$$F = -\alpha v - \kappa z,$$

a damped harmonic oscillator with $\kappa \propto B'$. This technique, known as a magneto optical trap (MOT) [114], is the first step in nearly every ultracold-atom experiment.

2.3.3 Three-level atoms

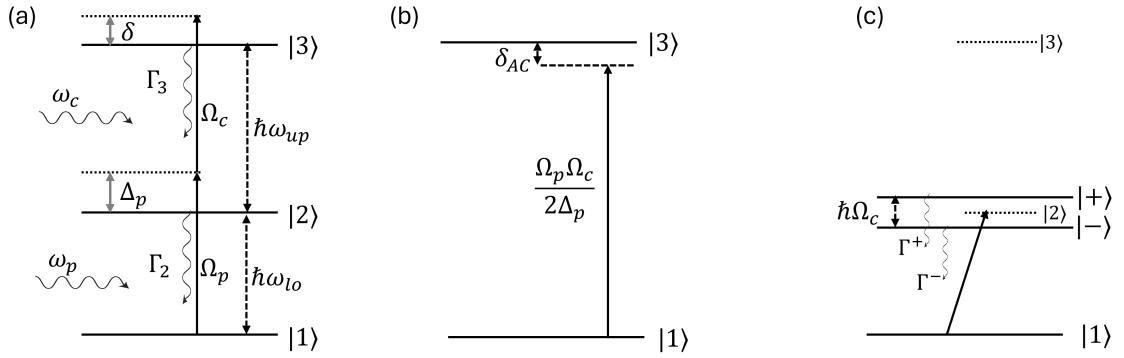


Figure 2.3: Atom-light interaction in a three-level cascade configuration. (a) General setup with ground state $|1\rangle$, an intermediate state $|2\rangle$, and an upper state $|3\rangle$. The transitions $|1\rangle \leftrightarrow |2\rangle$ and $|2\rangle \leftrightarrow |3\rangle$ are driven by probe and coupler laser with frequencies ω_p and ω_c, respectively. Corresponding detunings are Δ_p and $\delta - \Delta_p$, where δ is the two-photon detuning. The coherent drives are characterized by solid arrows with corresponding Rabi frequencies, Ω_p and Ω_c. (b) Off-resonant excitation through intermediate level $|2\rangle$ results in an effective two-photon excitation with Rabi frequency $\Omega_{2\mathrm{ph}} = \Omega_p\Omega_c/2\Delta_p$ with negligible population in $|2\rangle$ and a net Stark shift of $\delta_{AC} = \hbar(\Omega_c^2 - \Omega_p^2)/4\Delta_p$ (c) For on-resonant excitation with $\Delta_p = \Delta_c = 0$, a transparency feature emerges, explained here in the dressed state picture (solid lines) with bare states denoted in dashed lines. For $\Omega_c \gg \Omega_p$, dressed states $|\pm\rangle = (|3\rangle \pm |2\rangle)/\sqrt{2}$ are separated by $\hbar\Omega_c$. Interference of the excitation amplitudes from $|1\rangle$ to the dressed states results in vanishing absorption.

Coherent excitation of atoms to high-lying states often requires multiple lasers. The canonical model in such systems involves a three-level cascade shown in Fig. 2.3 (a). The dipole transition between $|1\rangle$ and $|3\rangle$ is parity-forbidden. The upper level $|3\rangle$ is metastable for most of this dissertation work so Γ_{32} is neglected. The detunings are

$$\Delta_p = \omega_p - \omega_{21}, \qquad \Delta_c = \omega_c - \omega_{32}, \qquad \delta = \Delta_p + \Delta_c$$

where δ is the two-photon detuning. In the frame rotating at ω_p for $|2\rangle$ and $\omega_p + \omega_c$ for $|3\rangle$), RWA yields the Hamiltonian:

$$\hat{H}_{3\mathrm{L}} = \frac{\hbar}{2}\begin{pmatrix} 0 & \Omega_p & 0 \\ \Omega_p & -2\Delta_p & \Omega_c \\ 0 & \Omega_c & -2\delta \end{pmatrix}, \tag{2.36}$$

Regarding the decoherence mechanism, a distinction must be drawn between pure dephasing processes such as laser jitter and incoherent processes causing population transfer such as spontaneous decay. Accordingly two Lindblad dissipators are used. The population decay Lindbladian is defined using the projection operators $\hat{\sigma}_{ij} = |i\rangle\langle j|$:

$$\mathcal{L}_{\text{decay}}(\hat{\rho}) = \Gamma_3 \left(\hat{\sigma}_{23}\hat{\rho}\hat{\sigma}_{32} - \frac{1}{2}\{\hat{\sigma}_{33}, \hat{\rho}\} \right) + \Gamma_2 \left(\hat{\sigma}_{12}\hat{\rho}\hat{\sigma}_{21} - \frac{1}{2}\{\hat{\sigma}_{22}, \hat{\rho}\} \right)$$

The dissipator for pure dephasing processes with rates γ_2^{dep} and γ_3^{dep} for states $|2\rangle$ and $|3\rangle$ respectively, is given as

$$\mathcal{L}_{\text{deph}}(\hat{\rho}) = \gamma_2^{\text{dep}} \left(\hat{\sigma}_{22}\hat{\rho}\hat{\sigma}_{22} - \frac{1}{2}\{\hat{\sigma}_{22}, \hat{\rho}\} \right) + \gamma_3^{\text{dep}} \left(\hat{\sigma}_{33}\hat{\rho}\hat{\sigma}_{33} - \frac{1}{2}\{\hat{\sigma}_{33}, \hat{\rho}\} \right)$$

Level $|3\rangle$ is usually a high-lying atomic level with negligible decay rate, so Γ_3 is ignored. With total decoherence rates defined as $\gamma_{12} = (\Gamma_2 + \gamma_2^{\text{dep}})/2$, $\gamma_{23} = (\Gamma_2 + \gamma_2^{\text{dep}} + \gamma_3^{\text{dep}})/2$, and $\gamma_{13} = \gamma_3^{\text{dep}}/2$, the population evolution is governed by

$$\begin{aligned} \dot{\rho}_{11} &= \Gamma_2 \rho_{22} + \frac{i}{2}\Omega_p(\rho_{12} - \rho_{21}) \\ \dot{\rho}_{33} &= \frac{i}{2}\Omega_c(\rho_{32} - \rho_{23}) \\ \dot{\rho}_{22} &= -\dot{\rho}_{11} - \dot{\rho}_{33} \end{aligned} \tag{2.37}$$

while the coherences evolve as

$$\begin{aligned} \dot{\rho}_{12} &= -\left(\gamma_{12} + i\Delta_p\right)\rho_{12} + \frac{i}{2}\Omega_p(\rho_{11} - \rho_{22}) + \frac{i}{2}\Omega_c\rho_{13} \\ \dot{\rho}_{23} &= -\left(\gamma_{23} + i\Delta_c\right)\rho_{23} + \frac{i}{2}\Omega_c(\rho_{22} - \rho_{33}) - \frac{i}{2}\Omega_p\rho_{13} \\ \dot{\rho}_{13} &= -\left(\gamma_{13} + i\delta\right)\rho_{13} - \frac{i}{2}\Omega_p\rho_{23} + \frac{i}{2}\Omega_c\rho_{12} \end{aligned} \tag{2.38}$$

The intermediate state detuning Δ_p plays a key role in the system dynamics. Large detuning leads to an effective two-level system while on-resonant excitation leads to interference effects, as detailed below.

2.3.3.1 Off-resonant excitation

For large intermediate detuning $|\Delta_p| \gg \Omega_p, \Omega_c, \Gamma_2, \gamma_{12}$, the intermediate state is barely populated and can be adiabatically eliminated *i.e.*, $\dot{\rho}_{22} \approx 0$. Two major features appear in this

effective two-photon regime. First, an effective Rabi frequency couples $|1\rangle$ and $|3\rangle$:

$$\Omega_{2\text{ph}} = \frac{\Omega_p \Omega_c}{2\Delta_p} \tag{2.39}$$

Second, each level picks up an AC Stark shift from the off-resonant coupling,

$$\delta E_1 = \frac{\hbar \Omega_p^2}{4\Delta_p}, \qquad \delta E_3 = \frac{\hbar \Omega_c^2}{4\Delta_p} \tag{2.40}$$

The two-photon resonance is shifted by the differential Stark shift

$$\delta_{\text{AC}} = \hbar \frac{\Omega_c^2 - \Omega_p^2}{4\Delta_p}, \tag{2.41}$$

so the resonance condition for the two-photon transition is $\delta = \delta_{\text{AC}}$, not $\delta = 0$. The off-resonant excitation scheme can effectively suppress the decoherence associated with the intermediate level. In the absence of pure dephasing processes, the effective decoherence arises from the residual $|2\rangle$ population, a small admixture given by $c_2 \sim \Omega_p/(2\Delta_p)$.

$$\gamma_{\text{eff}} \sim \Gamma_2 \frac{\Omega_p^2}{4\Delta_p^2} \tag{2.42}$$

The ratio of coherent to dissipative dynamics is $\Omega_{\text{eff}}/\gamma_{\text{eff}} \sim \Omega_c \Delta_p / \Gamma_2 \Omega_p$. Larger Δ_p enables coherent two-photon dynamics at the cost of a smaller Ω_{eff}, which must be compensated by higher laser power.

2.3.3.2 Electromagnetically Induced Transparency

For near-resonant coupling to $|1\rangle \rightarrow |2\rangle$, *i.e.*, $\Delta_p \approx 0$, , the probe experiences strong absorption in the absence of the coupling field. Adding a strong coupling field Ω_c on $|2\rangle \leftrightarrow |3\rangle$ dramatically modifies this response, producing a narrow transparency window known as electromagnetically induced transparency (EIT). The configuration of the three levels determines the specific physics. When energies increase monotonically as $|1\rangle \rightarrow |2\rangle \rightarrow |3\rangle$, the system realizes a ladder (or cascade) scheme, whereas when $|1\rangle$ and $|3\rangle$ share a common upper state $|2\rangle$, it forms a Λ scheme. While the underlying dynamics differ between configurations, EIT is generally interpreted as the result of destructive interference between excitation pathways. Throughout this section we consider stationary atoms. The modifications from thermal motion are taken up in Sec. 2.4.

The important features of EIT for a weak probe laser is discussed next, assuming coupler

laser is on resonance *i.e.*, $\Delta_c = 0$ and $\Delta_p = \delta$. In this limit, we approximate the steady-state coherences from by Eq. 2.38 using $\Omega_p \ll \Omega_c$, $\rho_{11} \gg \rho_{22}$ to yield

$$\begin{aligned} \rho_{31} &= \frac{-i\Omega_c/2}{\gamma_{13} - i\delta}\rho_{21} \\ \rho_{21} &= \frac{i\Omega_p/2}{\gamma_{12} - i\Delta_p + \dfrac{\Omega_c^2/4}{\gamma_{13} + i\delta}} \end{aligned} \tag{2.43}$$

We monitor the probe transmission, for which the linear susceptibility follows as

$$\chi(\delta) = \frac{2N|d_{12}|^2}{\epsilon_0\hbar\Omega_p}\rho_{21} = \frac{N|d_{12}|^2}{\epsilon_0\hbar}\frac{i\left(\gamma_{13} - i\delta\right)}{\left(\gamma_{12} - i\Delta_p\right)\left(\gamma_{13} - i\delta\right) + \Omega_c^2/4} \tag{2.44}$$

with the absorption and dispersion through the atomic medium are denoted by $\mathrm{Im}[\chi]$ and $\mathrm{Re}[\chi]$, respectively. Specifically, the absorption is given by

$$\mathrm{Im}[\chi(\delta)] \propto \frac{\gamma_{12}\delta^2 + \gamma_{13}\Omega_c^2/4 + \gamma_{12}\gamma_{13}^2}{\left(\gamma_{12}\gamma_{13} + \Omega_c^2/4 - \delta^2\right)^2 + \delta^2\left(\gamma_{12} + \gamma_{13}\right)^2} \tag{2.45}$$

which reduces to the two-level absorption in the absence of coupling laser *i.e.*, $\Omega_c = 0$.

With the probe laser on two-photon resonance ($\delta = 0$) and vanishing decoherence of $|3\rangle$ *i.e.*, $\gamma_{13} \to 0$, we find $\rho_{21} \to 0$ *i.e.*, the coupling field renders the medium transparent to the probe. This limit is particularly relevant in Λ systems *e.g.*, when $|1\rangle$ and $|3\rangle$ belong to a ground state hyperfine manifold. A physically illuminating interpretation is afforded by noting the eigenstate

$$|D\rangle = \frac{\Omega_c|1\rangle - \Omega_p|3\rangle}{\sqrt{\Omega_p^2 + \Omega_c^2}}$$

is decoupled from the lasers. Spontaneous emission optically pumps atoms into $|D\rangle$, where they no longer absorb the probe. The transparency is due to coherent population trapping in this dark state. Near $\delta = 0$, the dispersion $\mathrm{Re}[\chi]$ has a steep positive slope, resulting in group velocity $v_g \ll c$. This is the basis of slow-light experiments, CPT atomic clocks and quantum memory [115].

The following chapters use EIT in a ladder configuration, where $|3\rangle$ is a highly excited state. This setup requires a longer lifetime of $|3\rangle$ compared to $|2\rangle$ *i.e.*, $\Gamma_3 \ll \Gamma_2$. The transparency window is most easily understood in the dressed-state picture of $|2\rangle \leftrightarrow |3\rangle$ transition with zero energy reference set to $|2\rangle$. On resonance $\Delta_c = 0$, the coupling field dresses $|2\rangle$ and $|3\rangle$ into eigenstates $|\pm\rangle = (|2\rangle \pm |3\rangle)/\sqrt{2}$ split by $\hbar\Omega_c$. The probe, which would have been resonant with bare $|2\rangle$, is now detuned from both dressed states by $\pm\Omega_c/2$ and

the absorption profile becomes a doublet. When $\Omega_c \lesssim \gamma_{12}$, the two Lorentzian wings of the doublet interfere destructively and produce a narrow transparency window. The distinction between this interference picture and the resolved-doublet regime of Autler–Townes splitting has been the subject of explicit discussion in the literature [116], but is tangential to the later experiments that rely on EIT with thermal vapor. EIT linewidth for cold atoms is dominated by power broadening and approximated as

$$\gamma_{\mathrm{EIT}} \approx \frac{\Omega_p^2 + \Omega_c^2}{\gamma_{12}}.$$

EIT forms the workhorse for narrow-linewidth spectroscopy of $|3\rangle$. When $|3\rangle$ is a highly excited Rydberg state, as is the case in later experiments, the transparency feature is sensitive to perturbations of the Rydberg level arising from external electromagnetic field. The exaggerated response of Rydberg atoms to dc and rf electric fields via Stark shift coupled with the high-resolution, all-optical probing afforded by EIT has emerged as a robust promising quantum sensing platform.

2.4 Spectroscopy with room temperature atoms

The experiments in the following chapters are performed in warm atomic vapor, where atoms have a broad distribution of velocities. The principles of atom-light interaction described in the previous section neglect atomic motion. To describe spectroscopy in thermal ensembles, the master equation is solved at fixed atomic velocity using the Doppler-shifted detuning, and the result is averaged over the thermal velocity distribution. This process of Doppler averaging rests on a crucial assumption that coherences across velocity classes do not mix, a caveat that may break down in collisional environments. Such velocity changing collisions are primarily relevant for processes involving ground state hyperfine coherence, such as Λ-EIT, where the atomic coherences are robust against collisions, unlike optical coherences in ladder-EIT like systems.

An immediate application of the velocity averaging principle reveals the Doppler broadening in the absorption of a weak, near-resonant laser beam in a thermal atomic vapor. The absorptivity from Eq. 2.26 is modified as

$$\alpha(\delta) = \frac{N\omega\Gamma d_{eg}^2}{2c\epsilon_0\hbar}\sqrt{\frac{m}{2\pi k_B T}}\int_{-\infty}^{\infty}\frac{e^{-mv_z^2/2k_BT}}{\Gamma^2/4 + (\delta - kv_z)^2}\,dv_z \tag{2.46}$$

where T and m refer to the temperature and mass of the atoms. The Doppler broadened linewidth of room temperature rubidium vapor is ≈ 500 MHz, about two orders of magnitude

larger than the natural linewidth.

For multi-level processes, Doppler effect brings additional consideration with regards to the beam alignment and interpretation of the spectral features. Ladder-type EIT with Rydberg atoms in thermal vapor, the most relevant technique for this dissertation, is discussed below in detail.

2.4.1 Rydberg-EIT in thermal vapor

Rydberg-EIT with room temperature alkali atoms, often confined in vapor cells, has gained tremendous momentum in recent years as a quantum-sensing platform for electrometry, owing to the compact form factor and signal improvement afforded by large interaction volume. Thermally averaged ensemble response in such vapor cells is highly sensitive to beam alignment, wavelength mismatch between probe and coupling fields, cell geometry, atom-laser interaction region and cell wall material.

The most significant implication of Doppler averaging is the constraint on the geometry and wavelengths of the probe laser (λ_p) and coupler laser (λ_c). In order to maintain the two-photon resonance in the ladder shown in Fig. 2.3 despite Doppler effect, the following condition must be satisfied

$$(\omega_c - \vec{v} \cdot \vec{k}_c) + (\omega_p - \vec{v} \cdot \vec{k}_p) = \omega_{up} + \omega_{lo} \tag{2.47}$$

EIT fundamentally requires resonant lasers *i.e.*, $\omega_p \approx \omega_{lo}$ and $\omega_c \approx \omega_{up}$. Therefore the probe and coupler lasers must counter-propagate to cancel the Doppler shifts to the furthest extent possible. The linewidth remains limited by the residual Doppler shift in a wavelength mismatched ladder system, typically approximated as $|k_p - k_c| v_{th}$, where $v_{th} = \sqrt{2k_B T/m}$ is the most probable thermal velocity.

The constraint on the relative wavelengths is best explained in Fig. 2 of Ref [117], which shows the ensemble averaged probe transmission for various ratios of λ_p/λ_c. The window of transparency has been shown to vanish for $\lambda_p < \lambda_c$. As expected, the narrowest linewidth is achieved for equal probe and coupler wavelength. Such near-perfect Doppler cancellation enables sub-kHz linewidths in Λ-EIT [115, 118] and sub-MHz linewidths in three-photon ladder schemes [119]. However, no such pair of transitions are available for two-photon Rydberg-EIT with alkali atoms, which are the only species with adequate vapor pressure. This requirement constrains the choice of probe transition to the D1 ($\approx$ 795 nm) or D2 ($\approx$ 780 nm) line in rubidium vapor and accordingly the coupler wavelength to $\approx$ 476nm or $\approx$ 480 nm for two-photon EIT.

The Rydberg-EIT experiments described in later chapters have the probe laser frequency-

	Ground state	Intermediate state	Rydberg state
Probe locked, coupler scanned	$\frac{\lambda_p}{\lambda_c}$	$1 - \frac{\lambda_p}{\lambda_c}$	1
Probe scanned, coupler locked	1	$1 - \frac{\lambda_c}{\lambda_p}$	$\frac{\lambda_c}{\lambda_p}$

Table 2.2: Frequency scaling factors in a wavelength-mismatched ladder-EIT

stabilized to the intermediate state, while the coupler laser is scanned across the Rydberg resonance over ≈1 GHz. Since this scan range adequately covers the hyperfine structure of the intermediate state and fine structure of the Rydberg states in alkali atoms, multiple resonances are revealed in the EIT spectrum. These spectral features need to be corrected for wavelength mismatch, as shown in Table 2.2.

EIT in vapor cells is an active area of research for metrology of electromagnetic fields [51, 54, 120], quantum memories and slow light [121] as well as atomic clocks and magnetometry [122, 123]. Further information on the implementation of the EIT schemes, applications, broadening mechanisms and sensitivity limits are detailed in Refs. [51, 104].

CHAPTER 3

Physics of Rydberg Atoms and Plasma

This chapter introduces the three foundational topics underlying much of the rest of this thesis: Rydberg atoms, collisional broadening of Rydberg levels, and the low-temperature plasma regime, the setting for the field-sensing work in this thesis. I first present the key properties of alkali Rydberg states in Sec. 3.1 with particular emphasis on the relevant scaling laws. Sec. 3.2 develops a general framework for collisional broadening, applied in Chapter 4 and 5 to Rydberg spectra. Sec. 3.3 discusses the key physical concepts of low-temperature plasma.

3.1 Rydberg atoms

Conventionally "Rydberg" designation is used for $n \gtrsim 15$, although this boundary is context dependent. The scaling laws that follow from the valence electron's large orbital radius and small binding energy make the response of Rydberg states exaggerated yet tractable. By $n \sim 50$, a Rydberg atom is more than a thousand times the size of a ground-state atom and is roughly 10^6 times more polarizable [45]. This section develops a general description of Rydberg atoms and their scaling laws. The concepts presented here inform the choice of Rydberg states for electromagnetic field sensing in the later chapters, which require a trade-off between sensitivity, decoherence mechanisms and experimental constraints such as limitations on Rabi frequency due to laser powers.

3.1.1 Quantum Defects

The model-potential framework described in Chapter 2 works particularly well for Rydberg states compared to low-lying ones. Numerical solutions for the radial wavefunction avoid the near-core difficulties that complicate low-lying states since the Rydberg electron has little

Property	Scaling	Expression
Orbital radius, $\langle r \rangle$	$(n^*)^2$	$[3(n^*)^2 - \ell(\ell+1)]/2$
Binding Energy, E_{n^*}	$(n^*)^{-2}$	$-R_y/(n^*)^2$
Energy level spacing, ΔE	$(n^*)^{-3}$	$E_{n^*+1} - E_{n^*}$
Rydberg-Rydberg transition dipole moment, μ	$(n^*)^2$	$\langle n^{*\prime}\ell' = \ell \pm 1 \vert er \vert n^*\ell\rangle$
Rydberg-ground transition dipole moment, μ_{rg}	$(n^*)^{-3/2}$	$\langle n^*\ell \vert er \vert g\rangle$
Polarizability, α	$(n^*)^7$	$\mu^2/\Delta E$
Radiative lifetime (at 0 K), $\tau_{n\ell}(n \gg \ell)$	$(n^*)^3$	$\tau_0(n^*)^{\alpha_\ell}$
BBR lifetime (300 K), $\tau^{bb}_{n\ell}$	$(n^*)^2$	$3\hbar(n^*)^2/4\alpha^3 k_B T$

Table 3.1: Scaling laws of Rydberg atoms [45]

overlap with the core. The radial wavefunction is given by solving

$$\left[-\frac{\hbar^2}{2m_e}\frac{d^2}{dr^2} + \frac{\hbar^2\ell(\ell+1)}{2m_e r^2} + V_{nlJ}(r) + V_{\text{model}}(r)\right] u_{n\ell J}(r) = E_{n\ell J} u_{n\ell J}(r), \tag{3.1}$$

with spectroscopically determined values $E_{n\ell}$. The spin-orbit coupling potential $V_{nlJ}(r) = (j(j+1) - \ell(\ell+1) - s(s+1))\,\xi_{n\ell}(r)$ relies on a coupling function $\xi \sim 1/r^3$ mostly localized within the core and therefore ignored. Instead, the fine structure is included in the radial wavefunction through the appropriate values of $E_{n\ell J}$ as the input.

The energy levels are well-characterized by the quantum defect-based correction to hydrogenic levels. For sufficiently high n, the Ritz expansion converges rapidly and the quantum defect is well-approximated by the constant value of δ_0

$$E_{n\ell j} = -\frac{\text{Ry}}{(n-\delta_0)^2} = -\frac{\text{Ry}}{n^{*2}}. \tag{3.2}$$

Low-ℓ states with core penetration feature a large correction e.g., $\delta_S \approx 3.13$ in Rb, so the nS series lies a few hundred GHz below the prediction of a hydrogenic series. The quantum defect falls off rapidly with increasing ℓ, since the centrifugal barrier keeps high-ℓ electrons outside the core. For $\ell \gtrsim 4$, δ_ℓ is essentially zero and the levels are hydrogenic.

3.1.2 Scaling Laws

Important scaling laws of Rydberg atoms with respect to n^* have been tabulated in Table 3.1. Some salient features highly relevant for this dissertation are discussed below.

3.1.2.1 Transition dipole moment and radiative lifetime

The experiments in this dissertation are conducted with nS and nD states, which are considered low angular momentum states since $\ell \ll n^*$. The spontaneous decay rate from a Rydberg state $|n\ell\rangle$ to a lower energy state $|n'\ell'\rangle$ is governed by the Einstein A coefficient as

$$A_{n\ell\to n'\ell'} = \frac{\omega^3_{n\ell\to n'\ell'}}{3\pi\epsilon_0\hbar c^3}|d_{n\ell\to n'\ell'}|^2, \tag{3.3}$$

where $d_{n\ell\to n'\ell'}$ is the transition dipole moment and $\omega_{n\ell\to n'\ell'}$ is the transition frequency.

The radiative lifetime, $\tau_{n\ell} = (\sum_{n'\ell'} A_{n\ell\to n'\ell'})^{-1}$ is dominated by decay to the low-lying states due to the limited number of dipole-allowed transitions and large scaling with the transition frequency. On the other hand, the $1/n^2$ scaling of binding energy renders $\nu_{n\ell\to n'\ell'}$ almost constant for large n. Thus, the radiative lifetime is essentially determined by the transition dipole moment of $|n\ell\rangle$ with a low-lying $|n'\ell'\rangle$.

The scaling of Rydberg-ground transition dipole moment arises from the weak overlap of Rydberg electron with the localized low-lying state. With the latter approximated as a delta function, the dipole moment depends on the normalization constant of the Rydberg radial wavefunction leading to a $n^{-3/2}$ scaling. Thus, the radiative lifetime scales as n^3. While not used in this dissertation, states with $\ell \sim n^*$, also known as circular states, have substantially longer lifetime that scales as n^5 due to the scarcity of allowed lower-lying decay channels.

While the radiative lifetime at large n ranges from 10µs to several 100µs, at room temperature, blackbody-driven transitions to nearby Rydberg states often dominate over spontaneous emission and reduce the effective lifetime substantially [124]. The overall decay rate is a major contributor to γ_{32} in Fig. 2.3, which must be substantially below 1 MHz for Rydberg-EIT experiments.

3.1.2.2 Dipole Polarizability

Unlike Rydberg-ground dipole moment, the dipole moment between adjacent Rydberg states scales as n^2 following $\langle r\rangle$. For $n \gtrsim 30$, these dipole moments are two to three orders of magnitude larger than the typical optical-transition dipoles. Combined with the much smaller energy spacing ($\sim n^{-3}$), this means that microwave fields drive Rydberg-Rydberg transitions with Rabi frequencies orders of magnitude larger than what optical fields drive between low-lying states.

For static fields and $\ell \ll n^*$ and a weak electric field, the interaction does not surpass the splittings induced by the quantum defect and fine structure. In this limit, the first order Stark shift vanishes just like low-lying states. With quantization axis z chosen along

the electric field and electron coordinate along the axis given by z_e, the resulting shift is estimated by second order non-degenerate perturbation theory

$$\Delta W_{n,l,j,m_j} = -\frac{1}{2}\alpha_{nljm_j}E^2, \quad \alpha_{nljm_j} = 2e^2 \sum_{n'l'j'm'_j} \frac{|\langle nljm_j|z_e|n'l'j'm'_j\rangle|^2}{W_{n'l'j'm'_j} - W_{nljm_j}}. \tag{3.4}$$

The polarizability α_{nljm_j} combines the n^2 scaling of Rydberg-Rydberg transition dipole element with the n^3 scaling of energy level spacing in the denominator, resulting in a steep n^7 scaling. For instance, α grows by nine orders of magnitude between the ground state and $n = 50$. Stray fields that are negligible for ground-state spectroscopy become dominant perturbations for Rydberg states. While this scaling makes Rydberg atoms exquisite electrometers, it erodes ground-Rydberg coherence in poorly shielded environments.

It is important to note that the perturbative treatment and quadratic dependence is valid only in the limits of weak field, which depends on n^*. Direct diagonalization with an adequately large basis states is required for accurate calculation of Stark maps. Fig. 3.1 shows the Stark map for states lying between the $26H$ and $27H$ Hydrogenic manifold. The breakdown of the perturbative treatment is clear from the mixing of fine structure component beyond 20 V/cm. This has important implications for Rydberg-EIT based modeling of electric field performed in Chapter 5.

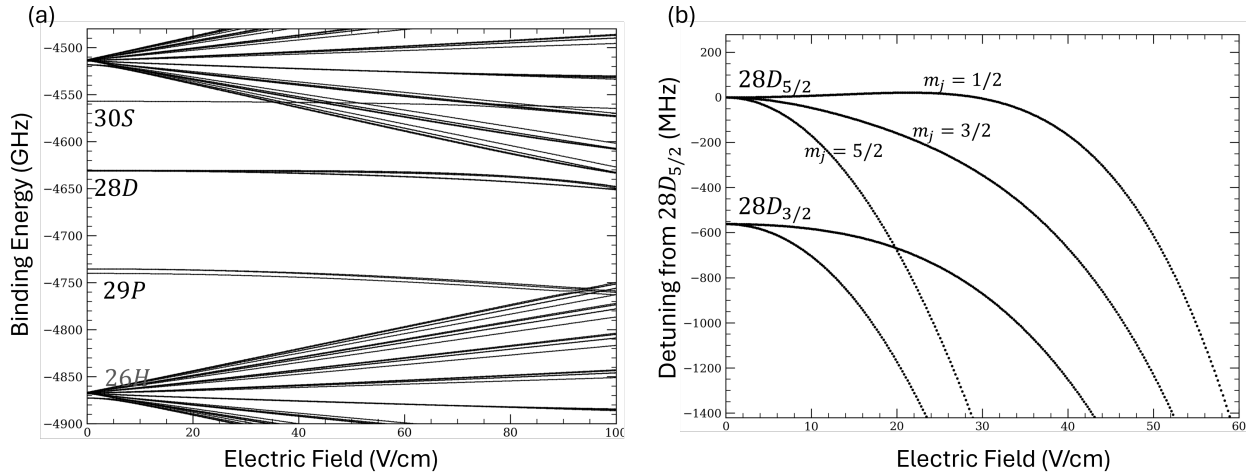


Figure 3.1: Stark map of ^{85}Rb (a) in the range between 26H and 27H manifolds, (b) for the $28D$ state

3.1.2.3 Ionization

The low angular momentum Rydberg states ionize at $E_{\text{ion}} \sim (2n^*)^{-4}$ in atomic units, equivalent to $3.2\times10^8/(n^*)^4$ V/cm. For the range of Rydberg states used in this experiment, several 100 V/cm are needed to ionize the atom. While this is commonly used in state-selective field ionization based detection in cold atom experiments, none of the room temperature experiments described in this thesis feature such strong fields.

A second characteristic field, the Inglis-Teller limit F_{IT}, marks the field at which adjacent hydrogenic n-manifolds overlap due to Stark mixing, so that individual Rydberg lines can no longer be resolved. The limit was first derived by Inglis and Teller in the context of stellar atmospheres, where the disappearance of high Balmer lines in stellar spectra can be used to infer electron density via the plasma microfield that Stark-broadens the lines. For alkali atoms, the analogous threshold is set by the field at which the Stark shift of low-ℓ states becomes comparable to their quantum-defect-induced separation from the hydrogenic manifold. The Rydberg states used in this work have n low enough that the corresponding F_{IT} is well above the plasma fields we measure.

3.2 Collision theory of Rydberg atoms

Collision-induced perturbations to atomic transitions play a central role in this dissertation. Such effects are particularly pronounced for Rydberg transitions due to the large orbital and weakly bound nature of Rydberg electron. Pressure broadening of Rydberg transitions has been studied for nearly a century, from emission spectroscopy in 1930s through the laser era beginning in the 1960s. The wealth of experimental record has been matched by an equally rich theoretical literature, beginning with Fermi's 1934 pseudopotential treatment [95] and culminating in the unified impact-approximation framework of Baranger [125] and the systematic Rydberg-specific calculations of Omont, Beigman, and others [96–99].

This section presents a brief overview of the semiclassical frameworks developed over the past half-century. They share three core approximations: the perturber-Rydberg interaction is weak (perturbative), the perturber moves slowly enough to be treated quasi-classically (low-energy), and the collision duration is short compared to bound-state timescales (the impact approximation). Sec. 3.2.1 connects experimentally observed line shapes to the quantum-mechanical atomic processes. For a general perturber interaction model, Sec. 3.2.3 presents a formulation for elastic scattering. Sec. 3.2.4 introduces the Born approximation to estimate the rates of inelastic collisions.

3.2.1 Origin of line shapes

In order to derive modifications to atomic levels, experimentally measured spectral profiles need to be related to atomic processes. The dipole autocorrelation function forms the bridge between the macroscopically observed line shape and the internal quantum dynamics of the atom. From classical electrodynamics, the radiated electric field in the far field is proportional to $\ddot{d}(t)$, and the spectrum of emitted radiation is the power spectral density of this field. By the Wiener–Khinchin theorem, the power spectrum of a stationary stochastic process is the Fourier transform of its autocorrelation function. Specializing to a narrow frequency range near a resonance ω_0, this gives the canonical relation

$$I(\omega) \propto \mathrm{Re} \int_0^\infty \langle d^*(0)\, d(t) \rangle\, e^{i\omega t}\, dt, \tag{3.5}$$

with $\langle \cdot \rangle$ denoting an ensemble average over emitters. For simplicity, the natural linewidth is ignored in this discussion.

Despite the classical origin, Eq. 3.5 follows quantum mechanically from Fermi's Golden Rule. Summing absorption rates over all initial states with thermal weights p_i and final states and rewriting the energy-conserving delta function as a Fourier integral, one obtains

$$I(\omega) \propto \int_{-\infty}^{\infty} dt\, e^{i\omega t} \sum_i p_i \langle i|\hat{d}(0)\hat{d}(t)|i\rangle = \int_{-\infty}^{\infty} dt\, e^{i\omega t}\, \langle \hat{d}(0)\hat{d}(t)\rangle. \tag{3.6}$$

The line shape is, in either formulation, the Fourier transform of a quantum-statistical correlation function $C(t) \equiv \langle \hat{d}(0)\hat{d}(t)\rangle$.

$C(t)$ is a property of the atom in its environment, not the isolated atom. Every physical mechanism that produces a finite linewidth such as spontaneous emission, collisions, fields, essentially modifies the time evolution of $C(t)$. The structure of $C(t)$ thus encodes all the physics of line formation, and the central task of any line shape theory involves solving its time evolution.

3.2.2 Collisional Broadening in the Impact Approximation

Apart from the Doppler broadening due to thermal motion, collisions with the background perturbers are the dominant source of line broadening for an atom embedded in a buffer gas of perturbers at density N. The simplest and most widely useful framework for treating this is the impact approximation, which exploits the timescale separation between the duration of an individual collision $\tau_c \sim r_c/V$ (where r_c is the interaction range and V the relative velocity), and the mean time between collisions $\tau_0 \sim 1/(N\sigma V)$ (where σ is a typical cross

section). When $\tau_c \ll \tau_0$, collisions are well-separated, statistically independent events that act on the timescale of τ_0 as instantaneous perturbations of the dipole.

Under these conditions, the dipole oscillates freely at ω_0 during the mean free time. Each collision modifies the dipole by a complex factor ξ_i representing either a phase change, an amplitude reduction, or a state change that may quench the dipole entirely. Since the number of collisions $N(t)$ follows Poisson statistics with mean $\langle N(t)\rangle = N\langle V\sigma\rangle t$, averaging over both the collision number and the independent and identically distributed ξ_i yields an exponential decay:

$$C(t) \propto e^{-i\omega_0 t}\left\langle \prod_{i=1}^{N(t)} \xi_i \right\rangle = e^{-i\omega_0 t}\exp\left[-N\langle V\sigma_c\rangle t\right], \tag{3.7}$$

where the complex collision cross section σ_c is defined through $\langle V\sigma_c\rangle \equiv \langle V\sigma\,(1-\xi)\rangle$, with the angle brackets denoting a thermal average. Defining $\Gamma + i\Delta \equiv N\langle V\sigma_c\rangle$, the correlation function decays as $C(t) \propto e^{-i(\omega_0+\Delta)t}\,e^{-\Gamma t}$. The Fourier transformation yields a Lorentzian profile

$$I(\omega) \propto \frac{\Gamma}{(\omega-\omega_0-\Delta)^2+\Gamma^2}, \tag{3.8}$$

centered at $\omega_0 + \Delta$ with half-width at half-maximum Γ. Thus broadening and shift are determined by the real and imaginary parts of the scattering cross section, respectively.

The substantive physics lies in computing σ_c from the underlying collision dynamics. The structure of this calculation depends on whether the collision leaves the radiating atom in its original internal state (an elastic process) or transfers it to a different state (an inelastic process).

3.2.3 Elastic Collisions: Phase-Shift Representation

In an elastic collision, the radiating atom remains in its original state $|a\rangle$ throughout the encounter. The collision perturbs the energy of $|a\rangle$ only momentarily as the perturber passes, resulting in a phase shift of the dipole oscillator. If the instantaneous interaction between the atom in state $|a\rangle$ and a perturber at position $\mathbf{R}(t)$ is $V_a[\mathbf{R}(t)]$, then over the course of a collision with impact parameter $|\boldsymbol{\rho}| = \rho$, the straight-line trajectory of the perturber is $\mathbf{R}(t) = \boldsymbol{\rho} + \mathbf{V}t$, and the dipole accumulates a phase

$$\eta_a(\rho, V) = \frac{1}{\hbar}\int_{-\infty}^{\infty} V_a[\mathbf{R}(t)]\,dt. \tag{3.9}$$

However, the spectroscopically relevant quantity is not η_a alone, rather the differential phase shift $\eta(\rho, V) = \eta_a(\rho, V) - \eta_b(\rho, V)$ between the upper and lower levels of the optical transition. For a Rydberg transition, the lower level $|b\rangle$ is typically a deeply bound state

whose interaction with the perturber is negligible compared to that of the diffuse Rydberg state $|a\rangle$, so $\eta_b \approx 0$ and the differential phase reduces to that of the Rydberg level alone.

A single passage of a perturber at impact parameter ρ with velocity V dephases the dipole by $\eta(\rho, V)$. Averaging over the Poisson distribution of collision events, integrating over impact parameters, and thermal-averaging over V, the impact-approximation expression for the complex collisional rate yields

$$\Gamma + i\Delta = N \left\langle V \int_0^\infty 2\pi\rho \, d\rho \left[1 - e^{-i\eta(\rho,V)}\right] \right\rangle_T . \tag{3.10}$$

This leads to the broadening and line shift rate given by

$$\Gamma = N \left\langle V \int_0^\infty 2\pi\rho \, d\rho \left[1 - \cos\eta(\rho,V)\right] \right\rangle_T , \tag{3.11}$$

$$\Delta = N \left\langle V \int_0^\infty 2\pi\rho \, d\rho \, \sin\eta(\rho,V) \right\rangle_T . \tag{3.12}$$

Two features of this result deserve emphasis. Firstly, the formula is non-perturbative in η since elastic phases simply add along the trajectory. The Born approximation is recovered as the leading term when $\eta \ll 1$, where $1 - \cos\eta \approx \eta^2/2$. Secondly, the broadening arises from variation of the phase, since $1 - \cos\eta$ is an even function of η that vanishes only when $\eta = 0$ identically. On the other hand, the shift arises from the mean phase since $\sin\eta$ is odd in η and changes sign with the interaction. While a purely fluctuating perturbation broadens the line, a coherent net interaction is required to produce a line shift.

Eq. 3.11 and 3.12 abstract away the specifics of the atomic state and perturber in the function $\eta(\rho, V)$. The final steps are formulating models of the atom-perturber interaction and then estimating $\eta(\rho, V)$. A model of the Rydberg-neutral collisions and the corresponding shift and broadening cross section are described in Chapter 4.

3.2.4 Inelastic Collisions

The phase shift representation cannot natively handle inelastic processes causing decays and loss of coherence. A unified framework, introduced by Baranger [125], incorporates both elastic and inelastic processes through scattering matrix theory. For a transition between an upper level a and a lower level b, the Baranger result for the complex collisional rate is

$$\Gamma - i\Delta = N \left\langle V \int 2\pi\rho \, d\rho \left[1 - \langle S_a^\dagger \, S_b \rangle\right] \right\rangle_T , \tag{3.13}$$

where S_a and S_b are the scattering matrices describing how a perturber scatters off the atom in each of the two levels. The angle brackets inside denote averages over collision

orientations and internal degrees of freedom of the perturber. The outer brackets denote thermal averaging over V. The scattering matrix in each level decomposes as $S_a = e^{i\eta_a} \cdot \mathcal{S}_a^{\text{inel}}$. Due to unitarity of the elastic channel, η_a is real and represents the elastic phase shift while $\mathcal{S}_a^{\text{inel}}$ encodes inelastic transitions to other states. For a deeply bound lower state, the lower state $|b\rangle$ has negligible interaction with the perturber ($S_b \approx 1$), yielding

$$\Gamma + i\Delta = N\left\langle V \int 2\pi\rho \, d\rho \left[1 - e^{-i\eta_a} \langle a|\mathcal{S}_a^{\text{inel}}|a\rangle\right]\right\rangle_T, \tag{3.14}$$

where, $\langle a|\mathcal{S}_a^{\text{inel}}|a\rangle = \sqrt{1 - \sum_{c\neq a} |S_{ca}|^2} = \sqrt{1 - P_a^{\text{inel}}}$ *i.e.*, the amplitude for the atom to remain in $|a\rangle$. The probability P_a^{inel} is controlled by the adiabaticity of the collisional encounter and the availability of energetically accessible final states [126]. In the limits of weak collision $\eta_a \ll 1$ and small inelastic transition $P_a^{\text{inel}} \ll 1$, the optical cross section expands in leading order to

$$1 - e^{-i\eta_a} \langle a|\mathcal{S}_a^{\text{inel}}|a\rangle \approx \underbrace{(1 - e^{-i\eta_a})}_{\text{elastic}} + \underbrace{\tfrac{1}{2} e^{-i\eta_a} P_a^{\text{inel}}}_{\text{inelastic}}. \tag{3.15}$$

Elastic processes contribute to both Γ and Δ as discussed in the previous section. However, the inelastic term primarily contributes to broadening through the real part $\frac{1}{2}P_a^{\text{inel}}$ representing loss of population from $|a\rangle$, while its contribution to the line shift is higher order in η_a. Although Baranger's formulation provides an elegant theoretical framework, computation of the cross section from the underlying interaction requires a semiclassical approach.

3.2.4.1 Computing Inelastic Rates: Born Approximation

In the impact-parameter representation, the perturber follows a classical straight-line trajectory $\mathbf{R}(t) = \rho + \mathbf{V}t$, and the perturbation is given by $V[\mathbf{r}_e, \mathbf{R}(t)]$. Treating $V[\mathbf{r}_e, \mathbf{R}(t)]$ in time-dependent perturbation theory, the first-order amplitude for a Rydberg-Rydberg transition $i \to f$ is

$$A_{fi}(\rho, V) = -\frac{i}{\hbar} \int_{-\infty}^{\infty} dt \, e^{i\omega_{fi}t} \langle c|V[\mathbf{r}_e, \mathbf{R}(t)]|a\rangle,$$

where $\omega_{fi} = (E_f - E_i)/\hbar$ is the energy defect of the transition. For strong perturbations, closed coupling methods must be used instead of perturbation theory, however this is not the case for any process in the experiments described later.

An important point regarding the interaction potential needs to be highlighted here. Due to the nature of inelastic process ($c \neq a$), the only interaction terms with non-zero contribution must include the Rydberg electron. With this in mind, the cross-section is

given by

$$\sigma_{fi}(V) = 2\pi \int_0^\infty W_{fi}(\rho, V)\rho \, \mathrm{d}\rho, \quad W_{fi}(\rho, V) = |a_f(\rho, V; t = +\infty)|^2. \tag{3.16}$$

The inelastic broadening is derived after ensemble averaging as $\Gamma^{\text{inel}} = N\langle V\sigma_{fi}(V)\rangle_T$. Broadening for common inelastic processes are discussed in Chapter 4.

3.3 Plasma Physics

Although non-neutral plasmas exist and form an active area of research, this dissertation deals with neutral plasmas, in particular a quasineutral, weakly ionized, low-pressure discharge sustained by a radio-frequency field. This section presents a compact and abridged set of relations needed to characterize the macroscopic state of the discharge.

Sec. 3.3.1 describes the collective behavior of a plasma and the characteristic length and time scales. Sec. 3.3.2 turns to the energy distributions of the charged species. Sec. 3.3.3 and 3.3.4 then address the two channels through which the discharge interacts with its environment *i.e.*, the sheath which mediates between bulk and boundary, and the collisional processes that sustain the bulk against losses. These elements come together in Sec. 3.3.5, where global particle and power balances act as the equations of state of the discharge. Finally Sec. 3.3.6 explains the response of the plasma to the time-varying fields of an rf source. A complete development of any of these topics can be found in standard texts [111].

3.3.1 Collective electrostatics

For the work presented in upcoming chapters, an ionized gas qualifies as a plasma upon the emergence of quasi-neutrality and collective dynamics dominated by long-range electromagnetic interactions rather than by binary collisions. The response of a charged ensemble to small perturbations reveals whether both of these conditions hold.

Electrons, being vastly more mobile than ions, rearrange to screen any test charge $+Q$ placed within an otherwise uniform plasma of density n_0 and electron temperature T_e. Therefore, the ions may be treated as a stationary neutralizing background on the timescales of interest here. Assuming thermal equilibrium, the electron density follows a Boltzmann distribution given by the resulting electrostatic potential $\phi(\mathbf{r})$,

$$n_e(\mathbf{r}) = n_0 \exp\left(\frac{e\phi}{k_B T_e}\right) \approx n_0 \left(1 + \frac{e\phi}{k_B T_e}\right), \tag{3.17}$$

where the linearization assumes $e\phi \ll k_B T_e$ away from the test charge. Given an ion background n_0, Poisson's equation n_0 yields

$$\nabla^2 \phi = \frac{1}{\lambda_D^2}\,\phi, \qquad \lambda_D \equiv \sqrt{\frac{\epsilon_0 k_B T_e}{n_0 e^2}}. \tag{3.18}$$

The solution is a screened Yukawa potential, $\phi(r) = (Q/4\pi\epsilon_0 r)\exp(-r/\lambda_D)$, which decays exponentially over the Debye length λ_D. Therefore, any local charge imbalance is neutralized within the plasma and the plasma appears quasineutral, $n_e \approx n_i$ over length scales $L \gg \lambda_D$. Deviations from neutrality at length scales smaller than λ_D give rise to a stochastic microfield, a topic investigated in Chapter 5. The derivation assumes an implicit constraint on the number of particles. The screening picture relies on having enough particles within a Debye sphere to support a statistical description, i.e. $N_D \equiv \frac{4}{3}\pi n_0 \lambda_D^3 \gg 1$. For representative low-pressure ICP conditions ($T_e \sim 3$ eV, $n_e \sim 10^{11}$ cm^{-3}), $\lambda_D \sim 40$ μm and $N_D \sim 3 \times 10^4$. Both are well within the plasma regime in Chapter 5 where reactor dimensions are several centimeters.

While screening describes the static response, the dynamic analogue reveals the characteristic frequency of collective motion. When a thin slab of electrons is displaced by a small distance ξ relative to the ion background, the resulting surface charges produce a restoring a harmonic force $m_e\ddot{\xi} = -eE = -n_0 e^2/\epsilon_0 \xi$, that yields the electron plasma frequency

$$\omega_{pe} = \sqrt{\frac{n_0 e^2}{\epsilon_0 m_e}}. \tag{3.19}$$

Physically, ω_{pe} sets the rate at which the electron population collectively responds to any perturbation of charge neutrality. For the conditions cited above, $\omega_{pe}/2\pi \sim 3$ GHz.

The ionization fraction, $\kappa = n_e/(n_e+n_g)$, is typically in the range 10^{-6}–10^{-3} in the weakly ionized discharges of interest. Neutral gas therefore remains the dominant species, with two consequences for the discharge dynamics. Firstly, the loss of energy and momentum from the electron population is governed almost entirely by collisions with neutrals. Although charged-particle dynamics are governed by collective electromagnetic fields, Coulomb collisions among charged particles are comparatively rare. Secondly, the electron-neutral momentum-transfer collision frequency, ν_{en}, becomes small enough at low pressure that electrons can traverse the discharge many times between energy-changing collisions. This weakly collisional regime is the focus of later chapters. The non-local transport and non-Maxwellian energy distributions underlying this regime is discussed in subsequent sections.

3.3.2 Electron and Ion Energy Distributions

Low-pressure, weakly ionized plasmas are characterized by the lack of thermal equilibrium between species. Electrons in typical ICP operation reach $T_e \sim 2$–5 eV. On the other hand, ions and neutrals couple only weakly to the electrons because of the large mass disparity, $m_e/m_i \sim 10^{-5}$. The energy exchange is instead dominated by charge exchange and elastic collisions with one another. Therefore, ion temperatures remain close to that of the background gas, $T_i \sim T_g \sim$ 300–600 K $\sim$ 0.03–0.05 eV, i.e. two orders of magnitude below T_e. In other words, the electron velocities vastly exceed ion velocities, which has important implications in Chapter 5.

The distribution of energies within the electron population is given by an electron energy distribution function (EEDF), $f(\mathcal{E})$. EEDF determines the rates of all electron-impact processes through averages of the form $\langle \sigma(\mathcal{E}) v \rangle$. In the low-pressure regime, electrons are heated stochastically and lose energy primarily through inelastic collisions with thresholds of several eV. Therefore the EEDF is generally non-Maxwellian, and often approximated by a Druyvesteyn or bi-Maxwellian distribution. The work presented in this dissertation does not rely on direct measurement or modeling of the EEDF.

3.3.3 The Plasma Sheath

The bulk plasma, as described so far, is quasineutral, nearly field-free, and dominated by collective dynamics. However, real plasmas are confined within reactors with the charged particles from plasma impinging on the walls. In the absence of a self-regulating mechanism, the electrons would leave the plasma at a rate far exceeding the ion loss rate due to the difference in mobility and quasineutrality in the bulk would break down. This is resolved by a thin non-neutral region adjacent to every bounding surface, known as the sheath, across which a potential drop forms that slows down electrons and accelerates ions, equalizing the fluxes to the wall.

The bulk plasma maintains a potential difference with adjacent surfaces, known as the floating potential. For an electrically isolated surface immersed in the plasma, electrons arrive faster than ions initially, charging the surface negatively. This negative charge repels further electrons and attracts ions until a steady state is reached in which the electron and ion fluxes to the surface are equal. The floating potential V_f is determined by equating the random electron flux, $\Gamma_e = \frac{1}{4} n_e \bar{v}_e \exp(eV_f/k_B T_e)$ with $\bar{v}_e = \sqrt{8k_B T_e/\pi m_e}$, to the ion flux entering the sheath (discussed below)

$$V_f - V_p = -\frac{k_B T_e}{2e} \ln\left(\frac{m_i}{2\pi m_e}\right), \tag{3.20}$$

where V_p is the bulk plasma potential. For argon and $T_e = 3$ eV, $V_p - V_f \approx 15$ V. While a biased surface like a grounded wall or an rf-biased electrode will acquire a different potential, the sheath structure itself is qualitatively unchanged.

3.3.3.1 The Bohm criterion

A self-consistent analysis of the sheath edge shows that ions must enter the sheath with a directed velocity at least equal to the ion acoustic speed,

$$u_B = \sqrt{\frac{k_B T_e}{m_i}}, \tag{3.21}$$

in order for a monotonically decreasing potential profile to exist. This Bohm criterion is a matching condition between the quasineutral bulk and the non-neutral sheath. It implies that a thin, weakly non-neutral presheath extends into the bulk, across which a modest potential drop of order $\frac{1}{2}k_B T_e/e$ accelerates ions from their near-thermal bulk velocity up to u_B. The ion flux to any bounding surface is therefore set not by local conditions at the wall but by bulk plasma properties,

$$\Gamma_i = n_s u_B, \tag{3.22}$$

where $n_s \approx 0.6\, n_0$ is the reduced density at the sheath edge, with the prefactor arising from the presheath drop. Notably, u_B depends on T_e, not T_i *i.e.*, the electron pressure drives the ambipolar acceleration and ion loss velocity.

The sheath itself is a few Debye lengths thick under low-bias conditions, widening as $(eV_{\text{sheath}}/k_B T_e)^{3/4}$ under larger applied biases according to the Child–Langmuir law. At $n_e \sim 10^{10}$ cm^{-3} and $T_e \sim 3$ eV, the unbiased sheath is a few hundred microns thick. Thus the quasineutral bulk and thin boundary layers can be treated separately.

3.3.4 Collisional Processes

Although the low-pressure plasma is weakly collisional, collisions are still the mechanism that sustains the discharge, provides energy to electrons, and ultimately equilibrates the plasma with the neutral background. For a process with cross-section $\sigma(\mathcal{E})$, the volumetric reaction rate between electrons and neutrals of density n_g is

$$R = n_e n_g \langle \sigma v \rangle \equiv n_e n_g\, k(T_e), \tag{3.23}$$

where the rate coefficient $k(T_e)$ is an average of σv over the electron distribution. The relevant processes in a low-temperature plasma fall into three categories.

- Elastic collisions or electron–neutral momentum transfer dominate the total collision frequency but exchange negligible energy per event, of the order $2m_e/M$ of the electron kinetic energy where M = mass of neutral atom. They set the electron mobility and the collisional contribution to rf power absorption, but do not themselves dissipate significant energy.

- Inelastic collisions, most importantly electron-impact excitation of a neutral atom A ($e + A \to e + A^*$, with A^* an excited state) and ionization ($e + A \to 2e + A^+$), have energy thresholds of the order of 10 eV. These processes are the primary energy sinks for the electron population. Though comparatively rare, ionization sustains the discharge against wall losses. Ionization rate coefficient $k_{iz}(T_e)$ enters directly into the particle balance of Sec 3.3.5.1. k_{iz} depends exponentially on T_e.

- Ion–neutral collisions, especially resonant charge exchange and elastic scattering, are important in the presheath and sheath region. These collisions limit the directed ion velocity acquired from the ambipolar field. At pressures below $\sim$ 100 mTorr the ion mean free path is comparable to or larger than the sheath thickness, thus ion transport to the walls is effectively collisionless.

3.3.5 Global Balance

Two global relations together determine the macroscopic state of a low-pressure plasma by imposing constraints on the particle numbers and energy conservation.

3.3.5.1 Particle Balance

The sheath analysis establishes how charged particles leave the plasma. Sustaining a steady-state discharge requires that they be replenished at the same rate. In steady state, the volumetric ionization rate must equal the rate at which charged particles are lost to the walls. For a reactor of volume V and wall area A, integrating over the discharge volume gives

$$\underbrace{n_e n_g k_{iz}(T_e)\, V}_{\text{bulk ionization}} = \underbrace{n_s u_B(T_e)\, A_{\text{eff}}}_{\text{loss to walls}}, \tag{3.24}$$

where $k_{iz}(T_e) = \langle \sigma_{iz} v \rangle$ is the rate coefficient for electron-impact ionization, n_g is the neutral density, and A_{eff} is an effective loss area after accounting for the density reduction factors at axial and radial boundaries. The Bohm flux $n_s u_B$, derived from the sheath analysis, enters

as the loss term because it is the flux at which ions cross the sheath edge. After rearranging Eq. 3.24 with density reduction factor $h_s = n_s/n_e$

$$\frac{k_{iz}(T_e)}{u_B(T_e)} = h_s \frac{A_{\text{eff}}}{n_g V}, \tag{3.25}$$

a striking result is obtained. The left-hand side is a function of T_e alone through the rate coefficient and the Bohm speed, while the right-hand side depends only on geometry and neutral pressure. Thus, the electron temperature is determined almost entirely by the reactor geometry and the operating pressure instead of plasma density, input power, or source type. Raising the input power increases n_e but leaves T_e largely unchanged. Reducing the pressure forces T_e upward to produce enough ionizations per electron to compensate for the faster loss rate. This decoupling of temperature from density is one of the defining features of low-pressure discharges.

The ionization rate coefficient $k_{iz}(T_e)$ depends sensitively on the high-energy tail of the electron energy distribution, since σ_{iz} has a threshold of ~ 15 eV for most gases of interest while T_e is only a few eV. Small departures from a Maxwellian distribution, which is quite common in the low-pressure regime, can alter k_{iz} substantially. Therefore, T_e from the simple particle balance from Eq. 3.24 should be interpreted as an effective temperature.

3.3.5.2 Power Balance

While particle balance fixes the electron temperature, a second relation is required to fix the electron density. This comes from the energy budget. In steady state, the power P_{abs} absorbed from the external source must equal the rate at which energy is carried out of the plasma by particles lost to the walls and by inelastic processes in the bulk.

Each electron-ion pair that reaches the wall removes a well-defined quantum of energy. An ion crossing the sheath gains $\mathcal{E}_i \approx eV_{\text{sheath}}$ from the sheath potential. On the other hand, an electron that climbs the sheath barrier carries an average energy $\mathcal{E}_e = 2k_B T_e$. In addition, each ionization event consumes the ionization energy $\mathcal{E}_{iz}$, and a comparable or larger amount of energy is lost to excitation and elastic collisions before an ionization ultimately occurs. These are conveniently collected into a single collisional energy loss per electron-ion pair created, $\mathcal{E}_c(T_e)$.

The total energy lost per electron-ion pair reaching the wall is therefore

$$\mathcal{E}_T(T_e) = \mathcal{E}_c(T_e) + \mathcal{E}_e + \mathcal{E}_i, \tag{3.26}$$

and the power balance reads

$$P_{\text{abs}} = e\,\Gamma_i A_{\text{eff}}\,\mathcal{E}_T(T_e) = e\,n_s u_B(T_e)\,A_{\text{eff}}\,\mathcal{E}_T(T_e). \tag{3.27}$$

Because T_e is already fixed by the particle balance and $\mathcal{E}_T$ and u_B are known, Eq. 3.27 determines the sheath-edge density n_s. The ratio of bulk density to sheath density depends on geometry and is discussed in standard texts [111]. The takeaway is that plasma density varies proportionally with the absorbed power:

$$n_0 \propto \frac{P_{\text{abs}}}{\mathcal{E}_T(T_e)\,u_B(T_e)\,A_{\text{eff}}}. \tag{3.28}$$

3.3.6 Radio-Frequency Driven Plasmas

The global model of Sec 3.3.5.2 treats the absorbed power P_{abs} as an external input. This energy input is delivered via either dc or rf fields to the electron population. In an rf discharge, this delivery is mediated by the response of the plasma to a time-varying field at frequencies typically in the MHz range. Notably this lies well below the electron plasma frequency, $\omega \ll \omega_{pe}$, but well above the ion plasma frequency, $\omega \gg \omega_{pi}$. Therefore electrons respond to the instantaneous field while ions respond only to its time average. The discussion that follows establishes the field structure inside the plasma and the mechanisms by which electrons absorb energy from it. This work uses an inductively coupled plasma, and the specific source geometry is described in Chapter 5.

3.3.6.1 Plasma conductivity

The equation of motion for an electron with velocity $\mathbf{v}$ in an oscillating field $\mathbf{E}(t) = \mathbf{E}_0 \exp(-i\omega t)$, including a phenomenological damping at the electron-neutral momentum-transfer frequency ν_m, is

$$m_e \frac{d\mathbf{v}}{dt} = -e\mathbf{E} - m_e \nu_m \mathbf{v}. \tag{3.29}$$

In steady oscillation, $\mathbf{v}$ oscillates at the same frequency, and the resulting current density $\mathbf{J} = -n_e e\mathbf{v}$ defines the complex plasma conductivity.

$$\sigma_p = \frac{n_e e^2}{m_e(\nu_m - i\omega)}. \tag{3.30}$$

The in-phase component of the current absorbs energy from the field, thus the dissipation

is quantified by $\mathrm{Re}(\sigma_p)$,

$$\sigma_p^R = \frac{n_e e^2 \nu_m}{m_e(\nu_m^2 + \omega^2)}, \tag{3.31}$$

while the imaginary part captures the reactive component. The limiting case of $\nu_m \gg \omega$, $\sigma_p \to n_e e^2/m_e\nu_m$ restores the familiar Drude dc conductivity and denotes the Ohmic dissipation in resistors. When $\nu_m \ll \omega$, the response is predominantly reactive as electrons oscillate nearly in quadrature with the field.

3.3.6.2 Field penetration and the skin depth

Propagation of electromagnetic fields through a plasma with finite σ_p using Maxwell's equations with $\mathbf{J} = \sigma_p \mathbf{E}$ yields a dispersion relation. An applied rf field with frequency ω is generally evanescent within a plasma with plasma frequency ω_{pe} when $\omega < \omega_{pe}$. In this limit, the rf field decays into the plasma over a characteristic skin depth given by

$$\delta = \frac{c}{\omega_{pe}} \frac{\left[1 + (\nu_m/\omega)^2\right]^{1/4}}{\cos\left(\frac{1}{2}\arctan\left(\nu_m/\omega\right)\right)}, \tag{3.32}$$

where ν_m is the electron-neutral momentum exchange collision frequency. For a gas with number density n_g, $\nu_m = n_g K_m(T_e)$, where $K_m(T_e)$ is the electron-neutral momentum exchange collision rate constant, which depends on electron temperature, T_e, and the gas species. The rate constants for argon for T_e ranging from 0.1 eV to 100 eV are reported in Fig. 3.16 of Ref. [111]. The limiting cases for Eq. 3.32 are collisionless plasmas with $\nu_m \ll \omega$ and highly collisional plasmas with $\nu_m \gg \omega$.

For a collisionless plasma ($\nu_m \ll \omega$), the skin depth reduces to

$$\delta_{\text{collisionless}} \approx \frac{c}{\omega_{pe}} \tag{3.33}$$

On the other hand, for a highly collisional plasma,

$$\delta_{\text{collisional}} \approx \frac{c}{\omega_{pe}} \sqrt{\frac{2\nu_m}{\omega}} \tag{3.34}$$

For typical low-pressure rf discharges with $n_e \sim 10^{11}$ cm^{-3}, δ is of the order of a centimeter.

3.3.6.3 Power absorption: ohmic and stochastic heating

The volumetric power absorbed by electrons from the local rf field follows from the time-averaged Joule expression,

$$p_{\text{abs}}(\mathbf{r}) = \tfrac{1}{2}\,\text{Re}[\mathbf{J}\cdot\mathbf{E}^{*}] = \tfrac{1}{2}\,\sigma_p^R\,|\mathbf{E}(\mathbf{r})|^2. \tag{3.35}$$

Integrating p_{abs} over the skin layer yields the total absorbed power P_{abs}, and now the global power balance is complete.

It is important to note that Eq. 3.35 captures only ohmic heating *i.e.*, the dissipation associated with the collisional conductivity $\sigma_p^R \propto \nu_m$. As $\nu_m \to 0$ at low pressure, the ohmic mechanism vanishes. Another channel called stochastic heating becomes important in this regime, defined by the electron mean free path exceeding the skin depth. In this regime, an electron entering the skin layer experiences the rf field over a transit time shorter than $1/\nu_m$ and exits with a velocity change set by the field's instantaneous phase. As an electron samples uncorrelated phases over a trajectory crossing the skin layer, it gains a net energy that mimics a collisional dissipation mechanism. The contribution can be folded into the conductivity expression by using an effective collision frequency, $\nu_{\text{eff}} = \nu_m + \nu_{\text{stoch}}$.

3.3.6.4 Implications for the plasma model

We complete this section by noting that the skin-depth and power-deposition expressions derived above provide the inputs needed for the global balance analysis of Sec. 3.3.5 for rf-driven discharges. The absorbed power P_{abs} that appears in Eq. 3.27 is given by the integral of the local Joule dissipation over a thin boundary layer of thickness δ. The plasma density n_e that emerges from the power balance is therefore consistent with field penetration. In particular, n_e enters P_{abs} through both σ_p^R and δ. A self-consistent solution is obtained when the assumed density and the absorbed power satisfy both the global balance and the heating relations simultaneously.

In summary, the three sections in this chapter, namely: field-sensitive properties of Rydberg states, collisional effects and dephasing mechanisms from the environment and the structure of the low-temperature plasma discharges, establish the physical context for reading out the electric field inside a plasma from the response of a Rydberg atom embedded within it. The collisional processes, heating mechanisms and scaling of the power balance with pressure, gas species, and geometry inform the design of the discharge experiment studied in this thesis. Chapter 5 describes the plasma apparatus built on these considerations and the interpretation of Rydberg spectra for electric field diagnostics.

CHAPTER 4

Rydberg-EIT in Inert Gas Background

This chapter is based on Refs. [127, 128].

This chapter presents an investigation of Rydberg-EIT in a collisional inert gas background. With an aim towards Rydberg-EIT enabled plasma field diagnostics, it is imperative to account for the collisional effect of common precursor gases used in low-pressure discharges. The effect of the inert gases argon, neon and nitrogen on rubidium Rydberg-EIT over a pressure range from 15 mTorr to 5 Torr is investigated. A semi-classical model based on Fermi pseudo-potential is found to be in close agreement with the sign and magnitude of corresponding pressure- and gas-species-dependent line shifts and broadening. While collision induced relaxation effects arise in several Torrs of pressure, broadening effects in the sub-100 mTorr regime are minimal compared to the inert-gas-free EIT linewidth. Additionally, addition of low-pressure inert gas is found to suppress photoelectron-induced electric fields inside vapor cells. These results establish the feasibility of Rydberg EIT for electric field mapping in low-pressure inert gas plasmas.

4.1 Introduction and Motivation

High resolution Rydberg spectroscopy in vapor cells, afforded by EIT, has emerged as a promising non-invasive probe for electric field in recent years. There is considerable interest in pursuing Rydberg electrometry beyond hermetically sealed vapor cell environments with plasma field diagnostics being a salient example.

Although pressure broadening and shifts of Rydberg lines were extensively investigated in the 1970s after the advent of laser, these experiments were based on off-resonant, two-photon excitation with spectral resolution of several GHz. The spectroscopy aimed at population transfer to Rydberg state, measured directly and destructively through ionization. Rydberg-EIT differs fundamentally in both detection scheme and physical mechanism from these experiments. EIT monitors probe-laser transmission and relies on a quantum interference

effect to probe the Rydberg level non-destructively. While the ground-Rydberg coherence produces narrow and bright resonances that enable high resolution, all-optical spectroscopy of Rydberg levels, it renders Rydberg-EIT additionally vulnerable to collisional dephasing.

Moreover, Rydberg-EIT is substantially different from EIT with low-lying states with smaller dephasing cross-sections. In particular, hyperfine coherence in the ground state is not affected by collisions with neutral perturbers, thus Λ-EIT and CPT experiments benefit from several Torrs of buffer gas background to achieve Dicke-narrowing [129]. Building on a recent measurement of Rydberg-EIT in a room-temperature vapor cell containing 5 Torr of neon [130], the effects of gas species and pressures have been investigated in this work.

4.2 Methods

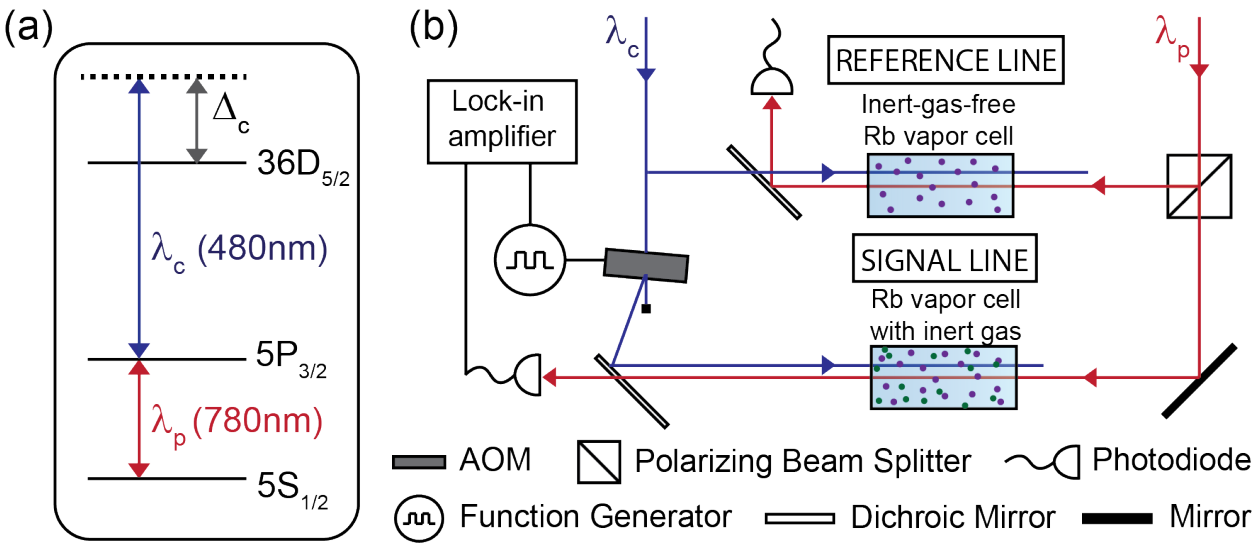


Figure 4.1: (a) Energy levels of ^{85}Rb used in our experiment. The probe laser (λ_p =780 nm) is locked to the $5S_{1/2}, F = 3 \leftrightarrow 5P_{3/2}, F' = 4$ resonance, and the coupling laser is scanned across the $5P_{3/2} \leftrightarrow 36D_{5/2}$ transition. (b) Experimental setup. Some elements are omitted for simplicity.

Our Rydberg-EIT experiments utilize the energy levels of ^{85}Rb atoms as shown in Fig. 4.1(a). The two-photon scheme uses laser beams of wavelengths λ_p =780 nm and λ_c =480 nm, referred to as probe and coupler lasers, respectively. The probe laser is an external-cavity diode laser (ECDL) locked to the $5S_{1/2}, F = 3 \leftrightarrow 5P_{3/2}, F' = 4$ transition on the D_2 line of ^{85}Rb using saturation spectroscopy. EIT spectra are obtained by measuring the transmission of the probe power as the coupler-laser frequency is scanned over the $5P_{3/2} \leftrightarrow nD_{5/2}$ transition. The results presented in this chapter use $n = 36$, an intermediate

range where the collisional physics laid out in Sec 3.2 produces shifts and broadening that have no n-dependence in the leading order according to semiclassical calculations [96, 98] and past experiments [130]. As discussed in Sec. 4.4, for low $n \lesssim 15$, both the collisional shift and broadening grow with n as the Rydberg orbit increasingly overlaps the perturber distribution, while at high n inelastic processes driven by the closer spacing of nearby Rydberg manifolds begin to dominate. Intermediate states provide a field sensitivity adequate for the diagnostics envisioned in Chapter 5 while remaining in a regime where the collisional response can be appropriately modeled by the semi-classical pseudo-potential treatment.

The coupler-laser beam is generated by frequency-doubling the output of another ECDL, which operates at $\sim$ 960 nm. The frequency of the coupler laser is calibrated using the transmission of a beam sample of the 960-nm ECDL through a temperature-stabilized Fabry-Pérot (FP) etalon [131] with a free spectral range of 250 MHz. The probe and coupler laser beams are split by respective polarizing beam-splitter cubes (PBS) and counter-propagated along two separate paths, each containing a vapor cell (see Fig. 4.1(b)). The polarizations of both beams are linear and parallel in each path. The beams along the upper path in Fig. 4.1(b) (reference line) are aligned through a room temperature inert-gas-free Rb vapor cell of length 7.5 cm. There, the probe and coupler beams are Gaussian in shape with respective $1/e^2$ beam waists of 300 μm and 500 μm. The EIT spectra obtained from this cell are used as a reference for the shifts observed in the signal line. The detuning of the coupler laser, Δ_c, is measured relative to the strongest EIT peak in the reference cell (which corresponds to the $5S_{1/2}, F = 3 \leftrightarrow 5P_{3/2}, F' = 4 \leftrightarrow 36D_{5/2}$ cascade). The transmitted probe power is measured using a fast photo-diode (model - Thorlabs FDS100) and recorded after amplification by a trans-impedance amplifier (TIA) (model - SRS SR570).

The waists of probe and coupler beams are key parameters in vapor cell EIT experiments, in particular in the presence of collisional effects. Beams focused too tightly suffer from a smaller atom-light interaction volume and transit-time broadening. On the other hand, signal is degraded in large beam waists due to optical pumping to non-participating states and lack of adequate Rabi frequency.

The EIT signals from the signal line in Fig. 4.1(b) are recorded in the presence of Ar, Ne or N_2. The probe and coupler beams are focused to respective beam waists of 150 μm and 170 μm and counter-propagated through a 4 cm long Pyrex vapor cell custom-fabricated by Precision Glass Blowing that contains Rb and one of the specified inert gases. The optical powers in the signal line are $\approx$ 22 mW for the coupler beam and $\approx$ 1.7 μW for the probe beam; the latter corresponds to a Rabi frequency of 30 MHz. The coupler beam in the signal line is pulsed at 15 kHz at a 50 % duty cycle using an acousto-optic modulator (AOM) for detection of the EIT signal with a lock-in amplifier (MFLI-500, Zurich Instruments). The

lock-in detection provides sufficient sensitivity to observe weak EIT lines in cells with higher inert-gas pressures.

Using the setup described above, we have obtained EIT signals in 11 inert-gas cells. During data acquisition, the cells are heated to 303 K. The TIA in the signal line has a constant sensitivity of 1 μA/V. The TIA bandwidth is sufficiently high to prevent signal distortion. The EIT spectrum from the reference cell, the EIT spectrum from the cell with inert gas, and the transmission of the 960-nm beam sample through the above-described FP etalon are recorded simultaneously to ensure the absence of coupler-laser frequency drifts between the measurements. For each individual scan, the FP transmission of the 960-nm sample is used to map the coupler-laser scan onto a well-defined frequency axis. The zero-point of the frequency axis is set to the position of the $5S_{1/2}, F = 3 \leftrightarrow 5P_{3/2}, F' = 4 \leftrightarrow 36D_{5/2}$ EIT line from the reference line. The method eliminates the effects of slow frequency drifts of the coupler laser. The spectra shown in the following figures are obtained from taking averages over 200 such scans, for each of the 11 inert-gas Rb cells.

4.3 Results

Selected EIT spectra obtained using inert-gas-filled and inert-gas-free cells are shown in Fig. 4.2. The strongest peak in the reference EIT spectra obtained from the inert-gas-free vapor cell corresponds to the $5S_{1/2}, F = 3 \leftrightarrow 5P_{3/2}, F' = 4 \leftrightarrow 36D_{5/2}$ EIT line. The smaller EIT peaks are due to the other $5P_{3/2}$ hyperfine sublevels, $F' = 3$ and 2. EIT peak frequencies are determined by local parabolic fits. The full-width-at-half-maximum (FWHM) linewidths reported in Fig. 4.6 are extracted graphically by locating the frequencies at which the EIT reaches half of the peak value above the baseline. For 0.05 Torr and 0.5 Torr, the line shifts are given by the separations between the $F' = 4$ EIT peaks in the inert-gas-filled and the inert-gas-free cells. At 5 Torr, the comparatively minor $F' = 3$ and 2 peaks become indiscernible. In these cases, the FWHMs are determined from the merged EIT resonances, and the line shifts are given by the separation between the peak of the merged resonances and the $F' = 4$ peak in the inert-gas-free cell.

EIT measurements were made at pressures ranging from 15 mTorr to 5 Torr of Ar and 50 mTorr to 5 Torr of Ne and N_2. Fig. 4.5 shows the shift and FWHM of the Rydberg-EIT lines versus pressure, respectively. The FWHM of an EIT peak in the presence of an inert gas is assumed to be the quadrature sum of collisional broadening (γ) and inert-gas-free EIT linewidth ($\Gamma \sim 5$ MHz). The latter is primarily limited by saturation broadening of the probe transition and the laser linewidths (~ 1 MHz) in our experiment. Below 50 mTorr, the measured FWHM approaches Γ, and the comparatively small contribution from the

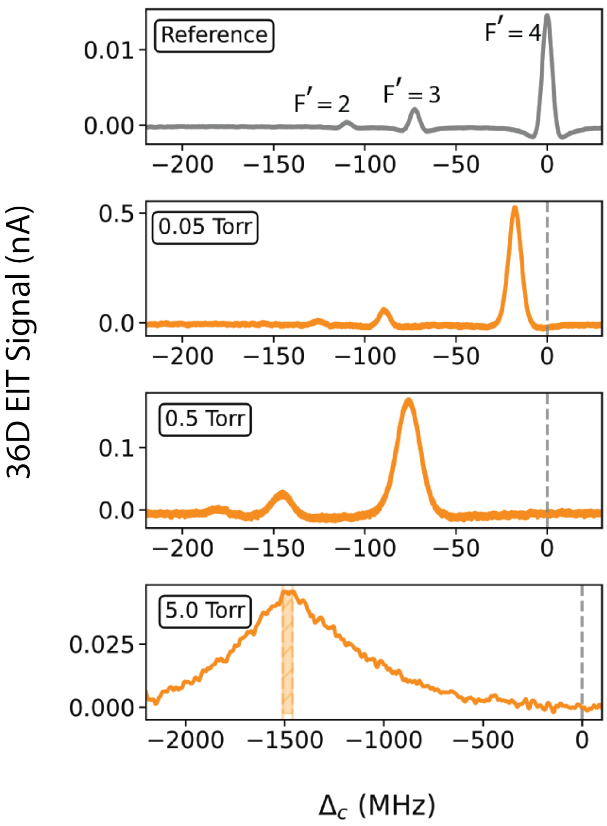


Figure 4.2: Rydberg-EIT spectra for selected Argon pressures. The top row shows EIT spectra from the inert-gas-free reference cell. Ar induces a large negative frequency shift. The dashed grey lines represent the locations of the strongest EIT peak in the reference cell. The spectra in the bottom row, obtained from 5 Torr cells, are smoothed by a moving average over a 5 MHz window. The shaded regions in the bottom row denote the experimental uncertainties in the peak frequency.

collisional broadening, γ, cannot be extracted. Therefore, for our quantitative studies of γ we only consider measurements in the higher-pressure cells (0.5 Torr and 5 Torr), for which γ practically equals the measured FWHMs.

We find that Ar induces a large negative frequency shift, unlike other inert gases considered here. The Rydberg-EIT line is shifted by -1485 ± 25 MHz and broadened by 610 ± 30 MHz in the 5 Torr Ar cell. It should be noted that the log-log plot in Fig. 4.5 shows the absolute value of the frequency shift in Ar. In the 5 Torr Ne cell, we observe a moderate positive frequency shift of 105 ± 5 MHz and a line broadening of 140 ± 5 MHz. The results in the 5 Torr Ne cell agree well with previous findings [130] (which were obtained without using lock-in detection). At 5 Torr of N_2 we observe a large line broadening of 600 ± 85 MHz, which contrasts with a rather small positive frequency shift of only 68 ± 20 MHz. In the cells with lower pressure, the FWHMs of the resolved F' lines differ by up to 40%. We attribute this

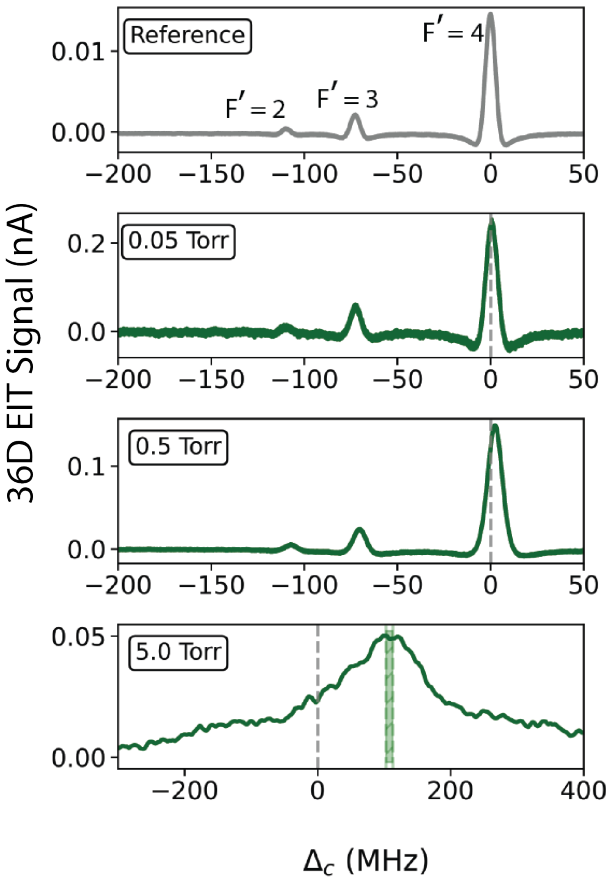


Figure 4.3: Rydberg-EIT spectra for selected Neon pressures. The top row shows EIT spectra from the inert-gas-free reference cell. Ne induces a moderately positive frequency shift and smaller broadening than other gases.

to different degrees of saturation broadening, caused by the F'-dependence of the transition matrix elements.

The experimental uncertainties in line shifts and FWHMs in cells with pressures below 0.5 Torr are $\approx$ 1 MHz and are attributed to coupler-laser frequency calibration uncertainty. In high-pressure cells (5 Torr), EIT signals are two to three orders of magnitude weaker than in low-pressure cells due to large inert-gas-induced EIT line broadening. The large linewidths in the high-pressure cells result in larger experimental uncertainties, which are determined by visual inspection of the spectra. Another important systematic uncertainty in our experiments arises from the uncertainty of the inert gas pressures within the cells. The reported pressures are nominal manufacturer values, which have up to 5 % error in the high-pressure cells and 10 % for the cells with pressures below 50 mTorr.

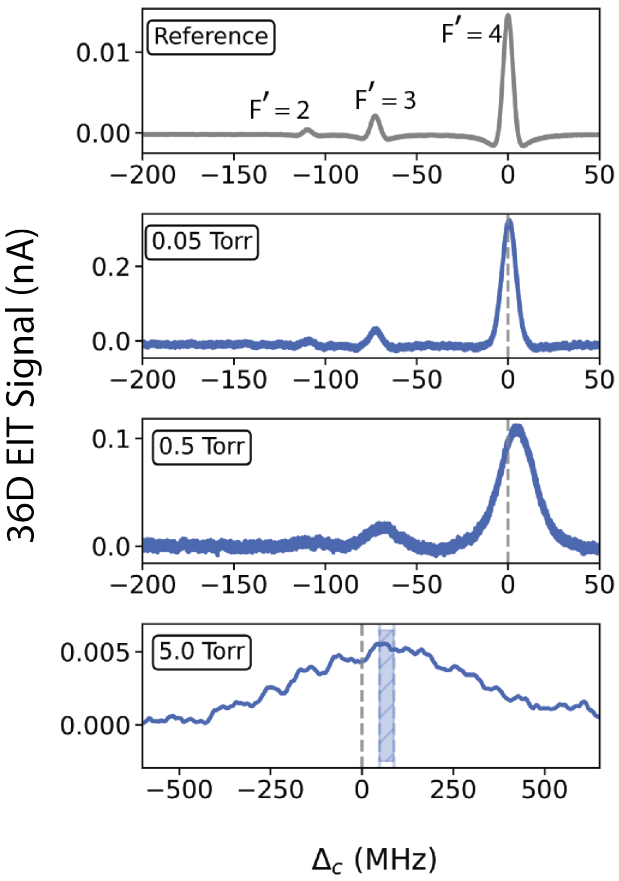


Figure 4.4: Rydberg-EIT spectra for selected Nitrogen pressures. The top row shows EIT spectra from the inert-gas-free reference cell. Line shift is close to zero in N_2, and broadening rates are similar to Ar.

4.4 Semiclassical Model

The collisional shifts of Rydberg transitions were first explained by Fermi using a so-called pseudo-potential [95] that treats the ionic core and the Rydberg electron separately in their corresponding interactions with the background-gas particles (perturbers). The perturbers can be inert-gas atoms or molecules. The model as described includes two components: scattering between the perturber and the Rydberg electron, and a long-range attractive potential experienced by the perturber due to polarization by the ionic core of the Rydberg atom. The general form is given by

$$V_a[\mathbf{R}] = V_{A^+B}[\mathbf{R}] + V_{eB}[\mathbf{r}_e - \mathbf{R}], \tag{4.1}$$

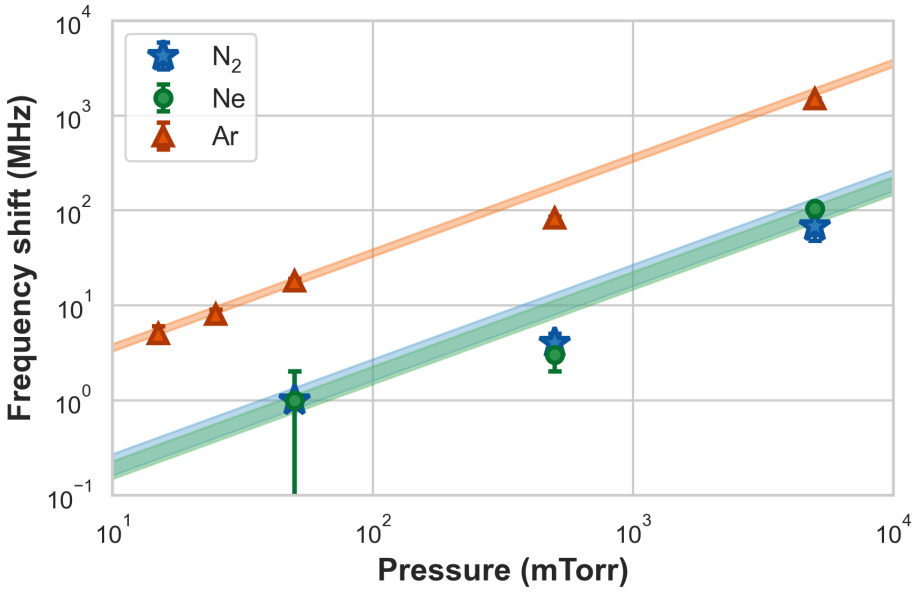


Figure 4.5: Absolute values of the EIT line shifts in the inert-gas-filled cells versus pressure. The shifts are positive for Ne and N_2 and negative for Ar. Systematic uncertainties arise from the average frequency step size of the coupler-laser scans (1 MHz) and the residual error of the procedure that maps the scans onto a linear frequency scale. These uncertainties are dominant at pressures $\leq$500 mTorr. In the 5 Torr cells, the error bars are dominated by statistical uncertainties resulting from large linewidth and low signal-to-noise ratio. The shaded lines are calculated using Eqs. 4.5 and 4.7. The widths of the shaded lines reflect the full variation ranges of the scattering lengths listed in Table 4.3.

where $\mathbf{r}_e$ is the Rydberg electron coordinate, $\mathbf{R}$ is the perturber position relative to the ionic core and the center of mass of the Rydberg atom is located at the origin. The two pieces are further simplified by separate physical arguments.

The core–perturber interaction V_{A^+B} depends on $\mathbf{R}$ alone and is independent of the Rydberg electron's quantum state. At long range, it reduces to the polarization form

$$V_{A^+B}(\mathbf{R}) \approx -\frac{\alpha}{2R^4}\left(\frac{e}{4\pi\epsilon_0}\right)^2, \tag{4.2}$$

where α is the perturber's static dipole polarizability in SI units.

The electron–perturber interaction V_{eB} is treated by exploiting the separation of length scales: the perturber's interaction range r_{eB} is much smaller than the Rydberg orbital radius $n^2 a_0$, so the encounter is effectively point-like. The detailed shape of V_{eB} is irrelevant in this regime and only the low-energy scattering amplitude matters. Retaining the s and p-wave

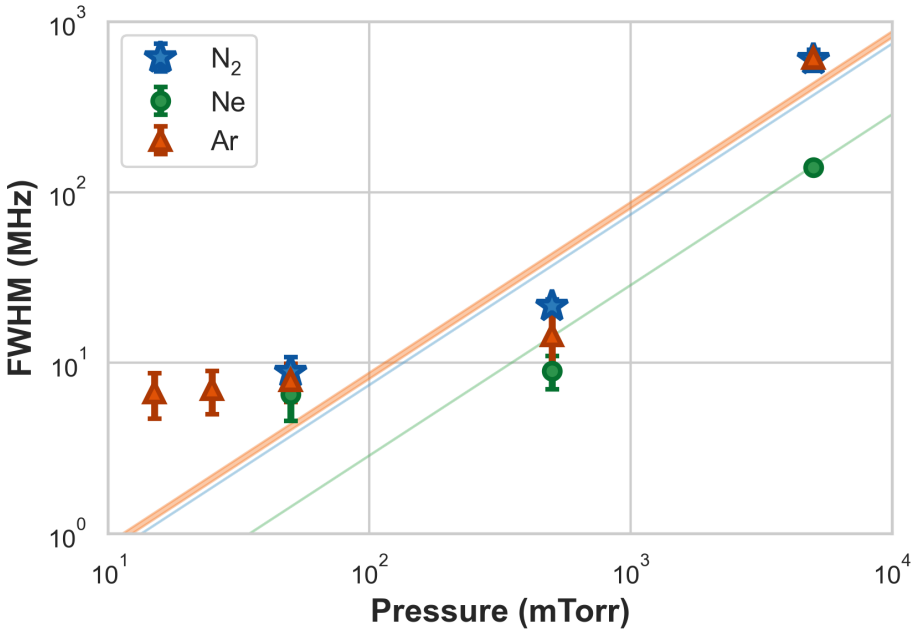


Figure 4.6: Full widths at half maxima (FWHM) of the EIT line in the inert-gas-filled cells versus pressure. The FWHM at pressures ≤ 50 mTorr are dominated by inert-gas-free EIT linewidth ($\approx 5\,$MHz). The shaded lines are calculated using Eqs. 4.6 and 4.7. The widths of the shaded lines reflect the full variation ranges of the scattering lengths listed in Table 4.3.

contributions, the total interaction in atomic units is given by

$$V_{eB}[\mathbf{r}_e - \mathbf{R}] = \left[2\pi a_s(k) + 6\pi a_p^3(k)\,\overleftarrow{\nabla}\cdot\vec{\nabla}\right]\delta^3(\mathbf{r}_e - \mathbf{R}), \tag{4.3}$$

where a_s and a_p are the s- and p-wave scattering lengths, respectively.

Beyond collisional effects, the pseudo-potential model has been instrumental in elucidating the quantum behavior of long-range molecules of Rydberg atoms and ground-state perturbers [132]. Adiabatic potentials for the internuclear coordinate $\mathbf{R}$, obtained from the perturbative treatment of Eqs. 4.2 and 4.3 in the ultracold regime reveals long-range molecules between Rydberg and neutral atoms [133, 134]. The $s-$wave term generates the so-called trilobite molecules [135], while the next-order p-wave interaction has a low-energy resonance for alkali perturbers that facilitates the so-called butterfly Rydberg molecules [136].

When the actual electron-perturber interaction has internal structure such as resonances, energy dependence, or angular dependence beyond s-wave, the Fermi description breaks down and one must use the more general impulse approximation, which uses the full scattering amplitude $f_{eB}(k,\theta)$ and the Rydberg electron's momentum distribution. For most rare-gas perturbers at thermal energies, the s-wave scattering is an excellent approximation, as the

mean momentum of Rydberg electron scales as $\hbar/(na_0)$, well below the energies at which higher partial waves contribute. Thus, the essential physics is captured by

$$V(\mathbf{r}_e, \mathbf{R}) = -\frac{\alpha e^2}{2(4\pi\epsilon_0)^2 R^4} + \frac{2\pi a_s \hbar^2}{m_e}\delta^3\left(\mathbf{r}_e - \mathbf{R}\right), \tag{4.4}$$

where α and a_s have SI units. This interaction model is used in the rest of the analysis.

Phase shift induced by core polarization, η^{core}, and pseudopotential, η^{eB}, can be computed using impact approximation and phase-shift representation introduced in Sec. 3.2. The net frequency shift (Δ_r) and broadening (γ_r) of a Rydberg line is given by the sum of respective contributions from η^{core} and η^{eB}:

$$\Delta_r = \Delta_{sc} + \Delta_p, \tag{4.5}$$

$$\gamma_r = \gamma_{sc} + \gamma_p, \tag{4.6}$$

Subscripts sc and p denote the scattering and polarization contributions, respectively. A semiclassical approach [96, 99] yields:

$$\Delta_{sc} = a_s N \left[\frac{e^2 a_0}{4\pi\epsilon_0\hbar}\right] \tag{4.7a}$$

$$\Delta_p = \frac{-6.21N}{2\pi}\left[\frac{e^2\alpha}{(4\pi\epsilon_0)^2\hbar}\right]^{2/3} v^{1/3} \tag{4.7b}$$

$$\gamma_{sc} = 2 \times \frac{4a_s^2 N}{2\pi n}\left[\frac{e^2}{4\pi\epsilon_0\hbar}\right] \tag{4.7c}$$

$$\gamma_p = 2 \times \frac{3.59N}{2\pi}\left[\frac{e^2\alpha}{(4\pi\epsilon_0)^2\hbar}\right]^{2/3} v^{1/3} \tag{4.7d}$$

where a_s is the zero-energy s-wave electron scattering length of the perturber in m, v is the root-mean-square velocity of the perturbers in m/s, n is the effective quantum number of the Rydberg state, and N is the volume number density of perturbers in m^{-3}. All physical quantities in Eq. 4.7 are in SI units, including the line shift and the broadening being in units of Hz. The negative sign of Δ_p is due to the attractive polarization potential produced by the ionic core. However, the Rydberg-electron scattering can induce a positive or negative shift, depending on the sign of the scattering length.

We have surveyed the electric-dipole polarizability, α, and the s-wave scattering length, a_s, of the relevant inert gases in the existing literature. Techniques such as dielectric constant gas thermometry [147], optical spectroscopy [148], and capacitance measurement [149] have been used to measure α for common inert gases within 1 % variation. The range of the

a_s (in au)	Reference
-1.50	Milloy et al. (1977) [137]
-1.488	Haddad and O'Malley (1982) [138]
-1.506	McEachran and Stauffer (1983) [139]
-1.449	Ferch et al. (1985) [140]
-1.492	Buckman and Lohmann (1986) [141]
-1.641	Weyhreter et al. (1988) [142]
-1.686	Pack et al. (1992) [143]
-1.442	Buckman and Mitroy (1989) [144]
-1.459	Petrović et al. (1995) [145]
-1.365	Kurokawa et al. (2011) [146]

Table 4.1: Survey of s-wave scattering length (a_s) of Ar reported from past experiments.

reported α-values has a negligible effect on the uncertainties of line shifts and broadenings relevant in our work.

The s-wave scattering length is typically estimated by extrapolating experimentally measured electron collision cross-sections to zero energy electrons using modified effective range theory (MERT) [150, 151]. Experimentally reported values of a_s have up to 20 % of variation depending on the collision experiments, *e.g.*, crossed-beam, swarm and time-of-flight measurements, among others (see topical reviews in [152–154]), as well as specifics of the MERT model. As an example, in Table 4.1 we show the variation range of experimental values reported for a_s of Ar. Table 4.2 presents a survey of the polarizability as well as upper and lower bounds of a_s-values reported for Ar, Ne and N_2. The latter are used for the uncertainty ranges of the calculated shaded lines in Fig. 4.5 and 4.6.

Species	Range of a_s (au)	α (au)
Ar	-1.365 to -1.69 [137, 138, 140–146]	11.07 [147–149, 155]
Ne	0.20 to 0.24 [144, 156–162]	2.66 [147, 155, 163]
N_2	0.404 to 0.460 [164–167]	11.74 [148, 155]

Table 4.2: Reported values of s-wave scattering length (a_s) and dipole polarizability (α) for gases used in this experiment. For a_s we show the upper and lower bounds of the results from the references cited. a_s is estimated by using MERT to extend scattering results from crossed-beam or swarm experiments to $k \to 0$. The values shown for α are consistent with the references cited, at the level of precision given in our table.

After accounting for shifts of the ground state and the intermediate state in the utilized EIT energy-level cascade and assuming that the probe laser is on resonance, the final shift

Species	Δ_{sc}	Δ_p	Δ_r	γ_{sc}	γ_p	γ_r
Ar	-290.9	-58.1	-349.0	15.9	67.1	83.0
Ne	41.8	-24.5	17.3	0.3	28.2	28.5
N_2	78.9	-63.1	15.8	1.2	72.8	74.0

Table 4.3: Line shifts and broadenings rate (in MHz/Torr), based on pseudo-potential model calculated using Eq. 4.7. In our calculation of Δ_* and γ_*, with $* = sc$, p or r, we use the most commonly accepted values of a_s *i.e.,* $-1.49\ a_0$, $0.214\ a_0$ and $0.404\ a_0$ for Ar, Ne and N_2, respectively, as well as the α-values shown.

of the EIT resonance is given by [59]

$$\Delta = \Delta_{sc} + \Delta_p + \left(\frac{\lambda_p}{\lambda_c} - 1\right)\Delta_e - \frac{\lambda_p}{\lambda_c}\Delta_g \tag{4.8}$$

where Δ_e and Δ_g denote the absolute energy shifts of the intermediate $5P_{3/2}$ and the $5S_{1/2}$ ground state, respectively. It is seen that the EIT shift depends independently upon Δ_g, Δ_e and $\Delta_r = \Delta_{sc} + \Delta_p$, with different scaling factors. Notably, collisional shifts of the D_2 line, as commonly reported in literature [168–170], only provide $\Delta_e - \Delta_g$, which is not sufficient to evaluate Eq. 4.8. Under the assumption that the collisional shift of the ground state $5S_{1/2}$ is smaller than that of the excited electronic state $5P_{3/2}$, one may conclude that $\Delta_e \approx \Delta_{D_2}$, the shift of the D_2 line. The inert-gas-induced shift of the D_2 line is ≈ 2 MHz/Torr for Ne [170] and ≈ 6 MHz/Torr for Ar and N_2 [168]. The line broadening rates are ≈ 10 MHz/Torr for Ne and ≈ 20 MHz/Torr for Ar and N_2 [168–170]. These shifts and broadenings are a factor of three or more smaller than the respective Rydberg energy shifts and broadenings calculated from Eq. 4.7. Therefore, we neglect the inert-gas effects on the D_2 line at our current level of experimental precision. With this assumption, we attribute the Rydberg-EIT line shift and broadening solely to the Rydberg state, *i.e.,* $\Delta \approx \Delta_r$ and $\gamma \approx \gamma_r$.

Table 4.3 summarizes calculated polarization and scattering contributions, Δ_p and Δ_{sc}, respectively, and $\Delta_r = \Delta_p + \Delta_{sc}$, as well as corresponding broadenings, for the inert gases studied in our work, in units MHz/Torr at 303 K. Eq. 4.7 reveals the linear dependence of line shift and broadening on inert-gas pressure, which is an important result of the semi-classical model. We find in Fig. 4.5 that frequency shift scales linearly with inert-gas pressures and agrees with estimates from Eq. 4.7 within the uncertainty of our measurement.

4.4.1 Inelastic cross-sections with Fermi Pseudopotential

The state-independence of η^{core} implies that it is irrelevant for inelastic processes that involve a Rydberg-Rydberg transition $a \to c$. Only the pseudopotential representing the electron-

perturber interactions contributes to state mixing and quenching.

The delta function in the Fermi pseudopotential makes the matrix element local. Therefore, inelastic transition rates depend on the wavefunction overlap evaluated along the trajectory *i.e.*, in atomic units,

$$\langle c|V[\mathbf{r}_e, \mathbf{R}(t)]|a\rangle = 2\pi a_s \, \psi_c^*[\mathbf{R}(t)] \, \psi_a[\mathbf{R}(t)]. \tag{4.9}$$

The quantum numbers for state $a \equiv |nlJ\rangle$ and $c \equiv |n'l'J'\rangle$ are determined by the inelastic process under consideration. For a given a and c, angular momentum algebra and selection rules can be used to reduce Eq. 4.9 to radial integrals.

Then the calculation of the transition amplitude reduces to a one-dimensional time integral, structurally identical to the elastic phase-shift integral with an added transition energy dependent penalty given by $e^{i\omega_{ca}t}$. Squaring the amplitude gives the transition probability for a single collision at impact parameter ρ:

$$W_{ca}(\rho, V) = |A_{ca}(\rho, V)|^2 = \frac{(2\pi a_s)^2}{\hbar^2} \left| \int_{-\infty}^{\infty} dt \, e^{i\omega_{ca}t} \, \psi_c^*[\mathbf{R}(t)] \, \psi_a[\mathbf{R}(t)] \right|^2.$$

The inelastic cross section follows by integrating the transition probability over all impact parameters:

$$\sigma_{ca}(V) = \int_0^{\infty} 2\pi\rho \, d\rho \, W_{ca}(\rho, V).$$

This integral is typically dominated by impact parameters within or just outside the Rydberg orbit, $\rho \lesssim n^2 a_0$.

The contribution of the channel $a \to c$ to the linewidth follows from the standard impact-approximation formula:

$$\Gamma_{a\to c} = N \langle V \sigma_{ca}(V) \rangle_T,$$

with the thermal average taken over the Maxwell-Boltzmann distribution of relative velocities. The total inelastic broadening is the sum over all open channels:

$$\Gamma_{\text{inelastic}} = \sum_{c \neq a} \Gamma_{a\to c}.$$

For Rydberg states, the relevant channels include n-changing transitions to neighboring principal quantum numbers, ℓ-mixing within a manifold, fine-structure-changing collisions, and collisional ionization at high enough collision energies. Each is computed by specializing the steps above to the appropriate set of final states, with the radial integrals evaluated using semiclassical (JWKB) approximations for the Rydberg wavefunctions. For each inelastic channel, this procedure produces a semi-analytic expression for the cross section as a function

of velocity, parameterized by the perturber's scattering length a_s and quantum numbers of the relevant states.

The primary inelastic process induced by atomic perturbers like argon and neon is de-excitation to the nearest hydrogenic manifold. Other processes such as n-mixing or ℓ-mixing within the same n state are highly suppressed due to the quantum defect of the D state and relatively smaller principal quantum number. The total inelastic broadening contribution is of the order of a few MHz/Torr for argon and even smaller for neon, and therefore neglected. The channel-specific calculations are described in detail in the comprehensive review by Beigman [97]. The key takeaway is that the Born approximation with the Fermi pseudopotential, evaluated on classical straight-line trajectories, provides a unified framework for computing all inelastic Rydberg-perturber rates.

4.4.2 Validity of semiclassical model

Next we review the validity of assumptions used in Eq. 4.7. Semi-classical treatments of the pseudo-potential model [98, 171] have established that the broadening cross-section reaches an asymptotic value for effective quantum numbers exceeding $n_{\max} \approx |a_s|^{1/3}/(\alpha v^5)^{1/18}$ (a_s, α and v in atomic units). The broadening cross-section at higher Rydberg levels arises from the polarization potential of the ionic core, whereas the effect of the Rydberg electron is limited to the scattering described by the Fermi interaction. For the inert gases studied in our work, $n_{\max} \approx 10$, whereas our experiment is performed with $36D_J$ states. Therefore, the use of Eq. 4.6 is well-justified, *i.e.* the components from long-range polarization potential and electron scattering can be treated separately.

Next, we consider the validity of the impact approximation, which holds when the timescale of collisions is much faster than the mean-free time, or, equivalently, when the mean number of perturbers occupying the interaction volume is much smaller than unity. This limits the perturber density to $N \ll 3v/(\pi^2\alpha)$ (in atomic units) [98], corresponding to $\approx 100\,\text{Torr}$ of inert-gas pressure. This is considerably larger than the highest pressures utilized in our experiments.

The validity of the semi-classical treatment is highlighted by the observed linear scaling of the line shift and broadening with inert-gas pressure at sufficiently high inert-gas pressure. While the assumption of negligible inelastic scattering is generally justified for collision of low-energy Rydberg electrons with atomic perturbers like Ne and Ar, additional channels open up with a molecular perturber. Even non-polar molecular perturbers like N_2 possess a quadrupole moment and a rich rovibrational structure, leading to larger inelastic scattering processes [97]. The study of such additional cross-sections in the context of Rydberg-EIT is

beyond the scope of current investigation.

4.5 Effects beyond the Fermi pseudopotential treatment

In the low-pressure regime that has been the focus of this chapter, the EIT spectrum can be modeled simply by inheriting the Rydberg-level shift and broadening predicted by the Fermi pseudopotential. Heuristically, Rydberg-EIT in a buffer gas reflects a competition between laser-driven coherence set by Rabi frequencies and collisional decoherence set by the broadening rate of the Rydberg-state. The Rabi frequencies dominate below roughly 100 mTorr and the EIT line tracks the Omont-predicted level shift within the experimental precision.

The pseudopotential treatment captures only the collisional modification of the Rydberg level itself. The inert gas also alters the transport of charged and neutral particles through the cell, with effects that go beyond a simple level shift. Two consequences of this transport physics are addressed in the remainder of this section. At higher buffer-gas pressures, the diffusive transport of rubidium atoms through the laser interaction region produces a time-dependent EIT response with long response time. Separately, in inert-gas-filled cells exposed to UV illumination, the buffer gas suppresses photoelectron-induced dc fields that arise robustly in evacuated cells, through a screening mechanism mediated by diffusive electron transport. The works presented in the section were carried out in collaboration with other group members.

4.5.1 Relaxation effects at high pressures

In the range of a few Torr, the picture changes qualitatively. Collisional rates exceed the Rabi frequencies, and additional effects emerge beyond the semiclassical shift-and-broadening model. These effects are summarized here, both to delineate the boundary of the low-pressure analysis and as motivation for future work.

Several empirical signatures point to a relaxation process much slower than the natural Rydberg dynamics. As shown in Fig. 4.7 (a), the lock-in-detected Rydberg spectrum features enhanced transparency, while a dc measurement of the same line shows enhanced absorption. A similar trend is found with increasing cell temperature and probe power as shown in Fig. 4.7 (b), indicating a dependence on Rb vapor density and probe Rabi frequency. The line shape itself depends on laser scan rate and direction (Fig. 4.8), with the system relaxing toward an absorption feature when allowed to reach steady state. This timescale is resolved in a pulsed-coupler measurement (Fig. 4.9), where the transient settles over several milliseconds,

roughly four orders of magnitude slower than in buffer-gas-free cells. The settling time depends on the buffer-gas species but not on the Rydberg state, laser powers, or detuning.

Two regime changes account for these observations. First, at 5 Torr the ℓ-mixing cross-section corresponds to a rate of several hundred MHz [97], well above the Rabi frequencies of tens of MHz. Thus, Rydberg atoms are collisionally redistributed out of the EIT cascade faster than they are coherently driven into it. Second, the Rb mean free path between buffer-gas collisions falls to a few microns, an order of magnitude below the laser beam diameter. Thus atomic transport through the interaction region enters a diffusive regime. The slow relaxation and the probe-power-dependent steady state are attributed to diffusive transport combined with strong optical pumping.

This regime, where the mean free time is shorter than the atom-laser interaction time, opens an interesting line of inquiry but lies beyond the scope of this dissertation. The main takeaway for the present work is that the semiclassical pseudopotential analysis applies cleanly below ∼100 mTorr, while pressures above ∼1 Torr require a treatment that incorporates collisional redistribution and diffusive transport explicitly.

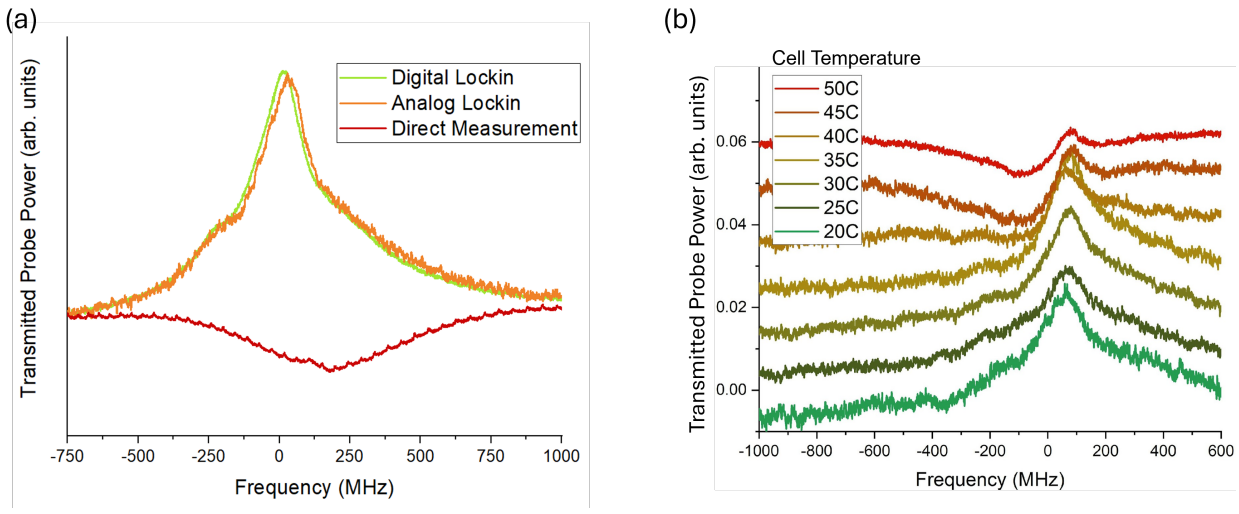


Figure 4.7: EIT spectra in 5 Torr Neon measured in various configurations. (a) Lock-in measurements reveal a transparency window, while direct measurement shows enhanced absorption at high cell temperature. (b) For direct measurements made without lock-in amplifier, enhanced transparency gives way to enhanced absorption as cell temperature and Rb vapor pressure increases.

4.5.2 Shielding of photoinduced electric field

In two-photon EIT of alkalis, photoelectrons induced by the coupler laser itself have been found to generate significant electric field for over a few millimeters [172]. I contributed to

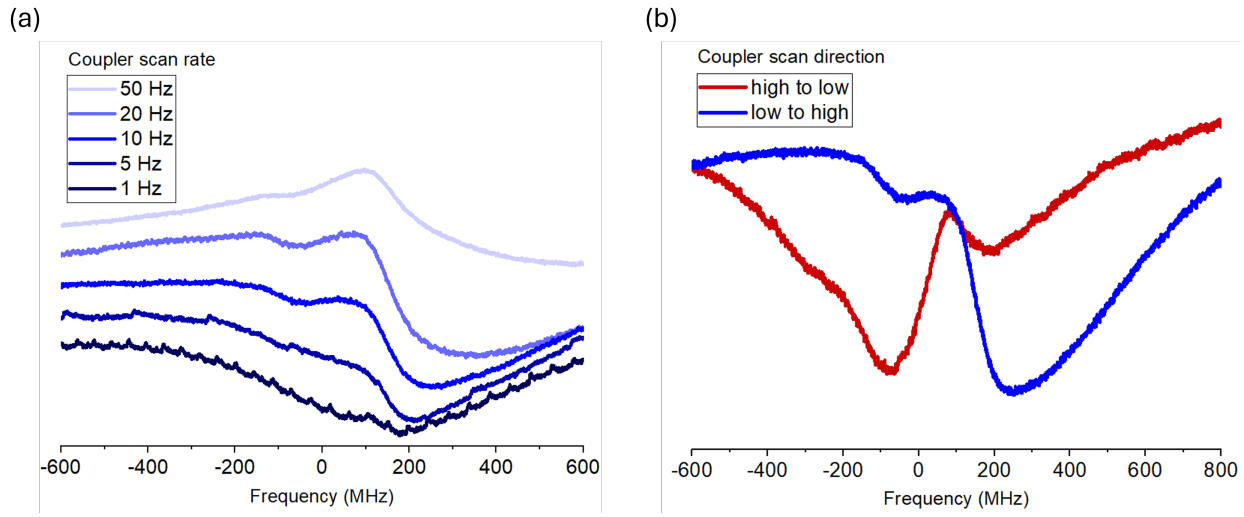


Figure 4.8: Relaxation effects in 5 Torr Neon. (a) Probe transmission changes based on how fast coupler laser detuning changes across the resonance. The scan direction of coupler laser frequency is low to high. An asymptotic steady state is reached at 1 Hz scan rate, indicating relaxation effects. (b) At a fixed scan rate of 10 Hz, the location of the absorption window depends on the scan direction.

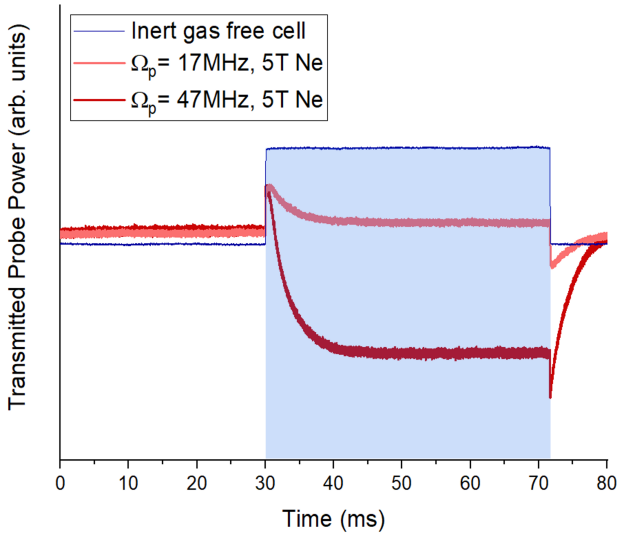


Figure 4.9: Transient behavior at high inert-gas pressure. Transmitted probe power is measured as a function of time without a lock-in amplifier, with the coupler pulsed during the shaded region (30–70 ms) and constant cell temperature at 50°C. Three conditions are compared: a reference trace with no buffer gas (gray), and two traces at 5 Torr Ne with probe Rabi frequencies $\Omega_p = 17$ MHz (light red) and $\Omega_p = 47$ MHz (dark red). The probe is locked to the $5S_{1/2}, F = 3 \rightarrow 5P_{3/2}, F' = 4$ transition in a buffer-gas-free reference cell; the coupler is locked to the pressure-shifted $5P_{3/2} \rightarrow 36D_{5/2}$ transition at 5 Torr Ne. Traces are vertically offset so that their coupler-off baselines coincide. Note the millisecond-scale recovery toward steady-state, in contrast to the near-instantaneous response in the buffer-gas-free cell.

an experiment with three-color, all-infrared Rydberg EIT where such photoinduced electric fields are found to be suppressed in the presence of small inert gas pressure. The experimental setup is shown in Fig. 4.10 with details in Ref. [128]. The three-photon EIT enables us to reach nF states following the cascade in Fig. 4.10 (b) and the Hydrogenic manifold with substantially larger polarizability. Photoinduced electrons are generated by illuminating the cell wall with a 453 nm laser.

Fig. 4.11 demonstrates the central observation. In a buffer-gas-free cell, UV illumination of the cell walls produces a substantial dc electric field at the EIT excitation region, but the addition of a few mTorr of an inert gas suppresses this field almost entirely. The effect is shown using two complementary spectroscopic schemes that differ in their electric-field sensitivity.

The first scheme, shown in Figs. 4.11(a) and (c), uses the rf-coupled triplet $25F_{5/2} \leftrightarrow 25H_{9/2} \leftrightarrow 25I_{11/2}$. Two rf dressing fields, at 2×3.16 GHz and 345 MHz, drive the $F \leftrightarrow H$ two-photon and $H \leftrightarrow I$ one-photon transitions respectively, producing three optically-accessible rf-dressed levels due to $25F$ admixtures. Because the high-ℓ states $25H$ and $25I$ have polarizabilities an order of magnitude larger than $25F$, even a moderate dc field Stark-shifts them out of resonance with the rf dressing and decouples them from $25F$. The signature of a photoinduced field is therefore the collapse of the dressed-state triplet into a single $25F$ peak. In the buffer-gas-free cell [Fig. 4.11(a)], the triplet collapses fully when the 453-nm laser is applied, consistent with $E_{\mathrm{dc}} \gtrsim 50$ V/m. In the 50-mTorr Ar cell [Fig. 4.11(c)], the triplet is essentially unchanged by UV illumination, indicating that the photoinduced field is suppressed.

The second scheme [Figs. 4.11(b),(d)] uses the $50F_{5/2}$ state alone, exploiting the n^7 scaling of polarizability for high field sensitivity without the need for rf dressing. In the buffer-gas-free cell [Fig. 4.11(b)], the EIT peak vanishes entirely under UV illumination ($E_{\mathrm{dc}} \gtrsim 20$ V/m). In the 50-mTorr Ar cell [Fig. 4.11(d)], the peak persists with at most a 5-MHz shift, bounding any residual field at $\lesssim 3$ V/m. The two schemes together imply that 50 mTorr of Ar suppresses the photoinduced field by a factor of $\gtrsim 16$. Equivalent results are obtained with Ne and N_2.

To explain the shielding effect, we consider the mean free distance (MFD) of the photoelectrons in Rb and Ar gases using approximately 2×10^{-20} m^2 and approximately 7×10^{-19} m^2 for electron-Ar and electron-Rb momentum transfer collision cross sections, respectively. At room temperature, the Rb pressure is approximately 3×10^{-7} Torr, and the photoelectron MFD is approximately 100 m. Hence, in the inert-gas-free cells, the photoelectrons propagate freely within the cell volume, and electric fields due to photoelectric charging of the cell walls will extend throughout the cell. However, in Ar at our pressure range, the elec-

tron MFD is $\lesssim 1$ cm. In that case, the photoelectron spread is diffusive, and the electrons may form a negative space charge layer above the photoelectrically charged cell wall. Using Gauss's law, our field estimate of 50 V/m, and assuming a layer of 1 cm thickness, the electron density is estimated at approximately 3×10^{11} m^{-3}, leading to a Debye length in the range of 1 cm. Therefore, the origin of the inert-gas-induced dc electric-field shielding phenomenon may be attributed to a combination of electron-inert-gas collisions and Debye screening.

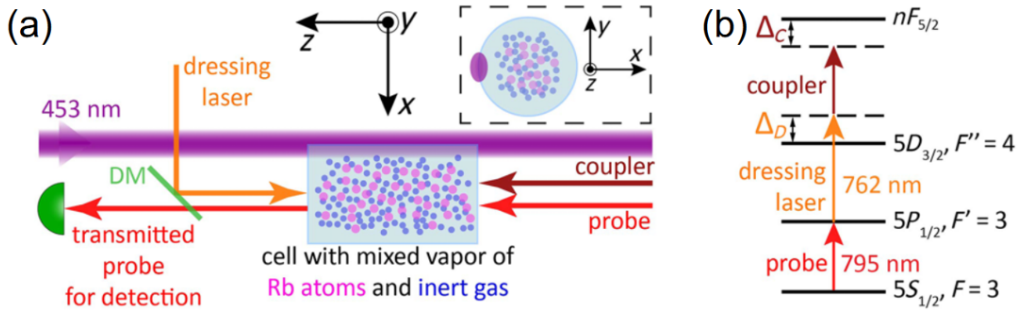


Figure 4.10: Adapted from [128]. (a) Sketch of the experimental setup, with a cross sectional view provided in the inset (DM = dichroic mirror). (b) Energy-level diagram of ^{85}Rb for three-color Rydberg excitation.

4.6 Conclusion

The results presented above have important implications for future applications of Rydberg-EIT to plasma field diagnostics. The gases studied in our experiment are common choices for low-pressure plasma discharges, including inductively coupled and dc plasmas. Rf discharges in gases at pressures above 1 mTorr rely on power absorption through collisional heating. This mechanism is most efficient at gas pressures at which the effective rate of collisions between electrons and neutral atoms is close to the angular frequency of the rf power applied, *i.e.*, $\nu_{en} \approx 2\pi f_{\mathrm{rf}}$. For instance, Ar offers efficient rf power absorption at the standard frequency of 13.56 MHz over a range of pressures from 10 mTorr to 100 mTorr due to favorable values of ν_{en} [173, 174]. In this regime, the gas-induced EIT broadening is negligible in comparison to typical EIT linewidths, as shown in Fig. 4.6, and the estimated line shift is less than 20 MHz for Ar and 2 MHz for Ne and N_2. This indicates the viability of Rydberg-EIT as a diagnostic tool for electric fields in low-temperature rf plasma generated using the gases utilized in our study.

We have demonstrated that Rydberg-EIT presents a viable spectroscopic method in the

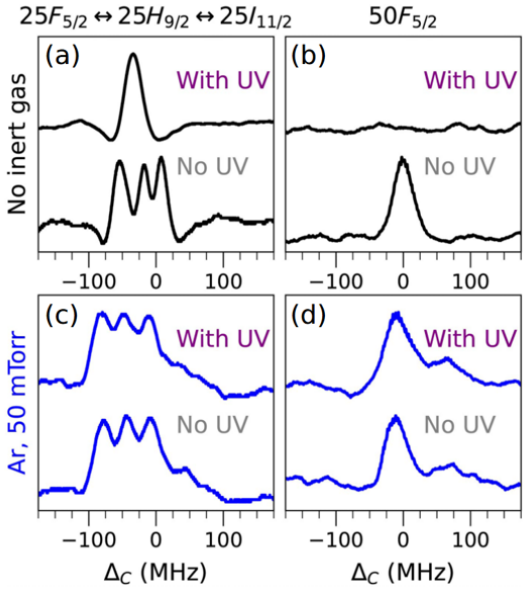


Figure 4.11: Adapted from [128]. Rydberg EIT with the rf-coupled triplet of states, $25F_{5/2}$, $25H_{9/2}$, and $25I_{11/2}$ (left column) and with the $50F_{5/2}$ state (right column), without and with the 453-nm light shone onto the cell walls. Top row: inert-gas-free cell; bottom row: cell with 50 mTorr of Ar. EIT peaks obtained from the inert-gas-free cell with the 453-nm light and the rf dressing fields turned off were used to mark the location $\Delta_C = 0$.

presence of the commonly used inert gases Ar, Ne and N_2 at pressures up to about 5 Torr. Estimates based on the semi-classical pseudo-potential model of interactions between a Rydberg atom and an inert-gas atom agree well with our experimentally observed EIT line shifts and broadenings, within the achieved uncertainty. In the sub-100 mTorr pressure regime, inert-gas-induced broadening is negligible compared to the typical linewidth of our Rydberg-EIT signals. This pressure range is frequently used for low-temperature rf plasma discharges. Considering EIT shift, broadening and signal strength, this study indicates Ar to be a particularly good choice in future plasma-physics applications of Rydberg-EIT.

CHAPTER 5

Plasma Field Measurement Using Rydberg Atoms

This chapter is based on Ref. [175]

The vapor-cell measurements of Chapter 4 established that, below ∼100 mTorr of inert-gas pressure, Rydberg-EIT lines remain narrow and largely undistorted, opening the technique as a viable diagnostic for low-pressure inert-gas environments. When immersed in a plasma environment, a Rydberg atom now experiences the stochastic microfields and additional dephasing from electron–Rydberg collisions. This chapter presents the high-resolution spectroscopy of Rydberg atoms inside a weakly ionized, low-temperature plasma, revealing the microfield distribution in the bulk region of the plasma.

A brief review of noninvasive plasma field diagnostics is presented in Sec. 5.1. Sec. 5.2 describes the design choice and experimental considerations for an inductively coupled plasma (ICP) chamber that supports continuous rf discharge while sustaining a constant rubidium vapor pressure. Sec. 5.3 presents Rydberg spectra in the strong rf fields within the chamber in the absence of plasma discharges. This near-field measurement features substantial rf magnetic field rivaling the Stark effect, unlike the usual Rydberg electrometry in the far field. Sec. 5.4 presents Rydberg-EIT spectra of rubidium tracer atoms immersed in the plasma environment. The EIT spectra provide direct evidence of the screening of rf drive field in the interior of the plasma volume. The residual line shape reveals the Holtsmark microfield distribution and collisional broadening, allowing direct measurement of the plasma microfield in the range ~ 5 to 10 V/cm.

5.1 Motivation

Conventional plasma diagnostic methods employing electrostatic metal probes are fundamentally limited by back action of the probe on the local plasma state, and often lack the necessary spatial resolution. State-of-the-art non-perturbative spectroscopic techniques [79], such as Electric Field Induced Second Harmonic Generation (E-FISH) [83, 176, 177] and

Coherent Anti-Stokes Raman Scattering (E-CARS) [80, 81], exploit plasma-driven nonlinear susceptibilities, while passive methods like Optical Emission Spectroscopy (OES) [85, 87] infer fields from the Stark broadening of emission line profiles. These techniques typically require strong electric fields, often on the order of several kV/cm, thereby restricting their practical application to intermediate or near-atmospheric-pressure discharges.

In contrast, low-temperature rf discharges generated at pressures below 100 mTorr are characterized by weak internal electric fields, typically in the few V/cm range. These low-pressure plasmas are critical for a wide array of applied technologies including semiconductor processing, biomedical applications, and advanced propulsion systems [178, 179], as well as for fundamental studies of magnetized plasmas [180] and dusty plasmas [181]. Spatial mapping of these weak fields with existing probe-based or optical methods remains a challenge due to insufficient field sensitivity. Electric fields above 40 V/cm in low-pressure discharges have been measured using laser-induced fluorescence of field-mixed molecular levels [182] and optogalvanic laser spectroscopy [183].

Rydberg atoms are well-suited for electric field measurement via the Stark effect due to their exaggerated dipole polarizabilities that scale as n^7. The Stark effect of Rydberg atoms has been used to characterize electric fields in cold Rb^+ ion clouds [61, 184] and in photoexcited plasma [185, 186]. The Laser-Induced Fluorescence (LIF)-dip technique [90–93], which monitors the loss of fluorescence from one of the involved states during two-photon excitation, offers extended sensitivity of a few V/cm. However, the performance of LIF-dip is limited by the reliance on incoherent population transfer to obtain the dip and by the technical difficulty of detecting a small signal reduction against a large baseline fluorescence. Moreover, the microfield and collisional broadening features are typically absorbed into a multi-GHz technical linewidth and not resolved in earlier Rydberg spectroscopy of plasmas using LIF-dip and related techniques.

Over the past decade, Rydberg-EIT in alkali vapor cells has been demonstrated as a robust quantum-sensing methodology for dc [58] and radio frequency (rf) electrometry [54, 55]. Rydberg-EIT is an attractive candidate for measurement of weak electric fields in low-pressure plasmas. Particularly impactful applications include spatio-temporal field mapping near sheath regions and impurities in the case of dusty plasma. To this end, we present the results from Rydberg-EIT in the bulk of a continuous rf plasma in the remainder of the chapter. These results establish the feasibility of Rydberg-EIT for field diagnostics in low-pressure plasma discharge.

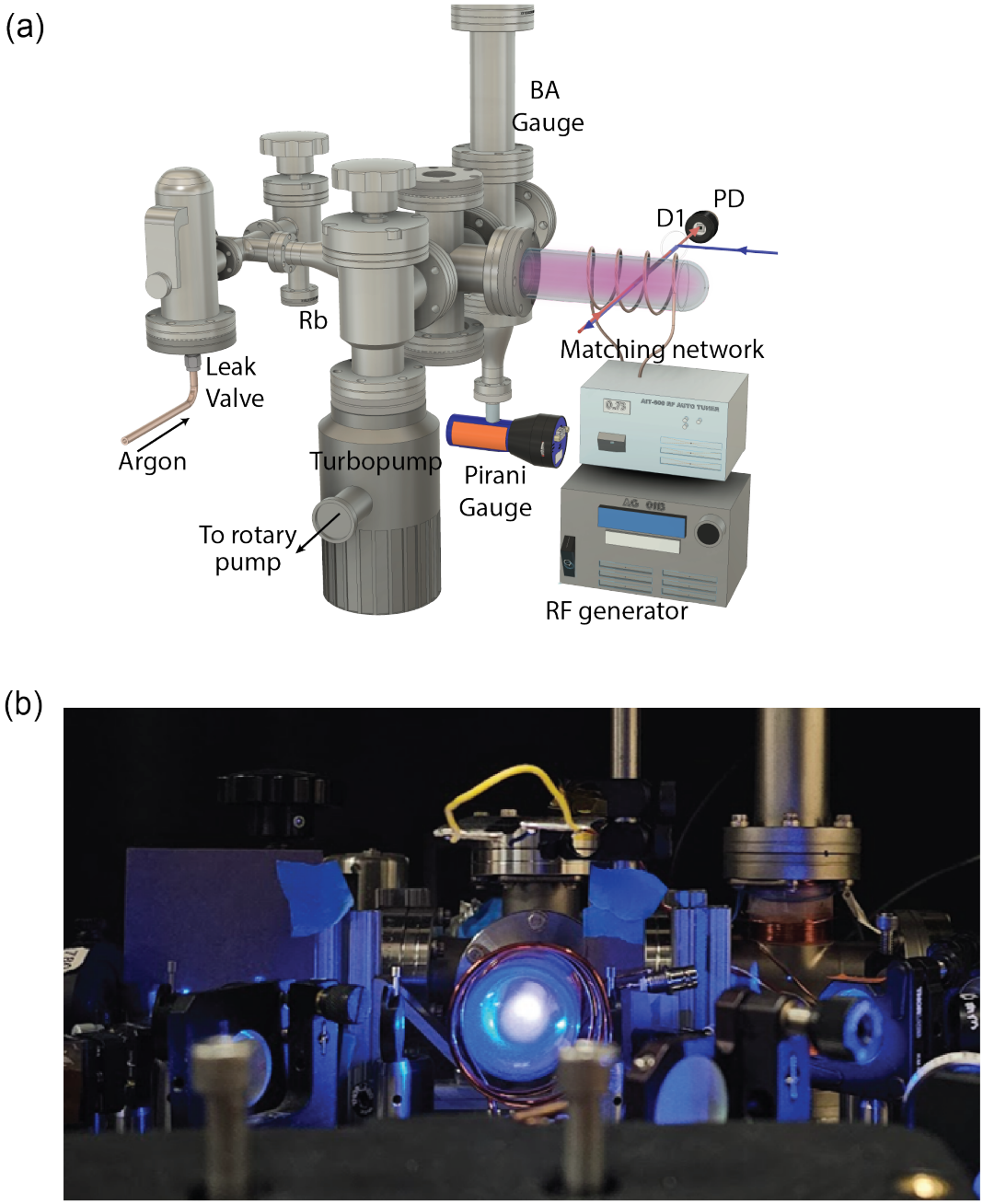


Figure 5.1: (a) Schematic of the experimental setup for plasma discharge and EIT spectroscopy. An inductively coupled Ar plasma (pressure range $\sim$ 5 to 50 mTorr) is generated inside the depicted domed glass cylinder by a 13.56 MHz rf source, a matching network, and a helical drive coil. Near-thermal Rb vapor, entrained into the Ar flow and the plasma discharge, is optically interrogated for Rydberg-EIT-based electric-field diagnostics. (b) The plasma chamber, as viewed into the glass dome. The purple glow denotes the plasma column, generated in a 10 mTorr discharge by 0.5 W rf power.

5.2 Experimental Methods

5.2.1 The Inductively Coupled Plasma Source

The plasma regime of our interest is generated by ionizing gas at pressures below 100 mTorr. Ionization and plasma discharge can be driven by applying either dc or rf power. We chose inductive coupling of rf power because it requires no in-vacuum electrodes, which simplified iteration on the chamber design during initial development. Other advantages, compared to dc plasma, include a more uniform plasma and prevention of electrode etching.

We drive the discharge at 13.56 MHz, a standard ISM band frequency, well-suited for argon discharges. At this frequency, $\omega \ll \omega_{pe}$ across the operating range, ensuring that the plasma is overdense and inductive coupling is robust. Secondly, $\nu_m \approx \omega$ over the pressure range of interest, ensuring optimal power delivery.

The rf power is supplied by a commercial generator (T&C Power Conversion, model AG-0113) and delivered via a matching network to a helical coil. Impedance matching is crucial in a high power rf line to prevent damage to the generator from reflected power. The combined impedance of the coil and plasma system is transformed to 50 Ω by the matching network (T&C Power Conversion, model AIT-600), which has an L-type topology with two variable capacitors. While the model features an autotuner, often manual tuning of the capacitors is required to ensure best matching. The reflected power is kept below 5% during normal operation.

The ICP discharge is generated within a domed glass cylinder measuring 4 cm in diameter and 10 cm in length appended to the UHV chamber described next. Rf power is delivered by a 3-turn helical rf drive coil of 5 cm diameter, constructed from AWG 11 copper wire. The rf magnetic field produced by this coil couples through the domed glass cylinder into the ICP. In the absence of plasma, it extends along the axis of the glass cylinder and amounts to about 0.8 G/A.

5.2.1.1 Inductive coupling in helical geometry

An rf current $I_{\text{coil}}(t) = I_0 \cos(\omega t)$ in the helical coil produces an axial oscillating magnetic field within the chamber. By Faraday's law, this time-varying field induces an azimuthal electric field,

$$\oint \mathbf{E} \cdot d\boldsymbol{\ell} = -\frac{d\Phi_B}{dt}, \tag{5.1}$$

which accelerates electrons along closed azimuthal trajectories. Subsequent collisions with neutrals produce ionization and sustain the discharge. The configuration is the canonical air-core transformer with the coil as the primary winding and the plasma as a single-turn lossy

secondary driven by the induced azimuthal current. A Pyrex cell wall provides dielectric isolation between the coil and the plasma.

In general, ICPs feature two coupling modes [187]. At low input power, the discharge is sustained primarily by the capacitive voltage between coil windings and the plasma through the dielectric wall. This so-called E-mode produces a tenuous, low-density discharge. The discharge transitions abruptly above a certain threshold to the H-mode, in which inductive coupling dominates and the plasma density rises by one to two orders of magnitude. The transition between the two modes is hysteretic and can lead to instability. We avoid mode instability by seeding photoelectrons before the plasma ignition. In future experiments, a probe-based measurement of the EEDF can confirm the mode of operation. This is however tangential for the results presented in this chapter, where it suffices to avoid hysteresis and ensure stable operation.

5.2.1.2 Field penetration and operating regime

Field penetration in an ICP is described in Sec. 3.3.6, with the general expression given by Eq. 3.32. The operating range of this work involves n_e ranging from a few 10^{10} cm^{-3} to 10^{11} cm^{-3} (see Fig. 5.10 and Sec. 5.4) and argon pressures of 5 to 50 mTorr. Effective electron temperature for this pressure range has been reported in literature as $T_e \sim$ 2–5 eV [188], the relevant scales are summarized in Table 5.1:

Parameter	Order of magnitude	Comments
$\omega_{pe}/2\pi$	2–3.5 GHz	$\omega_{pe} \gg \omega$, plasma is overdense
ν_m	10^7–10^8 s^{-1}	comparable to $\omega = 8.5\times10^7$ rad/s
Collisionless $\delta = c/\omega_{pe}$	1.4–2.4 cm	comparable to chamber dimension ($\approx$ 2 cm)
Electron mean free path λ_{mfp}	2–5 cm	comparable to chamber dimensions ($\approx$ 2 cm)

Table 5.1: Operating regime of the ICP source

It should be noted that this apparatus is substantially different from larger-volume processing ICPs in two ways.

Firstly, the collisionless skin depth is comparable to the chamber radius. The thin-skin-layer picture appropriate to large reactors does not apply here. The induced field penetrates a substantial fraction of the discharge volume. The radial field profile is better described by modified Bessel functions of imaginary argument than by a simple exponential decay. Nonetheless, the plasma is overdense at the driving frequency. Direct measurements of the rf electric and magnetic fields inside the discharge using Rydberg electromagnetically induced

transparency, as described in Sec. 5.3, confirm strong screening of the vacuum-coil field upon ignition.

Secondly, the electron mean free path is comparable to or even exceeds the chamber dimensions. The discharge is therefore weakly collisional in the transport sense, and electron energy distributions are expected to be non-local *i.e.*, set by the field averaged over the electron's trajectory rather than by local conditions.

5.2.1.3 Power absorption and heating

Power is delivered to the electron population through the time-averaged Joule dissipation integrated over the entire volume,

$$P_{\text{abs}} = \int \tfrac{1}{2}\,\sigma_p^R\,|\mathbf{E}(\mathbf{r})|^2\,dV = \frac{1}{2} I_{\text{rf}}^2 \frac{\pi e^2 n_0 \nu_{\text{eff}} \mu_0^2 \mathcal{N}^2 R^4}{8ml}, \tag{5.2}$$

where $\mathcal{N}$ = number of turns, l, R = length, radius of the helical coil, respectively and $\nu_{\text{eff}} = \nu_m + \nu_{\text{stoch}}$. ν_m and ν_{stoch} refer to electron-neutral elastic collision rates corresponding to Ohmic and stochastic heating, respectively. The heating mechanisms are discussed in Sec. 3.3.6. The main takeaway from this regime is that

$$P_{\text{abs}} \propto n_0 I_{\text{rf}}^2, \tag{5.3}$$

i.e., the ratio of absorbed to applied rf power is not constant. Rather the fraction of power absorbed itself increases with plasma density. Both Ohmic and stochastic heating mechanisms contribute to this ICP.

- At $p \gtrsim 25$ mTorr: $\nu_m \gtrsim \omega$, so Ohmic heating is the principal channel. This mechanism scales with $\sigma_p^R \propto \nu_m/(\nu_m^2 + \omega^2)$ and is most efficient when $\nu_m \sim \omega$.
- At 5 mTorr $\lesssim p \lesssim 25$ mTorr: both contribute comparably, and the effective dissipation is captured by an effective collision frequency $\nu_{\text{eff}} = \nu_m + \nu_{\text{stoch}}$ in the conductivity. Stochastic heating becomes important when $\lambda_{\text{mfp}} \gtrsim \delta$.

The pressure dependence of the source's power-coupling behavior reported later in Fig. 5.11 reflects this transition.t

5.2.2 UHV Plasma Chamber

Initial attempts involved applying rf power to argon-filled vapor cells used in Chapter 4. No plasma could be ignited in this geometry, even at 50 W of rf drive. We attribute this

to rapid electron loss to the cell walls, which prevented the avalanche ionization needed for breakdown. Sustained plasma operation at our desired pressure range requires a continuous flow of pure Ar gas, while maintaining the desired Ar pressure. In fact, this is the standard practice for rf plasma reactors, where precursor gases are constantly admitted through a mass flow controller and pumped out. Since typical plasma experiments operate at several mTorrs to Torrs of pressure, a rough vacuum enabled by KF flanges and rotary pumps suffices. However, our experiment uses rubidium vapor as the sensing element, which reacts readily with atmospheric contaminants. This imposes vacuum and gas-purity requirements well beyond those of a standard rf plasma reactor.

Therefore, the plasma discharge and EIT spectroscopy take place in the ultrahigh vacuum (UHV) chamber shown in Fig. 5.1 (a). Pure Ar from a commercial gas cylinder is supplied into a service line at 1.5 atm. The overpressure prevents back-diffusion of atmospheric contaminants into the service line. The Ar flows via an Alicat mass flow controller (MFC-20 sccm) held at positive pressure, and then through a UHV leak valve into the plasma chamber. The MFC provides precise Ar flow rate control at a constant mass flow setpoint, which can be remotely adjusted by an external PID controller to maintain a constant pressure in the chamber. The leak valve is critical to attain the purity in the argon flow required to sustain Rb vapor pressure. Early attempts with MFC alone resulted in Rb depletion even at the smallest flow rate due to contaminants leaking into the MFC outlet.

The UHV chamber is evacuated by a 70 L/s turbomolecular pump (Varian V-70), which connects via a right-angle valve to a 1.6 L/s rotary pump. The plasma chamber is initially evacuated to a base pressure of 5×10^{-7} Torr, as measured by a Bayard-Alpert (BA) ionization gauge. When Ar is flowed through the system, the pressure is measured with a Pirani gauge. We study ICPs with Ar pressures ranging from $\sim$ 5 mTorr to 50 mTorr. The Ar pressure is determined by balancing the flow through the leak valve, which is metered by the MFC, against the effective pumping speed (EPS), which is throttled down by partially closing the right-angle valve.

The optimal EPS, in turn, follows from the requirement to pump outgassing effectively. The outgassing rate can be reduced to $\approx 4 \times 10^{-6}$ Torr-L/s by cleaning and assembling the chamber at UHV standards. In this case $\approx$ 2 L/s of EPS suffices to maintain a small enough base pressure to sustain Rb vapor. With appropriate throttling, Ar flow within a range of 1 sccm to 10 sccm results in equilibrium pressure of 5 mTorr to 50 mTorr.

Downstream of the leak valve, the Ar flow is merged with a Rb vapor stream from a Rb reservoir, which is pre-filled with $\sim$ 1 g of natural isotopic Rb. At equilibrium, Rb pressure is maintained near 3×10^{-7} Torr within the Ar, approximately equivalent to the thermal Rb vapor pressure at room temperature ($\approx$ 295 K). The Rb pressure is monitored via the

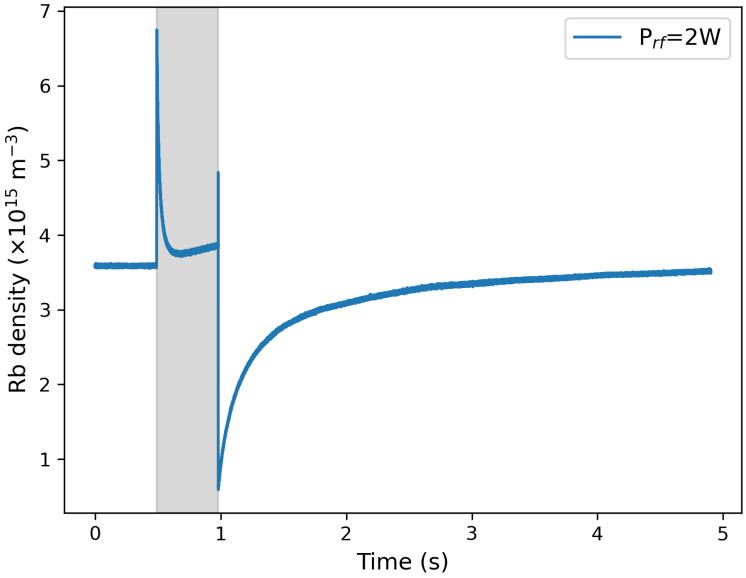


Figure 5.2: Transient effects in Rb vapor density upon plasma ignition at moderate rf power. Rf drive is turned on at t =500ms for a duration of 500 ms (marked in gray).

absorption coefficient of the ^{85}Rb vapor on the 780-nm D_2 line observed in the domed glass cylinder in Fig. 5.1 (a). Heating the Rb reservoir to an appropriate temperature is important to compensate for the continuous removal of Rb vapor entrained within the Ar flow system. Inadequate heating eventually leads to loss of vapor pressure, while overheating deposits Rb on the glass dome walls, screening the applied rf power. The optimal Rb reservoir temperature, determined empirically, is 45 °C under our operating conditions.

Running plasma at a moderate power was another crucial factor to ensure a sustainable coexistence of Rb vapor in plasma. Fig. 5.2 shows the transient response of Rb vapor density when plasma is pulsed. The spike in Rb vapor density after plasma ignition is attributed to plasma-induced desorption, which settles to a steady state in ≈200 ms. During steady operation, Rb atoms ionized by the plasma are constantly replenished by the adsorbed layer on the cell wall. Upon plasma extinction, the cell walls resume adsorption, acting as getters, and thermal equilibrium takes several seconds. A particularly deleterious effect is the E-H mode transition which leads to a rapid increase in plasma density and complete loss of Rb pressure. This is attributed to a combination of plasma etching of the cell wall and subsequent surface chemistry that eliminates metallic Rb adsorbed on the glass. To avoid this and facilitate stable ICP operation, photoelectrons are seeded into the Ar gas by illuminating the glass cylinder with UV light before ICP ignition. The seeding mechanism allows plasma operation at P_{rf} as low as 0.15 W. We keep the rf power $\lesssim$ 5 W to avoid

etching effects and loss of Rb pressure.

5.2.3 EIT spectroscopy

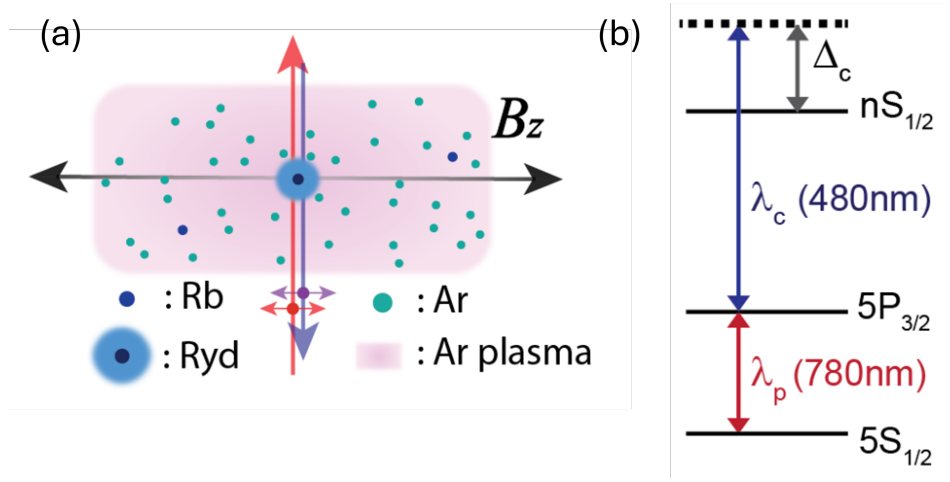


Figure 5.3: (a) Illustration of the discharge volume and EIT interrogation region. The 780-nm EIT probe (red) and 480-nm coupling laser beams (purple), combined with a dichroic mirror, counter-propagate and overlap each other inside the domed glass cylinder. The transmitted EIT probe power is measured with a photodiode (PD). Both laser beams are linearly polarized parallel to the rf drive magnetic field, B_z. (b) Rb energy levels used in this work. The probe laser (wavelength $\lambda_p = 780$ nm) is on-resonance with the $5S_{1/2}, F = 3 \leftrightarrow 5P_{3/2}, F' = 4$ transition, while the coupling laser (wavelength $\lambda_c = 480$ nm) is scanned across a $5P_{3/2}, F' = 4 \leftrightarrow nS_{1/2}$ transition for Rydberg-EIT-based plasma electric field diagnostics.

The choice of Rydberg states for plasma field diagnostics involves an additional competition not present in the neutral-gas studies of Chapter 4. The plasma microfield-induced line shift scales as $n_e^{4/3}n^7$ for plasma n_e, so field sensitivity climbs steeply with principal quantum number n. Working against this, the collision cross sections scale as n^4 at lower n before decreasing at higher n [97] and coupler Rabi frequency decreases monotonically as $n^{-3/2}$. The choice of n window therefore depends on plasma density and temperature. The range $n = 25$–30 used in this work was selected as a compromise for the density range $n_e \sim 10^{11}$ cm^{-3} accessed here, beyond which collisional broadening at $n = 30$ already approached the Holtsmark width (see Fig. 5.8). Moreover, since the primary electric field of interest is the stochastic microfield, nS states were chosen due to their isotropic response and large quantum defect that suppresses state quenching due to ℓ-mixing. Vector electrometry in dilute and afterglow plasma will require a higher range of n and D states. The scaling laws of Rydberg states provide a rich design space for matching the EIT diagnostic for the plasma regime under investigation.

In the results reported here, EIT-based plasma diagnostics are performed with cascade EIT from the Rb ground state, $5S_{1/2}$, to an $nS_{1/2}$ Rydberg state through the intermediate $5P_{3/2}$ state, as depicted in Fig. 5.3 (b). This is achieved by counter propagating 780 nm and 480 nm EIT probe and coupler laser beams through the discharge volume, as shown in Fig. 5.3 (a). The laser beams have respective powers of ≈ 3.4 µW and 35 mW, are focused at the center of the ICP volume in the domed glass cylinder with Gaussian beam-waist parameters of $w_0 = 60$ μm and 75 μm, and are linearly polarized with polarizations parallel to the axis of the helical rf drive coil. The Rabi frequencies for the EIT probe (lower) transition range between ~ 12 MHz and ~ 20 MHz, and those for the EIT coupler (upper) transition into $25S_{1/2}$ between ~ 8 MHz and ~ 14 MHz, for the magnetic quantum number m_F ranging from 3 to 0.

The frequency of the 780 nm EIT probe laser is locked to the lower $F = 3$ to $F' = 4$ hyperfine transition using saturated absorption spectroscopy in an inert-gas-free vapor cell. The transmitted EIT probe power is acquired using a photodiode (FDS-100), which is protected from plasma fluorescence and other stray light by a 780 nm band-pass filter. The EIT probe power is recorded as a function of the frequency of the 480 nm EIT coupler beam, which is scanned across the Rydberg transition. The coupler-laser frequency scans are calibrated and linearized using the transmission spectrum of a low-power beam sample passed through a Fabry-Perot reference cavity, which has a stability on the order of 10 MHz per 24 hours [131]. In our data, zero coupler detuning marks the field-free Rydberg-EIT resonance between the intermediate $5P_{3/2}, F' = 4$ level and the target Rydberg level with the Ar gas present, which causes small shifts [175]. The Rydberg-EIT spectra, *i.e.*, the transmitted EIT probe power measured as a function of coupler detuning, Δ_c, then reflect the accumulated effects of Zeeman and Stark shifts averaged over the length of the EIT probe's path through the glass cylinder in Fig. 5.1.

The number density of the Rb tracer atoms in the ICP is about five orders of magnitude lower than that of Ar. Hence, the Rb tracer atoms are presumed to have no significant effect on the characteristics of the Ar ICP under study, beyond an attenuation of the RF coupling efficiency caused by Rb deposition on the glass walls.

5.3 Rydberg atom in ICP antenna without plasma

We first investigate Rydberg-EIT spectra of Rb vapor within the fields generated by the rf drive coil under Ar-free conditions, for a set of rf powers. The drive frequency of 13.56 MHz, which is in the High Frequency (HF) radio band, generates electric and magnetic Rydberg level shifts that are quasi-static on the intrinsic atomic time scale. These shifts manifest

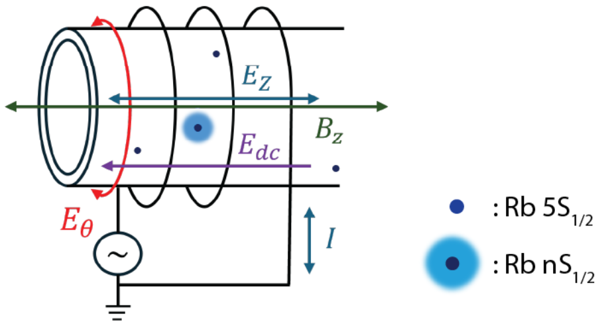


Figure 5.4: Fields arising inside the ICP chamber from applied rf power, P_{rf}, at 13.56 MHz in the chamber in the absence of Ar: axial rf magnetic field B_z, induced rf electric field E_θ, capacitive rf electric field E_z, and dc electric field E_{dc} (self-bias).

in the form of frequency modulation sidebands as well as AC Stark shifts in Rydberg-EIT spectra [189, 190]. In the absence of dc electric fields and rf magnetic fields, only even harmonics of the drive field's frequency occur. The sideband structures and shifts observed inside solenoidal rf coils, shown in Fig. 5.5, are considerably richer and include both even- and odd-harmonic rf bands.

The complexity of Rydberg-EIT spectra in solenoidal rf coils is due to the presence of several types of fields interacting with the atoms, which are indicated in Fig. 5.4 and listed below.

- The rf current through the helical coil generates an axial rf magnetic field with amplitude B_z, which induces linear rf Zeeman shifts in all atomic levels involved.
- The induced azimuthal rf electric field with amplitude E_θ induces quadratic rf Stark shifts in the utilized Rydberg levels. E_θ scales with the radial separation from the coil axis.
- The reactive voltage drop across the length of the drive coil, which can reach hundreds of V, couples capacitively through the glass walls and gives rise to an axial rf electric field with amplitude E_z, which appears in-phase with the azimuthal induced field E_θ. E_z was found to be approximately homogeneous from finite element simulation with Ansys Maxwell with $< 10\%$ variation across the transverse plane.
- Due to our asymmetric driving configuration, in which one coil terminal is grounded and the other is driven by the rf potential, a longitudinal dc self-bias field [191], E_{dc}, develops due to vastly different electron and ion masses. Generally, highly mobile negative charges are removed near the polarized terminal of the drive coil, resulting in

a longitudinal charge distribution within the cell, which in turn causes the dc self-bias electric field, E_{dc}.

5.3.1 Analysis

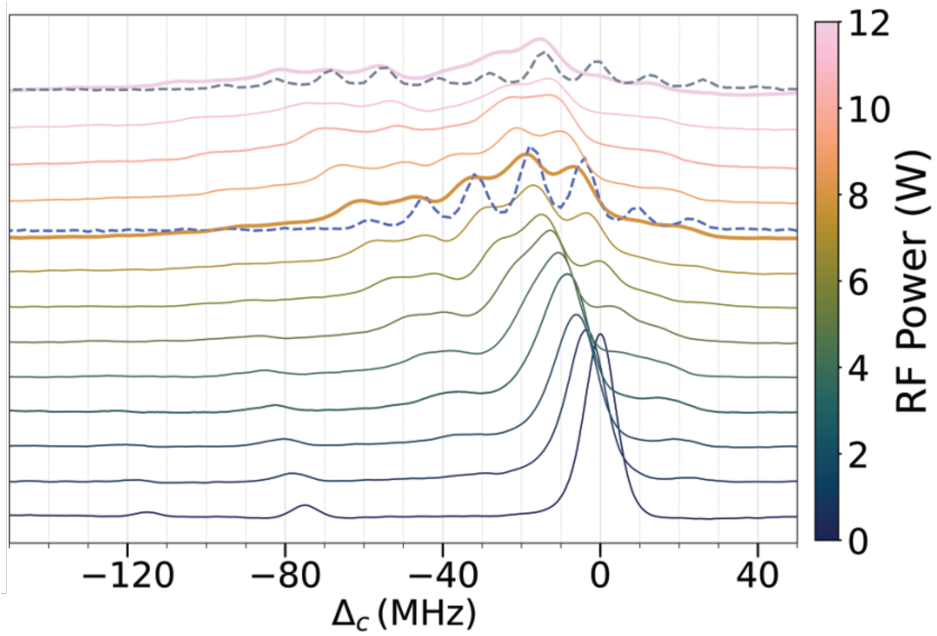


Figure 5.5: Measured Rydberg-EIT spectra (solid lines) of Rb $27S_{1/2}$ without plasma, with P_{rf} indicated by the color bar. The rf drive fields create electric and magnetic rf sidebands at integer multiples of ω_{rf}. Calculated spectra, shown in gray (black) dashed lines, are for EIT-beam polarizations along z, B_z = 7.5 G (15 G), E_{dc} = 2 V/cm (4 V/cm), and $E = \sqrt{E_\theta^2 + E_z^2}$ = 10 V/cm (12 V/cm). Aside from line broadening likely caused by field inhomogeneities along the EIT probe beam, the simulated spectra are a fairly close match to experimental spectra at $P_{\mathrm{rf}} = 8$ W (12 W).

We first note that the rf magnetic field within an rf drive coil is several orders of magnitude higher than that in traveling electromagnetic waves in source-free regions, leading to effects from rf Zeeman modulations that rival those of rf Stark modulations of the electric-field-sensitive Rydberg levels. Hence, Rydberg-EIT in spectroscopic cells located inside rf coils differs from Rydberg-EIT in freely propagating rf fields, where magnetic-field effects are typically negligible [189, 190].

Inside the rf drive coil and without plasma, the atoms interact with the three types of rf fields and one rf-induced, rectified static field. The rf drive coil's axis is pointing along the z-axis, and the coil generates a magnetic field $B_z(t) \equiv B_{\mathrm{rf}}(t) = B_{\mathrm{rf0}} \sin(\omega_{\mathrm{rf}} t)$.

For an initial qualitative explanation of the spectral features, let us assume that all atomic

levels are in the linear Zeeman regime, *i.e.* all levels experience linear Zeeman level shifts of $\mu_B\, B_{\rm rf}(t)\, g_F\, m_F$, with the Bohr magneton μ_B, Lande factors g_F, and magnetic quantum numbers m_F.

The magnetic-dipole Zeeman couplings are then linear in $B_{\rm rf}(t)$. The sinusoidal drive field generates rf sidebands on all atomic levels with non-zero magnetic moment. The Zeeman rf sidebands have shifts of

$$\Delta W^k_{\rm Brf} = k\omega_{\rm rf} \tag{5.4}$$

from the unperturbed atomic levels, with integers k = ..., -1, 0, 1, 2, ... and corresponding relative amplitudes of

$$A_{\rm Brf} = {\rm i}^k J_k\left(\frac{\mu_B g_F B_{\rm rf0} m_F}{\hbar\omega_{\rm rf}}\right) \tag{5.5}$$

This applies, in principle, to all ground, intermediate and Rydberg levels of the Rydberg-EIT system. The Lande factors g_F depend on n, ℓ, J, and F, the principal, orbital, electronic, and hyperfine quantum numbers of the $5S_{1/2}$, $5P_{3/2}$, and $nS_{1/2}$ levels, respectively.

Inside the rf solenoid, the rf magnetic field induces an azimuthal rf electric field

$$E_\theta(r,t) = E_{\theta 0}\cos(\omega_{\rm rf}t)$$

with amplitude $E_{\theta 0} = r\, B_{\rm rf0}\,\omega_{\rm rf}/2$ and radius r measured from the solenoid's axis. The reactive rf voltage drop, $V_{\rm z}$, along the solenoid causes an rf electric field

$$E_{\rm z}(t) = E_{\rm z0}\cos(\omega_{\rm rf}t)$$

with an amplitude $E_{\rm z0} = \eta_{\rm Ez}V_{\rm z}$. The two rf electric field components are in phase and add up to a total, linearly polarized rf electric field with amplitude $E_{\rm rf0}(r) = \sqrt{E^2_{\rm z0} + E^2_{\theta 0}}$. The polarization angle depends on r. The constant $\eta_{\rm Ez}$ is not exactly known, as it depends on numerous geometrical and electric parameters of the drive coil as well as the dielectric loads inside the coil. However, straightforward estimates show that under typical conditions $V_{\rm z}$ amounts to several hundred volts along a few inches of coil length. Hence, $E_{\rm z0}$ is typically $\gtrsim 10$ V/cm, which may significantly exceed $E_{\theta 0}$.

In our case we use $nS_{1/2}$ Rydberg states, which exhibit an isotropic quadratic Stark shift of $-(\alpha/2)E^2_{\rm rf}(t)$, with a well-known scalar electric polarizability α. Then,

$$E_{\rm rf}(r,t) = E_{\rm rf0}(r)\cos(\omega_{\rm rf}t) \quad .$$

The radially-dependent angle formed by the reactive rf field $E_{\rm z}$ and the induced field E_θ is not important, and the r-dependence of $E_{\rm rf0}(r)$ is often weak due to the dominance of

the approximately homogeneous reactive field. Due to the quadratic nature of the Rydberg Stark shift, a pure rf electric field generates even rf sidebands, which are shifted from the field-free Rydberg levels by amounts of

$$\Delta W_{\text{pure rf}} = -\frac{\alpha E_{\text{rf0}}^2}{4} + 2k\hbar\omega_{\text{rf}} \quad . \tag{5.6}$$

The electric rf sidebands have amplitudes [189, 190]

$$A_{\text{pure rf}}^{k} = (-1)^k J_k\left(\frac{\alpha E_{\text{rf0}}^2}{8\hbar\omega_{\text{rf}}}\right) \quad . \tag{5.7}$$

However, the self-bias field, E_{dc}, complicates the Stark modulation structure by introducing additional odd electric rf sidebands. Using independent integer indices k and p = ..., -1, 0, 1, 2, ..., the rf sidebands generated by both the rf electric fields and the dc bias electric field are shifted in energy by

$$\Delta W_{\text{Erf}}^{kp} = -\frac{\alpha}{2}(\frac{1}{2}E_{\text{rf0}}^2 + E_{\text{dc}}^2) + (2k+p)\hbar\omega_{\text{rf}} \quad , \tag{5.8}$$

and have amplitudes

$$A_{\text{Erf}}^{kp} = (-1)^k J_k\left(\frac{\alpha E_{\text{rf}}^2}{8\hbar\omega_{\text{rf}}}\right) \times J_p\left(\frac{\alpha E_{\text{dc}} E_{\text{rf}}}{\hbar\omega_{\text{rf}}}\right) \quad . \tag{5.9}$$

Due to the presence of multiple electric and magnetic rf modulation mechanisms, the rf sidebands are typically degenerate. The amplitudes of coinciding rf sidebands must be added coherently before taking the squares to obtain the net rf sideband strengths. More critically, most atomic levels are in the non-linear transition region of the hyperfine Zeeman and the hyperfine Paschen-Back effects. Hence, the above equations for the magnetic rf modulations do not generally apply. While this would enormously complicate the modulation structure in rf coils, the rf modulation structure follows directly and non-perturbatively from our direct, time-dependent model explained next.

5.3.2 Simulation

The EIT spectra shown in Fig. 5.5 are reproduced in their essential parts by a simulation of the time-dependent Lindblad equation. The optical EIT laser fields in the simulation are linearly polarized along the rf coil axis, as in the experiment. Since the induced electric and the magnetic rf drive fields, E_θ and B_z, are orthogonally polarized, all m_F-substates with the same n, ℓ, and J quantum numbers are generally coupled. For ^{85}Rb, there are 48

coupled atomic levels. We use the $\{|*, F, m_F\rangle\}$-representation, with $*$ denoting the n, ℓ and J quantum numbers of the involved states.

We include all magnetic and Stark couplings arising from the aforementioned rf fields, all magnetic-dipole and relevant electric-quadrupole hyperfine interactions, the detailed optical couplings caused by the EIT probe and coupler beams, detailed rates for the spontaneous decay of the $5P_{3/2}$ levels, as well as global atom recycling to account for the limited atom-field interaction time in the experiment. All rf-drive and optical-drive matrix elements and optical decay rates carry the proper dependencies on all involved angular quantum numbers. State mixing and optical pumping arises from both the coherent couplings and the decays, whose angular dependencies are accurately modeled. The Rydberg hyperfine structure, while included in the simulation, is too small to become resolved, but it plays a role in the overall dynamics. As all hyperfine and magnetic-dipole interactions are fully included, the atom dynamics are accurately modeled across the linear Zeeman and Paschen-Back regimes, including all non-linear behaviors in-between these regimes.

Due to the large number of states, we solve the time-dependent Lindblad equation using the quantum trajectory method, which yields an approximation to the density matrix using stochastic wave-functions, or quantum trajectories [192–195]. For given sets of parameters ($E_{\rm rf}$, $E_{\rm dc}$, $B_{\rm rf}$, EIT coupler and probe laser intensities etc), the EIT-coupler detuning, Δ_C, is stepped from -200 MHz to 50 MHz in steps of 2 MHz relative to the unperturbed transition from $5P_{3/2}, F' = 4$ into the Rydberg state $nS_{1/2}$. The EIT-probe detuning from the $5S_{1/2}, F = 3$ to $5P_{3/2}, F' = 4$ transition is held fixed at zero (as is done in the experiment). For each set of parameters, the atomic velocity along the laser beam direction, v, is scanned in steps of 1 m/s across the Maxwell distribution in the vapor cell.

An ensemble of quantum trajectories, $\{|\psi_i(t = 0)\rangle,\ i = 1, 2...i_{\rm max}\}$, is initialized in random superpositions of the magnetic sub-levels of the upper ^{85}Rb hyperfine ground state, $5S_{1/2}, F = 3$. Here we use $i_{\rm max} = 500$ quantum trajectories for each velocity and Δ_C-value. The trajectories are propagated over 2 μs of evolution time for each trajectory, the typical time of flight of an atom through the EIT probe region. The dynamics of the $|\psi_i(t)\rangle$ is governed by alternating intervals of Hamiltonian evolution and discrete quantum jumps that model atomic decay, dephasing and atom recycling. Each quantum jump involves several random numbers to select decay modes and to simulate the decay-specific results. For instance, if an atom decays out of $5P_{3/2}$, random numbers are used to select the polarization and the initial and final hyperfine states, F' and F, of the decay. The probabilities and quantum-jump outcomes of the decays depend on the state $|\psi_i(t)\rangle$ immediately before the jump, von-Neumann state reduction is employed to effectuate the decay, and after the decay the wave-function is renormalized. The quantum-jump timings are dictated by random

numbers and wave-function decay during the Hamiltonian evolution, implemented via appropriate anti-Hermitian decay terms in the effective Hamiltonian. The latter also includes the aforementioned hyperfine level shifts, laser-field detunings, Doppler shifts, optical EIT drive terms, and time-dependent magnetic and electric rf drive terms. The time-step size in the simulation is 1/75 of the rf period.

For each atom velocity, v, and coupler-laser detuning, Δ_C, the density operator is approximated by

$$\hat{\rho}(\Delta_C, v, t) = \sum_{i=1}^{500} \frac{|\psi_i(t)\rangle\langle\psi_i(t)|}{\langle\psi_i(t)|\psi_i(t)\rangle} \tag{5.10}$$

The partial atomic absorption coefficient for the EIT probe is

$$da(\Delta_C, v, t) = \sum_{F', m_F} \frac{4\pi n_{\text{vol}} P_{\text{v}}(v) dv}{\hbar \epsilon_0 \lambda_P} \frac{\text{Im}[\rho_{12}(F', m_F)]}{\Omega_{12}(F', m_F)} \tag{5.11}$$

where n_{vol} is the atom volume density, P_{v} the one-dimensional Maxwell velocity distribution, $\lambda_P = 780$ nm the probe-laser wavelength, ρ_{12} the density matrix element between $5S_{1/2}|F = 3, m_F\rangle$ and $5P_{3/2}|F', m_F\rangle$, and Ω_{12} the Rabi frequency of the probe transition between those states. To arrive at the actual Beer's absorption for the EIT probe, we integrate $da(\Delta_C, v, t)$ over the Maxwell velocity distribution and average the result over time. This yields the EIT spectrum as a function of Δ_C. The procedure is repeated for all rf- and optical-drive conditions of interest.

The simulation examples in Fig. 5.5, displayed as gray and black dashed lines for the cases $P_{\text{rf}} = 8$ W and 12 W, respectively, show good qualitative agreement with measured plasma-free rf spectra in terms of locations and relative strengths of rf sidebands. Deviations are attributed to field inhomogeneities. In view of the results discussed next, the plasma-free EIT spectra in the rf drive coil in Fig. 5.5 serve as baselines that allow us to determine to what extent the plasma surface shields the rf field from the plasma's interior volume, where most of the EIT signal originates from.

5.4 Rydberg atoms in plasma

Rydberg-EIT spectra of Rb tracer vapor immersed in Ar ICPs were recorded over a range of applied rf powers, P_{rf}, of up to about 5 W and Ar pressures ranging from ~ 5 to 50 mTorr. Selected EIT spectra in plasmas generated from 12 mTorr of Ar are shown in Fig. 5.7. The presented Rydberg-EIT spectra in the ICP plasma show a striking disappearance of the rf sidebands seen in Fig. 5.5. The suppression of rf sidebands demonstrates screening of electric and magnetic rf fields from the interior of the plasma volume, which is attributed to the skin

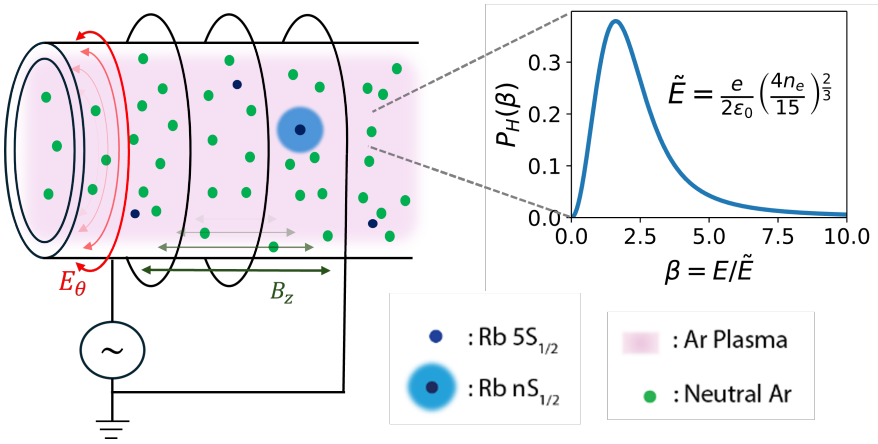


Figure 5.6: Within Ar plasma, the rf fields are shielded due to the skin effect, leaving the stochastic microfield as the dominant field. The microfield distribution is given by the Holtsmark distribution (inset).

effect. Further, even with a continuous rf ICP present, high-contrast Rydberg-EIT lines of the Rb tracer vapor remain, indicating considerable resilience of the Rb vapor against depletion that may result from plasma-induced ionization of Rb. The EIT lines in Fig. 5.7 exhibit an asymmetric line shape, indicative of inhomogeneous electric-field broadening inside the plasma. As P_{rf} is increased, the EIT lines experience larger broadening, along with an increasing red shift. Both features indicate an increase in electron density and plasma microfield strength. In the following, the EIT lineshapes shown in Fig. 5.7 are analyzed considering inhomogeneous Stark shifts and collisional broadening of the Rydberg-EIT line in the plasma environment.

5.4.1 Rydberg-plasma interaction

The interpretation of the Rydberg-EIT spectra in our ICP system is simplified by several factors. The dominant portion of the EIT signal results from the overlap of the EIT probe and coupler beam within the bulk discharge volume, where macroscopic quasineutrality is maintained (*i.e.*, electron density $n_e \approx n_i$, ion density). Furthermore, the plasma in question is a low-temperature plasma (LTP), with characteristic electron energies and ion temperatures ranging from 1 eV to 3 eV [188, 196] and 500 K to 800 K [197], respectively. In our case, EIT has a dynamic time scale τ_{EIT} on the order of a few tens of ns [198], corresponding to only a few μm of ion travel. Hence, the ions are near-stationary during τ_{EIT} and generate a stochastic electric-field distribution at the location of the Rydberg atoms, known as the plasma microfield (Holtsmark) distribution [85, 199].

Conversely, the much faster electrons primarily give rise to collisional Rydberg-level de-

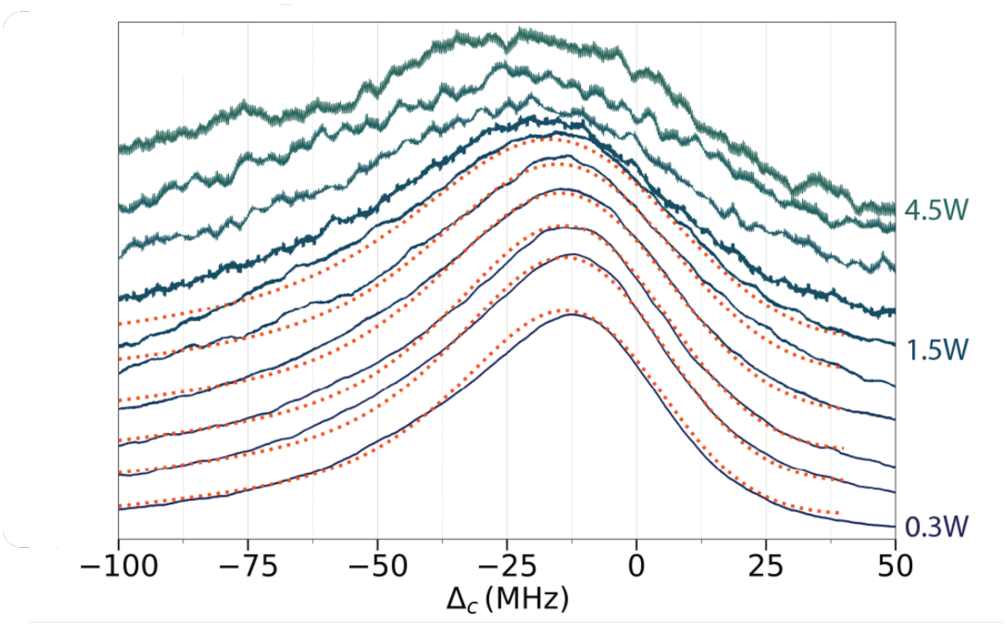


Figure 5.7: Rydberg-EIT spectra of Rb $27S_{1/2}$ in plasma generated from 12 mTorr of Ar. The asymmetric line shape is due to the Rydberg-atom Stark effect in the plasma's microfields, which follow a Holtsmark distribution. The red dashed curves show our fit results obtained from fits according to Eq. 5.20. Fit results are not reliable above 1.5 W due to excessive broadening. The same color scaling as $27S_{1/2}$ rf EIT spectra from Fig. 5.5 is used.

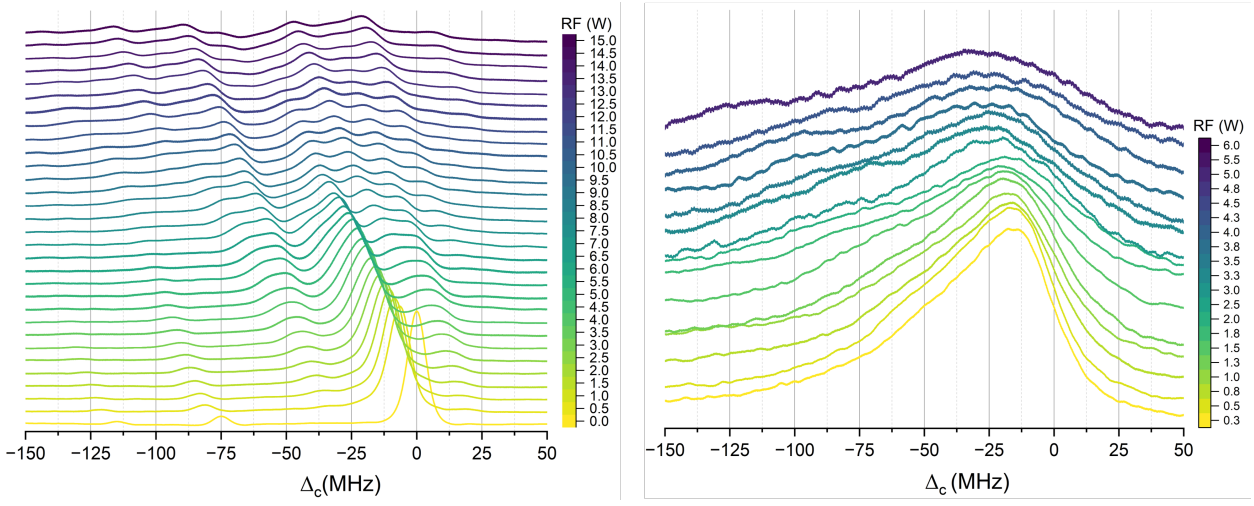


Figure 5.8: Rydberg-EIT spectra of Rb $30S_{1/2}$ (a) without plasma and (b) in plasma generated from 12 mTorr of Ar. The rf-induced sidebands in (a) disappear in (b) due to the skin effect. Fitting EIT spectra in (b) to Eq. 5.20 yields similar plasma density as reported in Fig. 5.10 within the error bars.

phasing, while their contribution to the electric microfield, averaged over τ_{EIT}, is negligible. The lower levels $5S_{1/2}$ and $5P_{3/2}$ are not significantly shifted or broadened by the plasma, as determined by saturation spectroscopy of the Rb D_2 line in the plasma. Therefore, shifts and broadening of the EIT lines are solely attributed to inhomogeneous Rydberg Stark shifts and homogeneous collisional broadening of the Rydberg levels in the plasma.

5.4.1.1 Plasma microfield

Hence, the stochastic microfield generated by the ions can be derived by considering $N = n_i V$ point charges in volume V, each contributing a Coulomb field at the location of the Rydberg atom. The probability that the total microfield takes the value $\mathbf{F}$ is

$$W(\mathbf{F}) = \int d^3r_1 \cdots d^3r_N \, P(\mathbf{r}_1, \ldots, \mathbf{r}_N) \, \delta(\mathbf{F} - \mathbf{E}(\mathbf{r}_1, \ldots, \mathbf{r}_n)) \,,$$

where $\mathbf{E}$ is the total field from the configuration and P is the joint probability density over charge positions. Fourier transforming W gives the characteristic function

$$A(\mathbf{k}) = \int d^3F \, e^{i\mathbf{k}\cdot\mathbf{F}} W(\mathbf{F}) = \langle e^{i\mathbf{k}\cdot\mathbf{E}} \rangle.$$

Further, the plasma is only weakly ionized, ensuring that correlation effects between charged particles are negligible. By treating charges as statistically independent [199], the characteristic function becomes a product of single-particle averages:

$$A(\mathbf{k}) = \langle e^{i\mathbf{k}\cdot\mathbf{E}_j} \rangle^n.$$

For a homogeneous, isotropic plasma with $P(\mathbf{r})\, d^3r = d^3r/V$, the single-particle average reduces to an angular integral:

$$A(\mathbf{k}) = \left[\frac{4\pi}{V} \int_V dr \, r^2 \, \frac{\sin(kE(r))}{kE(r)} \right]^n .$$

Substituting the bare Coulomb field $E(r) = e/(4\pi\epsilon_0 r^2)$ and changing variables to $x \equiv kE(r)$, the integral reduces to the numerical constant $\frac{4}{15}\sqrt{2\pi}$. Taking the thermodynamic limit $n, V \to \infty$ at fixed density $n_i \approx n_e$ yields the compact result

$$A(\mathbf{k}) = \exp\left[-(k\tilde{E})^{3/2} \right], \qquad \tilde{E} \equiv \frac{e}{2\epsilon_0} \left(\frac{4n_i}{15} \right)^{2/3} .$$

where the Holtsmark normal field $\tilde{E}$ sets the characteristic field scale. Inverting the Fourier transform and using the isotropy of $A(\mathbf{k})$, the probability density for the field magnitude is

$$P(E) = 4\pi E^2 W(\mathbf{E}) = \frac{2}{\pi}\frac{E}{\tilde{E}^2}\int_0^\infty dx\, x\, \sin\left(\frac{xE}{\tilde{E}}\right)\, \exp\left[-x^{3/2}\right].$$

With the dimensionless parameter $\beta \equiv E/\tilde{E}$, this defines the Holtsmark distribution:

$$H(\beta) = \frac{2}{\pi}\beta\int_0^\infty dx\, x\, \sin(\beta x)\, \exp\left[-x^{3/2}\right]. \tag{5.12}$$

Thus, the stochastic field in the bulk of a weakly correlated, quasineutral plasma with plasma density, $n_e = n_i$ is given by

$$\mathcal{P}_H(E, n_e) = H(\beta)/\tilde{E}. \tag{5.13}$$

The most probable microfield is given by $1.61\tilde{E}$ and the distribution has a long high-field tail scaling as $\beta^{-5/2}$. Both the line width and the line shift produced by this distribution scale as $n_i^{2/3}$, inherited from the density scaling of $\tilde{E}$.

An $nS_{1/2}$ Rydberg level, possessing a scalar polarizability $\alpha > 0$, experiences a frequency shift $\delta = -\frac{1}{2}\alpha E^2$ due to the quadratic Stark effect. In the quasistatic limit *i.e.*, neglecting ion movements during the EIT timescale, the plasma microfield effect manifests as a convolution of the field-free EIT line shape $I_0(\Delta_c)$ with the probability distribution of the Holtsmark-induced line shift,

$$\tilde{\mathcal{P}}_H(\delta, n_e) = \frac{1}{\sqrt{2|\delta|\alpha}}\, \mathcal{P}_H\left(E = \sqrt{\frac{2|\delta|}{\alpha}}\,,\, n_e\right)\frac{(1-\mathrm{sgn}(\delta))}{2}, \tag{5.14}$$

$$\tilde{I}(\Delta_c, n_e) = \int_{-\infty}^{0} I_0(\Delta_c + \delta)\, \tilde{\mathcal{P}}_H(\delta, n_e)\, d\delta \quad . \tag{5.15}$$

In Eq. 5.14, δ is limited to negative values because the Stark shift of Rb $nS_{1/2}$ states is intrinsically negative. The field-free EIT line shape, $I_0(\Delta_c)$, is measured with the same Ar pressure that is used for the ICP, but with the rf power disabled. In this way, we ensure that collisional shifts and broadening of the EIT line arising from the neutral gas background [175] are already accounted for in $I_0(\Delta_c)$. The convolution will then isolate the specific effects of the plasma microfield.

Since EIT measures the line-integrated effect of the microfield and the laser beams traverse through the diameter of the plasma discharge in the current geometry, variation of plasma density along the transverse plane must be included in Eq. 5.15. The plasma emission profile for a given pressure and rf power in the transverse plane has been used to account for the relative density variation in the radial direction. A sample emission profile after background elimination is shown in Fig. 5.9 (a) for $p = 12$ mTorr and $P_{\mathrm{rf}} = 0.5$ W. The relative density

extracted from this plot is shown in Fig. 5.9 (b). Estimating the relative density variation from this plot relies on a two-step procedure with certain considerations, as detailed below.

Firstly, it should be noted that at a given radius b, the camera captures a line-integrated emission along a chord of length $2\sqrt{R^2 - b^2}$. This is simplified by two assumptions: (i) negligible refraction effect and (ii) an optically thin axisymmetric source. Assumption (i) is justified by ray-tracing through the transverse region of the plasma discharge volume, as shown in Fig. 5.9 (c). This shows negligible refraction from the glass dome apart from the region roughly 2 mm from the edges. A rigorous determination of optical thinness in assumption (ii) requires testing line strength ratio of metastable lines with an absolutely calibrated spectrometer [85]. Nevertheless, this is a good approximation for our plasma due to the small chamber size comparable to the mean-free-path and small ionization fraction. With these assumptions, the observed projection at radius b, $I(b)$ is related to the underlying radial emissivity $\varepsilon(r)$ by the Abel transform

$$I(b) = 2 \int_{|b|}^{R} \frac{\varepsilon(r)\, r}{\sqrt{r^2 - b^2}}\, dr, \tag{5.16}$$

whose formal inverse,

$$\varepsilon(r) = -\frac{1}{\pi} \int_{r}^{R} \frac{dI/db}{\sqrt{b^2 - r^2}}\, db, \tag{5.17}$$

is however numerically ill-conditioned due to the singularity of the integrand at $b = r$, and noise amplification from numerical derivative of dI/db. Therefore, instead of direct evaluation using Eq. (5.17), we use regularized matrix-based inversion algorithms, specifically the Hansen–Law method and the BASEX basis-expansion method as implemented in the `PyAbel` package [200].

In the second step, the recovered emissivity is then converted to an electron density via two assumptions of radiative decay and uniform electron temperature T_e. The primary decay mechanism is assumed to be radiative rather than collisional quenching at our operating pressure, and homogeneous T_e is justified by the electron mean-free path at several cm being close to the chamber size. Under these conditions the emissivity at each radial position is given by

$$\varepsilon(r) = n_{\mathrm{Ar}}\, \xi(T_e)\, n_e(r), \tag{5.18}$$

with

$$\xi(T_e) = \sum_i \frac{\langle \sigma_i v \rangle_{T_e}}{\sum_k A_{ik}}\, A_{ij(\mathrm{vis})}\, h\nu_{ij}\, \eta_{\mathrm{cam}}(\nu_{ij}), \tag{5.19}$$

where A_{ij} are Einstein coefficients, $\langle \sigma_i v \rangle$ is the Maxwellian-averaged excitation rate coefficient, and η_{cam} is the camera spectral response. With T_e and n_{Ar} both spatially uniform,

the prefactor in Eq. (5.18) is independent of r, leading to the proportionality $\varepsilon(r) \propto n_e(r)$. Then, the relative density profile can be read off directly from the inverted emissivity as $h(r) = n_e(r)/n_e(0) = \varepsilon(r)/\varepsilon(0)$. A representative Abel inversion is shown in Fig. 5.9 (d). The recovered $\varepsilon(r)$ is approximately flat in the inner quarter and then decays smoothly along the radius. The density variation in the near-edge region, which includes the plasma sheath, cannot be captured reliably due to limitations of the imaging system.

Notably, effective electron temperature T_e in low-temperature, weakly-ionized plasmas depends primarily on the neutral density and chamber geometry, as shown in Eq. 3.25. Therefore, for a given argon pressure and Rydberg state, T_e has the same impact on the Rydberg spectrum to the leading order.

This analysis does not involve an absolute and direct measurement of the density, rather only the relative variation to be included in the EIT line shape analysis. In Eq. 5.15, $\tilde{\mathcal{P}}_H(\delta, n_e)$ is thus modified to $2\int_0^R \tilde{\mathcal{P}}_H(\delta, n_e(0)h(r))\, dr$. The peak central density $n_e(0)$ is treated as a free parameter constrained by the fit to the EIT line shape. For simplicity, plasma density, n_e, in the rest of the chapter refers to the peak density at the center, $n_e(0)$.

5.4.1.2 Collisional Broadening

The broadening added by plasma-induced collisions is treated as a homogeneous effect and empirically modeled by convolving $\tilde{I}(\Delta_c, n_e)$ with a Lorentzian broadening function, $\mathcal{P}_{\mathcal{L}}(\delta, \gamma) = 2\gamma/[\pi(4\delta^2 + \gamma^2)]$, in which γ is the FWHM arising from the collisional broadening. Consequently, the final fit function is given by the three-way convolution:

$$\tilde{\tilde{I}}(\Delta_c, n_e, \gamma) = \mathcal{P}_{\mathcal{L}}(\gamma) \otimes I_0(\Delta_c) \otimes \tilde{\mathcal{P}}_H(n_e) \quad . \tag{5.20}$$

We fit our experimental EIT lineshapes in the plasma using this comprehensive convolution model with the Levenberg-Marquardt algorithm [201]. The fit outcomes for the plasma density, n_e, and the collisional broadening, γ, are the main deliverables of the work in characterizing the plasma and the spectral broadening. Procedurally, we first obtain plasma EIT spectra dependent on three main parameters: Ar pressure, p, ranging from 5 mTorr to 50 mTorr, P_{rf} ranging from 0.25 W to 5 W, and principal quantum number, n, of the Rydberg $nS_{1/2}$ state, varied from $n = 25$ to 30. The Rydberg spectra corresponding to various rf powers at a given n and pressures are fit with the constraint of constant γ/n_e, since the collision cross-sections the rate constants depend on the Rydberg state and T_e, which itself depends on argon pressure via Eq. 3.25.

The line shape fits are performed within a window width of 60 MHz centered about the main EIT peak to exclude distortions from the hyperfine state $F' = 3$ of the intermediate

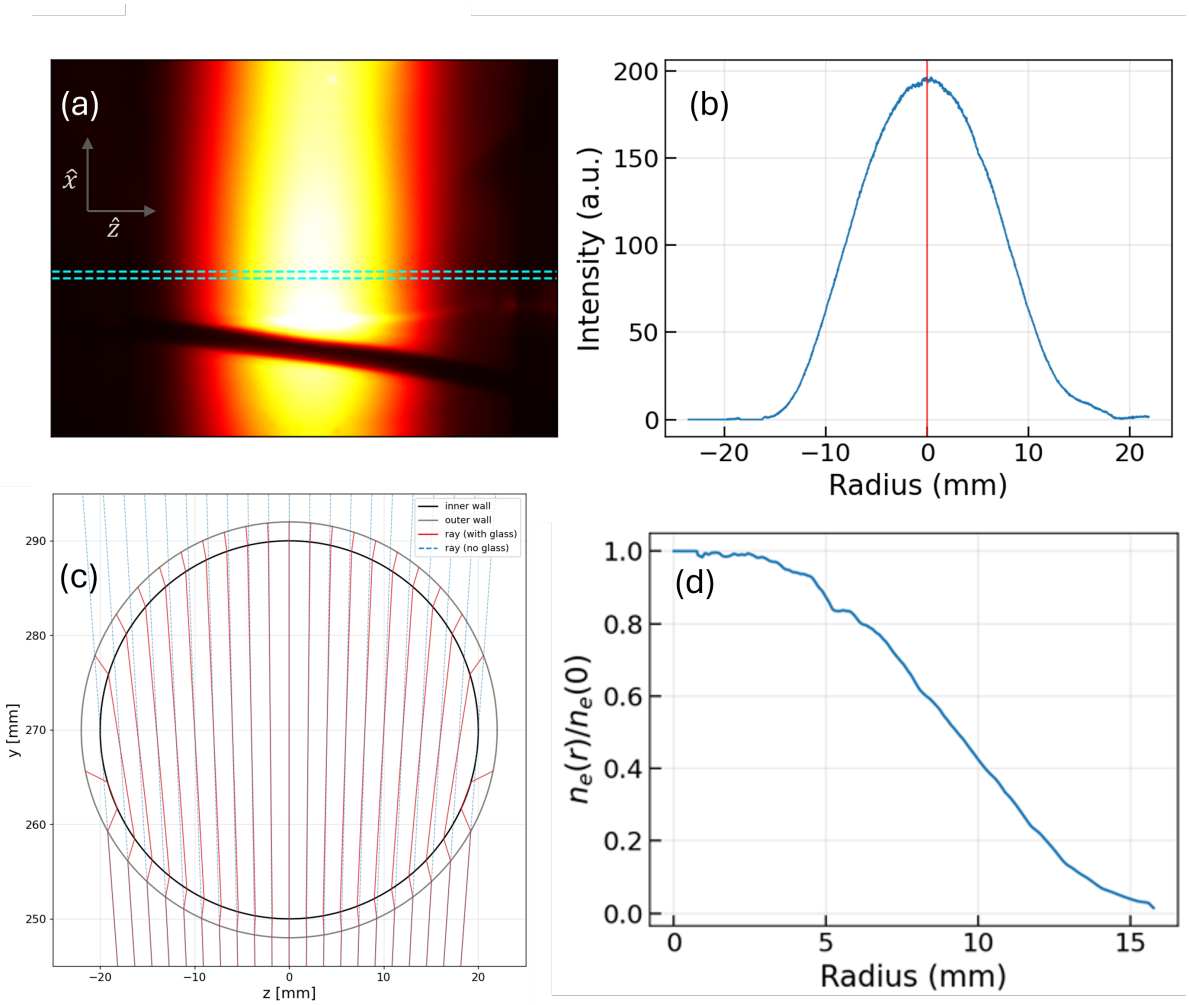


Figure 5.9: (a) A representative, background-subtracted plasma emission profile for argon pressure of 12 mTorr and 0.5 W applied rf power with EIT location marked in blue dotted line (Region of Interest). The turn of the helical coil nearest to the chamber is visible in the image, (b) Averaged intensity profile in RoI, (c) Ray tracing through the $y-z$ plane (transverse region) shows refraction effects 2 mm from the edge, (d) the recovered radial emissivity $\varepsilon(r) \propto n_e(r)$ following Abel inversion.

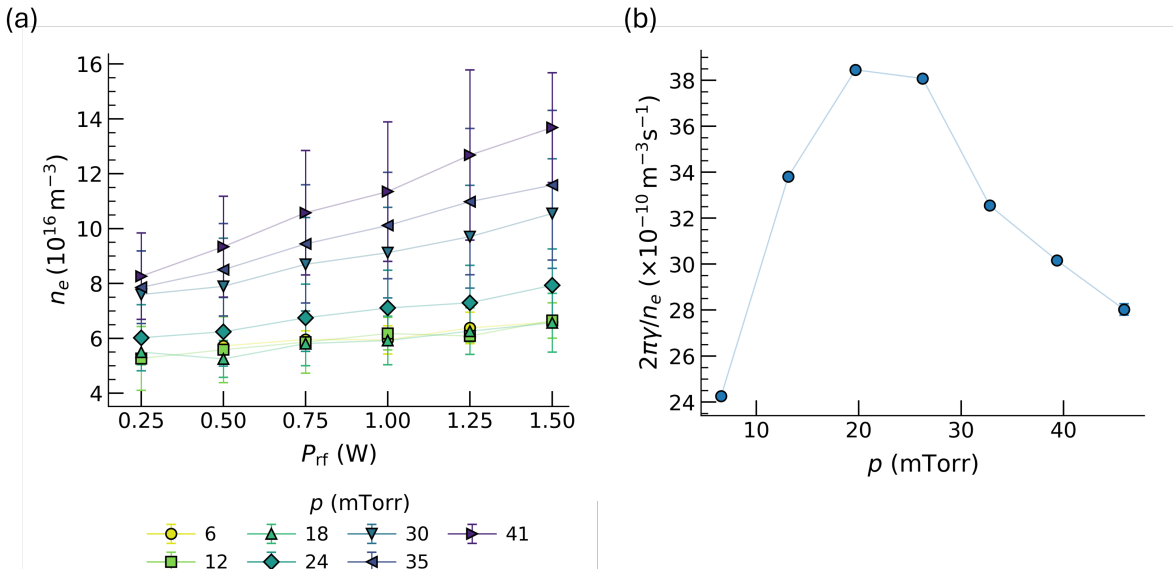


Figure 5.10: Plasma parameters extracted from Rydberg-EIT spectra for $25S_{1/2}$, obtained by fitting based on the the three-way convolution in Eq. (5.20), plotted vs P_{rf} with color-coded Ar pressure p. (a) Central plasma density n_e extracted from the Holtsmark part of the fits, assuming quasi-neutrality in the bulk ($n_e \approx n_i$). Over the n_e-range found, the most probable microfield ranges from 5.1 V/cm to 9.8 V/cm. At $p \gtrsim 25$ mTorr, the slopes $\Delta n_e/\Delta P_{\mathrm{rf}}$ undergo a significant increase. (b) Collisional broadening rate is estimated from $2\pi\gamma/n_e$. The decline in broadening rate in the Ohmic heating regime ($p \gtrsim 25$ mTorr) reflects the falling effective electron temperature T_e as pressure increases [202]. Error bars exceed statistical fit uncertainties and rather reflect confidence based on signal to noise ratio and drift in the underlying EIT spectra.

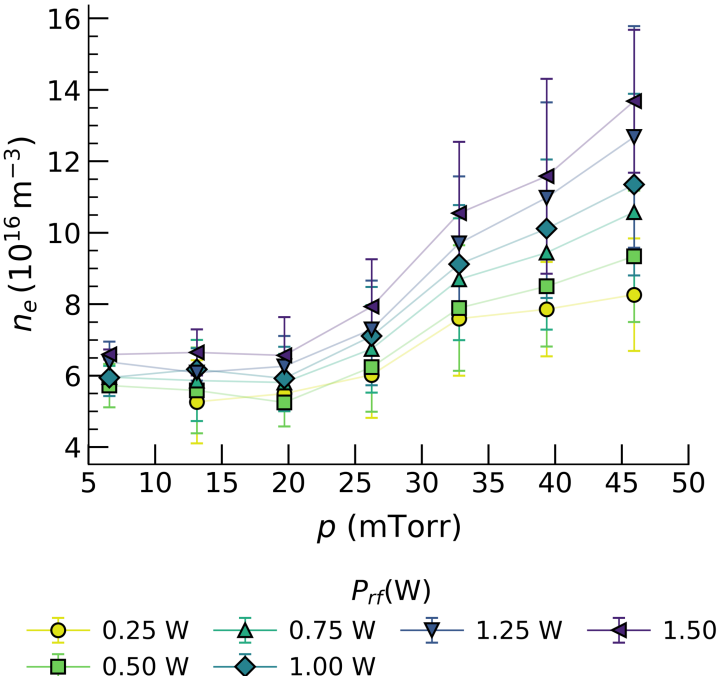


Figure 5.11: Electron density from Fig. 5.10, plotted vs Ar pressure with color-coded powers P_{rf}. The different-colored curves spread out for $p \gtrsim 25$ mTorr, reflecting the increase in $\Delta n_e/\Delta P_{\mathrm{rf}}$.

state $5P_{3/2}$, which appears approximately 75 MHz red-detuned from the central EIT resonance in Fig. 5.5 at zero P_{rf}. In our present work, the quantitative analysis is restricted to $P_{\mathrm{rf}} < 1.5$ W, as the line broadening becomes large at higher powers, which leads to increased fit uncertainties. The fit results for n_e and γ, obtained from EIT spectra for the selected case $n = 25$, are presented in Fig. 5.10.

As seen in Figs. 5.10 (a) and 5.11, the rate $\Delta n_e/\Delta P_{\mathrm{rf}}$ at which the plasma density n_e increases with P_{rf} exhibits a notable uptick at $p \sim 25$ mTorr. This behavior is generally consistent with the energy balance equation for rf plasma, $P_{\mathrm{abs}} \propto n_e$ [111]. We must caution that P_{abs}, the power absorbed into the plasma, is lower than P_{rf}, the measured power that is delivered into the drive coil [202, 203]. The latter, given by the difference between forward and reverse powers reported by the matching network, includes Ohmic losses and may not even be proportional to P_{abs}. The absorbed power P_{abs} is determined by the intrinsic plasma absorption efficiency, which depends on the plasma parameters. It has been established that power transfer efficiency at 13.56 MHz is maximal near a critical Ar pressure $p^* \approx 25$ mTorr, where the electron-neutral collision frequency becomes comparable to the rf drive frequency [111, 174]. Therefore, our observation that the plasma density n_e trends towards a faster and proportional scaling with power for $p \gtrsim p^* \approx 25$ mTorr likely results from the ICP entering

a regime of improved rf power delivery into the plasma [204].

Our plasma density results in Fig. 5.10 (a) and 5.11 are supported by probe-based measurements [187, 205–207], which have indicated plasma density values similar to our spectroscopic results under comparable pressure conditions. We note that comparisons across plasma experiments with different probing methods require a scaling of $P_{\rm rf}$ to plasma-chamber geometries and volumes as discussed in Chapter 3. Further, fit results from EIT spectra with $27S_{1/2}$ and $30S_{1/2}$, not shown, provide similar estimates for plasma density within the experimental uncertainties. The plasma densities from Figs. 5.10 (a) and 5.11 further yield skin depths ~ 2 cm, consistent with our observation in Fig. 5.7 that the rf field is largely screened from the bulk plasma volume.

We next focus on collisional broadening of EIT lines in the ICP. Fig. 5.10 (b) shows that our fit results for γ exhibit an increasing trend in $P_{\rm rf}$. The results for γ are in the range $\gamma \lesssim 20$ MHz and therefore below the Holtsmark Stark broadening, which ranges $\lesssim 100$ MHz in our work. As the EIT linewidth in the neutral Ar background gas is already accounted for in the field-free line shape $I_0(\Delta_c)$ in Eq. 5.20, the broadening γ in Fig. 5.10 (b) arises from plasma collisions, which include Rydberg-atom collisions with electrons, Ar^+, and metastable Ar^*. Based on previous treatments of $\ell-$mixing [208] and ionizing collisions of Rydberg atoms [97, 209], we assume electron-induced $\ell-$mixing to be dominant due to the n^5-scaling of its cross section, followed by inelastic electron scattering, which has cross sections $\propto n^4$ (with principal quantum number n). Lesser effects are expected from Ar^+ and metastable Ar^* due to lower collision velocities. Quantitatively, our estimates based on [45, 97] yield collisional linewidths in the range of 15 MHz for our plasma conditions, which is quite in line with the results in Fig. 5.10 (b). Further, in data not shown, fit results for γ were seen to rapidly increase with n, as expected from the n^5 and n^4 scalings of Rydberg-atom ℓ-mixing and inelastic collision cross sections. The predominant role of ℓ-mixing in collisional Rydberg system has also been noted in ZEKE spectroscopy [210] and cold Rydberg atom experiments [211, 212].

We finally ascertain that EIT spectroscopy of Rb Rydberg atoms in an Ar ICP is not affected by plasma emission lines from excited Ar species. To prove this, we perform optical emission spectroscopy with an Ocean Optics USB4000 spectrometer in parallel with EIT spectroscopy. The relevant spectral portion of the Ar ICP emission spectrum contains several strong emission lines, as shown in Fig. 5.12, but the peak at ≈ 780 nm is solely attributed to the fluorescence of Rb atoms from the resonant EIT probe laser. The 780-nm Rb EIT probe peak is well-separated from plasma emission lines and vanishes in the absence of Rb vapor or EIT probe light.

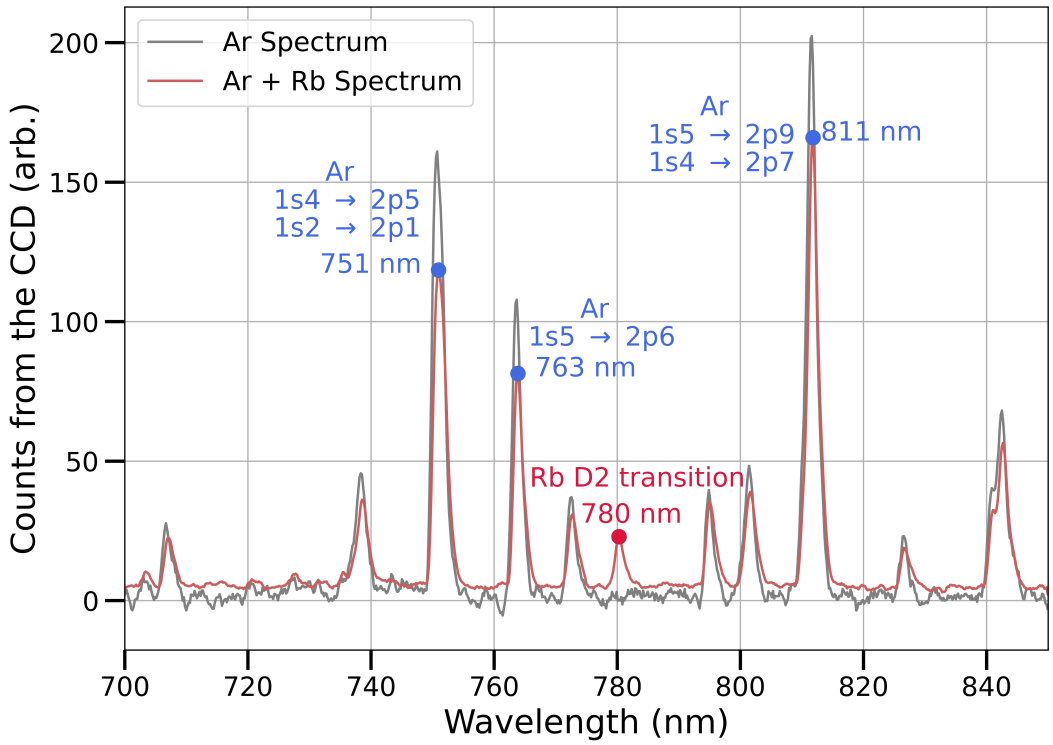


Figure 5.12: Optical emission spectrum of the Ar discharge with and without Rb present. The D_2 line of Rb at 780 nm is well isolated from the Ar transitions, the strongest of which are labeled (Paschen notation). The Rb emission arises from the fluorescence of Rb vapor in the EIT probe laser.

5.5 Conclusion

We have demonstrated Rydberg-EIT for electric-field diagnostics in low-temperature, low-pressure ICP discharges. The approach leverages the high electric polarizability of Rydberg states, which scales as n^7 and is conducive to high electric-field sensitivity. We have measured plasma microfields $\lesssim 10$ V/cm in a continuous ICP, generated in a few mTorr of Ar, over a range of plasma rf drive powers and Ar pressures, and we have observed efficient rf screening from the bulk of the plasma due to the skin effect. From our work, spectroscopic Rydberg-EIT-based plasma electric-field sensing emerges as a viable non-invasive method to assess Holtsmark microfields in continuous low-pressure ICP. In future work, electric-field sensitivity may be enhanced by using higher-n Rydberg states. The method may be translated to capacitively coupled rf or dc plasmas, with possible work on spatio-temporal electric-field measurement in plasma sheaths or near dust particles in plasma. In other applications, one may explore the measurement of rf waves in the HF radio band by leveraging the atoms' near-field response to both electric and magnetic fields inside rf load coils.

In summary, the work presented in this Chapter has used the internal states of atoms, specifically the Rydberg levels of rubidium, to measure electric fields in conditions where conventional probes are not suitable. The remainder of this dissertation turns to the second sensing modality outlined in Chapter 1 *i.e.*, the use of atomic center-of-mass wave function, rather than internal states, as the sensing resource. In this regime, the relevant degree of freedom is the atomic wave function itself instead of the electronic or spin state, and the observables of interest are inertial forces such as acceleration and rotation. The next chapter describes a proposed atom interferometer and its operation in this spirit, in which atoms are trapped uninterruptedly in 3D and coherently transported using optical lattices for inertial sensing.

CHAPTER 6

Tractor Atom Interferometry

This chapter is based on Refs. [213, 214].

In contrast to the previous chapter focused on measurement of electromagnetic fields, the observables in this chapter are inertial forces determined by acceleration and rotation. Internal-state sensing of the kind developed in the preceding chapters is well-suited to electromagnetic fields and operates naturally at the MHz–GHz scales set by atomic transitions and Stark and Zeeman shifts. Inertial sensing instead exploits the wave nature of the atom itself in Atom Interferometers (AI). As the matter-wave analog of optical interferometry, when an atom is placed in a superposition of two trajectories and later recombined, the accumulated phase difference encodes the forces acting on the atomic mass along the paths *e.g.*, gravity, linear acceleration, and rotation. In this modality, the center-of-mass (COM) wave function becomes the sensing resource, which is suited for operation at the Hz–kHz scales set by interrogation times and trap dynamics.

While varying in the sensing objectives, the core principle of atom-based sensing is shared across these designs. In both designs, atomic structure supplies absolute references, such as transition frequencies and the phase of COM wavefunction, against which the observable-induced shifts can be measured. Both rely on the preparation and readout of coherent superpositions, whether between ground and Rydberg states or between counter-propagating motional states. Atomic sensors of both modalities confront similar practical limits such as decoherence from environmental noise and lasers as well as the trade-off between sensitivity and bandwidth, though these manifestations differ in detail.

Recent progress in atom interferometers (AI) has raised promising prospects in fundamental physics [63–67], precision measurements [68–71] and practical applications [72] including geodesy, seismology and inertial sensing with atomic acceleration and rotation sensors. Traditionally, AIs have been limited by the requirement of large geometric footprint and power consumption needs, and there is growing interest in developing compact designs. This chapter presents the proposed architecture of a quantum rotation sensor based on tractor atom

interferometry (TAI), in which spin-dependent optical lattices coherently transport atomic wave packets along closed counter-rotating trajectories while maintaining three-dimensional confinement throughout.

This chapter is organized as follows. A "pinwheel" optical lattice to trap and transport the atomic wavefunction are outlined in Sec. 6.2. Aspects of the interferometer operation and its matter-wave dynamics are explained in Sec. 6.3. Numerical quantum-dynamics simulations, sensitivity estimates and the adiabatic limit of the wavepacket transport are presented in Sec. 6.4. In Sec. 6.5, possible nonadiabatic excitations during operation of the TAI interferometer are discussed quantitatively. Results that incorporate the application of optimal control theory to minimize detrimental nonadiabatic effects are presented in Sec. 6.5.1. The chapter is concluded with the consideration of technical issues relevant to possible experimental implementations of TAI.

6.1 Introduction and Motivation

The principle of interferometric measurement of rotation relies on the Sagnac phase $\phi_s = 2EA/hc^2$ arising between wave packets of energy E that are counter-rotating around an area A. Since their first demonstration in 1913 [215], optical Sagnac interferometers have achieved sensitivities beyond $10^{-10}\,\mathrm{rad/s}$ in fiber-optic gyroscopes (FOGs) and large-area pinwheel laser-based setups. The motivation to design Sagnac atom interferometers stems from the potential orders-of-magnitude enhancement in sensitivity that scales inversely with the associated de Broglie wavelength [62].

Previous experiments and proposals for the realization of Sagnac AIs include free-space [216–219] and point-source interferometers [220–222], where atomic fountains or dropped atomic clouds propagate freely along interfering paths, as well as guided-wave AIs [223–226]. Despite their much smaller particle flux and interferometric areas, these designs have recently surpassed the sensitivity of FOGs. However, free-space AIs can be space- and power-intensive, as their sensitivity scales as the interrogation time squared [62], fueling a push to increasing drop heights and apparatus sizes in earth-based experiments. In order to achieve higher sensitivity combined with compact setups, multi-pass guided-wave designs have been proposed based on trapped ions [227], weak magnetic traps [223, 228, 229], time-averaged adiabatic potentials [230–233], toroidal optical traps [234] and optical waveguide formed by collimated laser beams [226].

The performance of free-space and atom-guide AIs is often limited by the dispersion of the atomic wave functions along unconfined degrees of freedom, inefficient closure of interferometric paths, and Landau-Zener tunneling in spinor implementations [235–237]. Tractor atom interferometry (TAI) [238], a recently proposed technique, seeks to address these is-

sues by uninterrupted three-dimensional confinement and transport of atomic wave packets along programmable trajectories using optical or other traps. Robust AI implementations for acceleration sensing using deep, spin-dependent optical potentials and optical tweezers have been explored in recent proposals and experiments [214, 238–240].

6.2 Pinwheel optical lattice design

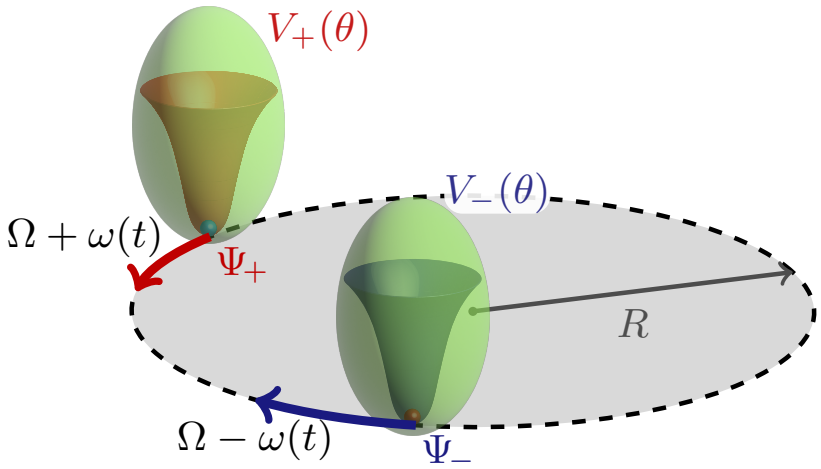


Figure 6.1: Concept of TAI as a Sagnac rotation sensor. Counter-rotating trapping potentials $V_+(\theta)$ and $V_-(\theta)$ provide uninterrupted three-dimensional (3D) confinement for the wave packet components $\Psi_\pm(\theta)$, represented here as well-localized dots. They are dragged by the respective tractor potentials, visualized with transparent green bubbles, along counter-wound circular trajectories of radius R in the instrument's rest frame at tunable angular velocities $\pm\omega(t)$. This occurs in the presence of a background angular velocity Ω of the instrument's rest frame against an inertial frame, in which the rotation speeds are $\Omega \pm \omega(t)$. The value of Ω is to be measured.

As depicted in Fig. 6.1, the principles of spinor-TAI [238] can be leveraged for rotation sensing by designing circular trajectories along which spin-dependent potentials carry trapped atomic wave-function components in opposite directions. The potentials must be designed to strongly confine the trapped wave functions in all spatial dimensions to minimize nonadiabatic effects and dispersion. The trajectory pairs are closed and cover a half- or full-integer number of loops in each trajectory. This can be realized by a pair of deep, spin-dependent, counter-rotating "pinwheel" optical lattices. Such lattices can be created using co-propagating Laguerre-Gaussian (LG) beams [241, 242], interference of Gaussian and hollow beams with a quadrupole magnetic moment [243], or interference of LG beams with plane waves in the presence of a conical magnetic field [244] for twisted boundary

conditions. Here we focus on the first approach, which is an all-optical technique suitable to create both bright (red-detuned) and dark (blue-detuned) lattices with several widely tunable parameters.

The electric field of an LG beam with azimuthal index l, zero radial index, frequency f_l and wave vector k_l propagating along the positive z-direction is given in phasor notation and cylindrical coordinates $\mathbf{r} \equiv (r, \theta, z)$ as

$$LG_l(\mathbf{r}, t) = \frac{\mathcal{E}_l(r, z)}{\sqrt{c\epsilon_0}}\, e^{\,i\left[2\pi f_l t + \varphi_l(z) + l\theta - k_l\left(z + \frac{r^2}{2R(z)}\right)\right]}\,, \tag{6.1}$$

where c and ϵ_0 are the speed of light and vacuum permittivity, respectively, and with the amplitude

$$\mathcal{E}_l(r, z) = \sqrt{\frac{4P}{\pi|l|!w(z)^2}}\left(\frac{\sqrt{2}r}{w(z)}\right)^{|l|} e^{-\frac{r^2}{w(z)^2}}\,. \tag{6.2}$$

P is the laser beam power and $w(z) = w_0\sqrt{1 + (z/z_R)^2}$ is the beam-waist parameter with the Rayleigh range $z_R = \pi w_0^2/\lambda$. The radius of the phase front's curvature is $R(z) = z\,(1 + (z_R/z)^2)$, and $\varphi_l(z) = (|l| + 1)\arctan(z/z_R)$ is the Gouy phase. Along the z-axis, the LG beam has an optical vortex line featuring a phase singularity and vanishing intensity. Due to the azimuthal (θ) phase dependence, the interference of two co-propagating LG beams with modes l_1 and $l_2 = l_1 + m$ and frequency f_1 and $f_2 = f_1 - \Delta f$ results in an intensity distribution

$$\begin{aligned}|\mathcal{E}|^2(\mathbf{r}, t) = {}& \mathcal{E}_{l_1}^2(r, z) + \mathcal{E}_{l_2}^2(r, z) + 2\mathcal{E}_{l_1}(r, z)\mathcal{E}_{l_2}(r, z) \\ & \cos\left[2\pi(\Delta f)t - \Delta\varphi(z) - \frac{2\pi(\Delta f)z}{c} - \frac{\pi r^2}{c}\left(\frac{f_1}{R_1(z)} - \frac{f_2}{R_2(z)}\right) - m\theta\right]\,.\end{aligned} \tag{6.3}$$

The salient feature of this interference pattern is the sinusoidal modulation of intensity in the azimuthal (θ) direction, in the very last term. In experimentally relevant cases, *e.g.*, for a pinwheel optical lattice of radius $10 - 100\,\mu\text{m}$ rotating at $10 - 1000\,\text{Hz}$, the terms proportional to $\Delta f/c$ and r^2/c inside the cosine are negligible. The difference in Gouy phase, $\Delta\varphi(z) = m\arctan(z/z_R)$, in principle twists the pinwheel azimuthally as a function of z. However, as described in the following, the atoms are further trapped along the z direction by a separate, far off-resonant one-dimensional static optical lattice with lattice planes extending transverse to z. The twisting angle due to the variation of $\Delta\varphi(z)$ within one spatial period of the static z-lattice is typically less than 1 mrad and is therefore negligible. With these approximations, the optical potential near $z = 0$ reads

$$V(\mathbf{r}, t) \approx V_1(r) + V_2(r)\cos\left[2\pi(\Delta f)t - m\theta\right]\,, \tag{6.4}$$

with $V_1(r) = -\frac{\alpha}{2c\epsilon_0}\left(\mathcal{E}_{l_1}^2(r,0) + \mathcal{E}_{l_2}^2(r,0)\right)$ and $V_2(r) = -\frac{\alpha}{c\epsilon_0}\mathcal{E}_{l_1}(r,0)\mathcal{E}_{l_2}(r,0)$, where α is the polarizability of the selected atomic state. Therefore, a pair of LG beams with a small detuning of Δf and with l-indices differing by m effectively create a pinwheel optical lattice with m azimuthal lattice sites, rotating at a tunable angular velocity $\omega = 2\pi\Delta f/m$.

A counter-rotating pinwheel lattice of similar size can be obtained from a second pair of LG beams with opposite detuning that are superimposed over the first pair. The pinwheel lattices can be made spin-selective by tuning the wavelengths of the beam pairs forming the lattice so that they trap different atomic spin states. A particular example of such spin states are the $\left|5S_{1/2}, F = 1, m_F = 0\right\rangle$ and $\left|5S_{1/2}, F = 2, m_F = 0\right\rangle$ states of ^{87}Rb, with the wavelengths of the respective pinwheel lattices set near the D_1 line ($\approx 795\,\text{nm}$) [214]. We discuss several technical details of such spin-dependent lattices in Ref. [214].

Trapping in such lattices requires blue-detuned light, where the atoms are trapped near intensity minima. In that case, the photon scattering rate of the atoms in the lattice light is minimal, thereby minimizing both photon-scattering-induced decoherence of the interferometer as well as decoherence caused by trap-laser intensity fluctuations. The beam parameters for LG_{l_1} and LG_{l_2}-modes in Eq. (6.4) must be chosen carefully to create a sufficiently deep and tightly confined radial potential in order to suppress wave-function dynamics in the radial direction. At the same time, this potential must go through a zero-intensity minimum to trap atoms with minimal coherence loss due to photon scattering. This can be achieved when both LG beams have similar maximum intensity, with the radial intensity maxima separated by more than one FWHM of the radial intensity distributions. For a Gaussian beam waist ratio $\eta = w_{0,2}/w_{0,1}$ and a power ratio $P_2/P_1 = \eta^2\sqrt{l_2/l_1}$, the radial intensity maxima are similar and separated by $\Delta r \approx w_{0,1}\left(\eta\sqrt{l_1} - \sqrt{l_2}\right)/\sqrt{2}$ near the focus. Since the FWHM of LG_{l_i} is on the order of $w_{0,i}$, for a given l_1 and l_2, the waist ratio η should be chosen such that $\Delta r \gtrsim (1+\eta)w_{0,1}$. The number of desired azimuthal wells in the pinwheel lattice, m, has an implicit effect on the best choice for η because $m = |l_2 - l_1|$. We have found that $\eta \sim 1.3 - 1.8$ works for most l_1 and $l_2 < 50$.

For the example of ^{87}Rb, Fig. ??(a) demonstrates the superposition of two 795 nm laser beams with modes LG_{20} and LG_{28}. In this case, $\eta = 1.67$ leads to an ideal pinwheel optical lattice with 8 sites, as shown in the optical potential in the transverse plane in Fig. ??(b). The trapping potential is about 4.4 MHz deep and perfectly sinusoidal along the azimuthal direction, acting as a lattice with periodic boundary conditions. Ultracold ^{87}Rb atoms can be trapped in these potential minima with minimal photon scattering [214]. As described below, this potential is sufficiently deep to prevent wave-function dispersion or tunneling between the lattice sites. Along the radial direction, the potential is about 274 MHz deep, and the radial trap frequency $\omega_r = 29 \times 10^3 \times \pi/\text{s}$, which approximately equals 5 times the

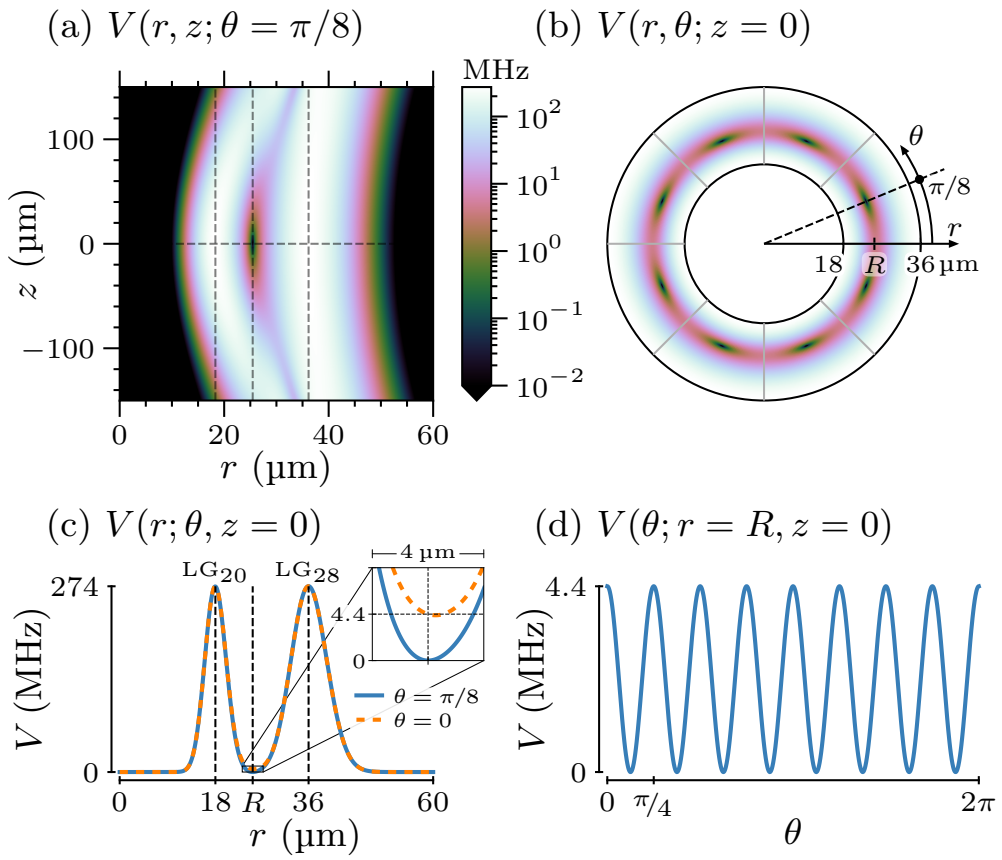


Figure 6.2: An 8-site pinwheel ^{87}Rb optical lattice is created from LG_{20} and LG_{28} laser modes with $\lambda = 795\,\text{nm}$ and respective Gaussian waists of $w_{0,1} = 5.78\,\mu\text{m}$ and $w_{0,2} = 9.66\,\mu\text{m}$, and powers of $P_1 = 5.38\,\text{mW}$ and $P_2 = 17.78\,\text{mW}$. The beams are assumed to be blue-detuned for an AC polarizability of $-0.16\,\text{Hz}/(\text{V/m})^2$. (a) Optical potential in the $r - z$ plane. (b) Optical potential in the transverse plane at the focus $z = 0$. (c) Potential along the radial direction for $z = 0$ and $\theta = 0$ and $\pi/8$. (d) Potential along the azimuthal direction at $R = 25.46\,\mu\text{m}$ and $z = 0$.

azimuthal trap frequency, $\omega_r \approx 5\omega_\theta$. This suffices to freeze out radial dynamics.

Next, we discuss TAI confinement in the axial (z) direction. Other experiments [243, 244] on ring-like traps have reported axial confinement using lattices created by counter-propagating laser modes. In the case of rotating pinwheel lattice, superposition of detuned counter-propagating LG beams can lead to unwanted axial movement. Therefore, we here suggest co-propagating LG beam pairs to form the pinwheel lattice, and to use a separate, far off-resonant one-dimensional optical lattice along the z-direction using counter-propagating Gaussian beams of a sufficiently large beam waist. This allows robust, all-optical axial confinement of the atoms on the pinwheel. For example, a 300 kHz-deep optical lattice can be created by counter-propagating ≈1 W 532 nm-wavelength Gaussian beams, focused to a

waist of 100 µm. This will generate an axial stack of many pinwheel lattices spaced by an axial lattice period of 266 nm. The structure of the pinwheel lattices, as shown in Fig. ??(b)-(d), remains largely constant over an axial range of about 5 µm from the focus, suggesting that several tens of near-identical pinwheel lattices with tight 3D confinement can be stacked.

With the radial and axial degrees of freedom being essentially frozen, the pinwheel optical lattices can be approximated as 1D lattices with periodic boundary conditions. Assuming that there is no linear background acceleration, the Hamiltonian of the system in a suitable inertial frame can be written as

$$H_{\pm}(\theta, t) = -\frac{\hbar^2}{2I}\frac{\partial^2}{\partial\theta^2} + V_0 \cos\Big[m(\theta + \phi_{\pm}(t))\Big] \,. \tag{6.5}$$

This expression is in the coordinate representation, and the labels "+" and "−" refer to the two atomic spin states (which are rotated in opposite directions). The kinetic term contains the effective moment of inertia $I = m_{\mathrm{Rb}} R^2$ of a ^{87}Rb atom (atomic mass m_{Rb}) rotating on a pinwheel of radius R. The radius R is defined as the center of mass of the tightly-confined radial wave function. The cosine potential with m sites moves with phases

$$\phi_{\pm}(t) = \int_0^t \omega_{\pm}(t')\, dt' = \int_0^t \left(\Omega \pm \omega(t')\right)\, dt' \,. \tag{6.6}$$

The angular velocities at which the pinwheel lattices counter-rotate in the instrument's rest frame ("lab frame"), $\omega_{\pm}$, and the corresponding phases, $\phi_{\pm}$, are controlled via the tunable angular-velocity control function $\omega(t)$. The goal of the present TAI scheme is to measure the constant rotation rate Ω of the instrument's rest frame against the inertial frame.

The Hamiltonian in Eq. (6.5) includes the effect of the Euler force, while other non-inertial forces like centrifugal and Coriolis force can be neglected in this scheme. During interferometer operation, the lattices are rotated much slower ($\omega_{\pm} \lesssim 10^2\,\pi/\mathrm{s}$) than the radial trap frequency ($\omega_r \sim 10^4\,\pi/\mathrm{s}$). In this regime, the relative displacement due to the centrifugal force, $\Delta R/R \simeq (\omega_{\pm}/\omega_r)^2$, is negligible, and the lattice radius R can be assumed to be constant throughout. As shown in Sec. 6.4, in the desired adiabatic regime the wave packets are at rest in frames that co-rotate with the pinwheel lattices, and therefore do not experience any Coriolis effect.

6.3 Operation

The interferometer is initialized by co-aligning the axes and azimuthal minima of the spin-dependent pinwheel lattices for the pair of utilized spin states. The internal spin states could

correspond, *e.g.*, to the $|+\rangle = \left|5S_{1/2}, F = 1, m_F = 0\right\rangle$ and $|-\rangle = \left|5S_{1/2}, F = 2, m_F = 0\right\rangle$ states in the ground-state manifold of ^{87}Rb. At $t = 0$, the wave function is prepared in the local ground state $\Psi_0(\theta)$ of one particular site in the "+"-lattice, that is, $|\Psi(\theta, t = 0)\rangle = \Psi_0(\theta)\,|+\rangle$. The shape and the width of the eigenstate depend on the radius implicit in the effective moment of inertia I, the number of lattice sites, m, and the V_0 of the trapping potential. For a given m and a sufficiently deep potential (large V_0), the wave packet $\Psi_0(\theta)$ will be close to the eigenstate of a quantum harmonic oscillator with frequency

$$\omega_\theta = m\sqrt{V_0/I}\,, \tag{6.7}$$

obtained by a Taylor expansion of the potential in Eq. (6.5) at the first site. In the remainder of the paper, we will consider optical lattices with a radius of $R = 25.46\,\mu\text{m}$ and $m = 8$ lattice sites, which corresponds to a lattice period of $10\,\mu\text{m}$ in the azimuthal direction. Without loss of generality, we choose lattice phases such that the initial wave packet is centered at $\theta_0 = \pi/8$ at the first site.

Driving a momentum-transfer-free optical Raman transition at a suitable Rabi frequency $\Omega_\pm$, we implement a $\pi/2$-pulse,

$$\hat{\mathsf{U}}_{\pi/2} = \frac{1}{\sqrt{2}}\begin{pmatrix} 1 & i \\ i & 1 \end{pmatrix}\,, \tag{6.8}$$

between the two spin components. This acts as a beam-splitter and creates an equal superposition of the two spin states. Thus, the wave packets in the two spin-dependent potentials immediately after the $\pi/2$-pulse are

$$\Psi_+(\theta, 0) = \frac{1}{\sqrt{2}}\Psi_0(\theta)\,, \quad \Psi_-(\theta, 0) = \frac{i}{\sqrt{2}}\Psi_0(\theta)\,. \tag{6.9}$$

The duration of the $\pi/2$-pulse typically is negligible compared to the overall duration of the interferometer sequence. An experimentally suitable choice for the duration of the $\pi/2$-pulse could be, for instance, $1.4\,\mu\text{s}$, corresponding to a Rabi frequency of $\Omega_\pm = \pm 2\pi \times 178\,\text{kHz}$.

After splitting, the two wave packets $\Psi_\pm(\theta, t)$ evolve independently (*i.e.*, without spin coupling) under the Hamiltonian in Eq. (6.5) with counter-rotating time-dependent angular velocities $\pm\omega(t)$. For the time being, we assume that $\omega(t)$ varies sufficiently slowly for the wave packet evolution to be adiabatic, *i.e.*, the $\Psi_\pm(\theta, t)$ remain in the ground state of the local lattice site potential at all times. For the azimuthal ramp of the pinwheel lattices, here we first choose the smoothly varying function

$$\omega(t) = \begin{cases} \omega_0 \sin^2\left(\dfrac{\pi t}{2t_r}\right) & 0 \le t < t_r \quad (6.10a) \\ \omega_0 & t_r \le t < t_r + t_{\text{loop}} \quad (6.10b) \\ \omega_0 \cos^2\left(\dfrac{\pi t'}{2t_r}\right) & T - t_r \le t \le T \ , \quad (6.10c) \end{cases}$$

with $t' = t - t_r - t_{\text{loop}}$ and the total duration $T = 2t_r + t_{\text{loop}}$.

During the ramp-up time t_r, the angular speeds of the lattice potentials in the instrument frame are accelerated from $\pm\omega(0) = 0$ to $\pm\omega(t_r) = \pm\omega_0$, and subsequently remain constant for a duration of t_{loop}. We first assume that t_r is sufficiently large to result in adiabatic dynamics. After the loop time t_{loop}, the lattices are decelerated from $\pm\omega_0$ to $\omega(T) = 0$ by running the ramp-up control backwards. At final time T, the two lattice potentials and, thus, the final wave packets must coincide (both in the instrument frame (lab frame) and in the lattice rest frames). This is achieved by adjusting t_{loop} such that

$$\int_0^T \omega(t)\, dt = n\,\pi \tag{6.11}$$

for an interferometer with n "cycles". The effective area of the TAI then equals $n \times \pi R^2$.

Some exemplary dynamics for adiabatic evolution under Eq. (6.10) are shown in Fig. 6.3. The interferometer has $n = 10$ cycles, as can be seen in panel (a). The expectation value of the momentum, seen in panel (b), follows exactly the movement of the potential, controlled by $\omega(t)$. In the moving frames, defined here as the rest frames of the rotating pinwheel lattices, the wave packets remain perfectly stationary, see panels (c, d).

The interferometric scheme is completed at final time T by an inverse $\pi/2$-pulse, denoted $\hat{\mathsf{U}}^\dagger_{\pi/2}$, see Eq. (6.8), to recombine the two spin-dependent components. For a non-zero constant background rotation Ω in Eq. (6.6), the wave packets $\Psi_+(\theta, T)$ and $\Psi_-(\theta, T)$ accumulate a differential phase $\Delta\Phi$ that is reflected in the recombined state

$$\hat{\mathsf{U}}^\dagger_{\pi/2}\,|\Psi(T)\rangle = c_+(\theta, T)\,|+\rangle + c_-(\theta, T)\,|-\rangle \tag{6.12}$$

with the populations

$$|c_\pm|^2 = \frac{1}{2} \pm \frac{1}{2}\mathrm{Re}\left[\eta e^{-i\Delta\Phi}\right] \tag{6.13}$$

and the overlap of the final-time wave packet components

$$\eta = \langle \Psi_-(\theta, T) | \Psi_+(\theta, T) \rangle\,. \tag{6.14}$$

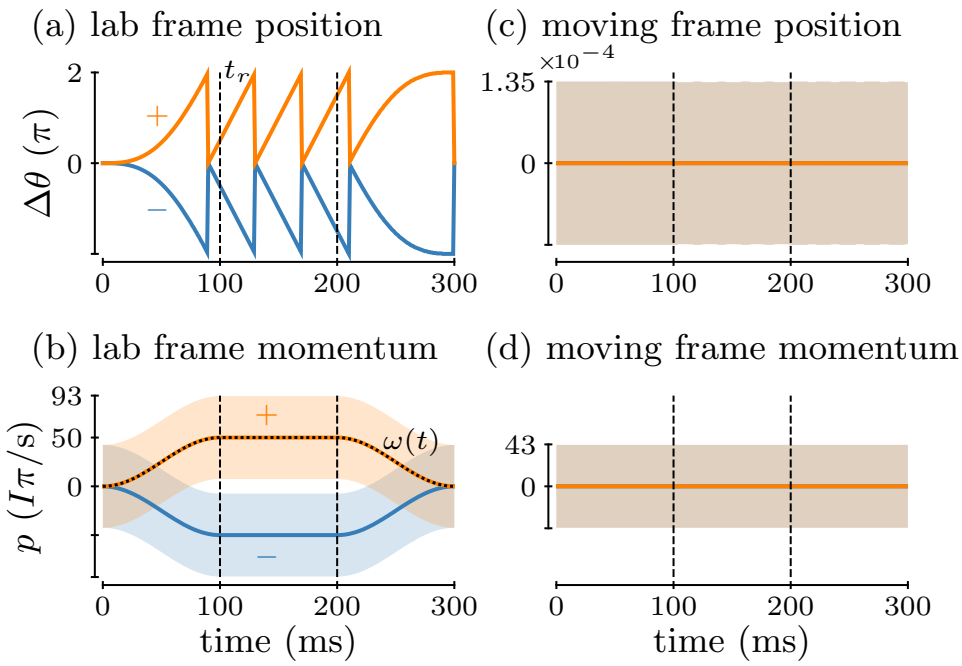


Figure 6.3: Adiabatic wave-function evolution in a rotating pinwheel optical lattice using $\omega(t)$ from Eq. (6.10) with $V_0 = h \times 4.4\,\mathrm{MHz}$, $t_r = t_{\mathrm{loop}} = 100\,\mathrm{ms}$, $\omega_0 = 50\,\pi/\mathrm{s}$, and $\Omega = 0$. (a) Expectation value of the azimuthal displacement of the wave packets relative to the initial position $\theta_0 = \pi/8$ of the ground state of the selected pinwheel-lattice well, $\Delta\theta \equiv \langle\theta\rangle - \theta_0$, as measured in the instrument's rest frame ("lab frame") for both counter-rotating states $\Psi_+(t)$ and $\Psi_-(t)$. The lattice has $R = 25.46\,\mu\mathrm{m}$ and $m = 8$ lattice sites. (b) Momentum expectation value in the lab frame, in units of effective moment of inertia $I = m_{\mathrm{Rb}}R^2$ of a ^{87}Rb atom rotating at $1\,\pi/\mathrm{s}$. The control function for the angular velocity of the pinwheel-lattices, $\omega(t)$, is shown as the dotted black curve. (c) Azimuthal-angle expectation value of the wave packet components in the lattices' moving frames,*i.e.*, the frames in which the lattices are stationary. (d) Angular-momentum expectation value in the moving frame, *i.e.*, average angular momentum relative to $\pm I\omega(t)$. The shaded regions in panels (b–d) indicate the standard deviations of the respective wave-function densities, that is, the widths of the wave packets.

For a closed interferometric path and adiabatic time evolution, $\Psi_-(\theta, T) = \Psi_+(\theta, T) = \Psi_0(\theta)$, and thus $\eta = 1$. In this case, Eq. (6.13) simplifies to

$$|c_-|^2 = \frac{1}{2} - \frac{\cos \Delta\Phi}{2} = \sin^2\left(\frac{\Delta\Phi}{2}\right) , \tag{6.15a}$$

$$|c_+|^2 = 1 - |c_-|^2 = \cos^2\left(\frac{\Delta\Phi}{2}\right) . \tag{6.15b}$$

Up to an offset of an integer multiple of π, the value of $\Delta\Phi$ can be derived from a measurement of the population in at least one of the two spin states.

6.4 Numerical Simulation

6.4.1 Quantum methods

The Crank-Nicolson (CN) method [229, 245, 246] has commonly been employed for simulations of wave packet dynamics in the position representation, including cases with moving potentials [238]. The method requires a computationally expensive ($\mathcal{O}(N_x^3)$) matrix inversion. In practice, for systems with 1D scalar potentials and non-PBC, this is usually reduced to $\mathcal{O}(N_x)$ due to the tridiagonal structure of the Hamiltonian in position space. In the context of the azimuthal optical lattice, periodic boundary conditions introduce additional corner entries in the Hamiltonian matrix, necessitating a generalized Crout reduction, as explained in Appendix A.

Here, we use CN simulations to study a TAI in a pinwheel optical lattice as a function of Ω. The results of CN simulations performed in the inertial frame according to the Hamiltonian in Eq. (3) are shown in Fig. **??** (a) as the points labeled "CN", with the parameters listed in the figure caption. A time-step $\Delta t = 50\,\text{ns}$ and 3200 spatial grid points for the full range of $\theta \in [0, 2\pi]$ have been used. From the simulations, we verify that for parameters as in Fig. **??**, a $h\times 4.4\,\text{MHz}$ deep pinwheel lattice effectively prevents any tunneling between the lattice sites. Consequently, the wave packet dynamics in the co-rotating frames of reference is confined within one lattice site, or equivalently within a θ-range of only $2\pi/m$ in width. Exploiting the localization of the wave packet components in their respective lattices, in the present case the spatial grid can be reduced in width by a factor of $m = 8$ to the region $[0, \pi/4]$ of a single lattice site by applying the transformation

$$\begin{aligned}\hat{U}_{\pm}(t) &= \exp\left(\frac{-i\hat{L}_z\phi_{\pm}(t)}{\hbar}\right) \\ &\equiv \exp\left(-\int_0^t \omega_{\pm}(t')\,dt'\,\frac{\partial}{\partial\theta}\right)\end{aligned} \tag{6.16}$$

into the lattices' rest frames, in which θ is relative to the moving lattice potentials. Applying the transformation in Eq. 6.16 on the Hamiltonian in Eq. (6.5), one finds the Hamiltonian in the lattice rest frames,

$$\tilde{H}_{\pm}(t) = -\frac{\hbar^2}{2I}\frac{\partial^2}{\partial\theta^2} + V_0\cos(m\theta) - i\hbar\omega_{\pm}(t)\frac{\partial}{\partial\theta}\,. \tag{6.17}$$

To simulate the dynamics under the Hamiltonian in Eq. (6.17), we have found the simple split-propagator method [247, 248] to be effective. The results of such simulations, which use 1024 spatial grid points to represent the wave packets in the range $[0, \pi/4]$ and a time resolution of $\Delta t = 1\,\mu s$, are shown in Fig. **??** as the points labeled "SP". An excellent agreement with the inertial-frame results from the CN method is observed. We have also verified the precision of the split-propagator method by comparing it to a Chebychev propagation [249], which is exact to machine precision, but slower by about a factor of four. It is noted in Fig. 4 that the implementation with faster ramps, cf. panel (b), is still adiabatic. The faster ramp allows a longer loop time, accommodating $n = 10$ cycles instead of just 2 within the same interferometer time T, and thus results in a higher sensitivity.

6.4.2 Path integral method

The interferometric response closely follows a semiclassical model based on path-integral propagators. The propagator phase of a wave packet equals $\exp(iS(\mathbf{x}_0(t))/\hbar)$, where $S(\mathbf{x}_0(t))$ is the action of the classical trajectory, $\mathbf{x}_0(t)$, followed by the centroid of the wave packet. Consequently, the phase difference $\Delta\Phi_S$ between our relevant pair of wave packets in spin states $|-\rangle$ and $|+\rangle$, arises from the difference of corresponding actions,

$$\Delta\phi_S = \frac{1}{\hbar}\int \left(\mathcal{L}(\mathbf{x}_-, \dot{\mathbf{x}}_-, t) - \mathcal{L}(\mathbf{x}_+, \dot{\mathbf{x}}_+, t)\right) dt\,. \tag{6.18}$$

where $\mathbf{x}_{\pm}$ are the paths followed by the centroids of the split wave-function components, and $\mathcal{L}(\mathbf{x}_{\pm}, \dot{\mathbf{x}}_{\pm}, t)$ are the corresponding Lagrangians. In TAI, the predetermined lattice trajectories serve as the classical paths since the atomic wave functions remain tightly trapped at the minima of the relatively slowly-moving lattice potentials, and the wave functions possess zero

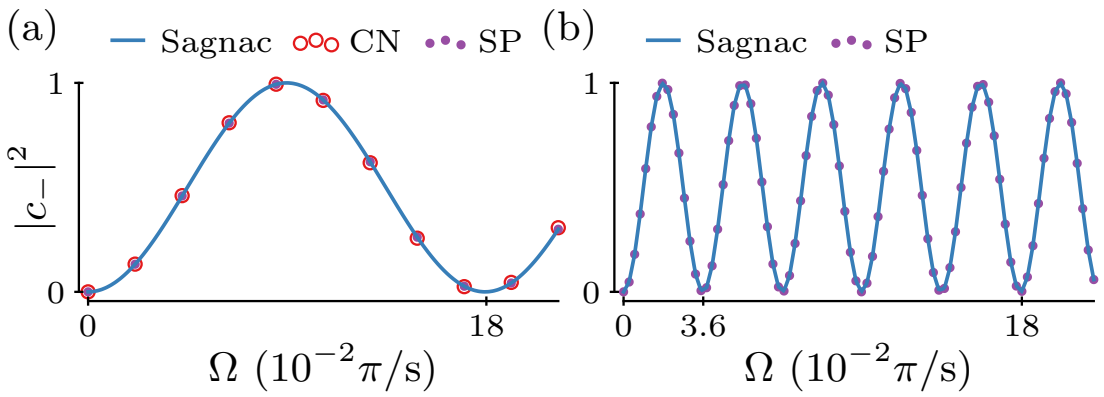


Figure 6.4: Interferometric response of TAI in a pinwheel optical lattice to a constant background rotation Ω for $V_0 = h \times 2.2\,\mathrm{MHz}$, $t_r = 100\,\mathrm{ms}$, and $T = 300\,\mathrm{ms}$ (other parameters see text). (a) Population in $|-\rangle$ for a recombination after $n = 2$ cycles, with $\omega_0 = 10\,\pi/\mathrm{s}$. The Sagnac curve is analytically calculated from Eq. (6.15a) with $\Delta\Phi = \Delta\Phi_S$, Eq. (6.19). The "CN" and "SP" points are obtained from simulations of the quantum dynamics with the Crank-Nicolson and split-propagator methods, respectively (see text for details). (b) Population in $|-\rangle$ after n=10 cycles with $\omega_0 = 50\,\pi/\mathrm{s}$, cf. the dynamics in Fig. 6.3.

degrees of freedom. That is, the $\mathbf{x}_\pm$ are simply given by the locations of the selected sites of the optical lattices for $|+\rangle$ and $|-\rangle$, and forces of constraint cause no significant alterations. The Lagrangians for the states $|+\rangle$ and $|-\rangle$ differ in the presence of a non-zero background angular velocity Ω due to the different lattice angular speeds in the inertial frame. In the semi-classical path-integral picture, Eq. (6.18) leads to the well-known Sagnac phase,

$$\Delta\Phi_S = \frac{4m_{\mathrm{Rb}}\Omega A}{\hbar}\,, \quad A = \frac{R^2}{2}\int_0^T \omega(t')\,dt'\,. \tag{6.19}$$

The final recombined population in the state $|-\rangle$ on its respective potential, Eq. (6.15a) with $\Delta\Phi = \Delta\Phi_S$, is shown in Fig. **??** as the solid curve. Figure 4 (a) shows the result for $\omega_0 = 10\,\pi/\mathrm{s}$ and two cycles (the minimum number of cycles possible for $t_r = 100\,\mathrm{ms}$ and $t_{\mathrm{loop}} > 0$, for a total of $T = 300\,\mathrm{ms}$). The parameters for Fig. **??** (b) match those for Fig. 6.3. The close agreement of the semi-classical results with the full quantum simulations (CN and SP) in both Figs. **??** (a) and (b) validates the principles of TAI in the adiabatic limit, in which unwanted spin couplings, wave packet excitation and tunneling on the spin-dependent lattice potentials do not affect the interferometric phase of the TAI.

6.4.3 Rotation sensitivity

Assuming that a phase resolution of $2\pi/100$ can be experimentally achieved [238], in Fig. ?? (a) the rotation sensitivity can be inferred to be about 5 mrad/s. This can be improved by increasing the lattice angular velocity for a given duration of the interferometric scheme. Fig. ?? (b) shows the response for $n = 10$ cycles, achieved by increasing ω_0 to $50\,\pi$/s. In Fig. ?? (b) the sensitivity is improved five-fold to roughly 1 mrad/s.

The interferometer sensitivity can be enhanced further by increasing both the lattice radius R and the angular velocity $\omega_\pm$ to an extent where centrifugal force and nonadiabatic excitation still remain negligible. In a lattice of depth $h \times 4.4$ MHz the orbital radius suffers $<$ 0.1% increase when rotated at $\omega_\pm \sim 1000\,\pi$/s. Nonadiabatic excitations are better explained in the co-rotating lattice frames given by Eq. (6.16). The first two terms of the Hamiltonian $\tilde{H}_\pm(t)$ in Eq. (6.17) describe stationary optical lattices, in which we initialize the wave functions in the respective ground states. As the lattices are accelerated, the last term, which is proportional to $\omega_\pm(t)\hat{L}_z$, may cause nonadiabatic transitions into excited vibrational states within the initially populated lattice wells. In shallow lattices, modified tunneling behavior may occur (Bloch oscillations and Wannier-Stark localization). In the following, we develop an estimate as to what rotation sensitivities may be possible under these constraints.

The departure from perfect adiabaticity can be quantitatively estimated in the momentum picture by exploiting the spatial periodicity of the Hamiltonian $\tilde{H}_\pm(t)$. Following the well-known Bloch formalism, any eigenstate of $\tilde{H}_\pm(t)$ can be characterized by quasi-angular momentum ℓ and band index n as $|\psi_\ell^n\rangle = e^{i\ell\theta}\,|u_\ell^n\rangle$ where $u_\ell^n(\theta + 2\pi) = u_\ell^n(\theta)$. Then the effective Hamiltonian for $|u_\ell^n\rangle$ is given by

$$\mathcal{H}_{\ell,\pm}(t) = \frac{(L_z + \hbar\ell)^2}{2I} + V_0 \cos(m\theta) + \omega_\pm(L_z + \hbar\ell)\,, \tag{6.20}$$

where $\mathcal{H}_{\ell,\pm(t)}u_\ell(t) = E_\ell^n(t)u_\ell(t)$. Scaling the Hamiltonian by and effective recoil energy $E_R = \hbar^2m^2/2I$ gives a dimensionless eigenvalue equation in terms of $\Theta = m\theta$,

$$\left[-\frac{d^2}{d\Theta^2} - \frac{2i\ell}{m}\frac{d}{d\Theta} + \left(\frac{\ell}{m}\right)^2 + \frac{V_0}{E_R}\cos(\Theta) + \frac{2I\omega_\pm}{m\hbar}\left(-i\frac{d}{d\Theta} + \frac{\ell}{m}\right)\right] u_\ell^n(\omega_\pm, \Theta) = \frac{E_\ell^n}{E_R}u_\ell^n(\omega_\pm, \Theta)\,. \tag{6.21}$$

Eq. (6.21) offers an estimate of the relative magnitudes of different terms in the Hamiltonian in the co-rotating frames. First, we consider tunneling effects for a ground-state wave function $u_0^0(0, \theta)$ trapped in a static lattice (*i.e.*, $\ell = \omega_\pm = 0$). In this simple case, tunneling-induced wave-function delocalization is suppressed when $V_0 \gg E_R$. When a lattice of such

potential depth is rotated at a constant angular velocity $\omega_\pm$, the final term on the left-hand side in Eq. (6.21) mixes the ground state of the stationary lattice with excited states from higher bands. This mixing can be minimized if the lattice depth $2V_0$ is much larger than the scale of the lattice-rotation-induced perturbation $m\hbar\omega_\pm$.

For the pinwheel lattice under consideration, the effective recoil energy E_R is $\sim h \times 250\,\mathrm{Hz}$ and the scale of the lattice-rotation-induced perturbation at $\omega_\pm \simeq 500\,\pi/\mathrm{s}$ is $\sim h \times 80\,\mathrm{kHz}$. Therefore, a lattice depth of $h\times$ 4.4 MHz can adequately suppress delocalization of the ground-state wave function and support a maximum angular velocity up to $\omega_\pm \sim 500\,\pi/\mathrm{s}$ with minimal nonadiabatic excitations. Pinwheel lattices of radius 2.5 mm rotated at $1000\,\pi/\mathrm{s}$ can potentially improve the sensitivity of Fig. **??** (b) by six orders of magnitude to 1 nrad/s for an operation time of 1 s.

The signal-to-noise ratio can be enhanced by loading a larger number of atoms into the lattices. This can be achieved, for instance, by creating pinwheel lattices with more sites (*i.e.*, larger m) and stacking several pinwheel lattices axially on a linear array of z-lattice sites. The axial stacking is limited to a range $|z| \ll z_R$, where the locations of the radial minima stay similar enough to avoid excessive inhomogeneous broadening of the TAI phase $\Delta\phi$. For example, in Fig. **??** (a), the position of the radial minima changes by less than 0.01% over $z = \pm 1.5\,\mu\mathrm{m}$. Therefore, for a stack of 10 pinwheel lattices separated by the lattice period 266 nm one can expect the average TAI fringe contrast to remain large for $\Delta\phi$ up to several $100 \times 2\pi$. In experimental realizations, LG beams with larger beam waists and Rayleigh ranges would allow a higher degree of axial stacking to improve signal-to-noise.

6.5 Nonadiabatic effects in lattice spin-up and -down

In order to further optimize the gyroscope sensitivity and to increase the dynamic range in rotation sensing, the time t_r in Eq. (6.10) during which the lattices are accelerated should be reduced. Additionally, the ability of the interferometer to operate with shallower lattices, which will accommodate laser power constraints and minimize signal loss due to photon scattering, has to be explored. When entering the nonadiabatic regime, the split wave function in each spin-dependent potential deviates from the ground state $\Psi_0(\theta)$ in the lattice rest frames. We have studied the nonadiabatic effects numerically by simulating the time evolution under the Hamiltonian in Eq. (6.17). In Fig. 6.5, we show the fidelity under the smoothly-varying ramp function $\omega(t)$ in Eq. (6.10a), which drives the ground state $\Psi_0(\theta, t = 0)$ in the initially selected optical lattice well into a state $\Psi(\theta, t_r)$. The fidelity is given by the magnitude-square of the overlap between $\Psi(\theta, t_r)$ and the desired target state, $\Psi_{\mathrm{tgt}}(\theta, t_r)$, which is the ground state of the potential rotating at the terminal constant speed $\pm\omega_0 =$

$50\,\pi$/s. The point marked by the red square in the top-right corner corresponds to the fully adiabatic time evolution shown in Fig. 6.3.

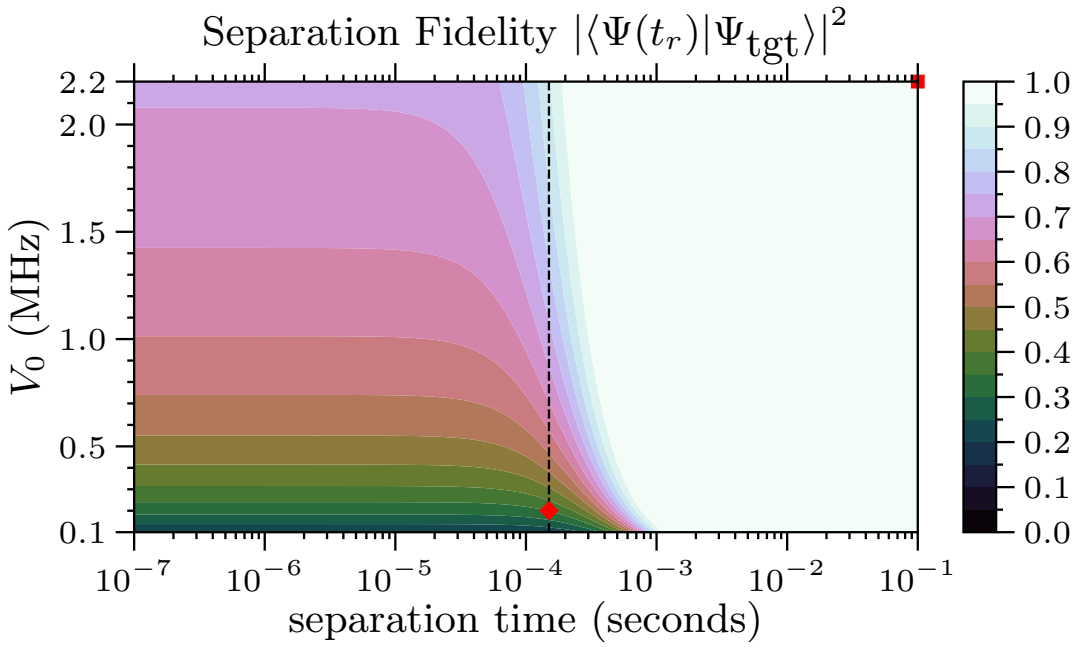


Figure 6.5: Fidelity of the initial splitting operation for varying separation time t_r and V_0 of the trapping potential. The separation fidelity is the overlap of the state $|\Psi(t_r)\rangle$ resulting from the evolution under Eq. (6.10a) with the ground state of the moving potential at t_r.

We observe a transition from adiabatic to nonadiabatic evolution for a separation time between 1 ms and 100 µs, depending on the depth of the potential. It is thus confirmed that the lattice acceleration conditions in Fig. 6.3 are deep in the adiabatic regime, allowing several orders of magnitude increase in acceleration before nonadiabatic effects actually become substantial. To gain a better understanding of the separation failure mode for small t_r and V_0 and of the effects of nonadiabaticity on the overall interferometric scheme, we show in Fig. 6.6 (a)-(e) the dynamics for $t_r = 150\,\mu$s and $V_0 = 0.2\,$MHz, marked with the red diamond in Fig. 6.5. Looking first at the initial separation phase, see left insets in Fig. 6.6 (c)-(e), we can see that the wave packet is not readily accelerated to terminal speed by the accelerating optical lattice. The lab-frame momentum, shown in panel (c), shows very little initial acceleration of the wave packet. Unlike in the adiabatic case in Fig. 6.3 (b), where $\langle p\rangle_+$ readily reaches $\omega_0 = 50\,\pi$/s at $t = t_r$, in Fig. 6 (c) it does not even come close. In the moving frame (lattice rest frame), shown in Fig. 6 (d) and (e), both position and momentum are far from zero, which also contrasts against the adiabatic case in Fig. 6.3 (c) and (d). In fact, initially the signs of momentum and position in the moving frame are opposite to that of the acceleration: as the lattice is accelerated to the left (counter-clockwise), the wave

packet in the moving frame is displaced to the right (clockwise).

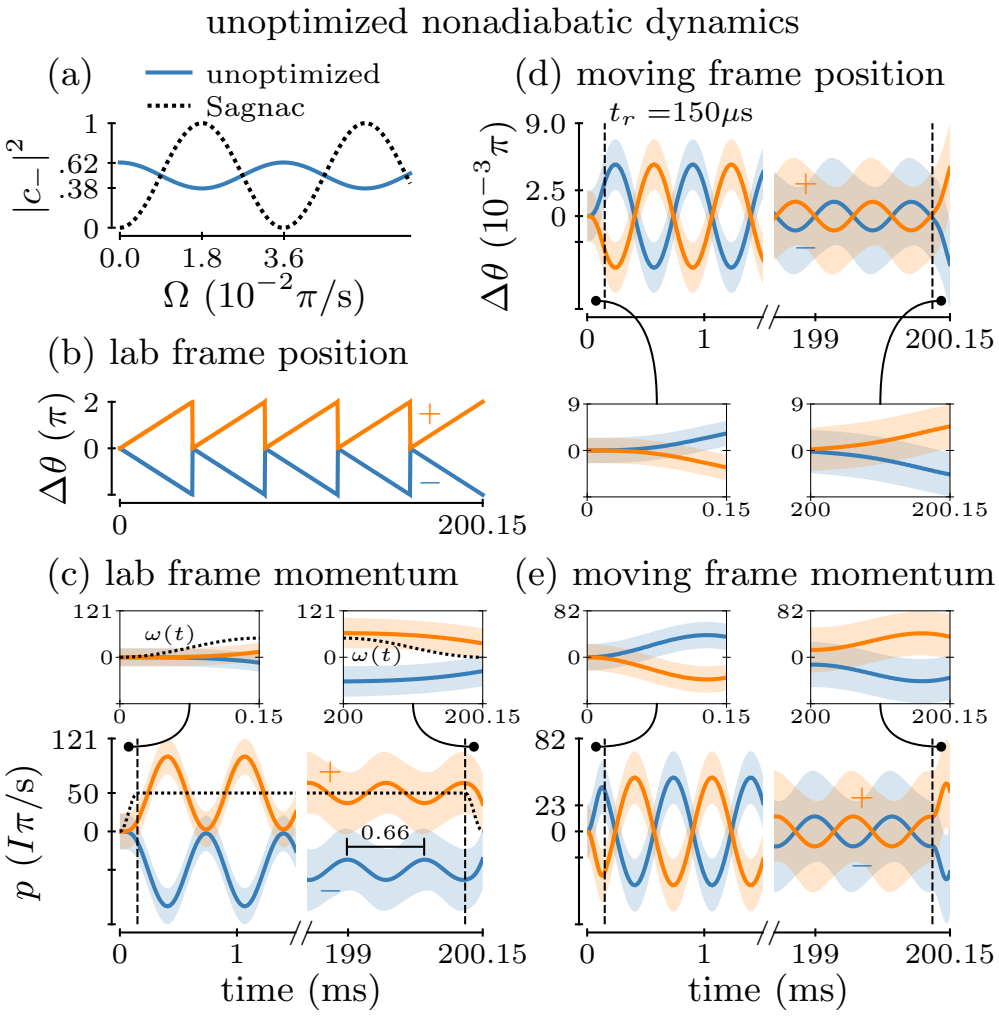


Figure 6.6: Dynamics of the TAI interferometer for a nonadiabatic separation time $t_r = 150\,\mu s$ and a shallow potential with $V_0 = 0.2\,\mathrm{MHz}$, as marked by the red diamond in Fig. 6.5. All other parameters are as in Fig. 6.3. Panels (b–e) show the results under the analytic drive function $\omega(t)$ given by Eq. (6.10)

To explain the observations in the previous paragraph, we first note that during the short separation time of 150 µs the actual displacement is very small: note the scale factor of 10^{-3} on the y-axis in Fig. 6.6 (d). In the subsequent 199.85 ms, when the optical lattices loop at constant counter-rotating speeds $\pm\omega_0$, the atoms eventually respond to the force that the trapping potential imparts on them. As a consequence, in the lattice rest frames the wave packets oscillate around zero, as seen in the panels (d) and (e), and around momentum $\pm\omega_0$ in the lab frame, as seen in panel (c). Visual inspection of Fig. 6.6 (c) reveals that the oscillation period is close to that of the harmonic ω_H in Eq. (6.7), which is 660 µs for $V_0 = 0.2\,\mathrm{MHz}$. However, the atoms oscillate in the anharmonic regions of the cosine potential

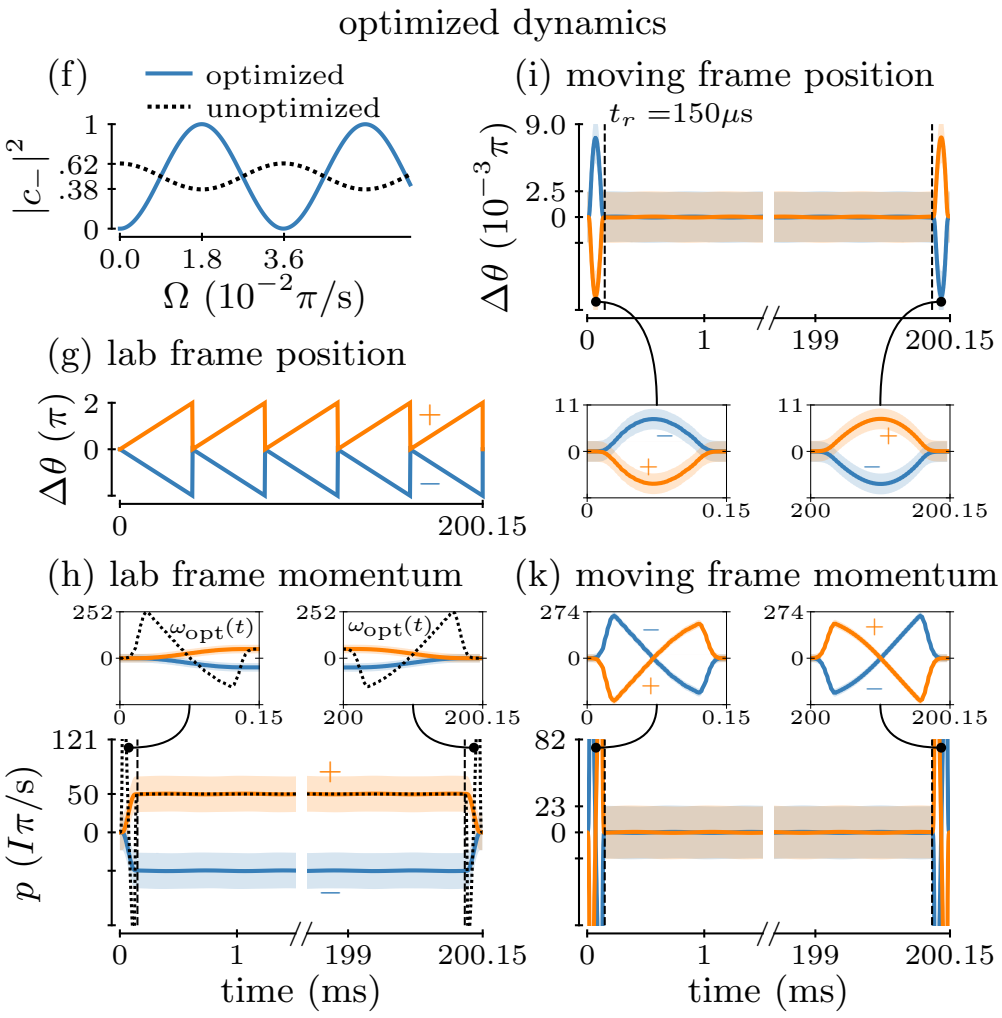


Figure 6.7: Dynamics of the TAI interferometer for a nonadiabatic separation time $t_r = 150\,\mu$s and a shallow potential with $V_0 = 0.2\,$MHz, as marked by the red diamond in Fig. 6.5. Panels (g–k) shows the results for an optimized field $\omega_{\rm opt}(t)$ (see text for details). Panel (f) shows the interferometric response of the un-optimized and the optimized drive functions to a constant background rotation Ω.

in Eq. (6.5), for this value of V_0. As a result, we also find a breathing of the oscillation, *i.e.*, the oscillation amplitude diminishes while the width of the wave packet increases, see the first and last 1.5 ms in panels (c) and (e). The breathing is absent when the atoms remain confined to the near-harmonic sections of the cosine function, *e.g.*, for potentials with larger values of V_0. The physical picture that summarizes and underlies these observations is that for $t_r \to 0$ and V_0 sufficiently large, the lattices instantaneously speed up to ω_0 underneath the atoms. If the corresponding kinetic energy in the lattice frame is less than $2V_0$, the atoms subsequently undergo a sloshing oscillation in the lattice frame. At longer times, the oscillation exhibits collapse and quantum revival phenomena caused by the anharmonicity of the potential.

In Figs. 6 (a-e), the ramp-down of the pinwheel lattice from ω_0 to a position at rest, in the lab frame, behaves fundamentally the same as the initial ramp-up: the wave packet does not slow down with the rapidly decelerating potential. Instead, the location of the oscillating wave packet at the time instant when the deceleration hits determines the wave packet's state within the lattice well after the lattice slowdown is complete. The final state may range from less excited to more highly excited than before the deceleration. In Fig. 6.6 (d) and (e) the latter is the case.

Overall, the lack of fidelity seen in Fig. 6.5, and the resulting oscillatory dynamics have a detrimental effect on the contrast of the full TAI interferometric scheme. First, as shown in Fig. 6.6 (b), the interferometer fails to close perfectly. Second, prior to the final recombination $\pi/2$ pulse the wave packets no longer match the ground state $\Psi_0(\theta)$, neither in position nor in momentum, and nor in width, as seen in panels (d) and (e). Thus, the magnitude of the overlap η in Eq. (6.14) typically is much less than 1, and the contrast of the resulting populations $|c_\pm|^2$ in Eq. (6.13) is correspondingly diminished. This result is shown in Fig. 6.6 (a). For the given parameters, the achieved contrast is only 24%. This falls well short of the contrast of the path-integral Sagnac curve, shown as the black dotted line, which matches exactly Fig. **??** (b). Because for small t_r the overall process approximates the physics of two impulsive kicks applied to a wave packet in a well, there also is an erratic dependence of the AI contrast on fine details. The phase of the wave packet sloshing motion at the time instant of the second kick largely determines visibility. The simplified two-pulse picture becomes more accurate at shorter t_r; the picture essentially applies in the left third of Fig. 5. An additional factor that plays a role is that at small V_0 and short t_r, the effective two-pulse wave packet drive may excite the wave packet partially into the continuum, causing further contrast loss. In the next section, we will attempt to correct these unwanted behaviors using methods of optimal control.

6.5.1 Optimal Control

Having observed the detrimental effect of a separation time t_r that is too short, we consider the use of optimal control to improve the fidelity in Fig. 6.5 for moderate values of t_r. Specifically, we seek to find an $\omega(t)$ that is an alternative to the analytical shape in Eq. (6.10a) such that $\Psi_\pm(\theta, t)$ reaches $\Psi_{\pm,\mathrm{tgt}}(\theta, t = t_r)$, that is, the ground state in the lattice rest frames. The optimized $\omega(t)$ must maintain the boundary conditions $\omega(0) = 0$ and $\omega(t_r) = \omega_0$. To this end, we parametrize

$$\omega_{\mathrm{opt}}(t) = \omega(t) + S(t)\delta\omega(t)\,, \tag{6.22}$$

where $\omega(t)$ is the original shape given by Eq. (6.10a), $\delta\omega(t)$ is a correction to be optimized, and $S(t) \in [0, 1]$ is a fixed shape with $S(0) = S(t_r) = 0$ to enforce the boundary conditions. Here, we use a shape that smoothly switches on and off with a Blackman shape during the first and last 20% of the time window. The initialization for $\delta\omega(t)$ is $\delta\omega(t) = 0$.

An optimized correction $\delta\omega(t)$ can be obtained using any of the standard gradient-based quantum control methods, including GRAPE [250] or Krotov's method [251]. Here, we have used the Krotov.jl package [252] within the QuantumControl Julia framework [253]. Within 300 iterations, using a square-modulus functional [254], we can bring the separation error from 0.648, see Fig. 6.5, to 1.26×10^{-5}. The resulting optimized $\omega_{\mathrm{opt}}(t)$ is shown in the left inset of Fig. 6.7 (h), with the full resulting dynamics for the entire interferometric scheme in panels (g)-(k). The optimized control function for the ramp-down is the time inverse of the ramp-up one, see the right inset of panel (h).

We observe a "throw and catch" behavior. The field ramps up rapidly to a relatively high (but still achievable) speed of $252\,\pi$/s, but then slows down and temporarily switches direction, before returning to the target speed of $50\,\pi$/s. The lab frame momentum does not follow this rapid motion, but smoothly accelerates from 0 to $50\,\pi$/s, as can be seen in the inset of Fig. 6.7 (h), and very much mimics the adiabatic dynamics in Fig. 6.3 (b). Likewise, the lattice-frame position, seen in panel (i), initially lags behind the accelerating lattice potential, but then smoothly catches up to the equilibrium position within the lattice frame. The subsequent dynamics while the optical lattices loop at constant speed ω_0 are near-identical with the adiabatic case in Fig. 6.3: both position and momentum are zero in the moving frame, see panels (i) and (k), and follow the position and momentum of the trapping potential in the lab frame, see panels (g) and (h). The ramp-down inverts the dynamics during the ramp-up, leaving the wave function in a state that is very close to the ground state of the lattice potential at rest. This results in near-ideal interferometric response following Eq. (6.15), as shown in Fig. 6.6 (f). This implies that the interferometric path in panel (g) is now perfectly closed, in contrast to the open path in panel (b).

In principle, a "throw and catch" optimal control solution can be found for even shorter t_r. However, the shorter t_r, the larger the amplitude that the control function $\omega_{opt}(t)$ will need to reach during the ramp-up and ramp-down phases. Hence, the maximum experimentally achievable angular control velocity will determine how far one may push to the left in Fig. 6.5.

A more general approach to accelerate the ramp-up and ramp-down phases is to exploit the dependency of the boundary between adiabatic and nonadiabatic behavior on V_0 (see Fig. 6.5). For instance, starting from the point marked by the red diamond in Fig. 6.5, one may temporarily increase the depth of the potential, move up along the dashed line in Fig. 6.5, in combination with tuning $\omega(t)$. However, an eigenstate of a shallower lattice well will not be an eigenstate of a deeper one, resulting in a breathing motion of the wave packet after the compression. To counter this, one would have to add another layer of "throw and catch" to suppress the breathing, or introduce additional control over the shape of the potential.

The control functions we have obtained here are already quite simple and can be readily implemented. As an alternative or an augmentation to the numerically optimized controls, one may in the future explore analytic control schemes under the umbrella of "shortcuts to adiabaticity" [255].

6.6 Conclusion

In summary, we have presented the design of a rotation sensor based on the principles of tractor atom interferometry [214, 238]. An experimental setup can be realized using readily available instrumentation. The parameters for the pinwheel lattice, which is at the heart of the envisioned devices, can be obtained following the considerations discussed in Sec. 6.2. In the adiabatic limit, quantum-dynamics simulations of the sensor's single- and multi-loop operation agree well with semi-classical path-integral predictions, in which one simply enters the known tractor trajectories into the applicable Lagrangian. Our proof-of-principle simulations allow rotation sensitivities of about 1 mrad/s. We have provided a discussion and concrete examples that illustrate the utility of quantum control to realize fast beam splitters and ramps to prepare coherently-split wave-function components that counter-rotate at high rotation speeds, allowing higher sensitivity. Estimates that extrapolate pinwheel area and rotation speed to reasonable limits predict sensitivities approaching 1 nrad/s, at a 1-second measurement time.

CHAPTER 7

Conclusion and Outlook

This thesis presented investigations into two modalities of atomic sensors, with coherence being the central sensing resource in both. Rydberg-EIT, the modern workhorse of atom-based field sensing, has been demonstrated in inert gases ranging up to several Torrs in pressure. The collisional effect is described with a semiclassical model using the Fermi pseudopotential. In the low-pressure regime, particularly below 100 mTorr, collisional broadening is found to be negligible compared to the inert-gas-free EIT linewidth. Building on these results, Rydberg-EIT is demonstrated for the first time in a continuous inductively coupled plasma discharge. The EIT line shape is modeled using the stochastic microfield produced by quasistatic ions and collisional broadening due to fast electrons. Plasma microfield ranging from 5 V/cm to 10 V/cm and electron density ranging from 5×10^{16} m^{-3} to 1.3×10^{17} m^{-3} are inferred from the line shape analysis. Along the inertial sensing front, a new design for a matter-wave gyroscope featuring continuous 3D confinement and transport is proposed and analyzed, with projected sensitivity of µrad/s at 1 s interrogation time. The results presented are complemented with a detailed description of experimental methods as well as the relevant concepts from atomic physics and plasma physics.

In the broader context, this thesis contributes to the ongoing effort to extend the principles of quantum mechanics and coherent control towards applied technologies. The specific interest here has been to push quantum sensing past pristine laboratory conditions and toward the systems where the measurements are scientifically interesting. The atomic toolkit has reached a level of maturity where, alongside foundational questions in metrology and distributed sensing, a practical line of inquiry concerns whether coherent techniques developed under carefully shielded conditions can survive contact with environments whose internal dynamics act as decoherence mechanisms. The presented work on field diagnostics demonstrates that coherent Rydberg spectroscopy is feasible in low-pressure plasmas and offers sufficient resolution to recover the stochastic microfield from the line shape. The work on tractor atom interferometry presents a step toward compact quantum inertial sen-

sors through continuous confinement and quantum control based decoherence mitigation. In what follows, I discuss the outlook for both of these modalities.

7.1 Tractor Atom Interferometry

Implementing the atom-based inertial sensing presented in Chapter 6 requires ultracold atoms from a Bose-Einstein Condensate (BEC) for maximal coherence. Experimental efforts from our group are already underway to revive a previous BEC apparatus. The path to a BEC presents substantial experimental challenges, primarily stemming from the stringent vacuum requirement, and will be the subject of many theses and papers to come. Beyond realizing the BEC, the implementation of a tractor atom interferometer will require careful management of noise sources such as residual intensity fluctuations and mechanical resonances. The non-adiabaticity introduced by such processes and potential mitigation through active feedback need further investigation. Future work can refine the numerical simulations presented here to characterize the effect of realistic noise profiles on fringe contrast and to explore mitigation strategies including quantum optimal control.

Looking further ahead, photonic integration offers a complementary approach to the free-space optical lattices considered so far. Trapping geometries generated by the evanescent modes of photonic waveguides can offer several orders of magnitude larger interferometric area at compact footprint. Recent work from our group on a Sagnac interferometer architecture based on a photonic waveguide [256] demonstrates sensitivity estimates approaching several nrad/s at 1 s interrogation time. Experimental realization along this direction is envisioned in collaboration with the Quantum Engineering group at the University of Michigan.

7.2 Rydberg atoms for plasma physics

Before moving towards plasma field measurement, Rydberg-EIT already has a use case for mapping the electric and magnetic field structure inside the plasma chamber resulting from the applied rf power. In particular, ICPs feature a rare case where the rf magnetic field can induce $M1$-transitions with similar strengths to $E1$-transitions. In future work with the existing ICP chamber, spatially resolved field mapping due to the applied rf power can shed light on the relative strengths of capacitive field and induced fields. Undesired capacitive coupling in ICPs leads to the low-density E-mode operation at low power and a hysteretic phase transition to H-mode at higher powers. Faraday shields are typically employed to preferentially cancel the capacitive field while keeping the induced azimuthal field relatively intact [257]. The efficiency of the Faraday shield and reduction of capacitive fields can be

verified *in situ* by mapping the electromagnetic field radially using Rydberg-EIT.

The presented results from Rydberg-EIT in ICP essentially serve as a proof-of-principle demonstration of coherent Rydberg spectroscopy inside a plasma environment. However, the current configuration accounts for line-integrated field measurement along the direction of propagation. Future readouts can be made spatially resolved e.g., by monitoring fluorescence or loss thereof along the beam path [258]. This will require a new imaging system and upgrading the coupler laser power.

The current results indicate brighter prospects for EIT-based field diagnostics in a capacitively coupled plasma (CCP) chamber for a host of reasons. Firstly, one of the primary motivations for EIT in plasma field measurement is the study of sheath regions. This includes spatially resolved field measurement near the electrode, and dielectrics or metals immersed in the plasma. CCPs feature a strong and stable sheath above the powered electrode, unlike ICPs. The current chamber geometry does not provide convenient optical access along the coil axis, which is easily manageable in a CCP chamber.

Another impactful application of EIT based field diagnostics pertains to dusty plasmas. Micron-scale dust particles charge negatively in plasmas due to superior electron mobility and equilibrate near the sheath region where the electric field balances gravity. Unlike typical plasmas with quasi-neutral bulk where Coulomb interaction is negligible compared to the kinetic energy, dusty plasmas are strongly-coupled, exhibit collective dynamics with nontrivial transport and heating mechanisms. There are longstanding open questions regarding the charging processes in dusty plasma, sheath electric field models and ion wake fields [259–261] among others, where a direct and non-perturbative electric field measurement would be a substantial step forward.

In the current experiment, plasma microfields of several V/cm arise from electron density $n_e \sim 10^{16}$ m^{-3}, typical for ICP discharges, which leads to significant broadening in the Rydberg spectrum. While it can be reduced in part by moving to a smaller principal quantum number, this roughly signals the upper end of the plasma density amenable to EIT. On the other hand, the electron density in CCP discharges ranges from $\sim 10^{14} - 10^{15}$ m^{-3}, which would render both microfield and collisional broadening negligible. Additionally, using nD Rydberg states instead of nS states can enable vector electrometry to distinguish directed, long-range fields *e.g.*, the sheath electric field from the microfield. In strongly magnetized plasmas, Debye screening becomes anisotropic and the plasma–wall transition acquires an additional magnetic presheath layer for oblique B [262], whose detailed structure is an active area of research. *In situ* vector electrometry of the resulting field anisotropy would provide a direct experimental probe of these effects.

Beyond the electric-field diagnostics developed in this dissertation, the AMO toolkit,

particularly principles of coherent spectroscopy, offers plasma physics a wider set of non-perturbative diagnostic capabilities. Salient examples include coherent Rayleigh–Brillouin scattering for velocimetry [263], quantum-beat spectroscopy for *in situ* magnetic-field imaging [264], and various four-wave-mixing techniques for state-resolved species detection. The convergence runs even deeper in the strongly-coupled regime [265, 266], where the cold-atom infrastructure of AMO laboratories provides the experimental platform itself as well as diagnostics based on particle imaging and laser spectroscopy. Strongly-coupled and magnetized plasmas created from laser-cooled atoms promise to unveil novel phases, transport dynamics and collective behaviors, ensuring that the synergy between AMO and plasma physics will continue to yield profound insights into the fourth state of matter.

Appendix A

Generalized Crout Reduction

The time evolution of the wave function under Schrödinger's equation is given by

$$\frac{\partial\psi(x,t)}{\partial t} = \frac{i\hbar}{2m}\frac{\partial^2\psi(x,t)}{\partial x^2} - \frac{iV(x)}{\hbar}\psi(x,t)\,. \tag{A.1}$$

Let us consider this in a 1-D system confined to $[-x_l, x_l)$ with the initial conditions $\psi(x,0) = \psi^0(x)$, $\psi(x_l,0) = \psi(-x_l,0) = 0$ and periodic boundary condition so that $\psi(x+2x_l) = \psi(x)$. By discretizing the derivatives, the right-hand-side is approximated up to $\mathcal{O}(\Delta x^2)$ as

$$\frac{i\hbar}{2m\Delta x^2}\left(\psi_{j+1}^{(k)} + \psi_{j-1}^{(k)} - 2\psi_j^{(k)}\right) - \frac{iV_j}{\hbar}\psi_j^{(k)} \equiv \sum_{m=0}^{N}\frac{iH_{j,m}\psi_m^{(k)}}{\hbar}\,, \tag{A.2}$$

where H is the position representation of the Hamiltonian. The Crank-Nicolson method discretizes the time domain by taking the average of forward and backward differences to approximate the time derivative $\frac{\partial\psi}{\partial t}$; and relates $\psi^{k+1} \equiv \psi(t=(k+1)\delta t)$ to ψ^k as

$$\left(1 - \frac{iH\Delta t}{2\hbar}\right)\psi^{k+1} = \left(1 + \frac{iH\Delta t}{2\hbar}\right)\psi^k\,. \tag{A.3}$$

The generalized Crout reduction algorithm for the PBC Hamiltonian is:

1. Initialize $\psi^{k+1}, l, u, z, \eta, \xi$ as zero arrays of size N
2. With $\lambda = \frac{i\hbar\Delta t}{2m\Delta x^2}$
   (a) Set $l_0 = 1 + \lambda + \frac{iV_0\Delta t}{2\hbar}$, $\eta_0 = -\frac{\lambda}{2}$, $\xi_0 = -\frac{\lambda}{2l_0}$
   (b) For i in $\{1,\ldots,N-2\}$:

$$u_i = -\frac{\lambda}{2l_i}$$
$$l_i = 1 + \lambda + \frac{iV_i\Delta t}{2\hbar} + \frac{\lambda}{2}u_i$$

(c) For i in $\{1, \ldots, N-2\}$:

$$\xi_i = \frac{\lambda^{i+1}}{2^{i+1} \prod_{j=0}^{i} l_j}, \quad \eta_i = \frac{\lambda^{i+1}}{2^{i+1} \prod_{j=0}^{i-1} l_j}$$

(d) Set the last entries of l and u:

$$\begin{aligned} u_{N-1} &= -\frac{\lambda}{2l_{N-2}} + \xi_{N-2} \\ l_{N-1} &= 1 + \lambda + \frac{iV_{N-1}\Delta t}{2\hbar} \\ &\quad - \sum_{j=0}^{N-3} \eta_j \xi_j - \left(\eta_{N-2} - \frac{\lambda}{2}\right) u_{N-1} \end{aligned}$$

3. Set $z_0 = \left(1 - \lambda - \frac{iV_0\Delta t}{2\hbar}\right)\psi_0^k + \frac{\lambda}{2l_0}\left(\psi_{N-1}^k + \psi_1^k\right)$

(a) For i in $\{1, \ldots, N-2\}$:

$$z_i = \left(1 - \lambda - \frac{iV_i\Delta t}{2\hbar}\right)\psi_i^k + \frac{\lambda}{2l_i}\left(\psi_{i+1}^k + \psi_{i-1}^k + z_{i-1}\right)$$

(b) Set last entry:

$$\begin{aligned} z_{N-1} &= \left(1 - \lambda - \frac{iV_{N-1}\Delta t}{2\hbar}\right)\psi_0^k \\ &\quad + \frac{\lambda}{2l_{N-1}}\left(\psi_{N-1}^k + \psi_1^k + z_{N-2} - \sum_{j=0}^{N-2} z_j \eta_j\right) \end{aligned}$$

4. Back-substitute to obtain ψ^{k+1}:

(a) Set $\psi_{N-1}^{k+1} = z_{N-1}$

(b) For i in $\{N-2, \ldots, 1\}$:

$$\psi_i^{k+1} = z_i + \frac{\lambda}{2l_i}\psi_{i+1}^{k+1} - \psi_{N-1}^{k+1}\xi_i$$

BIBLIOGRAPHY

[1] Wenhui Li, I. Mourachko, M. W. Noel, and T. F. Gallagher. Millimeter-wave spectroscopy of cold rb rydberg atoms in a magneto-optical trap: Quantum defects of the ns, np, and nd series. Phys. Rev. A, 67(5):052502, 2003. doi: 10.1103/PhysRevA.67.052502.

[2] Jianing Han, Yasir Jamil, D. V. L. Norum, Paul J. Tanner, and T. F. Gallagher. Rb nf quantum defects from millimeter-wave spectroscopy of cold ^{85}Rb rydberg atoms. Phys. Rev. A, 74(5):054502, 2006. doi: 10.1103/PhysRevA.74.054502.

[3] Jonathan P Dowling and Gerard J Milburn. Quantum technology: The second quantum revolution. arXiv preprint quant-ph/0206091, 2002.

[4] H. Levine, A. Keesling, A. Omran, H. Bernien, S. Schwartz, A. S. Zibrov, M. Endres, M. Greiner, V. Vuletić, and M. D. Lukin. High-fidelity control and entanglement of Rydberg-atom qubits. Phys. Rev. Lett., 121(12):123603, 2018. doi: 10.1103/PhysRevLett.121.123603.

[5] Manuel Endres, Hannes Bernien, Alexander Keesling, Harry Levine, Eric R Anschuetz, Alexandre Krajenbrink, Crystal Senko, Vladan Vuletic, Markus Greiner, and Mikhail D Lukin. Atom-by-atom assembly of defect-free one-dimensional cold atom arrays. Science, 354(6315):1024–1027, 2016.

[6] Matthew A Norcia, Aaron W Young, William J Eckner, Eric Oelker, Jun Ye, and Adam M Kaufman. Seconds-scale coherence on an optical clock transition in a tweezer array. Science, 366(6461):93–97, 2019.

[7] Zilong Chen, Hong Ming Lim, Chang Huang, Rainer Dumke, and Shau-Yu Lan. Quantum-enhanced velocimetry with doppler-broadened atomic vapor. Phys. Rev. Lett., 124(9):093202, 2020. doi: 10.1103/PhysRevLett.124.093202.

[8] Mingyong Jing, Ying Hu, Jie Ma, Hao Zhang, Linjie Zhang, Liantuan Xiao, and Suotang Jia. Atomic superheterodyne receiver based on microwave-dressed rydberg spectroscopy. Nature Physics, 16(9):911–915, 2020.

[9] M. A. Zentile, D. J. Whiting, J. Keaveney, C. S. Adams, and I. G. Hughes. Atomic faraday filter with equivalent noise bandwidth less than 1 ghz. Optics Letters, 40(9): 2000–2003, 2015.

[10] Noah Schlossberger, Andrew P Rotunno, Stephen P Eckel, Eric B Norrgard, Dixith Manchaiah, Nikunjkumar Prajapati, Alexandra B Artusio-Glimpse, Samuel Berweger, Matthew T Simons, Dangka Shylla, et al. Primary quantum thermometry of mm-wave blackbody radiation via induced state transfer in rydberg states of cold atoms. Physical Review Research, 7(1):L012020, 2025.

[11] Daniel S Barker, Bishnu P Acharya, James A Fedchak, Nikolai N Klimov, Eric B Norrgard, Julia Scherschligt, Eite Tiesinga, and Stephen P Eckel. Precise quantum measurement of vacuum with cold atoms. Review of Scientific Instruments, 93(12), 2022.

[12] Loïc Rondin, Jean-Philippe Tetienne, Thomas Hingant, Jean-François Roch, Patrick Maletinsky, and Vincent Jacques. Magnetometry with nitrogen-vacancy defects in diamond. Reports on progress in physics, 77(5):056503, 2014.

[13] Aishwarya Kumar, Aziza Suleymanzade, Mark Stone, Lavanya Taneja, Alexander Anferov, David I Schuster, and Jonathan Simon. Quantum-enabled millimetre wave to optical transduction using neutral atoms. Nature, 615(7953):614–619, 2023.

[14] Andrew M. C. Dawes, Lucas Illing, Susan M. Clark, and Daniel J. Gauthier. All-optical switching in rubidium vapor. Science, 308(5722):672–674, 2005. doi: 10.1126/science.1110151.

[15] Sebastian Borówka, Uliana Pylypenko, Mateusz Mazelanik, and Michał Parniak. Continuous wideband microwave-to-optical converter based on room-temperature rydberg atoms. Nature Photonics, 18(1):32–38, 2024.

[16] Dolev Bluvstein, Harry Levine, Giulia Semeghini, Tout T Wang, Sepehr Ebadi, Marcin Kalinowski, Alexander Keesling, Nishad Maskara, Hannes Pichler, Markus Greiner, et al. A quantum processor based on coherent transport of entangled atom arrays. Nature, 604(7906):451–456, 2022.

[17] H. J. Kimble. The quantum internet. Nature, 453(7198):1023–1030, 2008. doi: 10.1038/nature07127.

[18] Stephanie Wehner, David Elkouss, and Ronald Hanson. Quantum internet: A vision for the road ahead. Science, 362(6412):eaam9288, 2018. doi: 10.1126/science.aam9288.

[19] B. Hensen, H. Bernien, A. E. Dréau, A. Reiserer, N. Kalb, M. S. Blok, J. Ruitenberg, R. F. L. Vermeulen, R. N. Schouten, C. Abellán, W. Amaya, V. Pruneri, M. W. Mitchell, M. Markham, D. J. Twitchen, D. Elkouss, S. Wehner, T. H. Taminiau, and R. Hanson. Loophole-free Bell inequality violation using electron spins separated by 1.3 kilometres. Nature, 526(7575):682–686, 2015. doi: 10.1038/nature15759.

[20] Hannes Bernien, Sylvain Schwartz, Alexander Keesling, Harry Levine, Ahmed Omran, Hannes Pichler, Soonwon Choi, Alexander S Zibrov, Manuel Endres, Markus Greiner, et al. Probing many-body dynamics on a 51-atom quantum simulator. Nature, 551 (7682):579–584, 2017.

[21] Adam M Kaufman and Kang-Kuen Ni. Quantum science with optical tweezer arrays of ultracold atoms and molecules. Nature Physics, 17(12):1324–1333, 2021.

[22] Waseem S Bakr, Jonathon I Gillen, Amy Peng, Simon Fölling, and Markus Greiner. A quantum gas microscope for detecting single atoms in a hubbard-regime optical lattice. Nature, 462(7269):74–77, 2009.

[23] John Kitching. Chip-scale atomic devices. Applied Physics Reviews, 5(3), 2018.

[24] Christian L Degen, Friedemann Reinhard, and Paola Cappellaro. Quantum sensing. Reviews of modern physics, 89(3):035002, 2017.

[25] John Kitching, Svenja Knappe, and Elizabeth A Donley. Atomic sensors–a review. IEEE Sensors Journal, 11(9):1749–1758, 2011.

[26] A. Kramida, Yu. Ralchenko, J. Reader, and and NIST ASD Team. NIST Atomic Spectra Database (ver. 5.12), [Online]. Available: `https://physics.nist.gov/asd` [2016, January 31]. National Institute of Standards and Technology, Gaithersburg, MD., 2024.

[27] Andrew D Ludlow, Martin M Boyd, Jun Ye, Ekkehard Peik, and Piet O Schmidt. Optical atomic clocks. Reviews of Modern Physics, 87(2):637–701, 2015.

[28] Alexander Aeppli, Kyungtae Kim, William Warfield, Marianna S Safronova, and Jun Ye. Clock with 8× 10-19 systematic uncertainty. Physical Review Letters, 133(2): 023401, 2024.

[29] Kjeld Beeks, Tomas Sikorsky, Thorsten Schumm, Johannes Thielking, Maxim V Okhapkin, and Ekkehard Peik. The thorium-229 low-energy isomer and the nuclear clock. Nature Reviews Physics, 3(4):238–248, 2021.

[30] Samuel M Brewer, J-S Chen, Aaron M Hankin, Ethan R Clements, Chin-wen Chou, David J Wineland, David B Hume, and David R Leibrandt. Al+ 27 quantum-logic clock with a systematic uncertainty below 10-18. Physical review letters, 123(3):033201, 2019.

[31] Tobias Bothwell, Colin J Kennedy, Alexander Aeppli, Dhruv Kedar, John M Robinson, Eric Oelker, Alexander Staron, and Jun Ye. Resolving the gravitational redshift across a millimetre-scale atomic sample. Nature, 602(7897):420–424, 2022.

[32] Christian Sanner, Nils Huntemann, Richard Lange, Christian Tamm, Ekkehard Peik, Marianna S Safronova, and Sergey G Porsev. Optical clock comparison for lorentz symmetry testing. Nature, 567(7747):204–208, 2019.

[33] MS Safronova, D Budker, D DeMille, Derek F Jackson Kimball, A Derevianko, and Charles W Clark. Search for new physics with atoms and molecules. Reviews of Modern Physics, 90(2):025008, 2018.

[34] M Filzinger, S Dörscher, R Lange, J Klose, M Steinel, E Benkler, E Peik, C Lisdat, and N Huntemann. Improved limits on the coupling of ultralight bosonic dark matter to photons from optical atomic clock comparisons. Physical Review Letters, 130(25): 253001, 2023.

[35] Scott A Diddams, James C Bergquist, Steven R Jefferts, and Christopher W Oates. Standards of time and frequency at the outset of the 21st century. Science, 306(5700): 1318–1324, 2004.

[36] Bernardo Jaduszliwer and James Camparo. Past, present and future of atomic clocks for gnss. GPS Solutions, 25(1):27, 2021.

[37] Bonnie L Schmittberger and David R Scherer. A review of contemporary atomic frequency standards. arXiv preprint arXiv:2004.09987, 2020.

[38] Dmitry Budker and Michael Romalis. Optical magnetometry. Nature physics, 3(4): 227–234, 2007.

[39] Iannis K Kominis, Thomas W Kornack, Joel C Allred, and Michael V Romalis. A subfemtotesla multichannel atomic magnetometer. Nature, 422(6932):596–599, 2003.

[40] Brent Graner, Y Chen, EG Lindahl, and BR Heckel. Reduced limit on the permanent electric dipole moment of hg 199. Physical review letters, 116(16):161601, 2016.

[41] DP Aguillard, T Albahri, D Allspach, J Annala, K Badgley, S Baeßler, I Bailey, L Bailey, E Barlas-Yucel, T Barrett, et al. Measurement of the positive muon anomalous magnetic moment to 127 ppb. Physical review letters, 135(10):101802, 2025.

[42] Samer Afach, Ben C Buchler, Dmitry Budker, Conner Dailey, Andrei Derevianko, Vincent Dumont, Nataniel L Figueroa, Ilja Gerhardt, Zoran D Grujić, Hong Guo, et al. Search for topological defect dark matter with a global network of optical magnetometers. Nature Physics, 17(12):1396–1401, 2021.

[43] Elena Boto, Niall Holmes, James Leggett, Gillian Roberts, Vishal Shah, Sofie S Meyer, Leonardo Duque Muñoz, Karen J Mullinger, Tim M Tierney, Sven Bestmann, et al. Moving magnetoencephalography towards real-world applications with a wearable system. Nature, 555(7698):657–661, 2018.

[44] IM Savukov and Michael V Romalis. Nmr detection with an atomic magnetometer. Physical review letters, 94(12):123001, 2005.

[45] T.F. Gallagher. Rydberg Atoms. Cambridge University Press, 2005. doi: 10.1007/978-0-387-26308-3_14.

[46] Charles S Adams, Jonathan D Pritchard, and James P Shaffer. Rydberg atom quantum technologies. Journal of Physics B: Atomic, Molecular and Optical Physics, 53(1): 012002, 2019. doi: 10.1088/1361-6455/ab52ef.

[47] D. Jaksch, J. I. Cirac, P. Zoller, S. L. Rolston, R. Côté, and M. D. Lukin. Fast quantum gates for neutral atoms. Physical review letters, 85(10):2208–2211, 2000. doi: 10.1103/PhysRevLett.85.2208.

[48] M. Saffman, T. G. Walker, and K. Mølmer. Quantum information with Rydberg atoms. Rev. Mod. Phys., 82(3):2313–2363, 2010. doi: 10.1103/RevModPhys.82.2313.

[49] Antoine Browaeys and Thierry Lahaye. Many-body physics with individually controlled Rydberg atoms. Nat. Phys., 16(2):132–142, 2020. doi: 10.1038/s41567-019-0733-z.

[50] A. Osterwalder and F. Merkt. Using high Rydberg states as electric field sensors. Phys. Rev. Lett., 82(9):1831–1834, 1999. doi: 10.1103/PhysRevLett.82.1831.

[51] Noah Schlossberger, Nikunj Prajapati, Samuel Berweger, Andrew P. Rotunno, Alexandra B. Artusio-Glimpse, Matthew T. Simons, Abrar A. Sheikh, Eric B. Norrgard, Stephen P. Eckel, and Christopher L. Holloway. Rydberg states of alkali atoms in atomic vapour as SI-traceable field probes and communications receivers. Nat. Rev. Phys., 6(10):606–620, 2024. doi: 10.1038/s42254-024-00756-7.

[52] K.-J. Boller, A. Imamoğlu, and S. E. Harris. Observation of electromagnetically induced transparency. Phys. Rev. Lett., 66(20):2593–2596, 1991. doi: 10.1103/PhysRevLett.66.2593.

[53] J. A. Sedlacek, A. Schwettmann, H. Kübler, R. Löw, T. Pfau, and J. P. Shaffer. Microwave electrometry with Rydberg atoms in a vapour cell using bright atomic resonances. Nat. Phys., 8:819, 2012. doi: 10.1038/nphys2423.

[54] C. L. Holloway, J. A. Gordon, S. Jefferts, A. Schwarzkopf, D. A. Anderson, S. A. Miller, N. Thaicharoen, and G. Raithel. Broadband Rydberg atom-based electric-field probe for SI-traceable, self-calibrated measurements. IEEE Trans. Antennas Propag., 62(12):6169–6182, 2014. doi: 10.1109/TAP.2014.2360208.

[55] David Alexander Anderson, Rachel Elizabeth Sapiro, and Georg Raithel. An atomic receiver for AM and FM radio communication. IEEE Trans. Antennas Propag., 69: 2455–2462, 2021. doi: 10.1109/TAP.2020.2987112.

[56] Alexandra Artusio-Glimpse, Matthew T Simons, Nikunjkumar Prajapati, and Christopher L Holloway. Modern rf measurements with hot atoms: A technology review of rydberg atom-based radio frequency field sensors. IEEE Microwave Magazine, 23(5): 44–56, 2022.

[57] David H. Meyer, Paul D. Kunz, and Kevin C. Cox. Waveguide-coupled rydberg spectrum analyzer from 0 to 20 ghz. Phys. Rev. Appl., 15(1):014053, 2021. doi: 10.1103/PhysRevApplied.15.014053.

[58] Lu Ma, Eric Paradis, and Georg Raithel. DC electric fields in electrode-free glass vapor cell by photoillumination. Opt. Express, 28(3):3676–3685, 2020. doi: 10.1364/OE.380748.

[59] L. Ma, D. A. Anderson, and G. Raithel. Paschen-back effects and Rydberg-state diamagnetism in vapor-cell electromagnetically induced transparency. Phys. Rev. A, 95:061804, 2017. doi: 10.1103/PhysRevA.95.061804.

[60] A. Duspayev, R. Cardman, D. A. Anderson, and G. Raithel. High-angular-momentum Rydberg states in a room-temperature vapor cell for dc electric-field sensing. Phys. Rev. Res., 6(2):023138, 2024. doi: 10.1103/PhysRevResearch.6.023138.

[61] Alisher Duspayev and Georg Raithel. Electric field analysis in a cold-ion source using Stark spectroscopy of Rydberg atoms. Phys. Rev. Appl., 19(4):044051, 2023. doi: 10.1103/PhysRevApplied.19.044051.

[62] A. D. Cronin, J. Schmiedmayer, and D. E. Pritchard. Optics and interferometry with atoms and molecules. Rev. Mod. Phys., 81(3):1051, 2009. doi: 10.1103/RevModPhys.81.1051.

[63] M. G. Tarallo, T. Mazzoni, N. Poli, D. V. Sutyrin, X. Zhang, and G. M. Tino. Test of Einstein equivalence principle for 0-spin and half-integer-spin atoms: search for spin-gravity coupling effects. Phys. Rev. Lett., 113(2):023005, 2014. doi: 10.1103/PhysRevLett.113.023005.

[64] D. Schlippert, J. Hartwig, H. Albers, L. L. Richardson, C. Schubert, A. Roura, W. P. Schleich, W. Ertmer, and E. M. Rasel. Quantum test of the universality of free fall. Phys. Rev. Lett., 112(20):203002, 2014. doi: 10.1103/PhysRevLett.112.203002.

[65] T. Kovachy, P. Asenbaum, C. Overstreet, C. A. Donnelly, S. M. Dickerson, A. Sugarbaker, J. M. Hogan, and M. A. Kasevich. Quantum superposition at the half-metre scale. Nature, 528(7583):530, 2015. doi: 10.1038/nature16155.

[66] M. Jaffe, P. Haslinger, V. Xu, P. Hamilton, A. Upadhye, B. Elder, J. Khoury, and H. Müller. Testing sub-gravitational forces on atoms from a miniature in-vacuum source mass. Nat. Phys., 13(10):938, 2017. doi: 10.1038/nphys4189.

[67] G. Rosi, G. D'Amico, L. Cacciapuoti, F. Sorrentino, M. Prevedelli, M. Zych, Č. Brukner, and G. M. Tino. Quantum test of the equivalence principle for atoms in coherent superposition of internal energy states. Nat. Commun., 8(1):15529, 2017. doi: 10.1038/ncomms15529.

[68] J. B. Fixler, G. T. Foster, J. M. McGuirk, and M. A. Kasevich. Atom interferometer measurement of the Newtonian constant of gravity. Science, 315(5808):74, 2007. doi: 10.1126/science.1135459.

[69] R. H. Parker, C. Yu, W. Zhong, B. Estey, and H. Müller. Measurement of the fine-structure constant as a test of the Standard Model. Science, 360(6385):191, 2018. doi: 10.1126/science.aap7706.

[70] V. Xu, M. Jaffe, C. D. Panda, S. L. Kristensen, L. W. Clark, and H. Müller. Probing gravity by holding atoms for 20 seconds. Science, 366(6466):745, 2019. doi: 10.1126/science.aay6428.

[71] L. Morel, Z. Yao, P. Cladé, and S. Guellati-Khélifa. Determination of the fine-structure constant with an accuracy of 81 parts per trillion. Nature, 588(7836):61, 2020. doi: 10.1038/s41586-020-2964-7.

[72] K. Bongs, M. Holynski, J. Vovrosh, P. Bouyer, G. Condon, E. Rasel, C. Schubert, W. P. Schleich, and A. Roura. Taking atom interferometric quantum sensors from the laboratory to real-world applications. Nat. Rev. Phys., 1(12):731, 2019. doi: 10.1038/s42254-019-0117-4.

[73] National Academies of Sciences. Plasma Science: Enabling Technology, Sustainability, Security, and Exploration. The National Academies Press, Washington, DC, 2021. ISBN 978-0-309-67760-8. doi: 10.17226/25802.

[74] T Lafleur and P Chabert. Is collisionless heating in capacitively coupled plasmas really collisionless? Plasma Sources Science and Technology, 24(4):044002, 2015. ISSN 0963-0252. doi: 10.1088/0963-0252/24/4/044002.

[75] Igor Adamovich, Sumit Agarwal, Eduardo Ahedo, Luís Lemos Alves, Scott Baalrud, Natalia Babaeva, Annemie Bogaerts, Anne Bourdon, Peter J Bruggeman, C Canal, et al. The 2022 plasma roadmap: low temperature plasma science and technology. J. Phys. D: Appl. Phys., 55(37):373001, 2022. doi: 10.1088/1361-6463/ac5e1c.

[76] J Schulze, Z Donkó, A Derzsi, I Korolov, and E Schuengel. The effect of ambipolar electric fields on the electron heating in capacitive rf plasmas. Plasma Sources Science and Technology, 24(1):015019, December 2014. ISSN 0963-0252. doi: 10.1088/0963-0252/24/1/015019.

[77] Scott D Baalrud, Brett Scheiner, Benjamin T Yee, Matthew M Hopkins, and Edward Barnat. Interaction of biased electrodes and plasmas: sheaths, double layers, and fireballs. Plasma Sources Science and Technology, 29(5):053001, May 2020. ISSN 0963-0252. doi: 10.1088/1361-6595/ab8177.

[78] V A Godyak and V I Demidov. Probe measurements of electron-energy distributions in plasmas: what can we measure and how can we achieve reliable results? J. Phys. D, 44(23):233001, 2011. doi: 10.1088/0022-3727/44/23/233001.

[79] Benjamin M Goldberg, Tomáš Hoder, and Ronny Brandenburg. Electric field determination in transient plasmas: in situ and non-invasive methods. PSST, 31(7):073001, 2022. doi: 10.1088/1361-6595/ac6e03.

[80] Walter R. Lempert, Sean P. Kearney, and Edward V. Barnat. Diagnostic study of four-wave-mixing-based electric-field measurements in high-pressure nitrogen plasmas. Appl. Opt., 50(29):5688–5694, 2011. doi: 10.1364/AO.50.005688.

[81] Benjamin M Goldberg, Ivan Shkurenkov, Sean O'Byrne, Igor V Adamovich, and Walter R Lempert. Electric field measurements in a dielectric barrier nanosecond pulse discharge with sub-nanosecond time resolution. PSST, 24(3):035010, may 2015. doi: 10.1088/0963-0252/24/3/035010.

[82] Benjamin M. Goldberg, Stephan Reuter, Arthur Dogariu, and Richard B. Miles. 1D time evolving electric field profile measurements with sub-ns resolution using the E-FISH method. Opt. Lett., 44(15):3853–3856, 2019. doi: 10.1364/OL.44.003853.

[83] Arthur Dogariu, Benjamin M. Goldberg, Sean O'Byrne, and Richard B. Miles. Species-independent femtosecond localized electric field measurement. Phys. Rev. Appl., 7(2): 024024, 2017. doi: 10.1103/PhysRevApplied.7.024024.

[84] Grayson LaCombe, Jianan Wang, Kraig Frederickson, and Marien Simeni Simeni. Sub-1 v/cm e-fish-based picosecond electric field measurements in atmospheric pressure air. Plasma Sources Science and Technology, 34(2):025001, 2025.

[85] Hans R. Griem. Principles of Plasma Spectroscopy. Cambridge University Press, 1997.

[86] M. M. Kuraica and N. Konjević. Electric field measurement in the cathode fall region of a glow discharge in helium. Appl. Phys. Lett., 70(12):1521–1523, 1997. doi: 10.1063/1.118606.

[87] E. Brose. Stärke des elektrischen feldes und zerlegung der wasserstofflinien vor der kathode des glimmstroms. Ann. Phys. (Berlin), 363(8):731–752, 1919. doi: 10.1002/andp.19193630806.

[88] K. Takiyama, K. Kadota, T. Oda, M. Hamamoto, T. Ohgo, Y. Kamiura, K. Adati, and J. Fujita. Development of li beam probing and laser-induced fluorescence technique for electric field measurement in a plasma. Review of Scientific Instruments, 59(11): 2351–2356, November 1988. ISSN 0034-6748. doi: 10.1063/1.1139960.

[89] Ronald K. Hanson. Planar laser-induced fluorescence imaging. Journal of Quantitative Spectroscopy and Radiative Transfer, 40(3):343–362, September 1988. ISSN 0022-4073. doi: 10.1016/0022-4073(88)90125-2.

[90] U. Czarnetzki, D. Luggenhoelscher, and H. F. Doebele. Space and time resolved electric field measurements in helium and hydrogen RF-discharges. PSST, 8(2):230, may 1999. ISSN 0963-0252. doi: 10.1088/0963-0252/8/2/004.

[91] U. Czarnetzki, D. Luggenhölscher, V. A. Kadetov, and H. F. Döbele. Plasma diagnostics by laser spectroscopic electric field measurement. Pure and Applied Chemistry, 77(2):345–358, 2005. doi: 10.1351/pac200577020345.

[92] K. Takizawa, K. Sasaki, and A. Kono. Sensitive measurements of electric field distributions in low-pressure ar plasmas by laser-induced fluorescence-dip spectroscopy. Appl. Phys. Lett., 84(2):185–187, 2004. doi: 10.1063/1.1639943.

[93] K. Takizawa, A. Kono, and K. Sasaki. Distribution of electric field in the sheath of an electronegative plasma. Appl. Phys. Lett., 90(1):011503, 2007. doi: 10.1063/1.2429026.

[94] Julius Plucker and Johann Wilhelm Hittorf. I. on the spectra of ignited gases and vapours, with especial regard to the different spectra of the same elementary gaseous substance. Philosophical Transactions of the Royal Society of London, (155):1–29, December 1865. ISSN 0261-0523. doi: 10.1098/rstl.1865.0001.

[95] Enrico Fermi. Sopra lo spostamento per pressione delle righe elevate delle serie spettrali. Il Nuovo Cimento (1924-1942), 11:157–166, 1934. doi: 10.1007/BF02959829.

[96] A. Omont. On the theory of collisions of atoms in Rydberg states with neutral particles. J. Phys. France, 38(11):1343–1359, 1977. doi: 10.1051/jphys:0197700380110134300.

[97] I.L Beigman and V.S Lebedev. Collision theory of Rydberg atoms with neutral and charged particles. Phys. Rep., 250(3):95–328, 1995. doi: https://doi.org/10.1016/0370-1573(95)00074-Q.

[98] B Kaulakys. Broadening and shift of Rydberg levels by elastic collisions with rare-gas atoms. J. Phys. B, 17(22):4485, 1984. doi: 10.1088/0022-3700/17/22/010.

[99] V A Alekseev and I I Sobel'man. A spectroscopic method for the investigation of elastic scattering of slow electrons. Sov. Phys. JETP, 22:882, 1966.

[100] D M Bruce, M Y Mirza, and W W Duley. Collision broadening and shift of the S and D Rydberg levels of rubidium by He and Ar. Opt. Commun., 40(5):347–352, 1982. doi: 10.1016/0030-4018(82)90360-1.

[101] KH Weber and K Niemax. Impact broadening and shift of rb ns and nd levels by noble gases. Zeitschrift für Physik A Atoms and Nuclei, 307(1):13–24, 1982.

[102] Wan-Ü L. Brillet and A. Gallagher. Inert-gas collisional broadening and shifts of Rb Rydberg states. Phys. Rev. A, 22(3):1012–1017, 1980. doi: 10.1103/PhysRevA.22.1012.

[103] D. C. Thompson, E. Kammermayer, B. P. Stoicheff, and E. Weinberger. Pressure shifts and broadenings of rb rydberg states by ne, kr, and h_2. Phys. Rev. A, 36(5):2134–2141, 1987. doi: 10.1103/PhysRevA.36.2134.

[104] Ran Finkelstein, Samir Bali, Ofer Firstenberg, and Irina Novikova. A practical guide to electromagnetically induced transparency in atomic vapor. New J. Phys., 25(3):035001, 2023. doi: 10.1088/1367-2630/acbc40.

[105] Jun Ye. Essay: Quantum Sensing with Atomic, Molecular, and Optical Platforms for Fundamental Physics. Physical Review Letters, 132(19), 2024. doi: 10.1103/PhysRevLett.132.190001.

[106] M Marinescu, HR Sadeghpour, and A Dalgarno. Dispersion coefficients for alkali-metal dimers. Physical Review A, 49(2):982, 1994.

[107] James Mitroy, Marianna S Safronova, and Charles W Clark. Theory and applications of atomic and ionic polarizabilities. Journal of Physics B: Atomic, Molecular and Optical Physics, 43(20):202001, 2010.

[108] Daniel A. Steck. Rubidium 85 D line data. Available online at http://steck.us/alkalidata, 2025. Revision 2.3.4, August 8, 2025.

[109] Hidetoshi Katori and Fujio Shimizu. Lifetime measurement of the 1 s 5 metastable state of argon and krypton with a magneto-optical trap. Physical review letters, 70 (23):3545, 1993.

[110] Norma E Small-Warren and Lue-Yung Chow Chiu. Lifetime of the metastable p 2 3 and p 0 3 states of rare-gas atoms. Physical Review A, 11(6):1777, 1975.

[111] Michael A Lieberman and Allan J Lichtenberg. Principles of plasma discharges and materials processing. MRS Bulletin, 30(12):899–901, 1994. doi: 10.1002/0471724254.

[112] Myron L Zimmerman, Michael G Littman, Michael M Kash, and Daniel Kleppner. Stark structure of the rydberg states of alkali-metal atoms. Physical Review A, 20(6): 2251, 1979.

[113] Harold J Metcalf and Peter Van der Straten. Laser cooling and trapping. Springer Science & Business Media, 1999.

[114] Eric L Raab, Mara Prentiss, Alex Cable, Steven Chu, and David E Pritchard. Trapping of neutral sodium atoms with radiation pressure. Physical review letters, 59(23):2631, 1987.

[115] Michael Fleischhauer, Atac Imamoglu, and Jonathan P. Marangos. Electromagnetically induced transparency: Optics in coherent media. Rev. Mod. Phys., 77(2):633–673, 2005. doi: 10.1103/RevModPhys.77.633.

[116] Petr M. Anisimov. Objectively discerning autler-townes splitting from electromagnetically induced transparency. Physical Review Letters, 107(16), 2011. doi: 10.1103/PhysRevLett.107.163604.

[117] A Urvoy, C Carr, R Ritter, C S Adams, K J Weatherill, and R Löw. Optical coherences and wavelength mismatch in ladder systems. Journal of Physics B: Atomic, Molecular and Optical Physics, 46(24):245001, November 2013. ISSN 0953-4075. doi: 10.1088/0953-4075/46/24/245001.

[118] M Stähler, R Wynands, S Knappe, John Kitching, L Hollberg, A Taichenachev, and V Yudin. Coherent population trapping resonances in thermal 85rb vapor: D 1 versus d 2 line excitation. Optics letters, 27(16):1472–1474, 2002.

[119] Stephanie M Bohaichuk, Fabian Ripka, Vijin Venu, Florian Christaller, Chang Liu, Matthias Schmidt, Harald Kübler, and James P Shaffer. Three-photon rydberg-atom-based radio-frequency sensing scheme with narrow linewidth. Physical Review Applied, 20(6):L061004, 2023.

[120] Anu Babusenan, Jean-Baptiste Qu, et al. Rydberg atom rf sensing: State of the art, principles, metrics and roadmaps. IEEE Sensors Reviews, 2026.

[121] Ya-Fen Hsiao, Pin-Ju Tsai, Hung-Shiue Chen, Sheng-Xiang Lin, Chih-Chiao Hung, Chih-Hsi Lee, Yi-Hsin Chen, Yong-Fan Chen, Ite A Yu, and Ying-Cheng Chen. Highly efficient coherent optical memory based on electromagnetically induced transparency. Physical review letters, 120(18):183602, 2018.

[122] Jacques Vanier. Atomic clocks based on coherent population trapping: a review. Applied Physics B, 81(4):421–442, 2005.

[123] A Nagel, L Graf, A Naumov, E Mariotti, V Biancalana, D Meschede, and R Wynands. Experimental realization of coherent dark-state magnetometers. EPL (Europhysics Letters), 44(1):31–36, 1998.

[124] John W Farley and William H Wing. Accurate calculation of dynamic stark shifts and depopulation rates of rydberg energy levels induced by blackbody radiation. hydrogen, helium, and alkali-metal atoms. Physical Review A, 23(5):2397, 1981.

[125] Michel Baranger. General impact theory of pressure broadening. Phys. Rev., 112(3): 855–865, 1958. doi: 10.1103/PhysRev.112.855.

[126] HSW Massey. Collisions between atoms and molecules at ordinary temperatures. Reports on Progress in Physics, 12(1):248–269, 1949.

[127] Bineet Dash, Nithiwadee Thaicharoen, Eric Paradis, Alisher Duspayev, and Georg Raithel. Rydberg electromagnetically induced transparency of 85Rb vapor in Ar, Ne, and N2 gases. APL Quantum, 2(1):016132, 2025. doi: 10.1063/5.0237759.

[128] Alisher Duspayev, Bineet Dash, and Georg Raithel. Effects of inert background gases and photoillumination on three-color electromagnetically induced transparency of rubidium vapor. Physical Review Applied, 24(4):044057, 2025.

[129] O. Firstenberg, M. Shuker, R. Pugatch, D. R. Fredkin, N. Davidson, and A. Ron. Theory of thermal motion in electromagnetically induced transparency: Effects of diffusion, doppler broadening, and dicke and ramsey narrowing. Phys. Rev. A, 77(4): 043830, 2008. doi: 10.1103/PhysRevA.77.043830.

[130] N. Thaicharoen, R. Cardman, and G. Raithel. Rydberg electromagnetically induced transparency of ^{85}Rb vapor in a cell with Ne buffer gas. Phys. Rev. Appl., 21(6): 064004, 2024. doi: 10.1103/PhysRevApplied.21.064004.

[131] E. Hansis, T. Cubel, J.-H. Choi, J. R. Guest, and G. Raithel. Simple pressure-tuned Fabry–Pérot interferometer. Rev. Sci. Instrum., 76(3):033105, 2005. doi: 10.1063/1.1866237.

[132] Vera Bendkowsky, Björn Butscher, Johannes Nipper, James P Shaffer, Robert Löw, and Tilman Pfau. Observation of ultralong-range rydberg molecules. Nature, 458 (7241):1005–1008, 2009.

[133] Chris H. Greene, A. S. Dickinson, and H. R. Sadeghpour. Creation of polar and nonpolar ultra-long-range rydberg molecules. Phys. Rev. Lett., 85(12):2458–2461, 2000. doi: 10.1103/PhysRevLett.85.2458.

[134] JP Shaffer, ST Rittenhouse, and HR Sadeghpour. Ultracold rydberg molecules. Nature communications, 9(1):1965, 2018.

[135] Donald Booth, ST Rittenhouse, Jin Yang, HR Sadeghpour, and JP Shaffer. Production of trilobite rydberg molecule dimers with kilo-debye permanent electric dipole moments. Science, 348(6230):99–102, 2015.

[136] Thomas Niederprüm, Oliver Thomas, Tanita Eichert, Carsten Lippe, Jesús Pérez-Ríos, Chris H Greene, and Herwig Ott. Observation of pendular butterfly rydberg molecules. Nature communications, 7(1):12820, 2016.

[137] HB Milloy, R. W. Crompton, JA Rees, and AG Robertson. The momentum transfer cross section for electrons in argon in the energy range 0–4 eV. Aust. J. Phys., 30(1): 61–72, 1977. doi: 10.1071/PH770061.

[138] GN Haddad and T. F. O'Malley. Scattering cross sections in argon from electron transport parameters. Aust. J. Phys., 35(1):35–40, 1982.

[139] RP McEachran and AD Stauffer. Elastic scattering of electrons from neon and argon. J. Phys. B, 16(21):4023, 1983. doi: 10.1088/0022-3700/16/21/023.

[140] J Ferch, B Granitza, C Masche, and W Raith. Electron-argon total cross section measurements at low energies by time-of-flight spectroscopy. J. Phys. B, 18(5):967, 1985. doi: 10.1088/0022-3700/18/5/017.

[141] SJ Buckman and B Lohmann. Low-energy total cross section measurements for electron scattering from helium and argon. J. Phys. B, 19(16):2547, 1986. doi: 10.1088/0022-3700/19/16/013.

[142] M Weyhreter, B Barzick, A Mann, and F Linder. Measurements of differential cross sections for e-Ar, Kr, Xe scattering at E = 0.05-2 eV. Z. Phys. D, 7:333–347, 1988. doi: 10.1007/BF01439803.

[143] JL Pack, RE Voshall, AV Phelps, and LE Kline. Longitudinal electron diffusion coefficients in gases: Noble gases. J. Appl. Phys., 71(11):5363–5371, 1992. doi: 10.1063/1.350555.

[144] Stephen J Buckman and Jim Mitroy. Analysis of low-energy electron scattering cross sections via effective-range theory. J. Phys. B, 22(9):1365, 1989. doi: 10.1088/0953-4075/22/9/010.

[145] Z Lj Petrovic, T. F. O'Malley, and R. W. Crompton. e^--Ar scattering length from drift velocities measured in argon-hydrogen mixtures. J. Phys. B, 28(15):3309, 1995. doi: 10.1088/0953-4075/28/15/020.

[146] M. Kurokawa, M. Kitajima, K. Toyoshima, T. Kishino, T. Odagiri, H. Kato, M. Hoshino, H. Tanaka, and K. Ito. High-resolution total-cross-section measurements for electron scattering from Ar, Kr, and Xe employing a threshold-photoelectron source. Phys. Rev. A, 84(6):062717, 2011. doi: 10.1103/PhysRevA.84.062717.

[147] Christof Gaiser and Bernd Fellmuth. Polarizability of Helium, Neon, and Argon: New perspectives for gas metrology. Phys. Rev. Lett., 120(12):123203, 2018. doi: 10.1103/PhysRevLett.120.123203.

[148] A. C. Newell and R. C. Baird. Absolute Determination of Refractive Indices of Gases at 47.7 Gigahertz. J. Appl. Phys., 36(12):3751–3759, 1965. doi: 10.1063/1.1713942.

[149] Thomas J Buckley, Jean Hamelin, and Michael R Moldover. Toroidal cross capacitor for measuring the dielectric constant of gases. Rev. Sci. Instrum., 71(7):2914–2921, 2000. doi: 10.1063/1.1150716.

[150] T. F. O'Malley, Larry Spruch, and Leonard Rosenberg. Modification of effective-range theory in the presence of a long-range (r^{-4}) potential. J. Math. Phys., 2(4):491–498, 1961. doi: 10.1063/1.1703735.

[151] T. F. O'Malley. Extrapolation of electron-rare gas atom cross sections to zero energy. Phys. Rev., 130(3):1020–1029, 1963. doi: 10.1103/PhysRev.130.1020.

[152] F B Dunning. Electron-molecule collisions at very low electron energies. J. Phys. B, 28(9):1645, may 1995. doi: 10.1088/0953-4075/28/9/006.

[153] R. W. Crompton. Benchmark measurements of cross sections for electron collisions: Electron swarm methods. Adv. At. Mol. Phys., 33:97, 1994.

[154] Michael J. Brunger and Stephen J. Buckman. Electron–molecule scattering cross-sections. I. Experimental techniques and data for diatomic molecules. Phys. Rep., 357(3):215–458, 2002. ISSN 0370-1573. doi: https://doi.org/10.1016/S0370-1573(01)00032-1.

[155] RH Orcutt and RH Cole. Dielectric constants of imperfect gases. III. Atomic gases, hydrogen, and nitrogen. J. Chem. Phys., 46(2):697–702, 1967. doi: 10.1063/1.1840728.

[156] C. Sol, F. Devos, and J-C. Gauthier. Elastic electron-neutral interaction measurements in neon at ultralow energies. Phys. Rev. A, 12(2):502–507, 1975. doi: 10.1103/PhysRevA.12.502.

[157] R J Gulley, D T Alle, M J Brennan, M J Brunger, and S J Buckman. Differential and total electron scattering from neon at low incident energies. J. Phys. B, 27(12):2593, 1994. doi: 10.1088/0953-4075/27/12/018.

[158] C. R. Hoffmann and H. M. Skarsgard. Momentum-transfer cross sections and conductivity ratios for low-energy electrons in He, Ne, Kr, and Xe. Phys. Rev., 178:168–175, 1969. doi: 10.1103/PhysRev.178.168.

[159] T Koizumi, H Murakoshi, S Yamamoto, and I Ogawa. The characteristic energy and momentum transfer cross section for low-energy electrons in neon. J. Phys. B, 17(21):4387, 1984. doi: 10.1088/0022-3700/17/21/027.

[160] O'Malley T. F. and Crompton R. W. Electron-neon scattering length and S-wave phaseshifts from drift velocities. J. Phys. B, 13(17):3451, 1980. doi: 10.1088/0022-3700/13/17/023.

[161] R.P. McEachran and A.D. Stauffer. Electron scattering from neon. Phys. Lett. A, 107 (8):397–399, 1985. doi: https://doi.org/10.1016/0375-9601(85)90699-1.

[162] A G Robertson. The momentum transfer cross section for low energy electrons in neon. J. Phys. B, 5(3):648, 1972. doi: 10.1088/0022-3700/5/3/032.

[163] C. Gaiser and B. Fellmuth. Experimental benchmark value for the molar polarizability of neon. Europhys. Lett., 90(6):63002, jul 2010. doi: 10.1209/0295-5075/90/63002.

[164] Zbigniew Idziaszek and Grzegorz Karwasz. Modified effective-range theory for low energy e-N_2 scattering. Eur. Phys. J. D, 51(3):347–355, 2009. doi: 10.1140/epjd/e2009-00028-6.

[165] II Fabrikant. Effective-range analysis of low-energy electron scattering by non-polar molecules. J. Phys. B, 17(20):4223, 1984. doi: 10.1088/0022-3700/17/20/020.

[166] Michael A. Morrison, Weiguo Sun, William A. Isaacs, and Wayne K. Trail. Ultrasimple calculation of very-low-energy momentum-transferand rotational-excitation cross sections: e-N_2 scattering. Phys. Rev. A, 55(4):2786–2798, 1997. doi: 10.1103/PhysRevA.55.2786.

[167] E S Chang. Modified effective-range theory for electron scattering from molecules. J. Phys. B, 14(5):893, 1981. doi: 10.1088/0022-3700/14/5/023.

[168] Matthew D Rotondaro and Glen P Perram. Collisional broadening and shift of the rubidium D_1 and D_2 lines ($5^2S_{1/2} \rightarrow 5^2P_{1/2}$, $5^2P_{3/2}$) by rare gases, H_2, D_2, N_2, CH_4 and CF_4. J. Quant. Spectrosc. Radiat. Transf., 57(4):497–507, 1997.

[169] A. Sargsyan, D. Sarkisyan, U. Krohn, J. Keaveney, and C. Adams. Effect of buffer gas on an electromagnetically induced transparency in a ladder system using thermal rubidium vapor. Phys. Rev. A, 82:045806, 2010. doi: 10.1103/PhysRevA.82.045806.

[170] Ch Ottinger, Richard Scheps, G. W. York, and Alan Gallagher. Broadening of the Rb resonance lines by the noble gases. Phys. Rev. A, 11(6):1815, 1975. doi: 10.1103/PhysRevA.11.1815.

[171] Megan E Henry and Roger M Herman. Collisional broadening of Rydberg atom transitions by rare gas perturbers. J. Phys. B, 35(2):373, 2002. doi: 10.1088/0953-4075/35/2/313.

[172] Link Patrick, Noah Schlossberger, Daniel F Hammerland, Nikunjkumar Prajapati, Tate McDonald, Samuel Berweger, Rajavardhan Talashila, Alexandra B Artusio-Glimpse, and Christopher L Holloway. Imaging of induced surface charge distribution effects in glass vapor cells used for rydberg atom-based sensors. AVS Quantum Science, 7(2), 2025.

[173] V A Godyak, R B Piejak, and B M Alexandrovich. Electrical characteristics and electron heating mechanism of an inductively coupled argon discharge. PSST, 3(2): 169, 1994. doi: 10.1088/0963-0252/3/2/007.

[174] EA Kralkina, AA Rukhadze, VB Pavlov, KV Vavilin, PA Nekliudova, AK Petrov, and AF Alexandrov. RF power absorption by plasma of a low-pressure inductive discharge. PSST, 25(1):015016, 2016. doi: 10.1088/0963-0252/25/1/015016.

[175] Bineet Dash, Xinyan Xiang, Dingkun Feng, Eric Paradis, and Georg Raithel. Electric field diagnostics in a continuous rf plasma using rydberg-eit. arXiv preprint arXiv:2512.16867, 2025.

[176] Benjamin M. Goldberg, Tat Loon Chng, Arthur Dogariu, and Richard B. Miles. Electric field measurements in a near atmospheric pressure nanosecond pulse discharge with picosecond electric field induced second harmonic generation. Appl. Phys. Lett., 112(6):064102, 2018. doi: 10.1063/1.5019173.

[177] M Simeni Simeni, Y Tang, K Frederickson, and IV Adamovich. Electric field distribution in a surface plasma flow actuator powered by ns discharge pulse trains. PSST, 27 (10):104001, 2018. doi: 10.1088/1361-6595/aae1c8.

[178] P.K. Chu and X.P. Lu. Low Temperature Plasma Technology: Methods and Applications. Taylor & Francis, 2013.

[179] Stéphane Mazouffre. Laser-induced fluorescence diagnostics of the cross-field discharge of Hall thrusters. PSST, 22(1):013001, 2012. doi: 10.1088/0963-0252/22/1/013001.

[180] Tsv K Popov, MIGLENA Dimitrova, PAVLINA Ivanova, JERNEJ Kovačič, TOMAZ Gyergyek, RENAUD Dejarnac, J Stöckel, MA Pedrosa, D López-Bruna, and C Hidalgo. Advances in Langmuir probe diagnostics of the plasma potential and electron-energy distribution function in magnetized plasma. PSST, 25(3):033001, 2016. doi: 10.1088/0963-0252/25/3/033001.

[181] Andre Melzer, H Krüger, D Maier, and S Schütt. Physics of magnetized dusty plasmas. Reviews of Modern Plasma Physics, 5(1):11, 2021. doi: 10.1007/s41614-021-00060-2.

[182] Cameron A. Moore, Glenn P. Davis, and Richard A. Gottscho. Sensitive, nonintrusive, in-situ measurement of temporally and spatially resolved plasma electric fields. Phys. Rev. Lett., 52(7):538–541, 1984. doi: 10.1103/PhysRevLett.52.538.

[183] J. R. Shoemaker, B. N. Ganguly, and A. Garscadden. Stark spectroscopic measurement of spatially resolved electric field and electric field gradients in a glow discharge. Appl. Phys. Lett., 52(24):2019–2021, 1988. doi: 10.1063/1.99569.

[184] D. Feldbaum, N. V. Morrow, S. K. Dutta, and G. Raithel. Coulomb expansion of laser-excited ion plasmas. Phys. Rev. Lett., 89:173004, 2002. doi: 10.1103/PhysRevLett.89.173004.

[185] Daniel Weller, James P. Shaffer, Tilman Pfau, Robert Löw, and Harald Kübler. Interplay between thermal Rydberg gases and plasmas. Phys. Rev. A, 99(4):043418, 2019. doi: 10.1103/PhysRevA.99.043418.

[186] David A. Anderson, Georg Raithel, Matthew Simons, and Christopher L. Holloway. Quantum-optical spectroscopy for plasma electric field measurements and diagnostics, 2017.

[187] IM El-Fayoumi, IR Jones, and MM Turner. Hysteresis in the E-to H-mode transition in a planar coil, inductively coupled rf argon discharge. J. Phys. D: Appl. Phys., 31 (21):3082, 1998. doi: 10.1088/0022-3727/31/21/014.

[188] Young-Kwang Lee and Chin-Wook Chung. Ionization in inductively coupled argon plasmas studied by optical emission spectroscopy. J. Appl. Phys., 109(1):013306, 2011. doi: 10.1063/1.3530578.

[189] S A Miller, D A Anderson, and G Raithel. Radio-frequency-modulated Rydberg states in a vapor cell. New J. Phys., 18(5):053017, 2016. doi: 10.1088/1367-2630/18/5/053017.

[190] M G Bason, M Tanasittikosol, A Sargsyan, A K Mohapatra, D Sarkisyan, R M Potvliege, and C S Adams. Enhanced electric field sensitivity of rf-dressed Rydberg dark states. New J. Phys., 12(6):065015, 2010. doi: 10.1088/1367-2630/12/6/065015.

[191] Hideo Sugai, Kenji Nakamura Kenji Nakamura, and Keiji Suzuki Keiji Suzuki. Electrostatic coupling of antenna and the shielding effect in inductive rf plasmas. Jpn. J. Appl. Phys, 33(4S):2189, April 1994. ISSN 1347-4065. doi: 10.1143/JJAP.33.2189.

[192] Jean Dalibard, Yvan Castin, and Klaus Mölmer. Wave-function approach to dissipative processes in quantum optics. Phys. Rev. Lett., (5):580–583, 1992. doi: 10.1103/PhysRevLett.68.580.

[193] Klaus Mölmer, Yvan Castin, and Jean Dalibard. Monte Carlo wave-function method in quantum optics. J. Opt. Soc. Am. B, 10:524–538, 1993. doi: 10.1364/JOSAB.10.000524.

[194] Linjie Zhang, Shanxia Bao, Hao Zhang, Georg Raithel, Jianming Zhao, Liantuan Xiao, and Suotang Jia. Interplay between optical pumping and Rydberg EIT in magnetic fields. Opt. Express, 26:29931–29944, 2018. doi: 10.1364/OE.26.029931.

[195] Yongmei Xue, Liping Hao, Yuechun Jiao, Xiaoxuan Han, Suying Bai, Jianming Zhao, and Georg Raithel. Rydberg electromagnetically induced transparency in a large Hilbert space. Phys. Rev. A, 99(5):053426, 2019. doi: 10.1103/PhysRevA.99.053426.

[196] Vincent M Donnelly. Plasma electron temperatures and electron energy distributions measured by trace rare gases optical emission spectroscopy. J. Phys. D: Appl. Phys., 37(19):R217, 2004. doi: 10.1088/0022-3727/37/19/r01.

[197] G. A. Hebner. Spatially resolved, excited state densities and neutral and ion temperatures in inductively coupled argon plasmas. J. Appl. Phys., 80(5):2624–2636, 1996. doi: 10.1063/1.363178.

[198] Marlan O. Scully and M. Suhail Zubairy. Quantum optics. Cambridge University Press, Cambridge, 1997. doi: 10.1017/CBO9780511813993.

[199] J. Holtsmark. Über die Verbreiterung von Spektrallinien. Ann. Phys., 363(7):577–630, 1919. doi: https://doi.org/10.1002/andp.19193630702.

[200] Daniel D Hickstein, Stephen T Gibson, Roman Yurchak, Dhrubajyoti D Das, and Mikhail Ryazanov. A direct comparison of high-speed methods for the numerical abel transform. Review of Scientific Instruments, 90(6), 2019.

[201] Matthew Newville, Renee Otten, Andrew Nelson, Till Stensitzki, Antonino Ingargiola, Daniel Allan, Austin Fox, Faustin Carter, and Michal Rawlik. Lmfit: Non-linear least-squares minimization and curve-fitting for python, July 2025.

[202] V. A. Godyak, R. B. Piejak, and B. M. Alexandrovich. Electron energy distribution function measurements and plasma parameters in inductively coupled argon plasma. PSST, 11(4):525, 2002. doi: 10.1088/0963-0252/11/4/320.

[203] Valery Godyak. RF discharge diagnostics: Some problems and their resolution. J. Appl. Phys., 129(4):041101, 2021. doi: 10.1063/5.0024258.

[204] J.G. Yang, N.S. Yoon, B.C. Kim, J.H. Choi, G.S. Lee, and S.M. Hwang. Power absorption characteristics of an inductively coupled plasma discharge. IEEE Transactions on Plasma Science, 27(3):676–681, 1999. doi: 10.1109/27.774671.

[205] V. A. Godyak and R. B. Piejak. ICP diagnostics with magnetic probes. J. Phys. IV France, 08(PR7):Pr7–256, 1998. doi: 10.1051/jp4:1998720.

[206] Xi-Ming Zhu and Yi-Kang Pu. A simple collisional–radiative model for low-pressure argon discharges. J. Phys. D: Appl. Phys., 40(8):2533, 2007. doi: 10.1088/0022-3727/40/8/018.

[207] J. S. Kim, M. V. V. S. Rao, M. A. Cappelli, S. P. Sharma, and M. Meyyappan. Mass spectrometric and Langmuir probe measurements in inductively coupled plasmas in Ar, CHF_3/Ar and CHF_3/Ar/O_2 mixtures. PSST, 10(2):191, 2001. doi: 10.1088/0963-0252/10/2/309.

[208] James A Schiavone, David E Donohue, David R Herrick, and Robert S Freund. Electron-impact excitation of helium: Cross sections, n, and l distributions of high Rydberg states. Physical Review A, 16(1):48, 1977. doi: https://doi.org/10.1103/PhysRevA.16.48.

[209] Hans R Griem. Stark broadening by electron and ion impacts of nα hydrogen lines of large principal quantum number. Astrophysical Journal, 148:547, 1967. doi: 10.1086/149176.

[210] Edward W. Schlag. ZEKE Spectroscopy. Cambridge University Press, 1998.

[211] S. K. Dutta, D. Feldbaum, A. Walz-Flannigan, J. R. Guest, and G. Raithel. High-angular-momentum states in cold Rydberg gases. Phys. Rev. Lett., 86:3993–3996, 2001. doi: 10.1103/PhysRevLett.86.3993.

[212] A. Walz-Flannigan, J. R. Guest, J.-H. Choi, and G. Raithel. Cold-Rydberg-gas dynamics. Phys. Rev. A, 69:063405, 2004. doi: 10.1103/PhysRevA.69.063405.

[213] Bineet Dash, Michael H Goerz, Alisher Duspayev, Sebastián C Carrasco, Vladimir S Malinovsky, and Georg Raithel. Rotation sensing using tractor atom interferometry. AVS Quantum Science, 6(1), 2024.

[214] Georg Raithel, Alisher Duspayev, Bineet Dash, Sebastián C Carrasco, Michael H Goerz, Vladan Vuletić, and Vladimir S Malinovsky. Principles of tractor atom interferometry. Quantum Science & Technology, 8(1):014001, 2023.

[215] B. Culshaw. The optical fibre Sagnac interferometer: an overview of its principles and applications. Meas. Sci. Technol., 17(1):R1, 2005. doi: 10.1088/0957-0233/17/1/R01.

[216] F. Riehle, Th. Kisters, A. Witte, J. Helmcke, and Ch. J. Bordé. Optical Ramsey spectroscopy in a rotating frame: Sagnac effect in a matter-wave interferometer. Phys. Rev. Lett., 67(2):177, 1991. doi: 10.1103/PhysRevLett.67.177.

[217] T. L. Gustavson, P. Bouyer, and M. A. Kasevich. Precision rotation measurements with an atom interferometer gyroscope. Phys. Rev. Lett., 78(11):2046, 1997. doi: 10.1103/PhysRevLett.78.2046.

[218] C. Schubert, S. Abend, M. Gersemann, M. Gebbe, D. Schlippert, P. Berg, and E. M. Rasel. Multi-loop atomic Sagnac interferometry. Sci. Rep., 11(1):16121, 2021. doi: 10.1038/s41598-021-95334-7.

[219] B. Barrett, R. Geiger, I. Dutta, M. Meunier, B. Canuel, A. Gauguet, P. Bouyer, and A. Landragin. The Sagnac effect: 20 years of development in matter-wave interferometry. Comptes Rendus Physique, 15(10):875, 2014. doi: https://doi.org/10.1016/j.crhy.2014.10.009.

[220] S. M. Dickerson, J. M. Hogan, A. Sugarbaker, D. M. S. Johnson, and M. A. Kasevich. Multiaxis inertial sensing with long-time point source atom interferometry. Phys. Rev. Lett., 111(8):083001, 2013. doi: 10.1103/PhysRevLett.111.083001.

[221] G. W. Hoth, B. Pelle, S. Riedl, J. Kitching, and E. A. Donley. Point source atom interferometry with a cloud of finite size. Appl. Phys. Lett., 109(7):071113, 2016. doi: 10.1063/1.4961527.

[222] Y.-J. Chen, A. Hansen, M. Shuker, R. Boudot, J. Kitching, and E.A. Donley. Robust inertial sensing with point-source atom interferometry for interferograms spanning a partial period. Opt. Express, 28(23):34516, 2020. doi: 10.1364/OE.399988.

[223] S. Wu, E. Su, and M. Prentiss. Demonstration of an area-enclosing guided-atom interferometer for rotation sensing. Phys. Rev. Lett., 99(17):173201, 2007. doi: 10.1103/PhysRevLett.99.173201.

[224] E. R. Moan, R. A. Horne, T. Arpornthip, Z. Luo, A. J. Fallon, S. J. Berl, and C. A. Sackett. Quantum rotation sensing with dual Sagnac interferometers in an atom-optical waveguide. Phys. Rev. Lett., 124(12):120403, 2020. doi: 10.1103/PhysRevLett.124.120403.

[225] M. Beydler, E. R. Moan, Z. Luo, Z. Chu, and C. A. Sackett. Guided-wave Sagnac atom interferometer with large area and multiple orbits. arXiv:2308.11481, 2023.

[226] K. Krzyzanowska, J. Ferreras, C. Ryu, E. C. Samson, and M. Boshier. Matter wave analog of a fiber-optic gyroscope. arXiv:2201.12461, 2022.

[227] W. C. Campbell and P. Hamilton. Rotation sensing with trapped ions. J. Phys. B, 50 (6):064002, 2017. doi: 10.1088/1361-6455/aa5a8f.

[228] L. Qi, Z. Hu, T. Valenzuela, Y. Zhang, Y. Zhai, W. Quan, N. Waltham, and J. Fang. Magnetically guided cesium interferometer for inertial sensing. Appl. Phys. Lett., 110 (15), 2017. doi: 10.1063/1.4980066.

[229] P. Muruganandam and S. K. Adhikari. Bose–Einstein condensation dynamics in three dimensions by the pseudospectral and finite-difference methods. J. Phys. B, 36(12): 2501, 2003. doi: 10.1088/0953-4075/36/12/310.

[230] R. Stevenson, M. R. Hush, T. Bishop, I. Lesanovsky, and T. Fernholz. Sagnac interferometry with a single atomic clock. Phys. Rev. Lett., 115(16):163001, 2015. doi: 10.1103/PhysRevLett.115.163001.

[231] F. Gentile, J. Johnson, K. Poulios, and T. Fernholz. Ring-shaped atom-trap lattices using multipole dressing fields. arXiv:1909.01186, 2019.

[232] C. Ryu and M. G. Boshier. Integrated coherent matter wave circuits. New J. Phys., 17(9):092002, sep 2015. doi: 10.1088/1367-2630/17/9/092002.

[233] T. A. Bell, J. A. P. Glidden, L. Humbert, M. W. J. Bromley, S. A. Haine, M. J. Davis, T. W. Neely, M. A. Baker, and H. Rubinsztein-Dunlop. Bose–Einstein condensation in large time-averaged optical ring potentials. New J. Phys., 18(3):035003, 2016. doi: 10.1088/1367-2630/18/3/035003.

[234] Z. Y. Wang, Z. Zhang, and Q. Lin. Atom interferometers manipulated through the toroidal trap realized by the interference patterns of Laguerre-Gaussian beams. Eur. Phys. J. D, 53:127–131, 2009. doi: 10.1140/epjd/e2009-00116-7.

[235] J. A. Stickney and A. A. Zozulya. Wave-function recombination instability in cold-atom interferometers. Phys. Rev. A, 66(5):053601, 2002. doi: 10.1103/PhysRevA.66.053601.

[236] J. A. Stickney and A. A. Zozulya. Influence of nonadiabaticity and nonlinearity on the operation of cold-atom beam splitters. Phys. Rev. A, 68(1):013611, 2003. doi: 10.1103/PhysRevA.68.013611.

[237] G.-B. Jo, J.-H. Choi, C. A. Christensen, T. A. Pasquini, Y.-R. Lee, W. Ketterle, and D. E. Pritchard. Phase-sensitive recombination of two Bose-Einstein condensates on an atom chip. Phys. Rev. Lett., 98(18):180401, 2007. doi: 10.1103/PhysRevLett.98.180401.

[238] A. Duspayev and G. Raithel. Tractor atom interferometry. Phys. Rev. A, 104(1):013307, 2021. doi: 10.1103/physreva.104.013307.

[239] A. Steffen, A. Alberti, W. Alt, N. Belmechri, S. Hild, M. Karski, A. Widera, and D. Meschede. Digital atom interferometer with single particle control on a discretized space-time geometry. Proc. Natl. Acad. Sci. U.S.A., 109(25):9770, 2012. doi: 10.1073/pnas.1204285109.

[240] G. Premawardhana, J. Kunjummen, S. Subhankar, and J. M. Taylor. Investigating the feasibility of a trapped atom interferometer with movable traps. arXiv:2308.12246, 2023.

[241] T. Kuga, Y. Torii, N. Shiokawa, T. Hirano, Y. Shimizu, and H. Sasada. Novel optical trap of atoms with a doughnut beam. Phys. Rev. Lett., 78(25):4713–4716, 1997. doi: 10.1103/PhysRevLett.78.4713.

[242] S. Franke-Arnold, J. Leach, M. J. Padgett, V. E. Lembessis, D. Ellinas, A. J. Wright, J. M. Girkin, P. Öhberg, and A. S. Arnold. Optical ferris wheel for ultracold atoms. Opt. Express, 15(14):8619, 2007. doi: 10.1364/oe.15.008619.

[243] E. Courtade, O. Houde, J.-F. Clément, P. Verkerk, and D. Hennequin. Dark optical lattice of ring traps for cold atoms. Phys. Rev. A, 74(3):031403, 2006. doi: 10.1103/physreva.74.031403.

[244] L. Amico, A. Osterloh, and F. Cataliotti. Quantum many particle systems in ring-shaped optical lattices. Phys. Rev. Lett., 95(6):063201, 2005. doi: 10.1103/physrevlett.95.063201.

[245] R. E. Sapiro, R. Zhang, and G. Raithel. Atom interferometry using Kapitza-Dirac scattering in a magnetic trap. Phys. Rev. A, 79(4):043630, 2009. doi: 10.1103/PhysRevA.79.043630.

[246] Z. Pagel, W. Zhong, R. H. Parker, C. T. Olund, N. Y. Yao, and H. Müller. Symmetric Bloch oscillations of matter waves. Phys. Rev. A, 102(5):053312, 2020. doi: 10.1103/PhysRevA.102.053312.

[247] M. D. Feit, J. A. Fleck Jr., and A. Steiger. Solution of the Schrödinger equation by a spectral method. J. Comput. Phys., 47:412, 1982. doi: 10.1016/0021-9991(82)90091-2.

[248] R. Kosloff. Time-dependent quantum-mechanical methods for molecular dynamics. J. Chem. Phys., 92:2087, 1988. doi: 10.1021/j100319a003.

[249] H. Tal-Ezer and R. Kosloff. An accurate and efficient scheme for propagating the time dependent Schrödinger equation. J. Chem. Phys., 81:3967, 1984. doi: 10.1063/1.448136.

[250] N. Khaneja, T. Reiss, C. Kehlet, T. Schulte-Herbrüggen, and S. J. Glaser. Optimal control of coupled spin dynamics: design of NMR pulse sequences by gradient ascent algorithms. J. Magnet. Res., 172:296, 2005. doi: 10.1016/j.jmr.2004.11.004.

[251] D. J. Tannor, V. Kazakov, and V. Orlov. Control of photochemical branching: Novel procedures for finding optimal pulses and global upper bounds. In Time-Dependent Quantum Molecular Dynamics, pages 347–360. Springer, 1992.

[252] M. H. Goerz and Contributors. Krotov.jl, 2023.

[253] M. H. Goerz and Contributors. QuantumControl.jl, 2023.

[254] J. P. Palao and R. Kosloff. Optimal control theory for unitary transformations. Phys. Rev. A, 68:062308, 2003. doi: 10.1103/PhysRevA.68.062308.

[255] D. Guéry-Odelin, A. Ruschhaupt, A. Kiely, E. Torrontegui, S. Martínez-Garaot, and J. G. Muga. Shortcuts to adiabaticity: Concepts, methods, and applications. Rev. Mod. Phys., 91:045001, 2019. doi: 10.1103/revmodphys.91.045001.

[256] Lefeng Zhou, Anne Graf, and Georg Raithel. Sagnac tractor atom interferometer on a photonic integrated circuit. EPJ Quantum Technology, 13(1):42, 2026.

[257] J Hopwood. Review of inductively coupled plasmas for plasma processing. Plasma Sources Science and Technology, 1(2):109–116, 1992.

[258] Noah Schlossberger, Tate McDonald, Kevin Su, Rajavardhan Talashila, Robert Behary, Charles L. Patrick, Daniel Hammerland, Eugeniy E. Mikhailov, Seth Aubin, Irina Novikova, Christopher L. Holloway, and Nikunjkumar Prajapati. Two-dimensional imaging of electromagnetic fields via light-sheet fluorescence imaging with rydberg atoms. Optics Letters, Vol. 50, Issue 23, pp. 7312-7315, December 2025. doi: 10.1364/OL.566697.

[259] Job Beckers, Johannes Berndt, Dietmar Block, Michael Bonitz, PJ Bruggeman, Lénaïc Couëdel, Gian Luca Delzanno, Yan Feng, R Gopalakrishnan, Franko Greiner, et al. Physics and applications of dusty plasmas: The perspectives 2023. Physics of Plasmas, 30(12), 2023.

[260] Wentao Yu, Eslam Abdelaleem, Ilya Nemenman, and Justin C Burton. Physics-tailored machine learning reveals unexpected physics in dusty plasmas. Proceedings of the National Academy of Sciences, 122(31):e2505725122, 2025.

[261] RS Marshall and PM Bellan. Laser-induced fluorescence measurement of very slow neutral flows in a dusty plasma experiment. Review of Scientific Instruments, 91(6), 2020.

[262] Roland Chodura. Plasma–wall transition in an oblique magnetic field. The Physics of Fluids, 25(9):1628–1633, 1982.

[263] A. Gerakis, M. N. Shneider, and B. C. Stratton. Remote-sensing gas measurements with coherent rayleigh-brillouin scattering. Applied Physics Letters, 109(3):031112, 2016. ISSN 0003-6951. doi: 10.1063/1.4959778.

[264] Tyler J Gilbert, Thomas E Steinberger, and Earl E Scime. Non-intrusive measurement of magnetic field strengths in a low-pressure argon plasma using quantum beat spectroscopy. Plasma Sources Science and Technology, 34(2):025020, February 2025. ISSN 0963-0252. doi: 10.1088/1361-6595/adb784.

[265] Thomas C Killian, T Pattard, T Pohl, and JM Rost. Ultracold neutral plasmas. Physics reports, 449(4-5):77–130, 2007.

[266] Michael A. Viray, Stephanie A. Miller, and Georg Raithel. Coulomb expansion of a cold non-neutral rubidium plasma. Phys. Rev. A, 102(3):033303, 2020. doi: 10.1103/PhysRevA.102.033303.